X-ray scattering studies of compound semiconductors

Caroline Dale Moore

X-Ray Scattering Studies of Compound Semiconductors

by

Caroline Dale Moore

A Thesis submitted in partial fulfilment of the requirements for the degree of Doctor of Philosophy

University of Durham

1997

Abstract

In this thesis, techniques of high resolution x-ray diffraction, topography and grazing incidence reflectivity have been employed in order to gain information on compound semiconductors. A recent growth technique, Vertical Gradient Freeze (VGF), has been investigated for 2" InP wafers, and been found to produce virtually dislocation-free crystals. In the one wafer where dislocations have been imaged, they have a density of ~200cm^{-2}, with Burgers vectors lying in the plane of the wafer. This is in contrast to topographs of Liquid Encapsulated Czochralski (LEC) InP, where a dislocation density of up to 6.10^{4}cm^{-2} was observed at the wafer periphery. No growth striations were observed in VGF samples, implying a planar solid-melt interface. VGF GaAs wafers are seen to be virtually dislocation free when Si doped, have dislocation densities of 900cm^{-2} when undoped and 1200cm^{-2} when Zn doped.

Triple axis diffraction measurements showed a variation in tilts between samples, but no strain variation. The tilt variation was attributed to the polishing process. Asymmetric scans showed a variation in strain at high tilts. These data have been used to form a model for the crystal surface: mosaic blocks of perfect crystal surrounded by low angle boundaries consisting of rows of edge dislocations. During the polishing process, these blocks are physically rotated, evidence for which is supplied from analysis of the specular part of reflectivity scans. Specular and diffuse reflectivity scans on InP substrates have been simulated using the Distorted Wave Born Approximation (DWBA). In all cases a 30Å thick oxide layer was identified on the sample surface. In order to obtain a good simulation for transverse scans at two values of q_z, it was necessary to include a grading in electron density at the top surface.

Epitaxial layers of $Hg_{1-x}Mn_xTe$ (MMT) grown by the Interdiffused Multilayer Process (IMP) on GaAs with a CdTe buffer layer have been characterised using double and triple axis diffraction. Although reasonable compositional uniformity was observed across the wafers (from 0.3%mm^{-1}), dynamical simulations of pseudo-triple axis scans showed a grading in composition with depth. It was observed that the crystalline perfection deteriorated with increased Mn fraction. The MMT and CdTe layers were almost fully relaxed, and were found to have dislocation densities of 10^{7}-10^{9}cm^{-2}. In one sample the presence of zinc blende MnTe was established using double axis diffraction.

Finally, the high intensity of the European Synchrotron Radiation Facility (ESRF) has been exploited in order to topograph highly absorbing materials. The effect of heater failure in the growth of GaAs in space has been shown to produce high levels of strain and twinning. It has also been shown topographically that contact with the crucible during the growth of GaInSb from the melt leads to increased strain, so de-wetting phenomena improve crystalline growth.

Declaration

I declare that this thesis is original, and all the work presented in it is my own. No part of this thesis has been submitted for a degree in this or in any other University.

The samples analysed in this thesis were kindly provided by the following:

Chapter IV

InP 2" Wafers	:	Epitaxial Products International Ltd., Cardiff

Chapter V

GaAs 2" Wafers	:	Epitaxial Products International Ltd., Cardiff

Chapter VI

$Hg_{1-x}Mn_xTe$/GaAs epilayers	:	Dr. S. Oktik, University of Durham

Chapter VII

GaAs wafers	:	Dr. G. Mueller, University of Erlangen
GaSb and $Ga_{1-x}In_xSb$	:	Dr. T. Duffar, Centres d'Etudes Nucleaires de Grenoble

Acknowledgements

I would like to thank Prof. D. Bloor and Prof. B.K. Tanner for allowing me to use the facilities of the Department of Physics during the course of this work. During my Ph.D. I have been grateful for funding from the Engineering and Physical Sciences Research Council (EPSRC), Epitaxial Products International and Bede Scientific Ltd., the last two through a CASE studentship. Employees (and managers!) of these two firms have been especially generous with their time and expertise. Deserving of especial mention are Mr. R. Blunt, of E.P.I., for his infinite wisdom on materials and devices (not to mention the provision of most of the samples), Dr. N. Loxley and Dr. D.K. Bowen for the use of Bede equipment, Dr T. Lafford for knowing everything about D3 diffractometers, and Mr. M. Wormington for writing the excellent reflectivity code used here. In addition, I am grateful to my supervisor Prof. B.K. Tanner for his ideas and timely suggestions.

Much of the work presented here was carried out at the SRS Daresbury Laboratory. I would like to thank the control room and security staff for their assistance in times of need, and Mr D. Hands for his cheerful supplying of photographic equipment. I am grateful to Dr. C. Tang for his help on Station 2.3, and to Dr. G. Clark for introducing me to topography and Station 7.6. University groups in other countries have been most hospitable. Especial thanks go to Dr. J. Baruchel, Dr. J. Hartwig and the topography group at the ESRF, and to Prof. U. Pietsch and grazing incidence diffraction group at the University of Potsdam. In Durham, many people have assisted with experiments or analysis. Most notable among these are John Dobson, Tim Hallam, Thomas Hase, Valeriy Khrupa, Chaorong Li, Peter Möck, Ruth Port, Ian Pape, Dirk Rose and Mehdi Safa. Others in the group who have assisted in their own inimical ways are Nikki Bingham, John Clarke, Ian Daniel, Brian Fulthorpe, Hamidi Hamid, Alton Horsfall and Marco Poli. Most of all my thanks go to Chris Leighton for endless proof reading, discussions and ideas.

Finally I would like to thank my mother, father and sister Helen for their support and encouragement.

List of Publications

From Chapter IV:

C.D.Moore, I.Pape and B.K. Tanner "Triple axis x-ray diffraction study of polishing damage in III-V semiconductors", *Acta Cryst.* **A52**, C369, 1996

C.D.Moore, T.P.A. Hase and B.K.Tanner "Grazing incidence x-ray scattering for the characterisation of InP wafers", Accepted for *Adv. X-Ray Anal.* **40**, 1997

C.D.Moore, I.Pape and B.K.Tanner "Triple axis x-ray diffraction study of polishing damage in III-V semiconductors" Accepted for *Il Nuovo Cimento*, 1997

From Chapter VI

T.D.Hallam, S.Oktik, M.Funaki, C.D.Moore, A.W.Brinkman, K.Durose, B.K.Tanner "Uniformity in (Hg,Mn)Te films grown by metalorganic vapour phase epitaxy", *J. Cryst. Growth* **146** 604-609, 1995

and related..

R.I.Port, C.D.Moore, B.K.Tanner, K.Durose, J.E.Hails "Depth resolved x-ray studies of tilt distributions in CdTe/GaAs epilayers" *Inst. of Phys. Conf. Series* **146**, 309-312, 1995

From Chapter VII

N. Loxley, C.D.Moore, M.Safa, B.K.Tanner, G.F.Clark, F.M.Herrmann, G.Mueller "High resolution x-ray diffractometry and topography of float-zone GaAs crystals grown in microgravity" *Adv. X-Ray Anal.* **38** 195-200, 1995

Contents

CHAPTER VI IMP Grown Epitaxial Layers of $Hg_{1-x}Mn_xTe$

CHAPTER VII Investigation of Space Grown Crystals

Chapter I

Introduction

1.1 : Introduction

The semiconductor industry today is continually under pressure to produce devices which are cheaper, smaller, more powerful and efficient, and which operate at technologically important wavelengths. In order to achieve these, uniform epilayer growth on large, dislocation-free substrates is preferred, with controlled dopant levels and few defects. This need has fuelled research into growth methods, both for bulk and thin film semiconductors.

The most common substrate in use today is silicon, where the growth technique has been optimised to the extent that 8" diameter dislocation-free single crystal wafers are produced routinely. Growth of other useful substrates like GaAs and InP, however, is more difficult, and still merits much current research. In Chapter IV of this thesis the growth of InP substrates has been assessed, in terms of dislocation densities, residual strain, misorientation and surface roughness - all critical parameters for subsequent epilayer growth. The electrical properties of substrate materials often need to be changed by the use of doping, which can affect the dislocation density in the substrate, so an investigation into the effect of doping in Vertical Gradient Freeze (VGF) GaAs is described in Chapter V. In order to gain a better understanding of the physical processes involved in growth from solution on earth, the analysis of crystals grown in space is profitable. Two examples of these have been discussed in Chapter VII, where faults in the growth process have led to the development of interesting crystal structure.

The growth of thin films on substrates is necessary for most device manufacture. A class of materials of particular interest is diluted magnetic semiconductors (DMS), where a magnetic element is substituted into the crystal lattice. Studies on the DMS $Hg_{1-x}Mn_xTe$ are described in Chapter VI. These were performed in order to gain

structural information on the layers grown, and hence optimise the growth process and facilitate the interpretation of magnetic measurements.

These discussions on crystal growth and resultant morphology are supplemented by a brief review of the growth techniques involved, given in this chapter. Explanations of the theory and experimental aspects of the x-ray characterisation employed are provided in Chapters II and III. Overall conclusions on the growth and characterisation of compound semiconductor materials are given in Chapter VIII, together with suggestions for further work.

1.2 : Methods of Characterisation

The growth of the semiconductor industry in the past few decades has been matched by advances in the capabilities of characterisation techniques. Many companies have their own production line characterisation, where wafers are routinely tested. In many cases, this can be achieved without removing the samples from the clean-room environment. Ideal techniques for this kind of wafer processing are non-destructive, require little analysis time, and minimum sample preparation. For this reason, a combination of optical and x-ray diffraction techniques are often used. Substrate wafers from major suppliers come with a measure of thickness (to $\pm$ 10μm), warp, dopant level, and a value (for the seed and tail end of the boule) of resistivity, carrier concentration, Hall mobility, and etch pit density (EPD). In order to obtain these, it is necessary to remove the wafers from the production line, at which point an array of characterisation techniques become available.

The techniques which have been used in this thesis are double and triple axis x-ray diffraction, single crystal and double axis topography, and grazing incidence x-ray reflectivity [1-3]. These are all non-destructive, and provide a wealth of structural and compositional information. Diffraction is a useful tool for gaining information on crystallinity and crystalline quality, for example through taking a Laue pattern. The measurement of diffraction rocking curves allows an assessment of crystalline perfection, by comparison of full width at half maximum (FWHM) values. In the case of epitaxial layers, double axis diffraction allows layer composition (and/or strain),

layer thickness and layer-substrate tilt to be determined. Once an analyser crystal is introduced, the strain and tilt component to the rocking curve from a material can be resolved, yielding more information on mosaicity and relaxation. Diffuse scatter can be used to obtain a measure of surface roughness. This can be extended to include interfaces and amorphous films with the use of x-ray reflectivity. Topography is a popular technique for measuring low dislocation densities ($<10^6$ cm^{-2}), as it allows large areas of material to be imaged, yet still gives information on individual dislocations. It can also be used in high dislocation density crystals to yield the size of diffracting blocks and hence a measure of mosaicity.

These x-ray techniques all average over a relatively large crystal volume, hence allowing bulk crystal properties to be measured. The structural information obtained on unit cell size and orientation is vital for subsequent epilayer growth and device operation, while dislocations are known to degrade device performance (see Section 1.3). In some cases, however, information from a particular crystal area or a greater accuracy at depth profiling is required, which is where other characterisation techniques become important.

Most semiconductor characterisation techniques in common use can be divided into four broad categories - x-ray (and/or neutron), microscope-based, optical and electrical, which are discussed in this order below. X-ray techniques which are complementary to those used in this thesis include grazing incidence diffraction (GID), powder diffraction and x-ray absorption spectroscopy (XAS). GID is especially useful in the characterisation of thin, or buried layers as, by using incidence angles of up to 0.5^0 and a position sensitive detector, diffraction from planes perpendicular to the sample surface can be measured [4, 5]. This allows the position and thickness of layers to be determined to monolayer precision, and the technique, due to its sensitivity to the in-plane lattice parameter, is an excellent tool for studying relaxation. The low levels of scattering and need for high resolution, however, make the use of a synchrotron source advantageous. Powder diffraction is an invaluable technique for giving structural and phase information, where the detailed atomic arrangement, texture and morphology of a material can be obtained. By using XAS and studying the fine structure (EXAFS), the positions of atoms around the absorbing species can be

obtained, while the position and structure of the absorption edge contains information on the ground state properties and possible excitations of valence and conduction electrons [6].

Neutron diffraction and reflectivity are analogous to the x-ray case, with a few crucial differences [7]: they have mass and hence a much smaller velocity, so time-of-flight measurements can be made and they are useful for the imaging of highly absorbing materials or elements close in the periodic table, as the scattering factor does not vary monotonically with atomic number, as in the x-ray case. Their other main feature is that magnetic scattering is a strong component, allowing magnetic structures to be investigated at the unit cell level.

Microscope-based characterisation techniques include cross-sectional transmission electron microscopy (TEM), where individual dislocations are imaged allowing full characterisation, and Scanning Electron Microscopy (SEM), which, in its secondary electron mode, is used to provide micrographs of the top surface [8, 9]. The latter can also be configured as a scanning transmission electron microscope (STEM), with a lateral resolution of 5nm. Materials where one element or compound absorb strongly in the infra-red can be imaged using IR microscopy. As reflectivity is a function of carrier concentration, an IR microscope can be used in reflection mode to show dopant variations.

Other microscopy techniques where the surface topography is imaged are atomic force microscopy (AFM) and scanning tunnelling microscopy (STM) [10]. AFM provides a 3-dimensional surface map, where features less than 1μm in size can be imaged. For smooth samples it can even provide atomic locations, as well as grain boundaries and precipitates on etched surfaces.

Related to these techniques are some which provide more compositional information. The SEM can be used for Energy Dispersive Analysis of X-rays (EDAX) where the surface composition is obtained from the element peak ratios. The best depth profiling can be obtained using Secondary Ion Mass Spectroscopy (SIMS) where primary ions bombard the surface and the particles sputtered are fed into a mass spectrometer [11].

SIMS and Auger Electron Spectroscopy (AES) are useful for giving dopant levels and chemical compositions with depth.

The electrical properties of materials can be probed using electro-optical and optical techniques such as cathodoluminescence (CL) and photoluminescence (PL). In these an electron or photon is used to stimulate transitions between different energy levels, and the radiation emitted is analysed spectroscopically. These provide information on excitonic levels, carrier density of states, and donor and acceptor concentrations [12]. Raman Spectroscopy and Brillouin Light Scattering are useful optical techniques. In Raman spectroscopy the inelastic scattering from optical phonons is measured, while Brillouin scattering measures that from acoustic phonons [13].

Electron diffraction techniques, which are here classed as electron spectroscopy, such as reflection high-energy electron diffraction (RHEED) and low-energy electron diffraction (LEED) are useful surface-sensitive techniques. RHEED is often used with grazing incidence angles (0.1 to 5^0) in a manner similar to grazing incidence x-ray diffraction [14]. The larger scattering cross section, however, makes the need for intense sources less imperative. The information obtainable from these techniques is similar to that in the x-ray case, giving surface order, phase transformations, faceting and misorientation. Transmitted electron energy loss spectroscopy (EELS) can be used to measure both characteristic x-ray and Auger emission energies in an excited sample volume.

While some predictions concerning the electronic properties of a semiconductor can be made once the chemical composition, lattice defects, chemical impurities and structural dimensions are known, it is advantageous to measure them directly in order to understand better the physical processes involved [15]. In order to gain information on the electrical charge, and density of the current carriers, the resistivity and Hall co-efficient can be measured. The Hall effect allows the determination of the sign and density of the majority carriers. In combination with the resistivity this enables a measurement of the Hall Mobility to be made. The dependence of the Hall Mobility on temperature gives important information on the nature of the dominant scattering mechanisms. Donor and acceptor energies and densities can usually be inferred from a

combined resistivity and Hall effect measurement. In addition to this a good estimate (or in fact an exact value in certain cases) can be made for the dimensionless compensation ratio (N_A/N_D). Capacitance-voltage experiments allow the concentration of dopants to be measured as a function of depth. The density, energy level and capture cross section of deep states can be investigated using deep level transient spectroscopy (DLTS). In DLTS the traps are filled repetitively by pulsing the bias on a diode. As the sample is slowly heated a spectrum of peaks corresponding to each trap is obtained.

All these techniques are frequently used on semiconductor materials in order to learn more about the structure and behaviour of systems which will be used in device applications. In all cases, however, an understanding of the real structure of the material under investigation is invaluable, as is knowledge of the defects present. While this remains the case, the use and development of x-rays as a characterisation tool will continue to be an important aspect of semiconductor research.

1.3 : Impact of defects on device performance

The role that dislocations play in device performance is difficult to quantify, as the effects of the dislocations themselves are hard to separate from those of the electrically active point defects and impurities which they attract [16]. In general, dislocations break the translational symmetry of the crystal lattice so a large density of deep states is created within the bandgap all along the dislocation [17]. Around the dislocation, the material is depleted (i.e. the majority carriers fall into the deep states). In the same way as deep states, the dislocation provides a non-radiative recombination path for minority carriers. This affects devices, such as bipolar transistors, where the dislocations in the base reduce the base majority carrier density and the minority carrier lifetime. This leads to an increase in emitter-base current and reduced gain. In addition, hopping conduction can occur along a dislocation, which, if the dislocation penetrates the device, can give a leakage current through the semi-insulating or depleted region. For example, this increases the reverse current of a p-n diode. Types of defect which have been shown to affect device performance deleteriously are threading dislocations in the device substrate, misfit dislocations in the epilayers and dark line defects (DLDs) [18].

Threading dislocations in the substrate are believed to act as non-radiative recombination centres which cause regions of low radiative efficiency in lasers, LEDs etc. In LEDs the dislocation density has been proven to be proportional to the device efficiency, and the lifetime of lasers has been shown to be improved by the use of low dislocation density substrates [19]. These effects are less important for long wavelength devices, such as InGaAsP/InP lasers, as the non-radiative recombination rate is much lower than in GaAs based devices.

DLDs are related to the threading dislocations, as they are formed by the electron-hole recombination energy being kept at a recombination centre as vibrational energy. They consist of dislocation loops and dipoles, and helical dislocations. They result in device degradation, such as the need for an increased drive current in lasers and decreased output power in LEDs. As these defects depend on the presence of threading dislocations, their effects can be reduced by the use of low dislocation density substrates.

Threading dislocations are known to act as nucleation sites for misfit dislocations [20]. They have been shown to affect the Hall mobility of InGaAs/GaAs quantum wells [21]. For vertical gradient freeze (VGF) wafers in particular, the improvement in substrate quality compared to LEC has been shown to give metal-semiconductor field-effect transistors (MESFETs) better device performance [22]. MESFETs created by direct ion implantation into undoped semi-insulating (SI) GaAs show improved threshold voltage uniformity as averaged across the whole wafer. Pseudomorphic high electron mobility transistors (HEMTs) show improved device performance on VGF substrates [23]. In addition, thicker channel layers could be used without the introduction of misfit dislocations.

A low dislocation density substrate, therefore, appears to improve device performance both directly and indirectly. While more research in this area has been performed on GaAs based devices than InP, the potential advantages make the study of III-V substrate growth techniques of major industrial significance.

1.4 Comparison of Growth Techniques for Manufacture of III-V Substrates

Several features are required from commercial InP, which include the following; low or zero dislocation density with the absence of slip, uniform chemical properties and dopant distribution, circular wafers with diameters of 50 mm or above, a low optical absorption coefficient, minimum levels of grown-in strain and low cost. These factors can in theory be achieved by a combination of correct growth conditions and doping with various elements, but some factors make the growth of InP far from trivial. The high equilibrium vapour pressure of phosphorus (~26.5atm) at the melting point of InP (1063°C) enhances the decomposition of the crystal surface, a low stacking fault energy (17 ± 5 meV/atom) facilitates easy twin formation especially in the <100> directions, and a low yield stress (0.15MPa) allows dislocation formation and slip [24]. The factors which can be used to compensate for these unfavourable thermophysical properties are temperature distributions, rotation conditions, crystal shapes, melt composition stoichiometry and growth rate. These factors are considered below, mainly in the context of the two growth techniques which have been investigated in this study.

1.4.1 Liquid Encapsulated Czochralski (LEC)

Liquid encapsulated Czochralski (LEC) is at present the most commonly used growth technique for III-V semiconductors, especially high pressure LEC where a reasonable crystal yield is achieved even in <001> directions. A simplified sketch of an LEC puller with the dominant heat transfer mechanisms labelled is shown in Fig 1.1. A crucible contains a melt of InP topped by an encapsulant, in this case molten boric oxide, B_2O_3. The original InP is composed of polycrystalline material grown by other techniques such as Horizontal Bridgman (HB) or Gradient Freeze (GF) which is then regrown to form a single crystal. The role of the encapsulant is to help control the thermal conditions at the solid/liquid interface and to prevent the decomposition of the melt. Crucibles are often made of SiO_2, but this has been shown by Müller et al [25] to lead to a variable Si incorporation in InP crystals, increasing away from the seed. As the incorporation of Si in the crystal requires higher levels of dopants to be included to obtain semi-insulating and p-type materials, adversely affecting the epitaxy, a BN

crucible has been introduced. It is important that the crucible base is well shielded with reflectors and insulation, as freezing of the melt is possible.

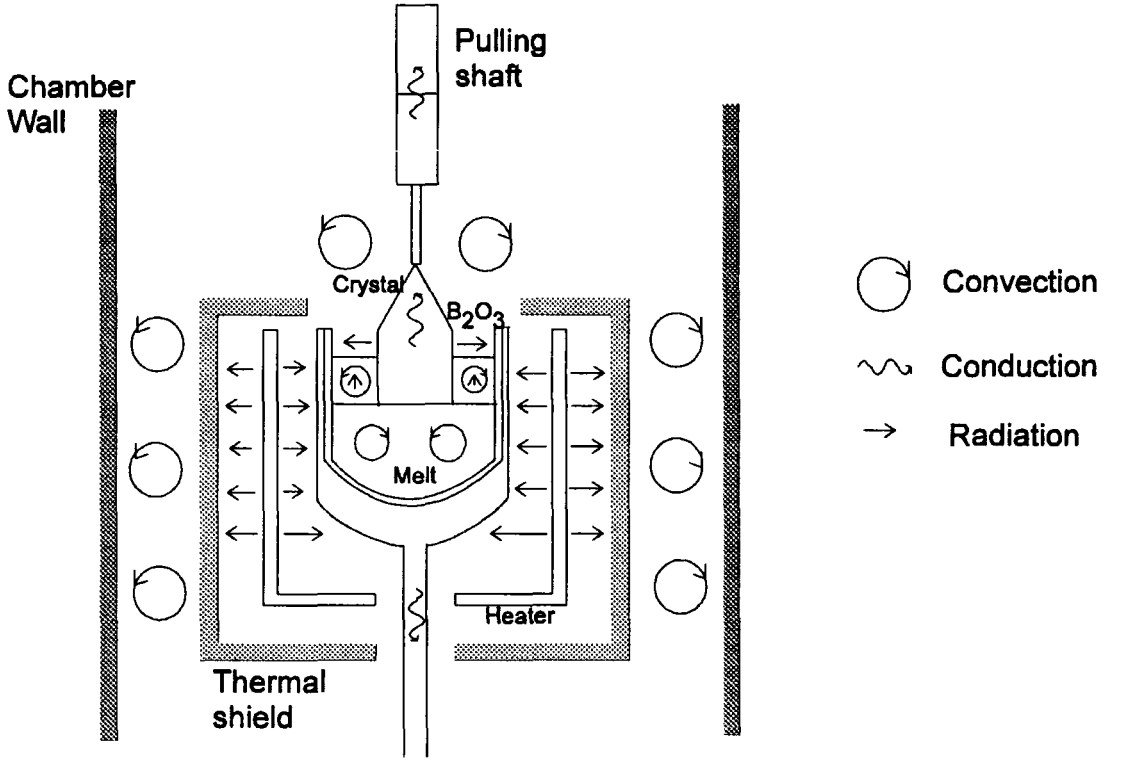

Fig 1.1 : Simplified sketch of an LEC puller showing the heat-transfer mechanisms

Several factors lead to dislocations in this arrangement. The first and hardest to control is thermal stress, caused by thermal gradients from the solid/liquid interface. Unfortunately, large axial temperature gradients are necessary in order to control the growing crystal diameter and create a single crystal [26]. For example, if the temperature of the melt is not much greater than its melting point, intermediate state crystallites are formed which carry dopants with them into the crystal, and cause inhomogeneities [27]. The largest temperature gradient occurs at the interface, where supercooling is the driving force towards solidification. The overall temperature difference, therefore, is the interface temperature, T_f minus the ambient temperature, T_a in the rest of the furnace. It has been shown in Vertical Bridgman systems that the critical factor on the maximum resolved shear stress (MRSS) that the crystal experiences is dependent on this temperature gradient [28]. This has also been shown theoretically for LEC by Jordan et al [29]. AXT Laboratories have studied this temperature gradient by adding thermocouples to a growing crystal, using no seed rotation, and have observed the heat flux to be radially inward in the hot crystal part

which is covered by the encapsulant, and radially outward in the crystal formed [30], while both axial and radial gradients were decreased by increasing the height of the B_2O_3. These temperature distributions cause a compressive stress within the ingot, and a tensile stress at the periphery, and if these forces exceed the critical resolved shear stress (CRSS) slip and dislocation generation ensue. It is obvious, therefore, that in order to reduce dislocation density either the thermal stresses have to be reduced, while maintaining the minimum gradient necessary for growth, or the CRSS of the crystal has to be increased by an impurity hardening effect like doping [31].

Investigations of Fe, Sn and S doped VGF InP [32] have shown that Fe (to give a semi-insulating crystal) and Sn (to give an n-type crystal) doping had little effect on the dislocation levels, but S-doped (lattice hardened) InP showed a lower dislocation level. The amount of slip dislocation was reduced, and dislocation climb out of the slip plane was prevented. When GaAs is In doped at high levels, in excess of $10^{20}cm^{-3}$, the CRSS is found to increase by a factor of 3, and 75% of a typical 3'' wafer was measured to be dislocation free [29]. Although this excessive In hardens the lattice and suppresses glide formation in the centre of wafers, the material formed is stressed and tetragonally distorted, leading to possible misfit dislocations in epitaxial films. In addition, heavy doping has been linked to strain from dopant inhomogeneities, and the cracking of large crystals when being sliced [33]. The reduction of dislocations via adjustment to the temperature gradient is therefore a keen issue.

The growth process is dependent on the orientation of the crystal/melt interface, as growth tends to occur perpendicular to it. A (111) seed which is only partially melted will result in a curved interface, where growth is at an angle and facet growth is possible. If this seed is completely melted, there is a large supercooling and a sharp interface perpendicular to the direction of growth. In the case of a (100) surface, growth occurs by step motion, and facet growth is likely, making the production of (100) crystals more difficult than (111). Yosheda et al [34] observed that in LEC growth of InP, two <110> planes grew in preference to the others. Once their lateral growth was complete, facet planes were formed and the temperature perturbations present in the system led to twin formation. The twins most often found in III-V materials are 60° rotation twins where the gallium atom replaces an arsenic atom by

rotation, and only Ga-As bonds are present at the interface [35]. Although twin formation has often been linked to the presence of growth facets, these facets are not necessarily the nucleation site, and their formation also depends on the stoichiometry of the melt and the raw materials used.

The easiest type of dislocations to remove from the grown crystal are dislocations propagating from the seed, by a process of necking. As dislocations in zinc blende systems tend to propagate in the {111} planes in the <110> directions, if the diameter of the growing crystal is reduced and kept narrow for about 10mm, dislocations are prevented from propagation. The most common unwanted feature in LEC growth is the occurrence of polycrystallisation. This is largely determined by the shape of the crystal/melt interface, which in LEC growth of GaAs tends to be sigmoidal with a concavity towards the melt at the periphery [36]. If the centre of curvature of this concavity is within the crystal, the grown-in dislocations perpendicular to the interface will accumulate in the crystal, causing polycrystallization whereas if the centre of curvature is outside the crystal, the dislocations grow towards the interface and disappear. In addition, the necking procedure reduces the thermal gradients, and hence the dislocation density.

Another type of defect present in melt-grown crystals are interstitial atoms, which are introduced just before melting. These interstitials are frozen in as the crystal changes from melting to regrowth, and can nucleate microdefects. Studies of the boric oxide encapsulant have shown that the presence of moisture can lead to clusters of etch pits, known as "Grappes", which are either tangles of dislocations emanating from the core [37], or dislocation loops from gaseous inclusions caused by reactions between water vapour and molten InP [38].

One of the most important aspects of wafer production is the introduction of dopants to the melt, and their homogeneous incorporation into the single crystal. Dopants are necessary, not only to reduce dislocation densities in grown crystals, but also to tune the properties of the crystal to the industrial requirements. Many studies on dopants have been performed [24, 31, 39-45] as well as on double-dopants [46-48]. It has been shown that inhomogeneous levels of doping lead to poorer performance of epitaxial

layers, yet constant levels of doping are hard to obtain due to random convection currents inside the melt and radial thermal asymmetry. Striation patterns are produced, which give information on the shape of the solid/liquid interface. Most bands will be regularly spaced, with a spacing similar to the growth rate of the crystal, but if remelting occurs the band structure is destroyed then reformed. The striation amplitude is reduced by introducing a rotation of the crystal and crucible, and for magnetic materials can be removed by the use of magnetic fields to control the thermal convection within the melt [49].

The uniformity of standard wafers produced by LEC has been characterised using electrical measurements, and etch pit density (EPD) counts after etching. In general, LEC wafers are found to give a characteristic 'W' shape when radial distance across wafer is plotted against EPD, with a high etch pit density at the sides of the wafer, and a slightly raised value at the wafer centre. At the edge of the wafer, dislocations are chiefly from slip dislocations propagating normal to the growth axis, while at the centre dislocations generated at the seed-on end are present.

Various adaptations to the LEC technique have been suggested, some of which are still being optimised. The use of magnetic fields of the order of 1000G, as already mentioned, has allowed control both of growth striations and the crystal diameter, allowing lower thermal gradients to be used, and hence reduced stress levels [50]. Twin boundaries can be controlled by optimising supercooling [34], and the use of low thermal gradient conditions allows high quality crystal production, particularly near the bottom of the ingot [41].

1.4.2 : Vertical Gradient Freeze (VGF)

The technique of Vertical Gradient Freeze (VGF) as shown in Fig 1.2 has been developed largely through the experimental work of Monberg et al [32, 51] who produced low dislocation density crystals of <111> seeded InP, even at low doping levels. The temperature gradients employed are much smaller than in the LEC process, by more than an order of magnitude in the axial direction. The lower gradients are below the CRSS so in theory dislocation-free crystals can be obtained [29, 52, 53].

While an axial temperature gradient is necessary for solidification, the radial gradient is chiefly caused by imperfections in the heat transfer between parts of the chamber. As the melt solidifies latent heat is released which decreases the axial temperature gradient and increases the radial gradient, unless the thermal conductivity is high. This leads to changes in the curvature of the melt/crystal interface, and unstable growth conditions. As the latent heat release is proportional to the growth rate, in VGF the crystal is grown at only ~1mmh^{-1} compared to a pull rate of 8mmh^{-1} in LEC material. A feedback system is built in so that the temperature is controlled and maintained by many heating elements, so removing the need for moving parts and mimicking the steady-state operation of vertical Bridgman systems. This also allows a modulating temperature profile so that the radial temperature gradient can be used to counteract the latent heat of solidification. It can also be used to control the shape of the interface [28, 54, 55]. A linear furnace profile favours a concave interface, while a non-linear one with low temperature gradients along the melt and solid/liquid interface and a high gradient at the bottom of the solid favours a convex one. Concave interfaces often result in radial dopant non-uniformity and the formation of twins, so a planar interface is preferred away from the seed, which leads to a reduction in facetting, twinning and polycrystallization. The control of the interface shape is also dependent on the growth rate, the latent heat of solidification and the crucible thickness [56]. The crucible is again rotated to ensure an even concentration of dopant, but if the rotation is not perfectly symmetric in the temperature field of the furnace, macroscopic dopant inhomogeneities occur, i.e. rotationals, which map out the shape of the interface. If the system is well optimised, however, these should be evenly spaced and continuous. Deviations from stoichiometry are reduced in this system, by the use of an encapsulant as in LEC, and in some cases by a separate reservoir of red phosphorus which helps to maintain the proper partial pressure of phosphorus vapour over the melt.

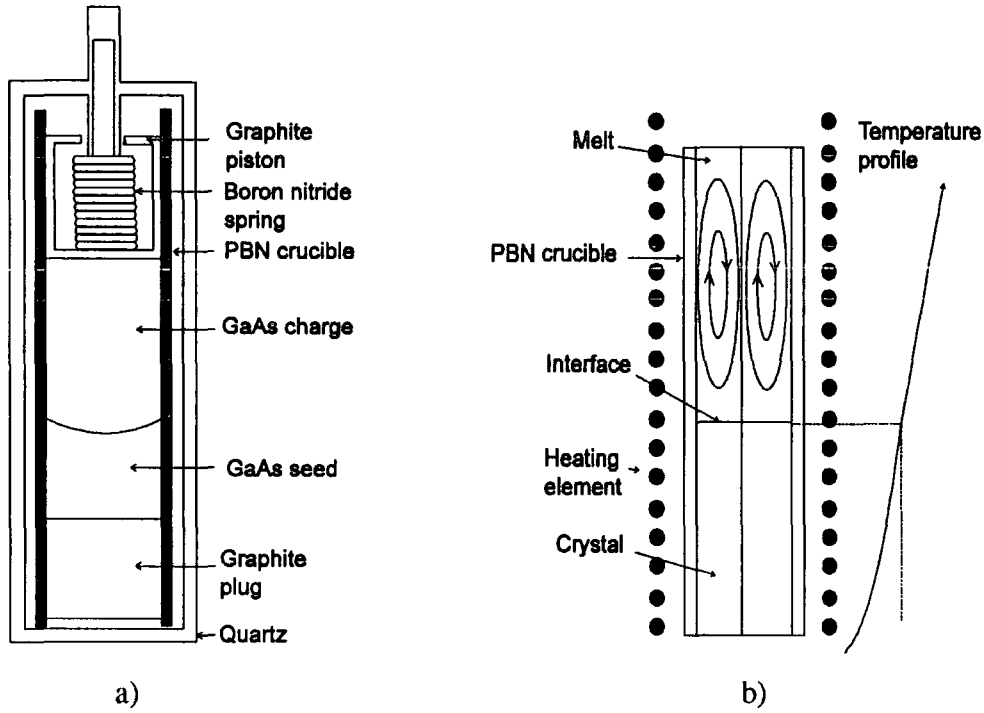

Fig 1.2 : Schematic diagrams of a) the crucible and b) the model for a VGF system

Initial studies of structural and electrical properties have shown the EPD to be greatly reduced compared to LEC [57], no 'W' distribution of defects, and room mobilities equal to or greater than those grown by other techniques with similar doping levels. Twin formation is still a problem, however, and the last-to-freeze sections of the crystal have been seen to have poor crystal morphology due to a considerable amount of charge still being liquid when cooling starts [58-60].

1.5 : MOVPE Layer Growth in II-VI Epitaxial Layers

Many electronic devices rely on the electrical properties which are created within a system of epitaxial layers. There is continuing interest, therefore, in optimising the uniformity and quality of these layers, as well as their degree of relaxation. The way in which a layer is deposited affects the type of growth which occurs (i.e. monolayer growth, nucleated growth, or nucleation followed by monolayer growth), the accuracy of the thickness of layer, the dislocation density and the composition [61]. Techniques which can be used include Liquid Phase Epitaxy (LPE), Molecular Beam Epitaxy (MBE) and Metal-Organic Chemical Vapour Deposition (MOCVD). Another name

for the latter is Metal-Organic Vapour Phase Epitaxy (MOVPE), which has been used in the preparation of all the II-VI epitaxial layers studied in this thesis.

1.5.1 : Fundamentals of MOVPE growth

In a MOVPE growth system [62], a carrier gas, such as purified hydrogen is passed through heated bubblers containing the precursors and reactant vapours. There will be a precursor for each of the elements required, for example in the growth of mercury manganese telluride, discussed in Chapter VI, the precursors used are di-isopropyl telluride (DIPTe), tricarbonyl methylcyclopentadienyl manganese (TCMn), dimethlyzinc (DMZn), and dimethylcadmium (DMCd). The mercury can either be included as an external source, or, as in this case, be introduced as an elemental source in an independently heated boat upstream of the susceptor. The susceptor (stainless steel) is heated by infra-red lamps or RF coils, and holds the substrate material. On reaching the susceptor, pyrolytic cracking of the gases occurs, and the group II and VI elements are deposited epitaxially onto the heated substrate. The breakdown products are flushed out in a H_2 gas stream. A diagram showing the MOVPE system used in the growth of (Hg,Mn)Te is shown in Fig 1.3.

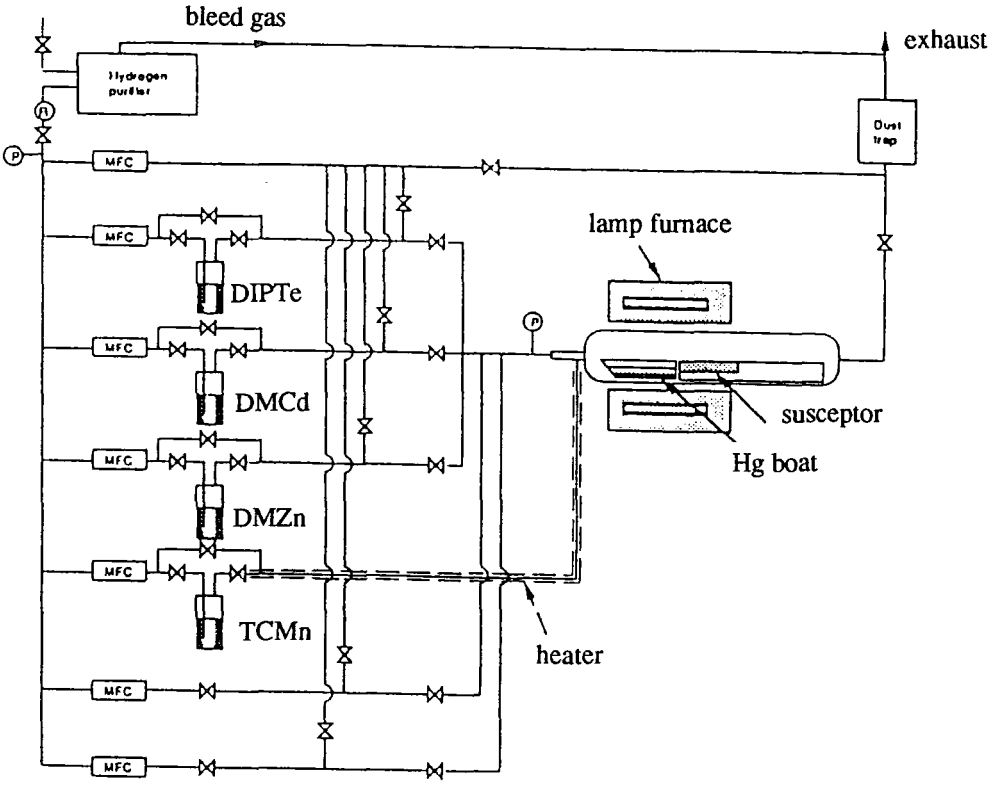

Fig 1.3 : A schematic of the MOVPE system used in the growth of (Hg,Mn)Te.

There are several problems associated with growing a layer with one lattice parameter on a substrate with a different lattice parameter. If the difference in lattice parameter is great, there will be a large strain within the layer as it will be forced to adopt the lattice parameter of the substrate. Once the strain of the misfit is sufficiently great, it can be relieved by misfit dislocations which are (simplistically) equivalent to arrays of edge dislocations which allow the layer to relax to its own lattice parameter. As dislocations are generally unwelcome in device applications, a buffer layer is often introduced, whose role is to bridge the gap in lattice parameter between substrate and layer. Most of the dislocations terminate in the buffer layer, as they bend at the top interface and meet with other dislocations, so cancel out. In addition, the presence of a buffer layer limits the amount of cross-diffusion which takes place from the substrate.

Another problem is that of the orientation in which the layer grows. If the substrate has a (100) surface, it does not necessarily follow that the layer will form with (100) orientation parallel to it. The factors which determine the orientation are the materials involved, the growth temperature and the temperature at which the substrate is heat-treated. It has been observed that ZnTe always grows with a (001) orientation on (001) GaAs [63], so is often grown as an inial buffer layer to ensure that this is the preferred growth direction.

Another problem of epitaxial growth is the uniformity of growth, with respect to both thickness and composition. A compositional variation of less than $0.5\%cm^{-1}$ is preferable in a material, but this is hard to achieve due to the gas flow patterns within the chamber and the varying partial pressure ratios of the precursors. Two main growth processes are employed, within MOVPE, which appear to yield different compositional fluctuations, and these are briefly outlined below.

1.5.2 : Direct Alloy Growth (DAG)

In Direct Alloy Growth (DAG) all the gases are transported to the susceptor simultaneously and react directly to form the compound required. The gas movement is controlled using mass flow controllers, and the composition of the compound obtained is determined by the ratio of partial pressures of the various gases present.

The temperature of the gas over the susceptor is kept constant with time, and the change in volume of the gas due to the reaction is negligible. The composition of the layers produced by this method has been extensively studied by Hallam et al [64], where the variation in compositional uniformity in (Hg,Cd)Te was found to be 5%cm^{-1}. As a result the growth process was altered to IMP, which is described below.

1.5.3 : Interdiffused Multilayer Process (IMP)

The Interdiffused Multilayer Process or IMP was developed by Tunnicliffe et al [65] in order to produce ternary layers, such as $Cd_xHg_{1-x}Te$. In this process layers of one compound, such as CdTe, are deposited alternately with layers of HgTe. If these layers are sufficiently thin, such as 0.1μm or less, diffusion causes the layers to mix into a layer of approximately uniform composition. The resultant composition is given by

[1.1] $$x = \frac{t_2}{t_1 + t_2}$$

where t_1 and t_2 are the thicknesses of the HgTe and CdTe layers respectively, and x is the Cd fraction in the resultant layer. In order to make the diffusion complete, a ten minute anneal at the growth temperature in a flow of hydrogen and under a mercury overpressure was suggested. In addition, it is practically advisable to allow for the finite response time of the switches by leaving a pause of some tens of seconds between each layer. Smooth switching can also be obtained by diverting the unwanted carrier gas to bypass around the bubbler instead of through it. A discussion on the effect which this technique has on the uniformity of growth will form some of the content of Chapter VI.

References

1. Halliwell, M.A.G., M.H. Lyons, and M.J. Hill, *The interpretation of x-ray curves from III-V semiconductor device structures.* J.Crystal Growth, 1984. **68**: p. 523-531.

2. Halliwell, M.A.G., *X-ray diffraction solutions to heteroepitaxial growth problems.* J.Crystal Growth, 1997. **170**: p. 47-54.

3. Fewster, P.F., *X-ray analysis of thin films and multilayers.* Rep. Prog. Phys., 1996. **59**: p. 1339-1407.

4. Rose, D., *et al., Investigation of InAs single quantum wells buried in GaAs[001] using grazing incidence x-ray diffraction.* J.Phys.D:Appl. Phys., 1995. **28**: p. A246-A249.

5. Renaud, G. *Surfaces.* in *Neutron and Synchrotron Radiation for Physics and Chemistry of Condensed Matter.* 1995. Grenoble.

6. Lengeler, B., *X-Ray absorption and reflection in the hard x-ray range,* in *Photoemission and Absorption Spectroscopy of Solids and Interfaces with Synchrotron Radiation,* M. Campagna and K. Rosei, Editor. 1990, North Holland. p. 157-202.

7. Scherm, R. and B. Fak, *Neutrons,* in *Neutron and Synchrotron Radiation for Condensed Matter Studies,* J. Baruchel, *et al.*, Editor. 1993, Springer-Verlag: Heidelberg. p. 113-147.

8. Holt, D.B., *Scanning Electron Microscopy (SEM) microcharacterisation of semiconducting materials and devices,* in *Growth and Characterisation of Semiconductors,* R.A. Stradling and P.C. Klipstein, Editor. 1990, Adam Hilger: Bristol.

9. Russel, P.E., *SEM-based characterisation techniques.* Mater. Res. Soc. Symp. Proc., 1986. **69**: p. 15-22.

10. Hues, S.M., *et al., Scanning probe microscopy of thin films.* Mat. Res. Soc. Bull., 1993. **Jan**: p. 41-49.

11. Clegg, J.B., *Depth profiling of semiconductor materials by secondary ion mass spectrometry,* in *Growth and Characterisation of Semiconductors,* R.A. Stradling and P.C. Klipstein, Editor. 1990, Adam Hilger: Bristol. p. 87-104.

12. Lightowlers, E.C., *Photoluminescence Characterisation,* in *Growth and Characterisation of Semiconductors,* R.A. Stradling and P.C. Klipstein, Editor. 1990, Adam Hilger: Bristol. p. 135-164.

13. Nemanich, R.J., *Raman spectroscopy for semiconductor thin film analysis.* Mater. Res. Soc. Symp. Proc., 1986. **69**: p. 23-38.

14. Lagally, M.G. and D.E. Savage, *Quantitative electron diffraction from thin films.* Mat. Res. Soc. Bull., 1993. **Jan**: p. 24-31.

15. P.Blood and J.W. Orton, *The Electrical Characterization of Semiconductors: Majority Carriers and Electron States.* 1992, Bodmin: Academic Press.

16. Look, D.C., *Defects relevant for compensation in semi-insulating GaAs,* in *Imperfections in III-V Materials,* E.R. Weber, Editor. 1993, Academic Press: San Diego. p. 91-114.

17. Beanland, R., D.J. Dunstan, and P.J. Goodhew, *Plastic relaxation and relaxed buffer layers for semiconductor epitaxy.* Advances in Physics, 1996. **45**(2): p. 87-146.

18. Swaminathan, V. and A.S. Jordan, *Dislocations in III-V compounds,* in *Imperfections in III-V Materials,* E.R. Weber, Editor. 1993, Academic Press: San Diego. p. 294-336.

19. Chin, A.K., *The effect of crystal defects on device performance and reliability.* J.Crystal Growth, 1984. **70**: p. 582-596.

20. Fitzgerald, E.A., *Dislocations in strained-layer epitaxy: theory, experiment and applications.* Mat. Sci. Rep., 1991. **7**(3): p. 92-139.

21. Klem, J.F., *et al., Role of substrate threading dislocation density in relaxation of highly strained InGaAs/GaAs quantum well structures.* Appl.Phys.Lett., 1990. **56**(14): p. 1350-1352.

22. Reynolds, C.L., W.C. Gibson, and J.E. Clemans, *Uniformity of threshold voltage for MESFETs fabricated on VGF GaAs substrates.* Elect. Lett., 1987. **23**(23): p. 1222-1223.

23. Meshkinpour, M. and M.S. Goorsky, *The role of substrate quality on misfit dislocation formation in pseudomorphic high electron mobility transistor structures.* in press.

24. Farges, J.P., *Growth of Dislocation-free InP,* in *Indium Phosphide : Crystal Growth and Characterisation,* R.K. Willardson and A.C. Beer, Editor. 1990, Academic Press, Inc. p. 1-36.

25. Mueller, G., *et al., Sources of silicon contamination in LEC-grown InP crystals.* J.Crystal Growth, 1983. **64**: p. 37-39.

26. Henry, R.L., *et al., Growth of (100) GaAs by vertical zone melting.* J.Crystal Growth, 1991. **109**: p. 228-233.

27. Chikawa, J. and J. Matsui, *Growth and evaluation of bulk crystals,* in *Materials, Properties and Preparation,* S. Mahajan, Editor. 1994, Elsevier Science. p. 1-71.

28. Parfeniuk, C., *et al., Measured critical resolved shear stress and calculated temperature and stress fields during growth of CdZnTe.* J.Crystal Growth, 1992. **119**: p. 261-270.

29. Jordan, A.S., E.M. Monberg, and J.E. Clemans, *A comparison of reducing the dislocation densities in GaAs grown by the vertical gradient freeze and liquid-encapsulated Czochralski techniques.* J.Appl.Phys., 1993. **73**(1): p. 477-479.

30. Mueller, G., J. Volkl, and E. Tomzig, *Thermal analysis of LEC InP growth.* J.Crystal Growth, 1983. **64**: p. 40-47.

31. Barrett, D.L., *et al., Low dislocation, semi-insulating In-doped GaAs crystals.* J.Crystal Growth, 1984. **70**: p. 179-184.

32. Monberg, E.M., *et al., The Growth and Characterisation of Large Size, High Quality, InP Single Crystals.* JECS, 1988. **135**(2): p. 500-503.

33. Farges, J.P., C. Schiller, and W.J. Bartels, *Growth of large diameter dislocation-free Indium Phosphide ingots.* J.Crystal Growth, 1987. **83**: p. 159-166.

34. Yoshida, S., *et al., InP single crystal growth with controlled supercooling during the early stage by a modified LEC method.* J.Crystal Growth, 1991. **113**: p. 221-226.

35. Chen, T.P., *et al., Study of twins in GaAs, GaP and InAs crystals.* J.Crystal Growth, 1992. **118**: p. 109-116.

36. Shibata, M., T. Suzuki, and S. Kuma, *LEC growth of large GaAs single crystals.* J.Crystal Growth, 1993. **128**: p. 439-443.

37. Brown, G.T., *et al., A Detailed Microscopic Examination Of Dislocation Clusters In LEC InP.* J.Crystal Growth, 1984. **67**: p. 495-506.

38. Franzosi, P., *et al., Inclusion-like defects in Czochralski grown InP single crystals.* J.Crystal Growth, 1984. **69**: p. 388-398.

39. Brozel, M.R., *et al., The incorporation of tin in indium phosphide.* J.Crystal Growth, 1984. **70**: p. 191-198.

40. Cockayne, B., G.T. Brown, and W.R. MacEwan, *Control of Dislocation Structures in LEC Single Crystal InP.* J.Crystal Growth, 1983. **64**: p. 48-54.

41. Elliot, A.G., C.L. Wei, and R. Farraro, *low dislocation density, large diameter, liquid encapsulated Czochralski growth of GaAs.* J.Crystal Growth, 1984. **70**: p. 169-178.

42. Fornari, R., *et al., Dislocation-free silicon-doped gallium arsenide grown by LEC procedure.* J.Crystal Growth, 1983. **63**: p. 415-418.

43. Kim, D.H. and R.A. Brown, *Transient simulations of convection and solute segregation of GaAs growth in gradient freeze furnace.* J.Crystal Growth, 1991. **109**: p. 66-74.

44. Naukkarinen, K., *et al., An Examination of Defects in InP single crystals grown by the Liquid-Encapsulated Czochralski Technique using Synchrotron X-ray Topography.* J.Crystal Growth, 1983. **64**: p. 485-491.

45. Katsui, A. and S.-i. Tohno, *LEC Growth and Characterisation of Ga Doped InP Crystals.* J.Crystal Growth, 1986. **74**: p. 221-224.

46. Coquille, R., *et al., Growth of low-dislocation semi-insulating InP(Fe,Ga).* J.Crystal Growth, 1987. **83**: p. 167-173.

47. Cockayne, B., T. Bailey, and W.R. MacEwan, *Dislocation-Free LEC Growth of InP Doped with Ge and S.* J.Crystal Growth, 1986. **76**: p. 507-510.

48. Haji, L., *et al., X-ray Topography and TEM studies of (Ga,Fe)-Double-Doped LEC Grown InP crystals.* J.Crystal Growth, 1987. **82**: p. 487-494.

49. Series, R.W. and D.T.J. Hurle, *The use of magnetic fields in semiconductor crystal growth.* J.Crystal Growth, 1991. **113**: p. 305-328.

50. Miyairi, H., *et al., Growth and Properties of InP Single Crystals Grown by the Magnetic Field Applied LEC Method.* J.Crystal Growth, 1986. **79**: p. 291-295.

51. Monberg, E.M., *et al., Vertical gradient freeze growth of large diameter, low defect density indium phosphide.* J.Crystal Growth, 1987. **83**: p. 174-183.

52. Jordan, A.S., E.M. Monberg, and J.E. Clemans, *Thermal stress theory of dislocation reduction in the vertical gradient freeze (VGF) growth of GaAs and InP.* J.Crystal Growth, 1993. **128**: p. 444-450.

53. Jordan, A.S. and E.M. Monberg, *Quasi-steady-state heat transfer/thermal stress model for dislocation generation in the vertical freeze growth of GaAs.* J.Appl.Phys., 1993. **73**(8): p. 4016-4022.

54. Brown, R.A. and D.H. Kim, *Modelling of directional solidification : from Scheil to detailed numerical simulation.* J.Crystal Growth, 1991. **109**: p. 50-65.

55. Hofmann, D., T. Jung, and G. Muller, *Growth of 2 inch Ge:Ga crystals by the dynamical vertical gradient freeze process and its numerical modelling including transient segregation.* J.Crystal Growth, 1993. **128**: p. 213-218.

56. Motakef, S., *Thermoelastic study of GaAs in vertical gradient freeze configuration: limits to the optimum growth rate and approaches to its augmentation.* J.Crystal Growth, 1989. **98**: p. 711-720.

57. Zemke, D., *et al., Growth and characterisation of 2 in InP crystals by the vertical gradient freeze technique.* Materials Science and Engineering, 1994. **B28**: p. 91-94.

58. Koh, H.J., *et al., Twins in GaAs crystals grown by the vertical gradient freeze technique.* Cryst. Res. Technol., 1995. **30**(3): p. 397-403.

59. Frank, C., K. Hein, and E. Buhrig, *Description of facet growth during VGF growth.* Cryst. Res. Technol., 1994. **29**(1): p. K12-K16.

60. Hofmann, D., *et al.*, *Model-based directional solidification of semiconductor materials by the VGF-technique using multi-zone cold wall furnace technology.* Materials Science and Engineering, 1993. **A173**: p. 67-71.

61. Pashley, D.W., *The basics of epitaxy,* in *Growth and Characterisation of Semiconductors,* R.A. Stradling and P.C. Klipstein, Editor. 1990, Adam Hilger: Bristol. p. 1-16.

62. Williams, J.O., *Metal Organic Vapour Deposition (MOCVD) for the preparation of semiconductor materials and devices,* in *Growth and Characterisation of Semiconductors,* R.A. Stradling and P.C. Klipstein, Editor. 1990, Adam Hilger: Bristol. p. 17-33.

63. Feldman, R.D., *et al.*, Appl.Phys.Lett., 1986. **49**: p. 797.

64. Hallam, T.D., *The Characterisation of Epitaxial Layers of the Dilute Magnetic Semiconductor* $Hg_{1-x}Mn_xTe$. 1995, University of Durham.

65. Tunnicliffe, J., *et al.*, J.Crystal Growth, 1984. **68**: p. 245.

Chapter II

Theory of X-Ray Diffraction and Reflectivity

In this chapter the fundamental principles behind the x-ray techniques used in this thesis will be outlined. The two main techniques, i.e. diffraction and reflectivity, differ in that the former is considered in terms of a dispersion surface formed by the interaction of the incident and diffracted x-ray wave, while the latter can be considered in terms of optical effects at an interface. As reflectivity is only sensitive to changes in electron density it is a technique which is not dependent on crystalline structure, so will be dealt with first.

2.1 : Grazing Incidence X-Ray Reflectometry

Surface characterisation is becoming more important due to advances in nanotechnology. Grazing incidence X-ray reflectometry (GIXR), pioneered by Kiessig in the 1930's [1], is useful as it is a non-destructive technique which can sample depths ranging from a few nanometres to about a micron for crystal, polycrystal and amorphous films. Both the experimental techniques and simulation procedures are developing rapidly, making it an exciting field of study. In this section, a brief review of the current status will be given. Far more detailed approaches are given in references [2-4].

2.1.1 : Principles of Reflectivity - Specular

Away from absorption edges, the refractive index, n, of a material is known to be

[2.1] $$n = 1 - \frac{N_A}{2\pi} r_o \lambda^2 \sum_j \frac{\rho_j}{A_j} f_j$$

where the material has an atomic number Z_j, atomic mass A_j and density ρ_j, and λ is the photon wavelength, N_A is Avogadro's number and r_o is the classical electron radius. Far from an absorption edge the scattering vector $f_j = Z_j$, but just below an edge the x-rays

interact with the material, causing an electron in the absorbing atom to become excited, or ionized. This leads to phase changes on scattering, so the refractive index becomes

[2.2] $$f_j = Z_j + f_j' + if_j''$$

where f' causes the sharp negative peak at the absorption edge. The refractive index, n, is now complex and contains a dispersion correction, δ and absorption term, β.

[2.3] $$n = 1 - \delta - i\beta .$$

[2.4] $$\delta = \frac{N_A}{2\pi} r_o \lambda^2 \sum_j \frac{\rho_j}{A_j} (Z_j + f_j')$$

[2.5] $$\beta = \frac{N_A}{2\pi} r_o \lambda^2 \sum_j \frac{\rho_j}{A_j} f_j'' = \mu \frac{\lambda}{4\pi}$$

where μ is the linear coefficient of absorption. As these typically have values in the range 10^{-5} or 10^{-6}, the resultant refractive index is just less than 1, so x-rays entering into matter are refracted away from the normal.

As we are considering surface reflection/refraction effects, we can take Snell's law with θ_1 being the incidence angle of the x-ray, and θ_2 the refracted angle.

[2.6] $$n_1 \cos\theta_1 = n_2 \cos\theta_2$$

This (neglecting absorption) gives a condition for the angle of total external reflection, θ_c, up to which virtually no penetration of the x-ray occurs.

[2.7] $$\theta_{1c} = \sqrt{2\delta_2} = \lambda \sqrt{\frac{N_A r_o}{\pi} \sum_j \frac{\rho_j}{A_j} (Z_j + f_j')}$$

If a system where many layers on top of a thick substrate are considered, the electric displacements, E, of the incident and reflected waves follow the pattern in Fig 2.1. As the substrate is thick, there is no reflected amplitude from it and $A_{N-1} = 0$, where A_N is the amplitude from the Nth layer.

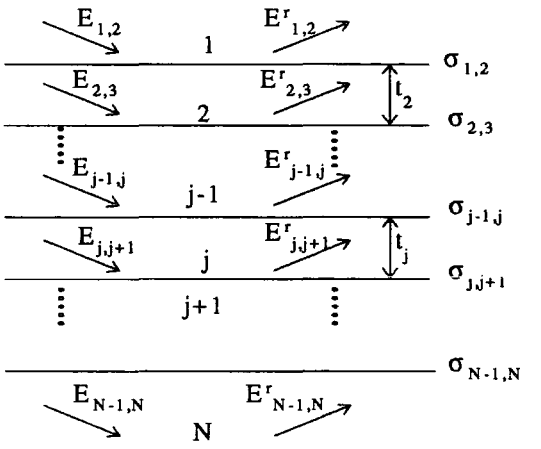

Fig 2.1 : Specular reflectivity from a multilayer structure

There must be continuity between the tangential components of the electric vectors across each interface, which leads to Parratt's recursive formulae [3] for the reflection amplitudes, R,

[2.8] $$R_{j-1,j} = a_{j-1}^4 \left[\frac{R_{j,j+1} + r_{j-1,j}}{R_{j,j+1} r_{j-1,j} + 1} \right]$$

and

[2.9] $$R_{j,j+1} = a_j^2 \left(\frac{E_{j,j+1}^r}{E_{j,j+1}} \right).$$

At an abrupt interface with no roughness,

[2.10] $$r_{j-1,j} = \frac{f_{j-1} - f_j}{f_{j-1} + f_j}$$

where

[2.11] $$f_j = \sqrt{\theta^2 - 2\delta_j - 2i\beta_j}\,.$$

In these equations a_j is the phase factor corresponding to half the layer thickness, t_j,

[2.12] $$a_j = \exp\left(-\frac{i\pi f_j t_j}{\lambda} \right),$$

and r_{j-1} is the Fresnel coefficient of reflection. The absence of amplitude from the substrate layer means that the first of these recursive formulae is the Fresnel equation (for the first interface). The layers are solved from the bottom to the top, noting that at the surface a_1 is unity so

[2.13] $$R_{1,2} = \frac{E_1^r}{E_1}$$

and the intensity is

[2.14] $$\frac{I_R}{I_0} = \left|R_{1,2}\right|^2 = \left|\frac{E_1^r}{E_1}\right|^2 .$$

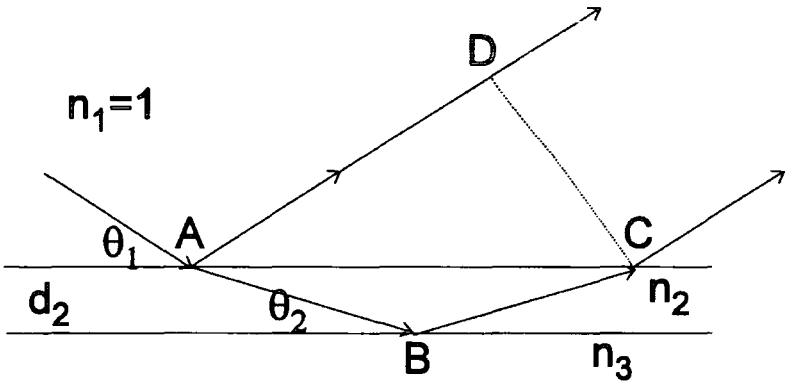

Fig 2.2 : Reflection of X-rays under grazing incidence from a layer of thickness d_2 with refractive index n_2 on a substrate with refractive index n_3

For small θ_2 the difference in optical path, as shown in Fig 2.2, is

[2.15] $$\Delta = (\overline{AB} + \overline{BC})n_2 - \overline{AD} = 2d_2\theta_2 \approx 2d_2\sqrt{\theta_1^2 - \theta_{1c}^2}$$

where the last substitution comes from Snell's law at grazing incidence. The maxima of the oscillations which are formed lie at

[2.16] $$n\lambda = 2d_2\sqrt{\theta_{1n}^2 - \theta_{1c}^2} \qquad n_2 > n_3$$

[2.17] $$(n + 1/2)\lambda = 2d_2\sqrt{\theta_{1n}^2 - \theta_{1c}^2} \qquad n_2 < n_3$$

where the factor 1/2 is due to a phase shift π when the dispersion correction $\delta_2 > \delta_3$. This theory assumes only one reflection at each interface so multiple reflections are ignored. This is a good approximation for vlaues of r_1 and $r_2 \leq 10\%$.

2.1.2 : Roughness in Specular Scans

The effect of roughness on a specular scan is to decrease the amplitude of the reflected peak. By averaging the roughness laterally this can be modelled as a series of flat lamellae of slightly differing electron density, Fig 2.3, which all interfere destructively. This is then described using the Born Approximation where,

[2.18] $$r = r_F \int_{-\infty}^{\infty} \left[\frac{1}{\rho_{-\infty}} \frac{d\rho(z)}{dz} \right] e^{-iQz} dz .$$

In this equation $\rho_{-\infty}$ is the electron density of the bulk substrate, r_F is the Fresnel reflection amplitude, and $Q=k_s-k_i$ is the difference between the incident and scattered wavevectors. Q is directed along q_z (the surface normal) with magnitude

[2.19] $$Q = \left(\frac{4\pi}{\lambda} \right) \theta \quad .$$

If the roughness is modelled as a Gaussian, with σ being the standard deviation of the distribution and z_o the mean position,

[2.20] $$\rho(z) = \frac{1}{\sqrt{2\pi\sigma^2}} \exp\left[-\frac{(z-z_0)^2}{2\sigma^2} \right]$$

an exponential damping factor in the Fresnel reflection is introduced, such that

[2.21] $$r_{j-1,j} = r_F \exp(\frac{1}{2}\sigma_{j-1,j} Q_j)^2 .$$

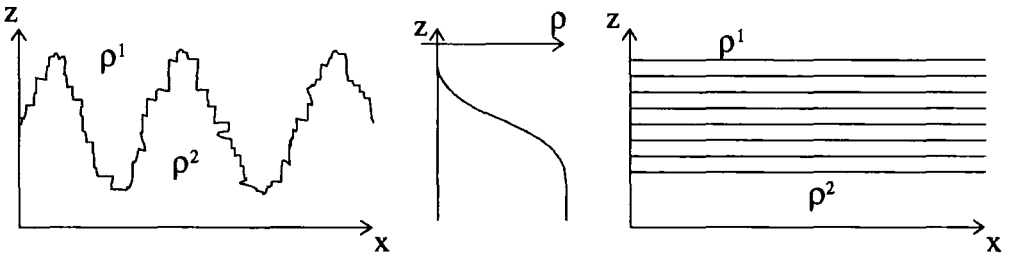

a) b)

Fig 2.3 : Model for roughness at an interface. The rough surface in a) is indistinguishable from the graded one in b).

As the Born approximation is valid only for small reflectivities the Distorted Wave Born Approximation (DWBA) must be used as the reflectivity approaches unity. Sinha et al [5] have used an expression which matches these two approximations in their respective regimes of validity,

[2.22] $$r_{j-1,j} = r_F \exp\left(-\frac{1}{2}\sigma^2_{j-1,j} Q_j Q_{j-1} \right).$$

When this is substituted into equation [2.8] we obtain

[2.23] $$r_{j-1,j} = \left(\frac{f_{j-1} - f_j}{f_{j-1} + f_j} \right) \exp\left(-\frac{1}{2}\sigma^2_{j-1,j} Q_j Q_{j-1} \right)$$

which can be used to simulate the reflectivity profile obtained. X-rays are best suited to view small roughnesses, of the order of Å, as this is comparable with the x-ray wavelength.

2.1.3 : Information from Specular Scans

Experimentally, a specular reflectivity profile is achieved by moving both detector and sample in a ratio of 2:1, so the incident and exit angle from the specimen are kept equal. The angle shown on the scans is that of the sample. For a perfect surface, the specular reflectivity will fall as a function of $(2\theta)^{-4}$ (far from the critical angle), as is shown in Fig 2.4. Roughness scatters x-rays diffusely out of the specular beam, leading to a decrease in intensity observed.

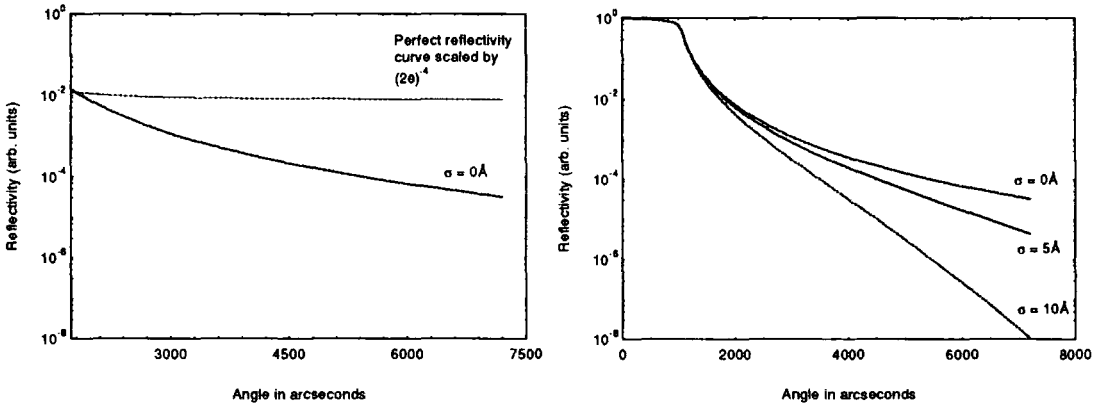

a) b)

Fig 2.4 : Simulated reflectivity scans for InP substrates a) showing a smooth surface with the characteristic fall in intensity and b) for various roughnesses

If a single layer is deposited on the substrate, interference fringes are seen as the angle of incidence is changed. For large θ (above $2\theta_c$) and ignoring the variation of x-ray refractive index with material, the condition holds that the layer thickness, t, is related to the fringe period $\Delta\theta$ by,

[2.24] $$t = \frac{\lambda}{2\Delta\theta}$$

As the amplitude of the fringe decreases as the interface roughness is increased, this allows us to determine simultaneously the interface roughness and layer thickness to Å precision.

The specular part of the scan is simulated using GIXS written by Wormington of Bede Scientific. In this code the reflectivity intensity is calculated using Parratt's recursive formalism. Values for refractive indices are derived from the atomic scattering factors listed in the International Tables for X-Ray Crystallography [6].

In specular scans the decrease in reflected intensity is normally simulated as being due to roughness. For a perfectly smooth surface with a change in electron density through the layer, (i.e. grading), however, many reflected waves which are out of phase are introduced, leading to destructive interference and a decrease in specular intensity. A specular scan cannot distinguish between these two effects. In order to achieve sensitivity to grading versus roughness, diffuse scans are also necessary.

2.1.4 : Principles of Reflectivity - Diffuse

Specular reflectivity occurs only when the incident angle exactly equals the exit angle. If roughness is present on the surface, x-rays are scattered out of the reflected beam, as mentioned above. An open detector integrates over both the specular beam and the diffuse scatter. When the detector acceptance angle is limited by slit or analyser, the specular and diffuse beam can be resolved. A perfectly smooth but compositionally graded surface will result in no diffuse scatter, whereas a very rough surface will result in high levels of diffuse scatter. In this way, diffuse scatter can be used to distinguish between grading and interface roughness. A transverse diffuse scan is achieved by scanning the sample around θ while the detector is set at 2θ. A typical diffuse scan is shown in Fig 2.5, showing the diffuse scatter and the two Yoneda wings - the first corresponding to the critical angle for the incident beam, and the second to the critical angle of the reflected beam. At these positions Fresnel's laws state that the component of the beam which would normally penetrate into the layer instead lies parallel to the surface. This will lead to an increase in scattered intensity.

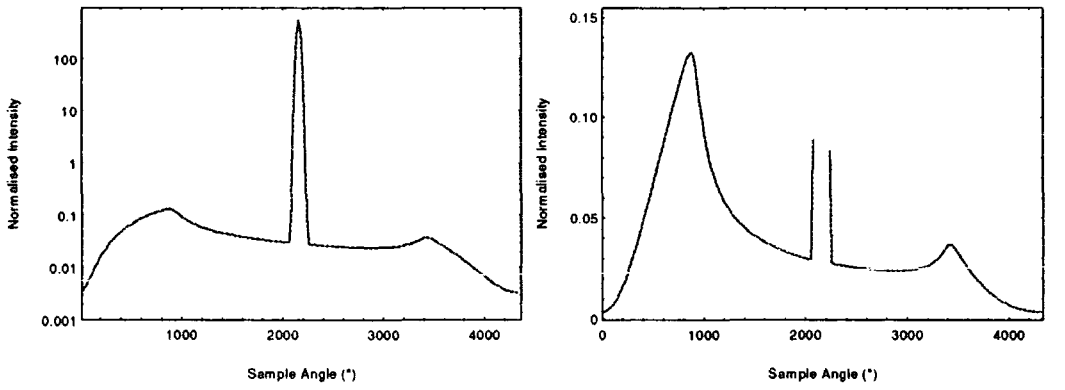

a) b)

Fig 2.5 : Typical diffuse scan for an InP substrate shown on a) logarithmic and b) linear scale.

In order to model the diffuse scatter in terms of the roughness in Fig 2.3, Sinha et al [5] have expressed the roughness in terms of a vertical height-height correlation function,

[2.25] $$C(x,y) = \langle z(0)z(x,y)\rangle = \sigma^2 \exp\left(-\frac{r}{\xi}\right)^{2h}$$

where *z(x,y)* is the height of the real surface measured from an average surface and *z(0,0)=0*. This equation describes a self-affine fractal surface†, where the cut-off is determined by the roughness correlation length, ξ. The fractal parameter, h, varies between 0 and 1, and is a measure of how jagged or smooth a rough surface is. It is possible for roughness to be replicated from one layer to the next, in which case the correlation between layers n-1 and n becomes,

[2.26] $$C_{n-1,n} = \langle z_n(0)z_{n-1}(x,y)\rangle = \sigma^2 \exp\left[\left(-\frac{(x^2+y^2)^{\frac{1}{2}}}{\xi}\right)^{2h}\right]$$

and the roughness is known as correlated, or conformal. This model has been extended by Wormington of Bede Scientific to include compositional grading by introducing a variation in electron density perpendicular to the surface. The full expressions for the integrated intensities are given in reference [7]. The diffuse scatter includes an inverse sin θ_1 term, where θ_1 is the incident angle. This is to account for the change in area

† These exhibit anisotropic scaling behaviour as the length scale of observation is changed. They are described by

$$z(x) \approx b^h z(bz)$$

where z(x) is the height of the interface at x and h is the self-affine exponent. For h=1, the surface becomes self-similar.

illuminated by the x-ray beam as the sample is rotated. Within the simulation code (GIXS and GIXR), a numerical approach based on look-up tables is used to evaluate the Fourier cosine integrals within the integrated intensity equations. If correlated roughness is present, the roughnesses must be added in quadrature,

[2.27] $$\sigma^2_{spec} = \sigma^2_{corr} + \sigma^2_{uncorr} + \Sigma^2_{grading}$$

where the grading has been introduced as an error function of width Σ.

A combination of specular and diffuse scans, therefore, allows us to characterise the surface morphology extremely well. In the case of a graded layer, the apparent roughness will change with scattering vector, so taking and simulating transverse diffuse scans for two different scattering vectors allows a far more sensitive fit.

2.1.5 : Scans in Reciprocal Space

In summary, the two types of scan, specular and diffuse, allow compositional grading and roughness to be resolved. Some forward diffuse scatter will be present in a specular scan, which can be measured by off-setting the sample by a small angle, and repeating the specular scan. This is called an off-specular scan. The path of these scans in reciprocal space is shown in Fig 2.6. The specular, or longitudinal scan, moves along q_z, while the off-set specular moves at an angle to it. The specular beam is only sensitive to vertical correlations, and is not sensitive to roughness correlations. The off-specular probes certain surface frequencies which have a vertical period, such as roughness which is correlated from one layer to the next. The transverse diffuse scan moves along q_y and is sensitive to horizontal spatial frequencies across the surface, so maps out lateral roughness correlations.

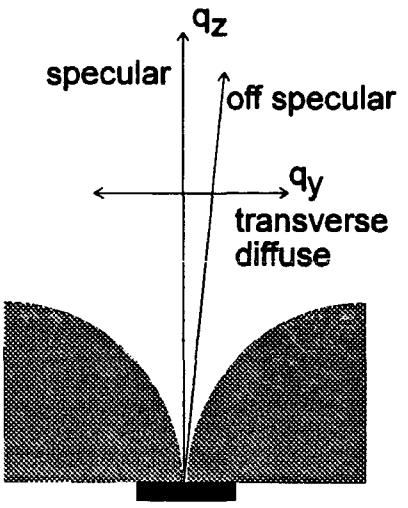

Fig 2.6 : View of the reflectivity scans in reciprocal space. The shaded area is outside the limit of observation.

2.1.6 : Coherence Length

In optics the coherence length, ξ, is defined as the distance apart two emitters can be and remain in phase. The situation is analogous to a Young's slit arrangement, and is given by,

[2.28] $$\xi = \frac{\lambda R}{r_s}$$

where R is the source to sample distance and r_s is the source size [8]. This length is therefore determined by the source characteristics.

2.2 : X-Ray Diffraction - Kinematical Approximation

The kinematical theory of x-ray diffraction is based on the simple assumption that the x-ray diffracted amplitude is small compared to the incident amplitude. This is true of very thin crystals, and those which are highly imperfect. The system can therefore be regarded as consisting of a plane, monochromatic wave incident on a small sample, where the magnitude of the incident wave amplitude is the same at all points in the sample, but the phase varies. The atoms are regarded as point scatterers but both

scattered intensity and absorption are assumed to be small, so are neglected in this treatment, which is covered in references [9, 10].

2.2.1 : The Reciprocal Lattice

If the Fourier transform of a Poisson distribution with period a is taken, another Poisson distribution is obtained with period $a^*=1/a$. If a periodic structure is described as the convolution of a shape function and the Poisson distribution,

[2.29] $$f_{periodic}(x) = f_{one\_period}(x) * P_{[a]}(x)$$

the Fourier transform of $f_{periodic}$ can be seen in Fig 2.7.

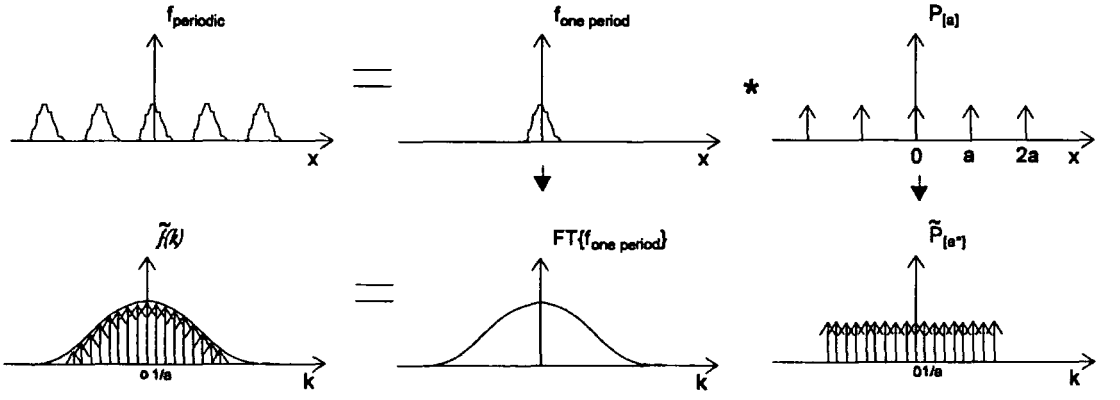

Fig 2.7 : Fourier transform of a periodic function

When this is regarded in three dimensions, we have a period with basis vectors a,b,c in the lattice. This gives rise to a potential of the form

[2.30] $$V(r) = \sum_{all\,\underline{K}} V_{\underline{K}} e^{i2\pi \underline{K}\cdot\underline{r}}$$

where non-zero results are obtained for $\underline{K} = ha^* + kb^* + lc^*$ where a^*,b^* and c^* are the basis vectors of the reciprocal lattice. In the convention used here,

[2.31] $$\underline{k} = \frac{2\pi}{\lambda}$$

although some conventions exclude the 2π term.

Having obtained a construction for reciprocal space, diffraction can be regarded in terms of the Ewald sphere [11], shown in direct and reciprocal space in Fig 2.8. It can

be seen that the direction of the diffraction vectors is the same in reciprocal and real space. From this diagram, Bragg's Law can also be deduced,

[2.32] $$2d_{hkl} \sin\theta = n\lambda .$$

We can see that diffraction occurs when the Ewald sphere passes through the origin and another reciprocal lattice node. The amount of scattering produced by each node varies, and is dependent on the structure factor.

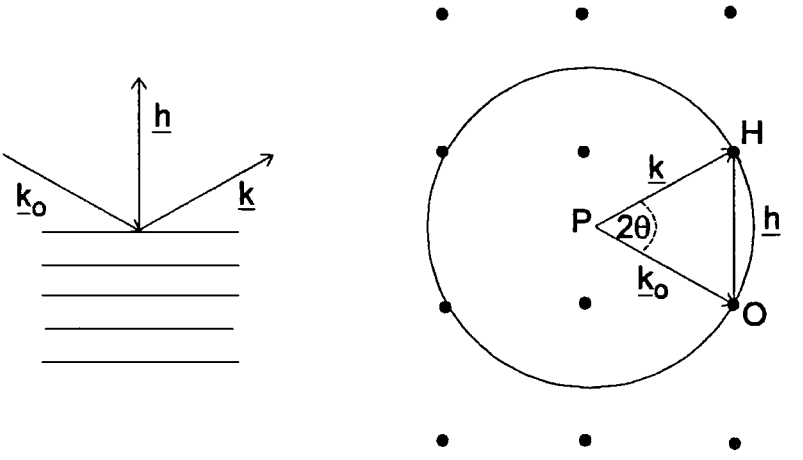

a) b)

Fig 2.8 : Ewald's construction in a) real and b) reciprocal space

2.2.2 : Structure Factors

As x-rays are sensitive to electron density (via Thomson scattering), the scattering amplitude is proportional to the Fourier transform of the (periodic) electron density in the crystal. This allows an expression for the structure factor to be obtained,

[2.33] $$F_h = \sum_{\text{unit cell}} f_{at,i}(h) e^{-2\pi i \underline{h}.\underline{r}_i} . e^{-W_i}$$

where $f_{at,i}(h)$ is the atomic scattering factor for atom i at position $\underline{r}_i$, which is tabulated against $(\sin\theta)/\lambda$ in the International Tables for Crystallography [6]. The factor e^{-W_i} is the square root of the Debye-Waller factor which takes into account the mean square displacement, $\langle u^2 \rangle$ of the atom around its equilibrium position at the temperature used, where

[2.34] $$W_i = 8\pi^2 \frac{\sin^2\theta}{\lambda^2} \langle u_i^2 \rangle$$

2.2.3 : Absorption Length

As an x-ray wave travels through a crystal, its intensity will be reduced. The rate at which this decrease occurs is described by,

[2.35] $$I = I_o e^{-\mu x}$$

where μ is the linear absorption coefficient and x is the path length in the crystal. For a compound semiconductor μ becomes

[2.36] $$\mu = \sum_i \left(\frac{\mu}{\rho}\right)_i \omega_i \rho$$

where i is the number of elements, (μ/ρ) is tabulated in the International Tables for Crystallography [6] for a given wavelength, ω_i is the atomic mass fraction, and ρ is the compound density.

2.2.4 : Integrated Reflectivities

The reciprocal node is a small volume rather than a point, so as the sample is rotated a curve of intensity against angle is obtained, a so-called rocking curve. The integrated reflectivity under this curve has been derived as [9],

[2.37] $$R_{hkl} = \lambda^3 r_o^2 \frac{|F_h|^2}{V_c^2}\left(\frac{1+\cos^2 2\theta}{2}\right)\frac{1}{\sin 2\theta} V$$

where the $1/\sin 2\theta$ term is the Lorentz factor which involves the experimental geometry. This determines how long the sphere takes to pass through the node. V and V_c are the volumes of the crystal and unit cell respectively and $(1+\cos^2 2\theta)/2$ is the polarisation factor for an unpolarised beam. In the case of σ polarisation (with E perpendicular to the scattering plane),the polarisation coefficient $C_\sigma=1$ and for π polarisation (E in the scattering plane) $C_\pi=\cos 2\theta$.

Within the kinematical approximation, therefore, measurement of the structure factor for a particular node of the reciprocal lattice allows information on the distribution of atoms within the unit cell to be obtained. This is the basis of much crystallographic work. The basic assumptions of kinematic theory, however, lead to failings in predicting experimental results. A plot of integrated intensity against sample thickness

is shown in Fig 2.9. As the sample thickness increases (shown here over the Pendellösung length, discussed later), fringes appear which are not reproduced by the kinematical theory. In addition, the development of large, extremely perfect crystals demands a theory in which the diffracted intensity is considered. This theory is known as the dynamical theory of x-ray diffraction.

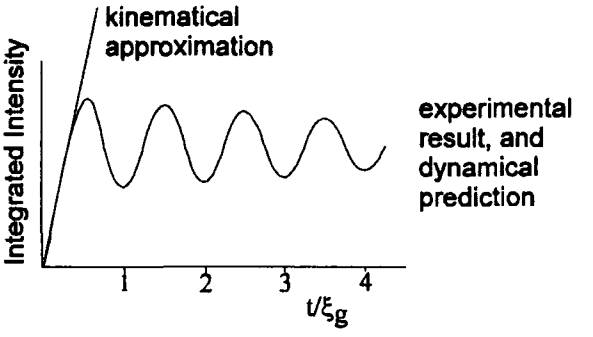

Fig 2.9 : Breakdown of the kinematical theory in predicting integrated intensities for thick samples

2.3 : X-Ray Diffraction - Dynamical Theory

In this theory the idea that a diffracted wave can be re-diffracted back into the incident direction is included, so energy is conserved. It relies on the concept of wavefields where the incident and diffracted wave are coherent, producing coupling. As it is no longer based on the Fourier transform of the electronic density, phase information on the reflected wave can also be obtained.

The approach which is taken here is that of von Laue, which has been reviewed in depth in references [9, 12-16]. Although both magnetic and electric interactions occur when an electromagnetic wave is incident on a charged particle, the magnetic interactions are weak and only the electric interactions are considered.

2.3.1 : Basic Equations

It is assumed that the crystal behaves as a perfect dielectric under the influence of the electromagnetic field, with an electric susceptibility of,

[2.38] $$\chi = -\frac{e^2\rho}{4\pi^2\varepsilon_o\nu^2 m} = -\frac{r_o\lambda^2\rho}{\pi} = \sum_h \chi_h \exp(2\pi i \underline{h}.\underline{r})$$

where r_o is the classical radius of the electron. A very small (10^{-5} or 10^{-6}) and negative electric susceptibility is therefore obtained. As this susceptibility is periodic, it can be expanded as a Fourier series over the reciprocal lattice, as shown above, with,

[2.39] $$\chi_h = -\frac{r_o\lambda^2 F_h}{\pi V_C}.$$

By considering Maxwell's equations and solving for the boundary conditions between two media, a propagation equation for the electromagnetic wave in a crystalline medium can be obtained in terms of $\underline{D}$, the electric displacement.

[2.40] $$\Delta D + \nabla \times \nabla \times (\chi D) + 4\pi^2 k^2 D = 0$$

The electric field is then given by

[2.41] $$E = \frac{D}{\varepsilon_o(1+\chi)} \cong \frac{D}{\varepsilon_o}(1-\chi).$$

The propagation equation is a second order differential equation with a periodic coefficient, so the solution will be of the form,

[2.42] $$D(r) = \sum_h D_h \exp(-2\pi i \underline{k}_h.\underline{r})$$

where $\underline{k}_h = \underline{k}_o + \underline{h}$.

The wavevectors have an imaginary part in an absorbing crystal, which is the same in all cases. All wavevectors, therefore, undergo the same absorption. As for x-rays there are, in general, only two reciprocal lattice points on the Ewald sphere equation [2.40] can be reduced to a set of linear, homogeneous equations. For a non-trivial solution, the determinant is set to zero, resulting in

[2.43] $$\alpha_o\alpha_h = \frac{1}{2}k^2C^2\chi_h\chi_{\bar{h}}$$

where

[2.44] $$\alpha_o = \frac{1}{2k}\left\{\underline{k}_o.\underline{k}_o - k^2(1+\chi_o)\right\}$$

$$\alpha_h = \frac{1}{2k}\left\{\underline{k}_h.\underline{k}_h - k^2(1+\chi_o)\right\}$$

In effect, propagation is taking place as Bloch waves, which are the superposition of the transmitted and diffracted wave, and are similar to standing waves.

2.3.2 : The Dispersion Surface

Equation [2.43] represents the locus of all the tiepoints, i.e. wavevectors of waves, which may propagate in a crystal with a given frequency, called the dispersion surface. This is shown in Fig 2.10, which is a modified version of the Ewald sphere used in Fig 2.8. The outer ring is propagation in a vacuum with radius k, while the inner ring is in the crystal, with radius $nk \approx k(1+\chi_0/2)$. The intersection of spheres in a vacuum, L_a, is the Laue point, while that in the crystal is the Lorentz point, L_o. Far from the Lorentz point, reflection and refraction occurs as normal, but close to L_o dynamical theory dominates. If a close up around L_o is taken, we see Fig 2.11. The two solutions obtained for the two-wave case result in a hyperbola with asymptotes lying through L_o. When the Bloch wave reaches the exit surface of the crystal, the coupling disappears. The tangential component of the wave must be conserved across the interface, so the wave splits into two - the transmitted and diffracted beam. Each of these has two polarisation states, so the dispersion surface is represented as two branches, each split into two, as shown in Fig 2.11. The hyperbola has two branches (labelled 1 and 2), one for each direction of polarisation, with σ polarisation being shown in full, and π polarisation being dashed. A sign difference exists between tie-points on the two branches, representing a phase difference of π. For a tie-point P the propagation direction lies perpendicular to the dispersion surface, along S.

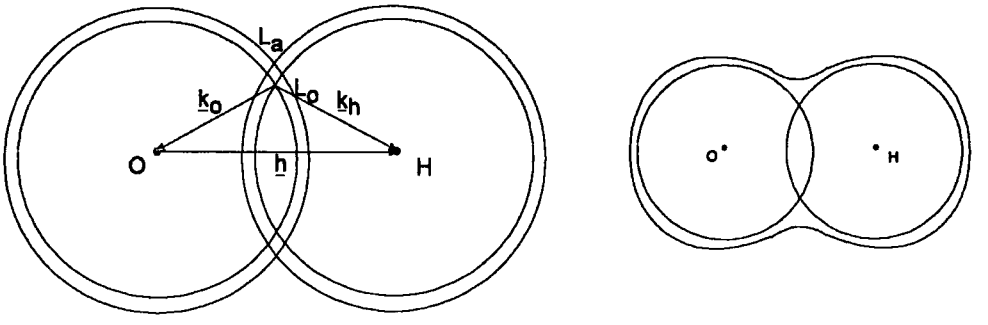

a) b)

Fig 2.10 : a) Construction of the dispersion surface seen in b)

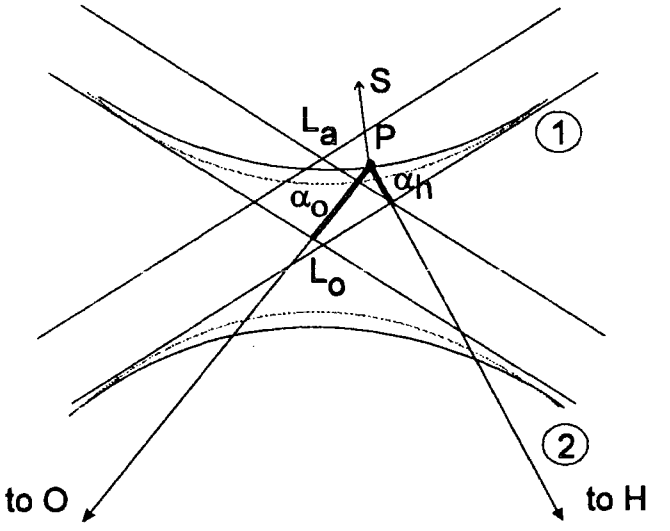

Fig 2.11 : The close up of the Lorentz point showing the two branches and polarisation states

2.3.3 : Transmission and Reflection Geometries

In the transmission, or Laue geometry, the normal to the crystal surface intersects both branches of the dispersion surface, and the diffracted wave is directed inside the crystal, as shown in Fig 2.12. If γ_o and γ_h are defined as the cosines of angles between the surface normal and incident and reflected directions respectively, an asymmetry ratio, γ, can be defined, where,

[2.45] $$\gamma = \frac{\gamma_h}{\gamma_o}$$

which is positive in this case.

In reflection, shown in Fig 2.13, three possible situations occur. The normal either intersects branch 1, branch 2, or neither, in which case it is imaginary. It is unphysical for the tie point pointing out of the crystal to exist, and γ is negative. In the symmetric Bragg case when no tie-point is available, the incident wave is totally reflected, which occurs over the Darwin width, ω.

[2.46] $$\omega = \frac{2|\chi_h|}{\sin 2\theta}$$

This is centred about the Lorentz point and gives a characteristic "top hat" function.

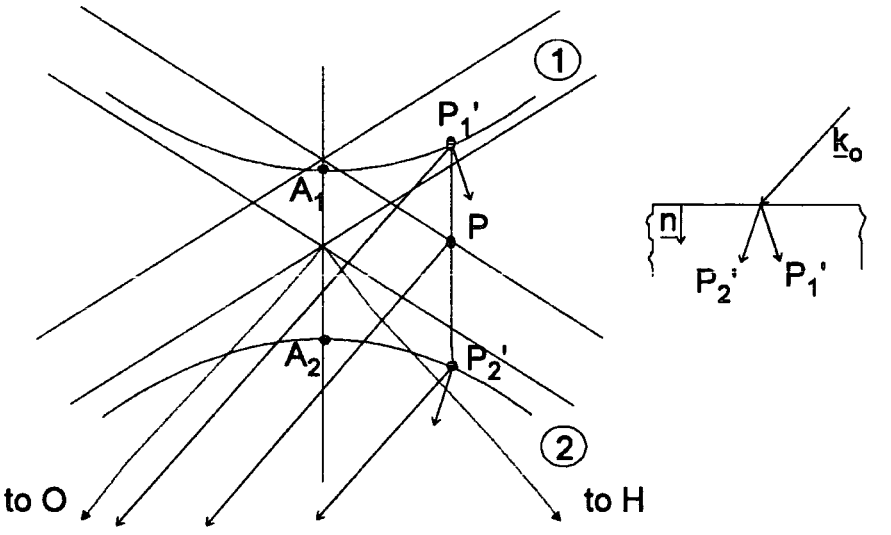

Fig 2.12 : The dispersion surface in Laue (transmission) case

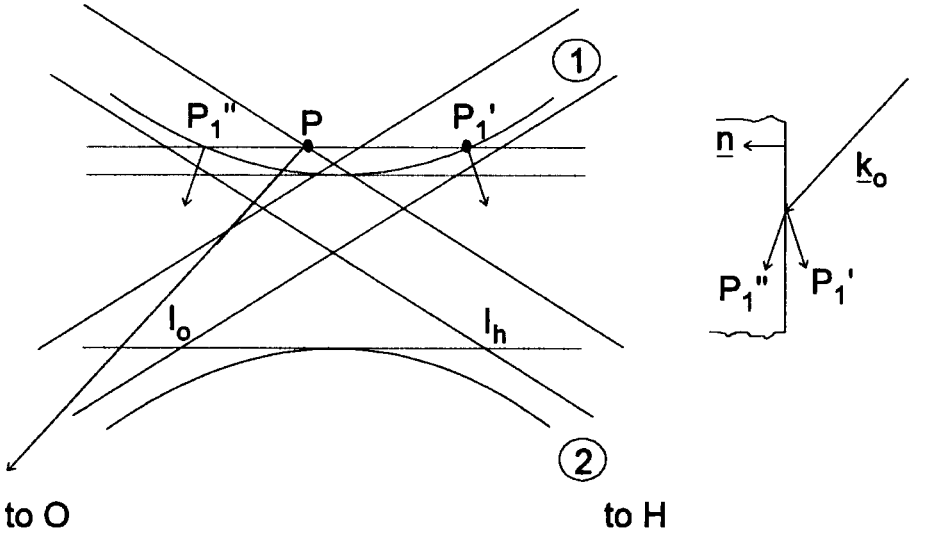

Fig 2.13 : The dispersion surface in Bragg (reflection) case

2.3.4 : Pendellösung Distance

The length, ξ_o, is defined by,

[2.47] $$\xi_o = \frac{\sqrt{\gamma_o|\gamma_h|}}{|C|\sqrt{\chi_h\chi_{\bar{h}}}}.$$

In the transmission geometry this is the interference period between the two wavefields, and is called the Pendellösung period. With no absorption it is the inverse distance $\overline{A_2A_1}$ in Fig 2.12. In reflection geometry, it is called the extinction distance,

being the inverse of the length $\overline{I_h I_o}$ in Fig 2.13, and gives the absorption distance during total external reflection. This extinction distance can also be described by [17],

[2.48] $$\xi = \frac{mc^2}{e^2} \cdot \frac{\pi V}{|C|\lambda|F|} \cdot \left[|\sin(\theta_B - \phi)|\sin(\theta_B + \phi)\right]^{1/2}$$

where C is the polarisation factor, m is the electron mass, V is the volume of the unit cell and ϕ is the negative angle between the crystal surface and the diffracting planes.

2.3.5 : Anomalous Absorption

If the ratio of the amplitudes of the diffracted and incident wavefields is taken a phase factor, Φ, is present, which is dependent on the diffraction geometry and governs the position of the nodes of the standing waves formed within the crystal. As the two branches in the dispersion surface are on opposite sides of the asymptotes, they have opposite sign, and Φ is equal to $(\pi + \varphi_h)$ for branch 1 and φ_h for branch 2, in the Laue case. In the Bragg case Φ varies continuously from $(\pi + \varphi_h)$ to φ_h as the angle of incidence moves from the low angle to high angle side by rocking the crystal. φ_h is the phase of the structure factor.

Therefore, in the Laue case, the nodes of the standing wave formed coincide with the atomic positions for branch 1, and the anti-nodes for branch 2. This is shown in Fig 2.14. As x-rays are mainly absorbed by interaction with electron clouds surrounding atoms, the branch with its nodes corresponding to atomic positions will suffer less absorption than if there was no diffraction, while the branch with its anti-nodes in this position will be absorbed more than normal. So, under conditions of anomalous absorption such as this, branch 1 wavefields are transmitted while branch 2 wavefields are absorbed. This provides a useful tool for imaging highly absorbing materials.

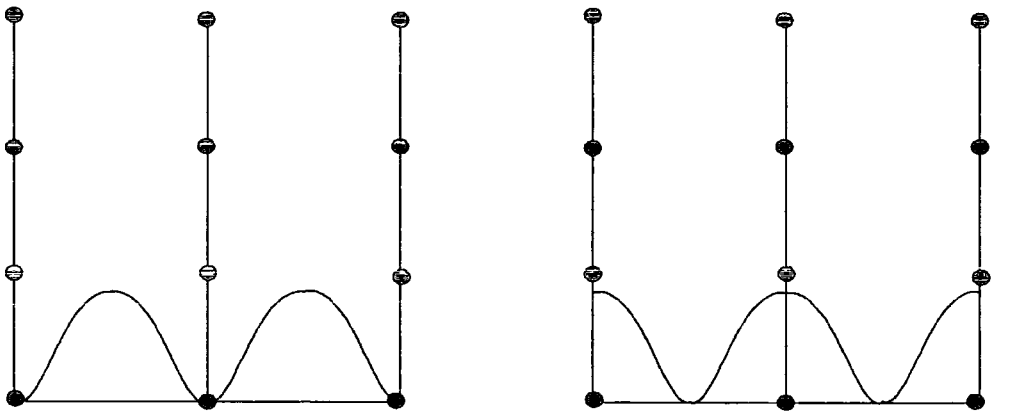

a) Branch 1 b) Branch 2

Fig 2.14 : Wavefields for branch 1 and 2 at the exact symmetric Bragg condition. Dots represent atomic positions.

2.4 : Extension to imperfect crystals

2.4.1 : Effective Misorientation

When a crystal is deformed, a position P which has a position vector r is transformed into one at position P', with position vector r', such that

[2.49] $$\underline{r}' = \underline{r} + u(\underline{r})$$

where u(r) is the displacement vector. This transformation has the effect of moving the Laue point and modifying the reciprocal lattice. This is shown in Fig 2.15.

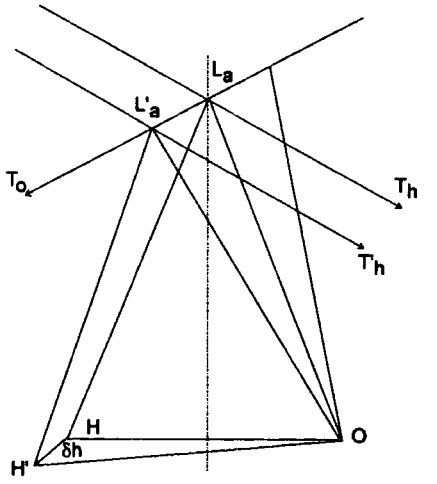

Fig 2.15 : Modification of the reciprocal lattice due to crystal deformation

The Bragg angle then becomes,

[2.50] $$\theta_o' = \theta_o - \frac{\delta d}{d}\tan\theta_o$$

and the effective misorientation, $\delta\theta$, is seen to be,

[2.51] $$\delta\theta = \Delta\theta' - \Delta\theta = \frac{\overline{L_a' L_a}}{k}.$$

2.4.2 : Takagi's Theory

When a crystal is deformed, the notion of wavefields is no longer appropriate. In fact, ray theory becomes more suitable for describing the waves, where a slowly varying index of refraction is used. A more ambitious approach, developed by Takagi, is a generalisation of the dynamical theory for any kind of incident wave, and deformed crystals.

The main assumption used is that the crystal wave is a modified Ewald wave, characterised as before by

[2.52] $$\underline{D} = \sum \underline{D}_h(\underline{r})\exp(-2\pi i \underline{k}_h . \underline{r}) .$$

In this case, however, $\underline{D}_h$ is slowly varying so that its derivatives are negligible. $\underline{k}_o$ now has an arbitrary orientation and is of length nk_{vacuum}. The exponential is a phase factor, which no longer has any physical meaning.

Substitution into the propagation equation produces an infinite set of terms which, in the two wave case, produce two sets of terms each with two equations. These again correspond to σ and π polarisations. Unfortunately, the final equations need to be solved numerically.

In summary, the Takagi theory mathematically relates the total amplitude and phase of a reflected or refracted wave to another point in the crystal, without the physical model of wavefields and tiepoints. Instead an influence function distribution is used, which depends on the strain distribution in the case of deformed crystals.

2.5 : Production of X-rays

The generation of x-rays can either be achieved through the interaction of electrons with matter, or through the relativistic behaviour of electrons. The first of these is exploited in conventional laboratory sources, and the second in synchrotron radiation.

2.5.1 : Laboratory Sources

An x-ray tube consists simply of a potential of the order of tens of keV applied across a heated cathode and a water cooled anode target. The thermally emitted electrons are accelerated towards the anode, and interact with the target nucleus via the Coulomb field, so transferring momentum to the nucleus and decelerating. This deceleration leads to the emission of a discrete number of Bremsstrahlung photons. As the electron can interact with many nuclei before coming to rest, losing a different amount of energy in each interaction, a spread of wavelengths are produced. As the maximum energy which can be transferred in a reaction is the total electron energy, a critical wavelength below which radiation is not produced is observed, which is dependent on the accelerating voltage. The power which can be used is limited by the rate of heat dissipation from the water cooled anode. Due to the shell structure of the electrons around a nucleus, discrete energy emissions are produced when an electron is excited from one shell to another. These form characteristic lines represented by the letters K,L,M etc, which correspond to levels n=1,2,3 etc.

By varying the elemental anode used, the wavelength of the Kα line can be varied from 0.559Å to 2.289Å (for Ag and Cr respectively). Radiation 6° from the anode surface is used, which can be viewed either as a line with dimensions 8mm x 40μm or as a spot with dimensions 800μm x 400μm. Increased intensity can be obtained by using a rotating anode. There are two main reasons, however, why this process is energy inefficient. Firstly, much of the electron energy is converted to heat in the anode, instead of x-rays. Secondly, as a non-relativistic radiator emits photons isotropically with a large solid angle, only a fraction of the x-rays produced are used. Synchrotron radiation has inherent advantages in both these areas.

2.5.2 : Synchrotron Radiation

Synchrotron radiation is produced by accelerating electrons in a linear accelerator, passing them through a booster, then injecting them into a main storage ring, where they are constrained to move in a circle by the addition of magnets [18-20]. The magnets used have fields of a few Tesla, and are placed perpendicular to the orbit plane. This provides the Lorentz force on the electron which causes acceleration towards the centre of the circle. This is shown in Fig 2.16. The radius of curvature is dependent on the magnetic field applied and the relativistic parameter γ where

[2.53] $$E = \gamma mc^2$$

and

[2.54] $$v = c\left(1 - \frac{1}{\gamma^2}\right)^{\frac{1}{2}}.$$

v is the particle velocity, c the velocity of light, m the rest mass and E the energy. As no interaction with matter occurs, the exchange from electron kinetic energy to x-rays can occur with almost 100% efficiency, ensuring a greater flux.

An increase in flux is also obtained through the radiation produced being mainly in the direction of motion of the radiating charge. This is due to the space-time Lorentz transformations, whereby the light emitted at θ' to the direction of motion is viewed at θ in the laboratory frame. This has been shown to approximate to an opening angle in the laboratory frame of $1/\gamma$, as shown in Fig 2.16. This provides a beam which is highly vertically collimated.

The range of wavelengths emitted is also defined by its relativistic properties. Due to the high collimation, an observer far from the particle will be able to see x-rays produced within a rotation angle $2/\gamma$. This corresponds to a very short pulse, which will provide the high frequencies observed, as well as the broad spectrum available. This geometry leads to a beam profile where the intensity of the beam varies with wavelength. At the Daresbury SRS the peak intensity corresponds to a wavelength of 1.39Å on Station 2.3. Synchrotron sources, therefore, provide increased flux with a high degree of collimation and the advantage of wavelength tunability.

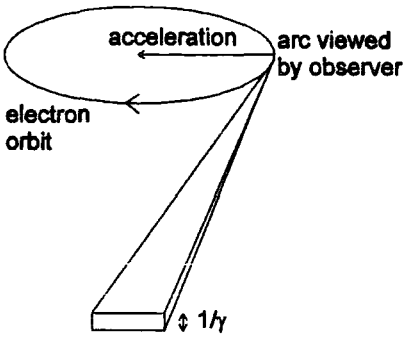

Fig 2.16 : Radiation emission of electrons travelling relativistically

References

1. Kiessig, H., Ann. Phys., 1931. **10**: p. 715.

2. Lengeler, B., *X-Ray absorption and reflection in the hard x-ray range*, in *Photoemission and Absorption Spectroscopy of Solids and Interfaces with Synchrotron Radiation*, M. Campagna and K. Rosei, Editor. 1990, North Holland. p. 157-202.

3. Parratt, L.G., *Surface studies of solids by total reflection of x-rays*. Phys. Rev., 1954. **95**(2): p. 359-369.

4. Pape, I., . in preparation, University of Durham.

5. Sinha, S.K., E.B. Sirota, and S. Garoff, *X-ray and neutron scattering from rough surfaces*. Phys. Rev. B, 1988. **38**(4): p. 2297-2311.

6. Buerger, M.J., *et al.*, ed. *International Tables for Crystallography*. 2nd ed. Vol. III. 1985, D. Reidel Publishing Company: Dordrecht, Holland.

7. Wormington, M., *et al.*, *Evidence for grading at polished surfaces from grazing-incidence X-ray scattering*. Phil. Mag. Lett, 1996. **74**(3): p. 211-216.

8. Salditt, T., *et al.*, *X-ray coherence and ultra small angle resolution at grazing incidence and exit angles*. Z. Phys. B., 1994. **96**: p. 227-230.

9. Schlenker, M., *Fundamentals of neutron and x-ray diffraction: kinematical theory, dynamical theory*, in *Neutron and Synchrotron Radiation for Condensed Matter Studies*, J. Baruchel, *et al.*, Editor. 1993, Springer-Verlag: Heidelberg. p. 148-178.

10. Warren, B.E., *X-Ray Diffraction*. 2nd ed. 1990, New York: Dover Publications.

11. Ewald, P.P., Ann.Phys.Dtsch., 1917. **54**: p. 519.

12. Tanner, B.K., *X-Ray Diffraction Topography*. 1st ed. International Series in the Science of the Solid State, ed. B. Pamplin. Vol. 10. 1976: Pergamon Press. 174.

13. Pinsker, Z.G., *Dynamical Scattering of X-Rays in Crystals*. Springer Series in Solid-State Sciences, ed. M. Cardona, P. Fulde, andH.-J. Queisser. 1978, Heidelberg: Springer-Verlag.

14. Authier, A., *Ewald waves in theory and experiment (Dynamical theory of X-Ray diffraction)*, in *Advances in Structure Research by Diffraction Methods*. 1970, Pergamon Press. p. 1-51.

15. Authier, A., *Dynamical theory of x-ray diffraction*, in *X-Ray and Neutron Dynamical Diffraction: Theory and Applications*, A. Authier, S. Lagomarsino, andB.K. Tanner, Editor. 1996, Plenum Press: New York. p. 1-30, 41-60.

16. Azaroff, L.V., *et al.*, *X-Ray Diffraction*. International Series in Pure and Applied Physics. 1974, New York: McGraw-Hill, Inc.

17. Armstrong, R.W., *Laboratory techniques : reflection topography*, in *Characterisation of Crystal Growth Defects by X-ray Methods*, B.K. Tanner and D.K. Bowen, Editor. 1979, Plenum Press: New York. p. 349-367.

18. Batterman, B., *Synchrotron radiation sources and synchrotron radiation facilities*, in *X-Ray and Neutron Dynamical Diffraction : Theory and Applications*, A. Authier, S. Lagomarsino, andB.K. Tanner, Editor. 1996, Plenum Press: New York. p. 71-83.

19. Magaritondo, G., *A primer in synchrotron radiation : everything you wanted to know about SEX (Synchrotron Emission of X-Rays) but were afraid to ask.* J. Synch. Rad., 1995. **2**: p. 148-154.

20. Raoux, D., *Introduction to synchrotron radiation*, in *Neutron and Synchrotron Radiation for Condensed Matter Studies*, J. Baruchel, *et al.*, Editor. 1993, Springer-Verlag: Heidelberg. p. 37-78.

Chapter III

Experimental Techniques of Diffraction and Reflectivity

3.1 : White Beam Topography

X-ray topography is a technique for investigating crystal defects, by mapping the scattering power of the crystal across the diffracted beam. The technique is based on the fact that Bragg reflection from undistorted lattice planes is different from that from distorted planes caused by the presence of strain fields of crystal defects. This allows an image to be obtained across a single crystal with contrast between the various crystal features. Several good reviews exist which cover both the fundamentals of topography, and include examples. These include the work of Tanner [1, 2], Klapper [3] and Franzosi [4].

3.1.1 : Orientation Contrast

If an x-ray beam is incident upon perfect crystal lattice planes, Bragg diffraction will occur as is shown in Fig 3.1 and no contrast is obtained on the topograph. If a crystal where twins or subgrains are present is considered, the lattice planes are misoriented and orientation contrast occurs. If monochromatic radiation is being used, and the angle by which the planes are misoriented is greater than the divergence of the incident beam, part of the crystal will not diffract and less intensity will be registered from these parts. If continuous white beam radiation is used, a different wavelength may be selected for diffraction by this part of the crystal and an increase or decrease in the intensity (depending on the sense of the misorientation) at the boundary will arise, as is shown in Fig 3.2. This is also the case if the misorientation angle is less than the divergence of the incoming beam. The second kind of contrast is extinction contrast, which is understood by considering the interaction of the incident and diffracted beams in the crystal, within the context of the dynamical theory. This will be dealt with in its three components, i.e. the direct (kinematical), dynamical and intermediary image.

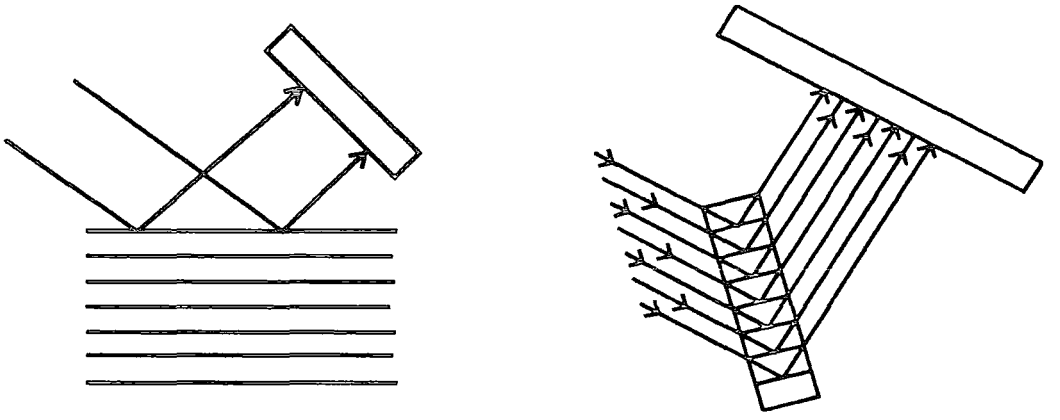

a) b)

Fig 3.1 : Diffraction from a perfect crystal in a) Bragg case, where the emergent beam is on the same side of the crystal as the incident beam and b) Laue case, where the beam emerges on the opposite side of the crystal. In both cases no contrast will be observed on the topograph.

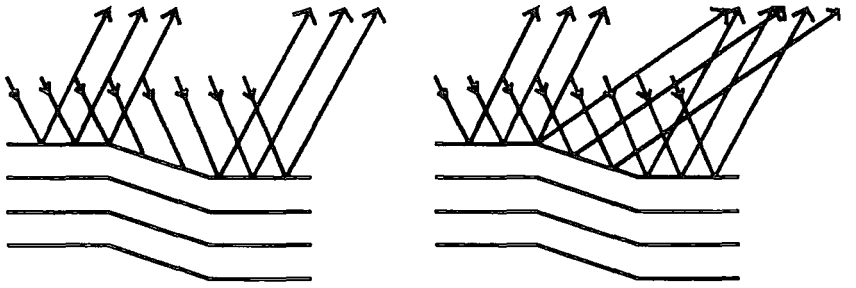

a) b)

Fig 3.2 : The origin of orientation contrast where the incident radiation is a) monochromatic and b) continuous. In the first case only a loss of intensity occurs, but in the second a loss of intensity is observed on the left hand side of the beam, and an increase on the right, due to the misoriented region selecting a different wavelength to diffract.

3.1.2 : Extinction contrast - direct image

This image is seen as an increase in intensity, leading to a dark area on a topograph. When an x-ray beam is incident on a perfect crystal only a small angular spread is reflected, called the Darwin width. Around a defect, the crystal is no longer perfect, and x-rays outside the perfect reflecting range are diffracted. This leads to enhanced scattering around the defect, which is called the direct image, and is due to purely kinematical diffraction effects. As the diffracted integrated intensity varies as shown in Fig 3.3 [5], for very thin crystals there is negligible kinematical scattering and no image

results. The minimum thicknesses to obtain an image are between $0.15\xi_g$ and $0.4\xi_g$, where ξ_g is the extinction distance (Section 2.3.4).

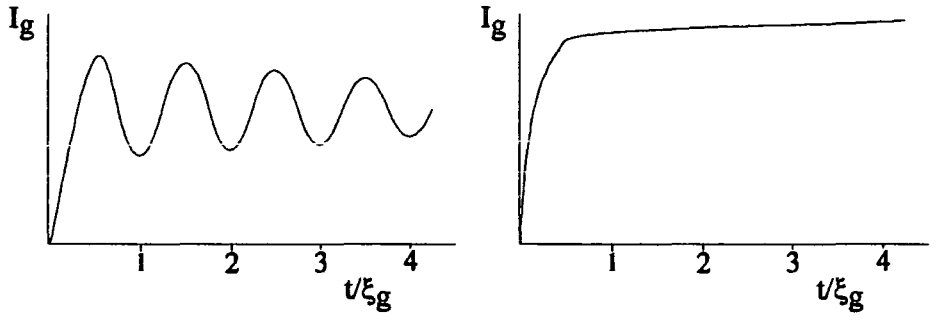

a) b)

Fig 3.3 : Integrated intensities for a dislocated crystal of thickness t and with penetration depth ξ_g in a) Laue case and b) Bragg case

The width of dislocation images can be determined for screw and edge dislocations using the fact that around a screw dislocation the effective misorientation $\delta\theta$ varies with distance from the core, r, as

[3.1] $$\delta\theta = \frac{b}{2\pi r}$$

where b is the Burgers vector of the dislocation. As the dislocation image, D, is twice the value for which $\delta\theta = \delta\omega$,

[3.2] $$D = \frac{b}{\pi\delta\omega}.$$

Using a symmetric reflection gives $\delta\omega = 2/g\xi_g$ and $D = gb\xi_g/2\pi$. More generally for a screw dislocation

[3.3] $$D = \frac{\underline{g}.\underline{b}\xi_g}{2\pi},$$

and for an edge dislocation

[3.4] $$D = \frac{0.88\underline{g}.\underline{b}\xi_g}{\pi}.$$

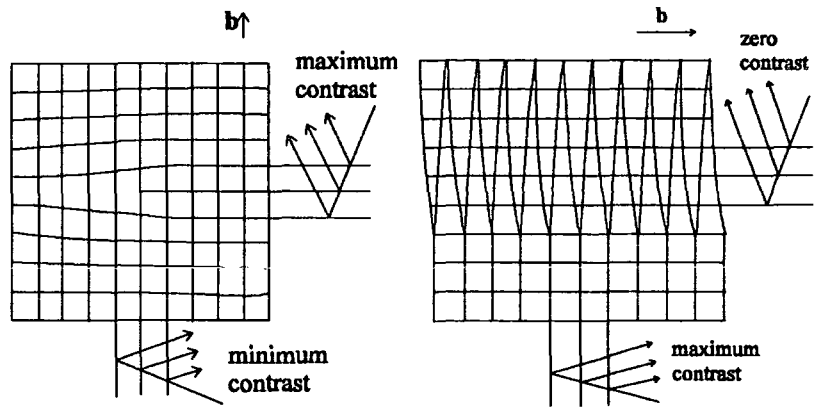

a) b)

Fig 3.4 : Lattice distortions and visibility criteria for a) an edge dislocation and b) a screw dislocation

The geometry for these two types of dislocation is shown in Fig 3.4. An edge dislocation can be visualised by the insertion of an extra plane of atoms, while the screw dislocation is a rotation of the lattice planes. Due to the geometry of these dislocations, it can be seen that minimum contrast occurs when $\underline{g}.\underline{b} = 0$. If the direction of the dislocation, $\underline{u}$, is also included we gain the condition $\underline{g}.\underline{b} \times \underline{u} = 0$ for the case of a pure edge dislocation. A mixed dislocation will never completely disappear, but $\underline{g}.\underline{b}=0$ is a good guide for minimum visibility. This allows a method of determining the Burgers vector of dislocations using topography as the imaging of several reflections with different directions of $\underline{g}$ allows a minimum contrast condition to be determined. This is useful as $\underline{b}$ may yield information on the nature and formation mechanism of a dislocation.

3.1.3 : Extinction contrast - dynamical image

When the crystal is under conditions of high absorption, the direct image is low in intensity and the dynamical image can be seen. As discussed previously, under conditions of anomalous transmission, an intense beam of predominantly σ polarised wavefields from branch 1 of the dispersion surface are transmitted. As this wave passes through the crystal, any strained regions encountered will destroy the conditions for wavefield propagation, and new wavefields will be created below the dislocation. As these new waves are no longer at the condition for anomalous transmission, they are strongly absorbed and a line of low intensity is seen around the defect. The

appearance of these images is dependent on whether the defect is close to the entrance or exit surface, the latter giving a sharper image. At this surface the wavefields decouple into diffracted and forward components, with the diffracted beam either increasing or decreasing in intensity depending on the direction of the diffraction vector. A topograph showing the presence of dynamical images is shown in Fig 3.5.

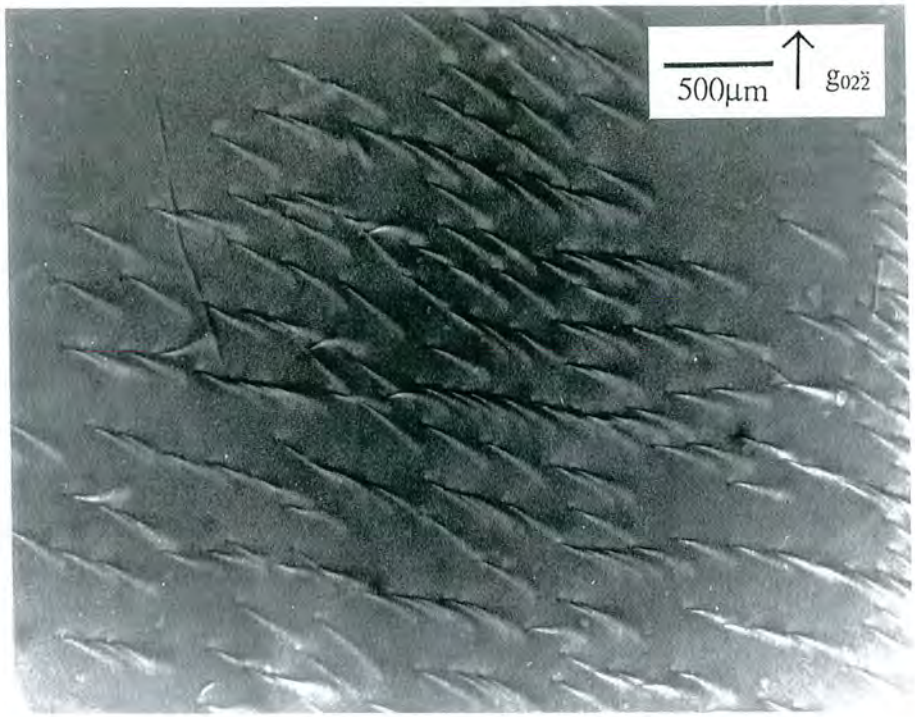

Fig 3.5 : Anomalous transmission topograph of LEC InP showing the dynamical imaging of dislocations.

3.1.4 : Extinction contrast - Intermediary Image

The new wavefields created below the defect interfere with the incident wavefield at the exit surface, and create the intermediary image. This image forms a fan within the limits set by the incident and diffracted beam's intersection with the defect, as shown in Fig 3.6. This results in oscillations of the width of direct images, giving them a bead-like contrast. An example of intermediary images in InP is shown in Fig 3.7.

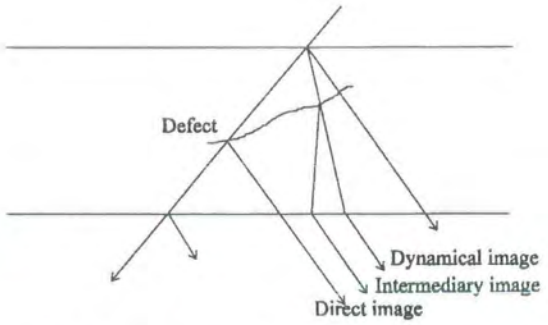

Fig 3.6 : Schematic of the different types of contrast viewed in a topograph

Fig 3.7 : Intermediary images in InP topographed at the ESRF

3.1.5 : Experimental arrangement at Daresbury Laboratory

The white beam topography beam line at Daresbury Laboratory, Station 7.6, was first commissioned in 1982, and was later combined with the double crystal station by the double axis goniometer being moved there [6, 7]. As the resolution, S, of a measurement is limited by the geometrical relation,

[3.5] $$S = \frac{hl}{d}$$

where h is the source dimension, l is the specimen to film distance and d is the specimen to source distance, it is clear that advantages in resolution are obtained by performing topography at large specimen to source distances, even if this involves

working with lower flux. Station 7.6 at Daresbury is positioned 80m from the tangent point of the beam, so resolutions of the order of microns are obtained. Two sets of slits are in use, both of which are computer controlled. The first set are outside the interlocked area, and are used to define the beam size, while those inside are set to a slightly larger value and are used as anti-scatter slits. A two axis goniometer is mounted parallel to the beam, so that the diffraction plane is vertical. This is initially calibrated to zero using a spirit level. The base is then rotated to twice the desired Bragg angle if Bragg geometry is required, or left horizontal if a Laue topograph is to be taken. The sample is mounted in a small goniometer head, and laser-aligned to be vertical in the beam. A marker is then placed next to the crystal, and it is rotated to ensure that it stays on the centre of rotation for all angles.

Small samples are mounted onto a rod using wax at the periphery of the crystal. This allows transmission topographs to be taken, but is inappropriate for large crystals as there is a tendency for them to move slightly during exposures. As many 2" thin wafers were investigated using this study, a sample holder was designed which consisted of a ring of perspex with a hole in the middle and a gap in the plane of the ring into which the crystal could be inserted. This allowed the crystals to be mounted in a strain-free environment while still having the bulk of the crystal exposed for transmission topography. In the case of Laue topographs the sample was placed roughly perpendicular to the beam, and a large amount of shielding was placed around it from the slits. The background scattered intensity became too high if the beam size exceeded $6x13mm^2$, and for small samples (of the order of 10mm) beam sizes of only $2x2mm^2$ were practicable.

Film was mounted in holders in the dark room, then positioned with clamps along a bar which would be fitted between the two goniometer axes. The types of film used, in decreasing order of resolution, were Ilford L4 nuclear emulsion plates, with a 25μm emulsion on glass, Agfa D2 film and Agfa D4 film. Polaroid PolaPan 52 sheet film and Kodak Dental film were used in alignment. The interlocked area had a photographic shutter in addition to the main safety shutter, so that exposure times of down to 0.1s could be obtained.

Daresbury is a 2GeV second generation source, with beam currents of typically 280mA after injection, and a lifetime of 30 hours [8]. Exposure times vary greatly depending on the reflection, the absorption co-efficient of the sample and the type of film (and hence resolution) required. Typical 220 anomalous transmission topographs of InP wafers at 1Å recorded on nuclear emulsion plates took 12 min to expose, while Laue patterns of GaAs recorded on D4 film required 2 hour exposures. In all cases the sample and path to the film were thoroughly shielded with lead, and in some cases with scatter slits, as the background in a white radiation hutch was unacceptably high. Developing and fixing of the films was performed on site in the adjacent dark room. Negatives were made from enlargement through a Wild microscope onto Ilford HP5 Plus film. Most of the image enlargement was done at this stage. The prints produced are thus positives, appearing as they did on the original film, with dark areas corresponding to regions of high x-ray scatter.

3.1.6 : Experimental Arrangements at the ESRF

The European Synchrotron Radiation Facility (ESRF) is a new synchrotron source, in full operation since 1994. It is a third generation source, with energy 6GeV, a 200mA current and lifetimes of about 25hours [9]. Although a dedicated topography beamline is now in operation (ID11), which is 145m from the source, and boasts a 14x40mm^2 homogenous beam, high photon flux and an 11-pole wiggler, this station was not in operation at the time that measurements described here were made [10, 11]. Instead, a temporary station had been set up on the D5 Optics Beamline, at the second experimental hutch [12]. This was about 55m from the source, and had the option of white or monochromatic radiation. The source size in the hutch was 7mm high (using the FWHM) and 165mm wide, allowing wide beam topography to be performed. The hutch was fitted with a prototype diffractometer, in addition to a simple camera for real-time Laue imaging. This was used to test the orientation of samples studied, and ensure that the sample position was optimised when particular reflections were required. The large-scale goniometer was mounted on air cushions which allowed the system to be moved easily on the marble floor. This was necessary as the diffraction plane is horizontal. Although there was the option of using a monochromator crystal, all the topographs represented here were taken using white beam only.

The ESRF is a low-emittance (small source size and divergence) and high brilliance source which produces x-ray photons up to 300keV. Although this decreases scan and exposure times, it creates problems with the heat load on a sample. Even on a beam line with no undulators or wigglers, but with just a bending magnet, the photon flux is about $2x10^{16}$photons s^{-1} $mrad^{-2}$ mm^{-2}. The effect of high harmonics on crystals has been shown by Barrett et al [11], where the Bragg planes are distorted and a bump is formed on the sample surface where the beam is incident. As the incident beam has a Gaussian profile in the vertical direction, in which the higher energies are concentrated at the centre, a temperature gradient is formed causing a distortion in the crystal, and hence variation in intensity in the topographs. A reduction in the incoming power is possible using filters, but this can lead to the suppression of the low energy part of the x-ray spectrum. In the topographs shown here, 1.5mm of aluminium was inserted in the beam, which transmits 77% of the incident beam intensity, and is a compromise between removing beam power and losing the lower energy components. In addition, a beam chopper was used, which rotates quickly in the beam allowing time to cool between each rotation. The slots were adjusted so that 10% of the flux was incident on the sample.

In most cases only short wavelength Laue images were recorded, so Kodak Industrex R film was used, which gave a good exposure in two seconds. Although this film is lower in resolution than nuclear emulsions, the use of short wavelengths means that the dislocation images are wide and comparable information can be obtained. InP is strongly absorbing in the normal regime used for topography, as is shown in the Daresbury topographs, where the images are produced by anomalous transmission. The use of such high energy photons in the range 50-100keV means that kinematical images can be obtained. Another advantage of these high energies is the ability to investigate heavy or bulky samples, such as the space-grown GaSb described later. Previous studies at the ESRF have achieved transmission topographs through 1cm thick silicon and 1.4mm iron [13, 14].

3.2 : Double Axis Diffraction

Single crystal diffraction has been shown to enable the imaging and characterisation of single crystal defects in bulk materials. If single crystal experiments are used in the measurement of rocking curves, however, the results obtained are affected by the beam divergence, source size and wavelength dispersion. As these broaden a peak, a limitation on the resolution is imposed, which in practice corresponds to only lattice mismatches of 10^{-4} or greater being accessible using this technique [15]. The current interest in epilayers closely matched to the substrate (such as InAsP on InP) demands higher resolution, which can be obtained via the introduction of a conditioning first crystal, as first described by Hart et al [16], based on the original work of Du Mond [17].

The effect of a conditioning crystal is different depending on the orientation and material chosen. Much of the double crystal work represented here was carried out on a Bede model 150 diffractometer, where the distance between the reference and sample is 150mm. The base of the diffractometer is aligned in the beam manually, so that the direct beam travels over the first axis, and the base is at twice the conditioning crystal's Bragg angle. The 1.5kW tube was used with a Cobalt target, producing characteristic lines at λ=1.78897 Å and 1.79285 Å for $K\alpha_1$ and $K\alpha_2$ respectively and one at 1.62079Å for $K\beta_1$. A brass channel 160mm long and 8mm wide, culminating in a pin-hole with diameter 0.5mm, is used to collimate the beam and remove the $K\beta$ wavelength. The source to sample distance is about 40cm. In this case the first crystal is GaAs with an (001) surface. The presence of two consecutive reflections brings broadening effects to the rocking curve due to dispersion and alignment limitations. The most important of these limitations will be outlined below, with a discussion of how important each of these factors is to the results presented in this thesis.

3.2.1 : Antiparallel (+n, +n) arrangement

An 004 reflection from an (001) GaAs crystal is shown in Fig 3.8, which is a graphical representation of Bragg's Law (called a Du Mond diagram [17]), with λ on the y axis and θ on the x axis. If we consider first the GaAs reference crystal, it is clear that a

spread of wavelengths incident on the sample will result in a range of Bragg angles. In fact, the line shown here is actually two lines, with the distance between them being the 004 GaAs crystal reflecting range (i.e. rocking curve width). The second crystal in the geometry shown inset has the same Bragg relationship, only with the angle reversed. This is called the antiparallel (+n, +n) diffractometer setting, so-called because the outward normals both point in the same general direction (down the page) [18]. At the Bragg angle the two curves intersect, which is highlighted in the box. Fig 3.9 shows an enlargement of this area.

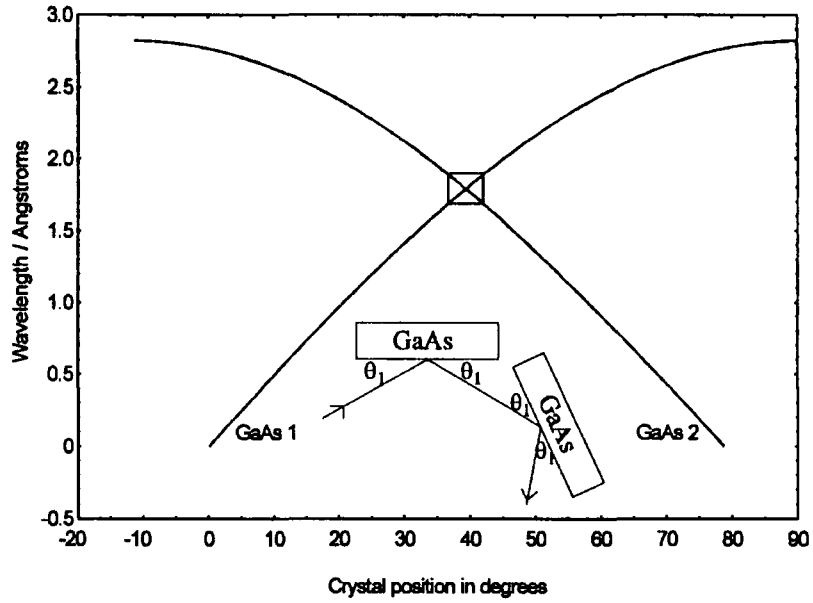

Fig 3.8 : Du Mond Diagrams for GaAs crystal set in the (+n,+n) setting

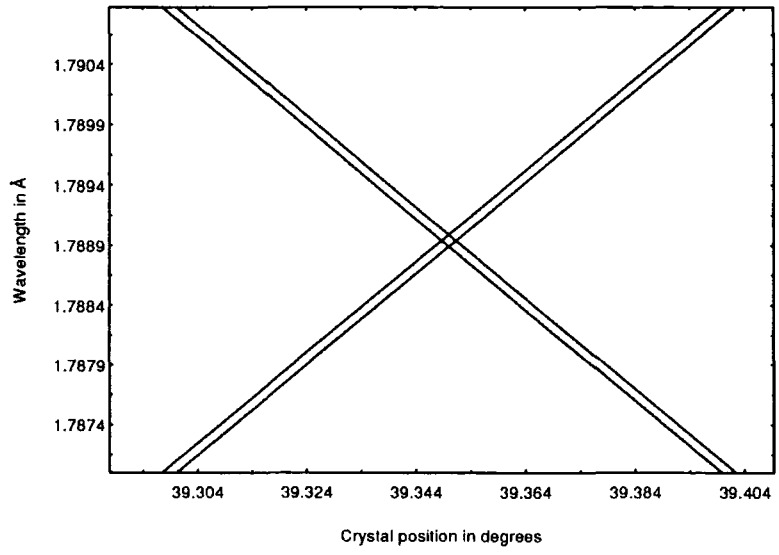

Fig 3.9 : Close up of intersection of two Du Mond curves for GaAs using $CoK\alpha_1$

One way of improving the resolution of the diffractometer is to use slits after the first crystal to remove the $K\alpha_2$ component in the beam. This is done by noting that the $K\alpha_2$ has half the intensity of the $K\alpha_1$, and removing a third of the total intensity from the high angle Bragg side. This can be improved by repeatedly scanning the peak, and checking with dental film. Typically, the wavelength spread present after this process is that shown in Fig 3.9. If only one crystal is present, diffraction can occur at almost any angle shown on the x axis. For both crystals to diffract simultaneously, however, only the overlapping square (of width 10") diffracts. It is the size of this overlap which limits the intensity obtained. If either of the crystals is misplaced diffraction still occurs as a different wavelength will be at the Bragg condition (wavelength dispersive). This means the geometry is relatively insensitive to sample angle, and is unsuitable for lattice strain measurements.

Within the diffracting FWHM there is a component due to the intrinsic width of the incident radiation used, which is obtained by differentiating Bragg's Law. If $\delta\lambda$ is the bandwidth of wavelength used, $\delta\varphi_1$ and $\delta\varphi_2$ are the FWHM and θ_1 and θ_2 are the Bragg angles of the reference and sample crystals respectively, then the peak broadening, $\delta\Theta$, is given by,

[3.6] $$\delta\Theta = \left|\delta\phi_1 + \delta\phi_2\right| = \frac{\delta\lambda}{\lambda}\left|\tan\theta_2 + \tan\theta_1\right|$$

In reality, the broadening this causes is unsuitable for most laboratory diffraction experiments, and has not been employed here. Topographical implications are discussed in Section 3.3.

3.2.2 : Parallel (+n, -n) and (+n, -m) arrangements

A more sensitive geometry is that shown in Fig 3.10, which is the non-dispersive (+n,-n) setting for matched crystals, and dispersive (+n,-m) in the case shown [19]. If the two crystals are of the same material, the two curves will overlap completely for a very precise angular setting but the intensity will fall to zero for a small displacement. The sensitivity to angular position makes this geometry most suitable for measuring lattice distortions or misorientations, as rocking curve widths are the convolution of two perfect crystal rocking curves.

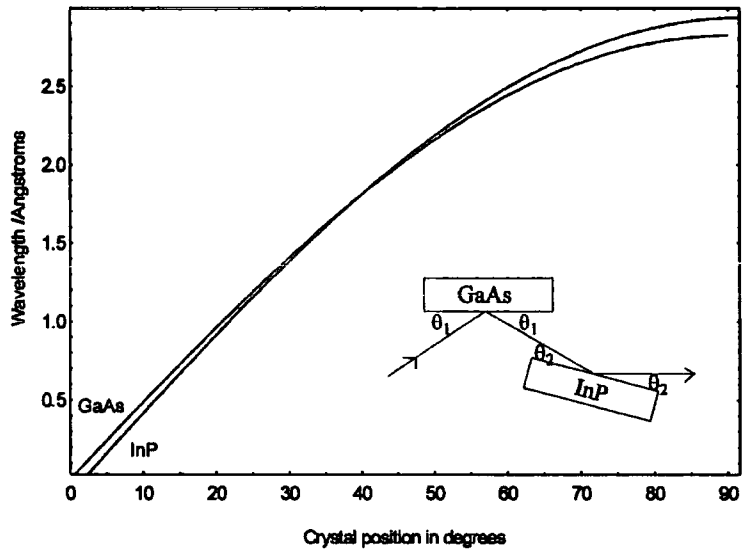

Fig 3.10 : Du Mond diagram for the (+n,-m) geometry

In cases where a high perfection collimating crystal is not available with the same lattice parameter, or a different reflection is required from the two crystals, the (+n,-m) setting is chosen, as is shown inset in Fig 4.2.3. In this case the curves intersect, and Bragg diffraction occurs in this area of overlap. As rocking the sample results in a different wavelength diffracting, it is less angularly sensitive than the (+n,-n) setting, and is broadened by,

[3.7] $$\delta\Theta = |\delta\phi_1 - \delta\phi_2| = \frac{\delta\lambda}{\lambda}|\tan\theta_2 - \tan\theta_1|$$

This is the geometry most frequently used in this study, where the broadening is 12" for an InP crystal with GaAs reference, and 39" for CdTe with GaAs. If only the width of the characteristic $K\alpha_1$ line is allowed through the slits between reference and sample, this falls to 1.4" and 4.7" respectively.

3.2.3 : Refractive Index Corrections

As the refractive index of x-rays propagating in air differs from that in semiconductor material, a slight change in direction of the x-ray occurs on entry to and exit from each crystal. This can be quantified using Snell's Law, and is most important for double crystal arrangements with materials widely differing in electron density. The corrective terms using $CoK\alpha_1$ for the most commonly used materials and reflections in this study are shown in Table 3.1. They have been calculated using formulae in the International

Tables for Crystallography [20]. It can be seen that the corrections are generally small, but are slightly larger for the asymmetric reflections. The studies on II-VI layers usually involve large FWHM which make the peak position hard to determine to high levels of accuracy and, in addition, the peak shift is the same (within experimental errors) for all three materials for a given reflection, so the HgTe (or HgMnTe) peak will move by the same amount (to the smaller Bragg angle) as the GaAs substrate, so relative measurements are unaffected.

Table 3.1 : Correction term for refraction using Co $K\alpha_1$

Material (001)	Reflection	Shift of peak position due to refraction in arc seconds
GaAs	004	3.4
GaAs	115	6.0
CdTe	004	2.9
CdTe	115	4.5
HgTe	004	3.8
HgTe	115	6.0

3.2.4 : Effects of Angular Divergence

It has been shown that an angular divergence of the incident x-ray beam in the diffraction plane broadens rocking curves in the dispersive geometry, but not in the non-dispersive geometry. Any diffractometer misalignment will lead to a component of divergence normal to the diffraction plane, which will affect all three double crystal geometries. This can be included in the Du Mond diagram by extending it into three dimensions, where the third axis is the vertical component of the angle between the sample and x-ray beam [21, 22].

Swarzschild in 1928 [23],through purely geometrical arguments deduced the following formulae for broadening of the rocking curve (ε).

[3.8] $$\varepsilon = 2\gamma\psi_n \text{ for } \gamma > 2M\psi_n$$

[3.9] $$\varepsilon = M\psi_n^2 + \gamma\psi_n + \frac{\gamma^2}{4M} \text{ for } \gamma < 2M\psi_n$$

where γ is the diffractometer tilt misalignment, ψ_n is the component of divergence normal to the diffraction plane (half the total angular divergence), and M is $M = \frac{1}{2}\{\tan\theta_1 \pm \tan\theta_2\}$ where the + is for antiparallel, and the - for parallel geometry.

In the double axis instrument used here, the divergence, ψ_n is 1.54×10^{-3}rad, so the broadening is therefore directly proportional to the diffractometer misalignment and ε varies between 5.6" and 1.1" for tilts between 0.5° and 0.1°. If two different materials are considered, such as GaAs followed by InP, the values for M are 0.793 and 0.024 for antiparallel and parallel respectively. The condition for formula [3.9] to apply is $\gamma<0.14°$and $\gamma<0.004°$. The parallel case tends towards the first formula, while for low tilts the second applies in the antiparallel setting, which only makes a small correction to the broadening. Similar values are obtained for larger mismatches, such as CdTe with a GaAs reference crystal. A last point to notice is that at a synchrotron source, the beam divergence is extremely low, so tilt optimisation is rarely worthwhile (for compound semiconductors).

In the light of these factors, a parallel crystal geometry has been chosen, and careful tilt optimisation (estimated at 0.2°) has been performed. As the integrated intensity remains constant with tilt, while the peak height varies, this is performed by an algorithm of tilting in steps, and noting the maximum peak height, then setting to the tilt position where the maximum height is obtained.

3.2.5 : Crystal perfection contributions to rocking curves

Once the instrumental broadenings have been removed from a rocking curve, any deviation form the perfect crystal FWHM is due to imperfections in the crystal itself. In double axis diffraction the detector integrates over all the rays reaching the opening (about 2cm diameter), so any tilt or distortion in the crystal lattice will broaden the peak. These can arise from sample curvature, tilted regions and subgrains and dislocations. It is often assumed [24] that if the broadening factors each have a Gaussian distribution, then the rocking curve FWHM can be written as the sum of the squares of the standard deviations of the broadening factors, as below.

[3.10] $$\beta_{tot}^2(hkl) = \beta_o^2(hkl) + \beta_d^2 + \beta_\alpha^2 + \beta_e^2 + \beta_l^2 + \beta_r^2$$

β_{tot} = total FWHM of double axis rocking curve

β_0 = intrinsic specimen rocking curve width

β_d = intrinsic monochromator rocking curve width

β_α = broadening cause by angular rotations at dislocations

β_e = broadening caused by strain surrounding dislocations

β_l = broadening due to crystal size

β_r = broadening due to crystal curvature

The first two of these have been dealt with in Chapter 2. The broadening due to the crystal size is related to the thickness of epitaxial layers, h, being measured by

[3.11] $$\beta_l^2 = \frac{4\ln 2}{\pi h^2}\left(\frac{\lambda^2}{\cos^2\theta}\right)$$

and the broadening due to radius of curvature, r is,

[3.12] $$\beta_r^2 = \frac{\omega^2}{\left(r^2\sin^2\theta\right)}$$

where ω is the width of the x-ray beam in the diffraction plane. The remaining components of the rocking curve are due to the tilt and straining effects of dislocations.

3.2.6 : Measurement Technique on D150 Diffractometer

The Bede D150 diffractometer is aligned using two precision micrometer screws which are driven by four phase stepper motors. These motors are connected via a Bede MINICAM electronics interface to a PC which runs Bede's Diffractometer Direct Control (DCC) software. The precision on the motors corresponds to 0.3" on the reference axis and 0.2" on the sample axis, although a backlash correction has to be made when changing the driving direction. The full range on these axes corresponds to 10°, but the micrometers are not sufficiently accurate to allow accurate positions of peaks to be taken over this angle. Lead shielding is placed around the first axis, followed by a set of manual slits. Sample holders are used which either allow automated sample rotation or move the sample in the XY direction (perpendicular to the diffraction plane). Both reference and samples are mounted using very finely glued tape ("blue paper") which causes a minimal distortion of the crystal lattice.

When running the x-ray generator at 40kV and 30mA, the intensity from the GaAs reference crystal before the addition of slits is 127,000 c.p.s., which falls to 50,000 c.p.s. from a III-V substrate specimen using an 004 reflection, giving a signal to noise ratio of 5000. A NaI scintillation detector was used which was connected to a signal channel analyser (SCA) and ratemeter. The window on the SCA was set to be sensitive to CoKα using a dial source. For a typical scan, count times were 2s per point, with the step size chosen to be at least a quarter of the narrowest peak.

The careful alignment of a double crystal diffractometer, therefore, allows the position, FWHM, height, shape and integrated intensity of a peak to be measured, which can be used to deduce parameters such as lattice mismatch and composition, layer thickness, crystal perfection and wafer curvature, as well as variations in these parameters across a wafer [25-27].

3.3 : Double Axis Topography

The advantages of double crystal topography [28, 29] over single crystal topography are similar to those in the double crystal diffraction case. These are discussed in references [3, 4, 30-34]. The use of a monochromator crystal eliminates the formation of double images due to the presence of two characteristic lines in laboratory sources, and makes the topographs sensitive to the presence of tilts and long range strains within the sample crystal [35]. While white radiation topography allows lattice parameter variations ($\delta d/d$) of 10^{-3} to be resolved and is useful for studying dislocations, wafer damage, heavy swirl and precipitates, double axis topography enables lattice parameter variations of up to 10^{-8} to be seen, making it a suitable technique for imaging strains, distortions and light swirl [36]. In addition, the contrast is better than that obtained in Lang topographs as in the latter the distorted region results in a higher intensity than in the perfect region, while in double crystal diffraction the intensity varies between zero and high intensities.

The diffraction parameters can be adjusted to achieve either monochromatic, or plane wave conditions. If the beam angular width is larger than the crystal diffracting width the former is achieved, while if it is much less plane wave topography occurs. These

very low divergence conditions have been used in the study of microdefects [37] and to map out misorientation contours across wafers [38].

3.3.1 : Choice of Source

There are several advantages of using a synchrotron source for double axis topography. If conventional sources are used, the incident beam is a narrow line, so for a reasonable amount of the sample to be imaged a grazing incidence reflection has to be used. This results in a low intensity image, which requires long exposure times, even for fairly low resolution film, and increases the effects of sample movement and diffractometer mechanical instability. A double crystal topograph can be taken at the SRS at Daresbury Laboratory in minutes. As the strain sensitivity of a topograph is dependent on the geometry used and the wavelength dispersion, the extremely low divergence available at a synchrotron source results in sharper strain images. The large distance from source to sample also results in broad dislocation images. The availability of wavelength tuning allows a suitable value of absorption coefficient to be chosen, and allows the diffracted intensity of one particular elemental component to be adjusted by working near an absorption edge.

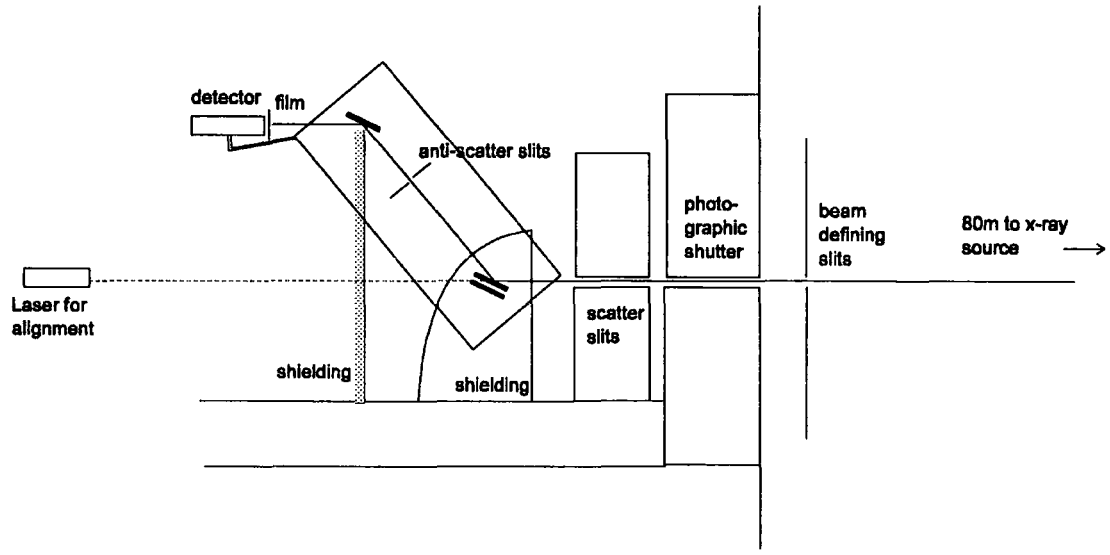

Fig 3.11 : Schematic of the experimental arrangement at Station 7.6, Daresbury Laboratory. The beam is diffracted first by the strain-relieved monochromator, then by the sample.

3.3.2 : Choice of Monochromator

The crystal perfection of a monochromator is important in double crystal topography, as the defects from the reference crystal are also imaged on the topograph. This is particularly important when using a synchrotron source, as the large distance between the source and reference compared to that between the reference and film means the defects from the reference will be almost as clearly imaged as those from the sample. As a large beam needs to be diffracted it is important that this crystal is mounted unstrained. To fulfil these criteria a strain-relieved Si (111) crystal was used, which topographs showed to be dislocation - free in the areas imaged.

As in diffraction, the reflection and materials used alter the width of the rocking curve. Asymmetric reflections produce a quasi-plane wave situation, with narrow rocking curves, while low order symmetric reflections produce a large FWHM. The best results are obtained by matching the lattice constants used. For example Ishikawa et al used a $55\bar{3}$ reflection off Si, followed by 008 reflection from GaAs, which yields lattice parameters of 0.7070Å and 0.7071Å respectively [39]. If the peak obtained is narrow, the change in intensity on the shoulder is very large, so the contrast of defects is high, and a smaller misorientation is needed to cause a drop in intensity, so the strain sensitivity increases.

A combination of monochromation, beam expansion and rocking curve reduction is being developed by various workers [40]. Korytar has used two or three non-coplanar successive asymmetric reflections from Si in order to provide magnified dislocation images using CuKα radiation [41]. Another useful tool for laboratory topography is the use of a bent collimator, which allows the curvature of the reference crystal to be matched to that of the specimen, so the whole wafer can be imaged [42, 43].

In these experiments, beam expansion was not required, so a 111 or 333 reflection was chosen depending on the wavelength (and hence Bragg angle) which was experimentally most convenient.

3.3.3 : Choice of Wavelength

The wavelength tunability has been exploited in this study to alter the penetration depth of the x-rays, so different regions of an epitaxial layer can be studied. This technique has been used previously in combination with varying the reflection, and hence the incident angle [44, 45]. For topographical experiments on HgMnTe a wavelength close to the absorption edge of Mn was used, in order to sensitise the topograph to the presence of this element. In this case, where an accurate wavelength is required, a lump or film of Mn was placed on the sample axis, and the monochromator was rotated. By positioning a detector a few centimetres from the sample but pointing at it, the x-ray fluorescence could be measured. When the absorption edge of Mn is passed through, a sudden decrease in the intensity is observed, which position corresponds to the edge. An example is shown in Fig 3.12, where the data was taken from Station 2.3 at Daresbury Laboratory.

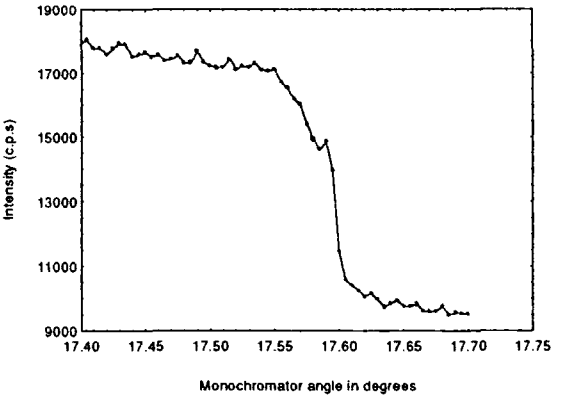

Fig 3.12 : Scan of monochromator crystal through the absorption edge of Mn at 1.8957Å

3.3.4 : Choice of Sample Orientation

A compromise has to be made in choosing the configuration of the sample between the monochromating properties and defect sensitivity. The (+n,-n) geometry gives the narrowest rocking curves and hence the most sensitivity to long-range strain (and has narrow defect images), but leaves a range of wavelengths, which can lead to double images. The use of a (+n, -m) configuration reduces the sensitivity but results in a monochromatic beam and larger defect images. This orientation is most often preferred in topography, as a different reflection in the reference crystal is often

required to expand the beam. Higher defect contrast is obtained in epitaxial layers by using Bragg reflection geometry so this was used in both symmetric and asymmetric reflections [46].

3.3.5 : Choice of position on rocking curve

The point on the rocking curve from which the topograph is taken determines the sensitivity of the image. The greatest sensitivity to angular distortions is obtained on the flank of the rocking curve, as the geometrical image contrast theory of Bonse [29] gives the change in intensity, $\delta I/I$ to be,

[3.13] $$\frac{\delta I}{I} = k\{(\tan\theta_B)\frac{\delta d}{d} \pm \underline{n}_t . \underline{n}_g \delta\theta\}$$

where k is the slope of the rocking curve, $\delta d/d$ is the fractional change in Bragg spacing, $\delta\theta$ is the sample tilt, and $\underline{n}_t$ and $\underline{n}_g$ are the unit vectors normal to the incidence plane and parallel to the defect misorientation axis. At the positions marked on the Bragg peak in Fig 3.13, a positive dilation will give an increase in intensity at A, and reduced intensities at B and C. As there are no angular or spectral components of the beam apart from those in the perfect crystal reflecting range, there are no kinematical images and orientation contrast dominates. If a position on the Bragg peak at D is chosen, outside the FWHM range, kinematical images are obtained which can be used to image microprecipitates and dislocation loops.

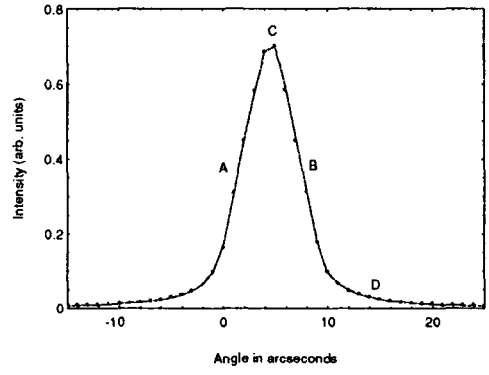

Fig 3.13 : Simulation of 113 InP rocking curve at 1Å

The position from which the reflection is taken will also affect the type of film used, as intensities are much lower on the tails of the Bragg peak. If a map of strain is needed across the wafer, low resolution film is normally sufficient, whereas the imaging of

defects will require film matched to the image width. As the defect image width decreases with distance from crystal to film, yet scatter is higher nearer the sample, a specimen-film distance of about 5cm is normally used.

3.4 : Triple Axis Diffraction

Double crystal diffraction or high resolution diffraction provides information on the position or FWHM of a diffraction profile, but gives no information on the cause of a broad or misplaced peak. Both variations in lattice parameter and the presence of tilts or subgrains will broaden a peak, making detailed analysis impossible. Triple axis diffraction [47, 48] employs an analyser crystal (or slits) before the detector to reduce the angular acceptance of the detector down to a level similar to the maximum beam divergence from the sample. As tilted regions and subgrains will come into the diffraction condition with a rotation of the sample, they are mapped by scanning θ, the sample axis, while keeping the detector still. As a different lattice parameter will only diffract when the detector is at twice the Bragg angle, these can be investigated by scanning both detector and sample, in a ratio of 2:1 (the so-called θ-2θ scan). In this way the lattice tilts ($\Delta\phi$) and lattice mismatch ($\Delta a/a$) can be resolved. These can be built up into a reciprocal space map by linking a number of θ-2θ scans, which can be plotted in real or reciprocal space. An example of the additional information obtained through reciprocal space mapping is shown in Fig 3.14, where a double axis diffraction scan and reciprocal space map are shown for a ZnTe layer on GaSb. The double axis scan in a) makes it impossible to distinguish between tilt distributions and strain, whereas changes in lattice parameter are mapped along Q_z and tilts along Q_y in b).

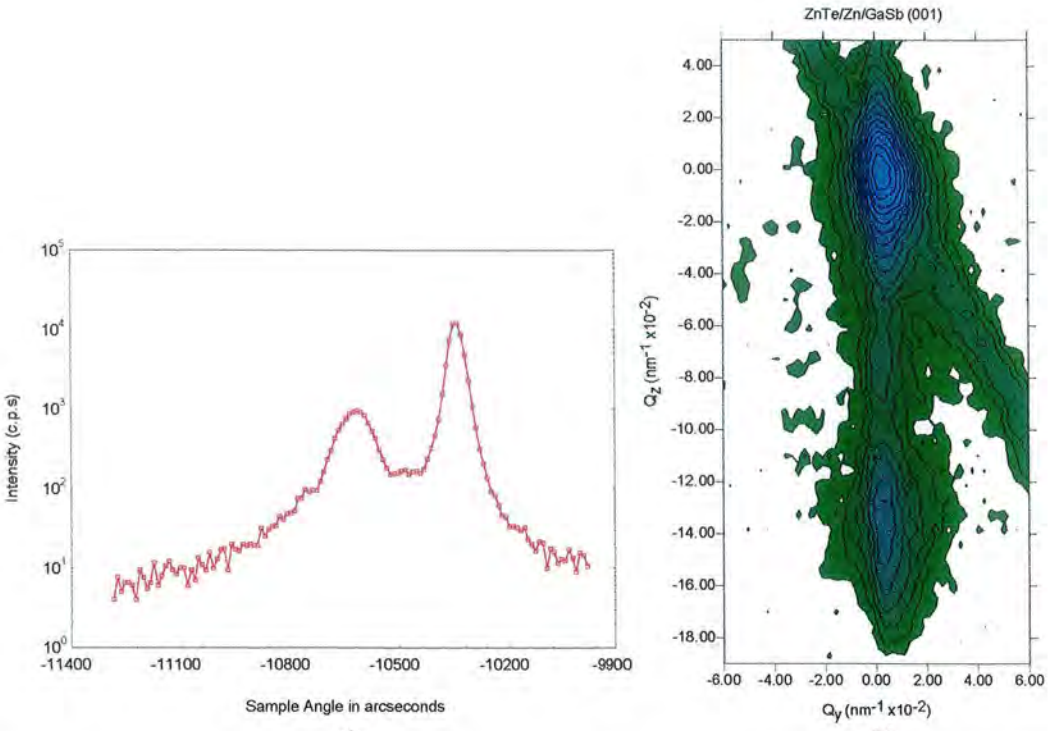

a) b)

Fig 3.14 : Comparison of a) double axis scan and b) triple axis map for ZnTe/GaSb

3.4.1 : Reciprocal Space

Reciprocal space is a suitable medium for diffraction analysis as closely packed peaks are representative of long lattice periodicity. Scans themselves can be viewed in reciprocal space, as shown in Fig 3.15, where a diffraction pattern is shown. The scattering actually comes from a small volume surrounding [ΔQ_y, ΔQ_z], which is defined by the divergence of the incident beam, the acceptance of the detector and a wavelength spread, as is shown in Fig 3.16. In some cases minimising these parameters is not essential, and for mosaic or poor quality crystals, such as II-VI epilayers, it is sufficient to employ a slit in front of the detector. Either the detector or analyser position can be stepped during a scan to provide a reciprocal space map, which can be transformed using the relations [49],

[3.14] $$\Delta Q_z = \frac{\Delta\phi \cos\theta_B}{\lambda}$$

[3.15] $$\Delta Q_y = (2\Delta\psi - \Delta\phi)\frac{\sin\theta_B}{\lambda}$$

where $\Delta\psi$ is the deviation of the specimen and $\Delta\phi$ is the deviation of the analyser from the zero (i.e. Bragg) condition.

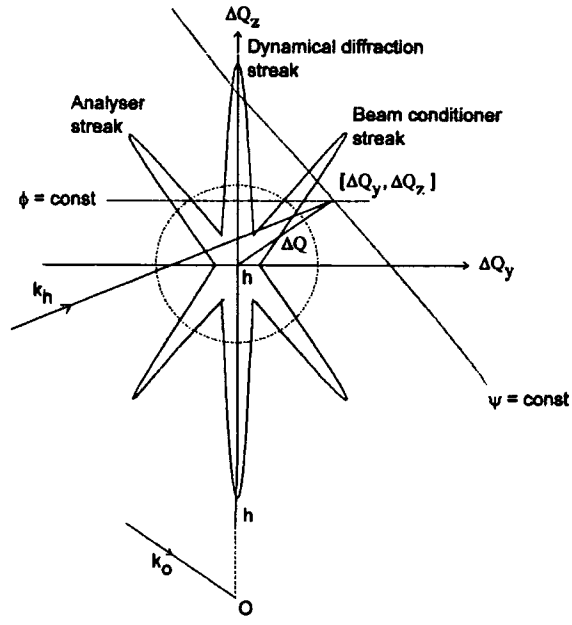

Fig 3.15 : A scattering map in reciprocal space, showing the scan geometry

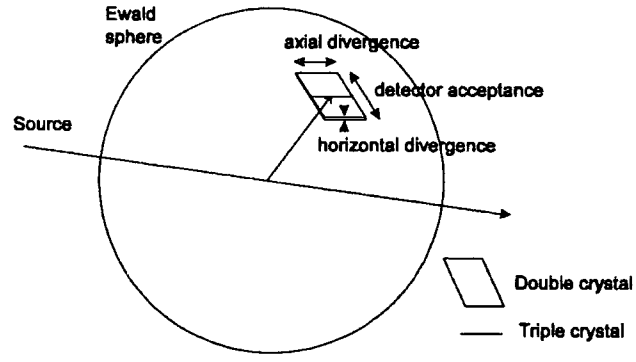

Fig 3.16 : Three dimensional probe in reciprocal space. After Fewster [50]

As the instrument function (and therefore the region of the Ewald sphere which is accessible) is determined by the diffraction arrangement, it is important to use effective monochromator and analyser crystals, which are discussed below.

3.4.2 : Multiple Crystal Diffraction

A channel cut collimator (CCC) consists of a perfect crystal cut to give several successive reflections in order to reduce the tails of the rocking curve and, in some cases, to provide monochromation. Four reflections are often employed, as this produces a beam parallel to that which entered the crystal. An example of the way in which the intensity of the tails of a rocking curve are reduced by successive reflections is shown in Fig 3.17, using as an example 022 reflections from Si. If an arrangement +n-n+n-n is used, the beam produced is highly conditioned angularly, but a fifth crystal is required to act as a monochromator. Alternatively, a +n-n-n+n arrangement or two, four bounce crystals in the +n+n geometry can be used. In the same way, it is useful to employ several bounces in the analyser crystal, although a single crystal could be used. Three experimental arrangements have been used in taking reciprocal space maps. These are outlined below.

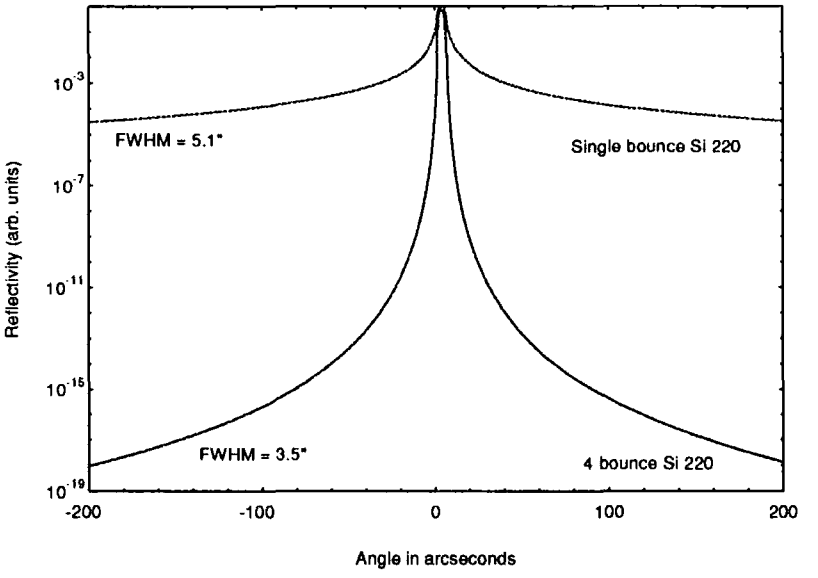

Fig 3.17 : Effect of successive reflections on the tails of a rocking curve

3.4.3 : Arrangement on the D3 Diffractometer

A schematic of the D3 diffractometer is shown in Fig 3.18, where the high resolution two 4-bounce monochromator is in place. This is the one used in these studies, where the eight symmetric 022 Si reflections give an angular divergence of 5" and $\Delta\lambda/\lambda = 5.5 \times 10^{-5}$. An alternative arrangement exists with two 2-bounce

monochromators using asymmetric 022 Si channels [51]. These give a 12" divergence and $\Delta\lambda/\lambda = 1.3x10^{-4}$, and result in higher intensity. The analyser crystal used was a 4 bounce Si 111 crystal. Scatter slits were used prior to the analyser, and the whole third axis (slits, analyser, detector) was moved during the scans. An EDR scintillation detector with a NaI(Tl) crystal in front of a low-radioactivity glass photo-multiplier tube was used [52]. This contains an active dynode chain, enabling count rates greater than 8.10^5cps without a dead time correction, and with an intrinsic background count of 0.15cps.

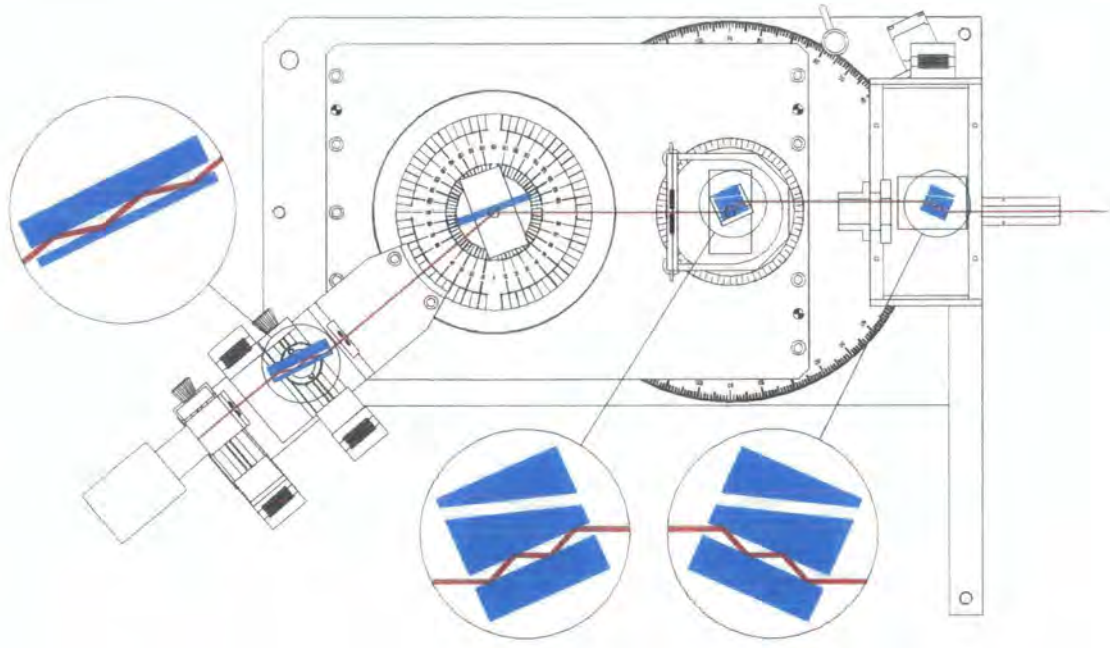

Fig 3.18 : A Bede D3 diffractometer, with the monochromator crystal used in this study [53]

The alignment is carried out in the same way as for double axis, but with the additional complication of position, angle and tilt optimising the analyser crystal. The x-ray generator is typically run at 40kV and 50mA, which allows a triple axis scan on a substrate such as InP to be performed in about 3 hours. The ability to translate the analyser crystal away from the detector means that slits can be used as the analyser for greatly tilted crystals, such as CdTe epitaxial layers on GaAs. In these conditions, the intensity is increased by using the asymmetric monochromator setting.

3.4.4 : Arrangement on the Model 200 Diffractometer

The Model 200 is similar to the D3, but with a smaller distance from Axis 1 to 2 (200mm), and is stepper motor driven with no absolute encoding of angular position. A 4 bounce channel cut collimator of Si 022 in the +n-n+n-n setting is used, followed by a Ge 111 monochromator crystal, giving an angular divergence of 16" and $\Delta\lambda/\lambda=3x10^{-4}$. The monochromator crystal is lead shielded and scatter slits are inserted after it. It is unnecessary to use the slits to remove the $K\alpha_2$ component of wavelength, as the separation between the peaks is now sufficiently great to choose which peak to diffract. The analyser crystal provided a 4 bounce 220 symmetrically cut channel, and a 2 bounce 220 asymmetrically cut channel. As the 2 bounce gave an analyser streak, as seen in Fig 3.14 , the 4 bounce channel was used most frequently. An analyser scan (with no sample in place) using the 2 and 4 bounce channels is shown in Fig 3.19. This shows that the analyser crystal diffraction range is not providing a δ function, as an enlarged tail is visible on the left hand side of the peak. In the case of the II-VI materials the need for maximum intensity made the two bounce channel more practical. An increased background was observed to result from air scatter, and this was reduced by adding scatter slits before the analyser and closing them around the channel used. As the detector axis was not very stable in movement, triple axis scans were performed by stepping the analyser crystal angle, and rotating Axis 2. The wavelength used was $CuK\alpha_1$, with the x-ray generator working at 40kV and 30mA. These conditions and the use of a Bede EDR detector allowed a reciprocal space map with a counting time of 2 or 3 seconds per point to be taken overnight.

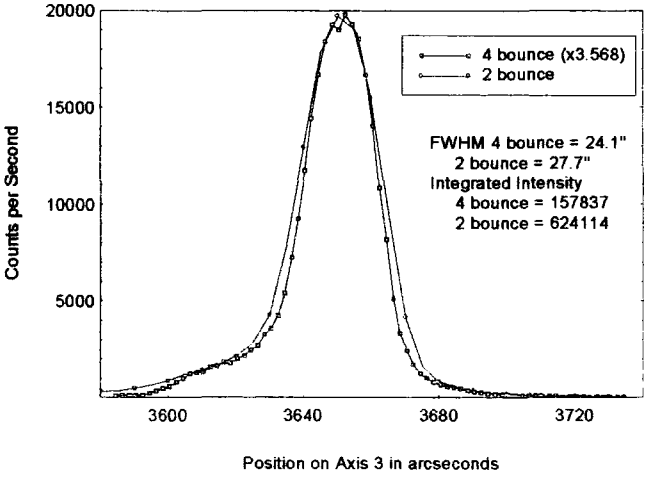

Fig 3.19 : Comparison of the 2 and 4 bounce channels of the Si 022 analyser crystal

3.4.5 : Arrangement at Station 2.3, Daresbury Laboratory

Station 2.3 at Daresbury Laboratory was employed for some pseudo-triple axis scans where the imperfections and spread of tilts in the samples made them difficult to study with the low intensity from conventional sources. The experimental arrangement is the same as that used for reflectivity, using slits to reduce the detector acceptance angle, and is described in section 4.5. Scans were collected by stepping θ-2θ and scanning θ.

3.5 : Grazing Incidence X-ray Reflectometry

A complementary technique to diffraction is that of grazing incidence x-ray reflectivity, which is sensitive to electron density changes at the surface or interface. This allows highly dislocated, or even amorphous materials to be studied, and gives a wealth of near surface information, such as interface roughness and compositional grading to angstrom precision. Although a Bede dedicated reflectometer (GXR1) has been used, the data represented in this thesis was taken at a synchrotron, as the high intensity allowed thin oxide layers to be resolved beyond incident angles of 3°, and provided very high resolution in the transverse diffuse scans.

3.5.1 : Station 2.3 at Daresbury Laboratory

The grazing incidence x-ray reflectivity data described here was taken at Station 2.3 at the Synchrotron Radiation Source (SRS) at Daresbury Laboratory using a 2-circle powder diffractometer [54, 55]. The experimental arrangement is shown in Fig 3.20. The white radiation is passed through a water-cooled Si 111 two-bounce monochromator then through slits with dimensions of 100μm vertically and 4mm horizontally, before reaching the sample. This low vertical beam size ensures that all the sample intercepts the beam at low incident angles. Placing the defining slits after the monochromator ensures that the beam stays in the same position when the monochromator is moved, which is essential for variable-wavelength diffraction experiments. In addition, this helps to remove additional reflections. The 111 reflection is selected, although a small component of 333 reflection will be present at a third of the wavelength. This contribution will be small due to the relative weakness of

the 333 reflection, and the profile of synchrotron intensity with wavelength. The small beam size selected means that the angular divergence is limited by the intrinsic rocking curve of Si, which gives $\delta\lambda/\lambda \approx 1.5 \times 10^{-4}$. After the sample an evacuated aluminium chamber with Kapton windows contains anti-scatter slits of height approximately 1mm, then detector slits with vertical height 100μm. Additional lead shielding is placed around the vacuum can and detector to reduce the background. The total distance from sample to detector is about 65cm, which gives a large projected lateral coherence length of about 100μm. A beam intensity monitor prior to the sample allows the data to be adjusted for variations in synchrotron beam current, and in particular the decay of the beam with time after refill. The sample and detector axes are optically encoded, which give an accuracy of 0.36" on the detector and 0.72" on the sample axis. A detector-only scan of the beam gives a Gaussian distribution with a FWHM of 36" shown in Fig 3.21. In these scans, a wavelength of 1.3926Å has been used, where the incident intensity is a maximum at 10^8c.p.s. An EDRa detector is used which has a highly efficient Yttrium Aluminium Oxide scintillation crystal with a short decay time. This allows countrates as high as 1.2×10^6 c.p.s., while keeping a background of 0.15c.p.s [56]. In this case, therefore, the background is set by the scatter within the experimental hutch, rather than detector efficiency. Despite the large dynamic range of the detector, when the sample is positioned above the critical angle, saturation occurs. To overcome this a piece of aluminium is inserted in front of the beam for the first part of the scan, then the scan is scaled to the rest of the data later. The overlap between the two sets of scans is very smooth, and no undesirable effects are observed.

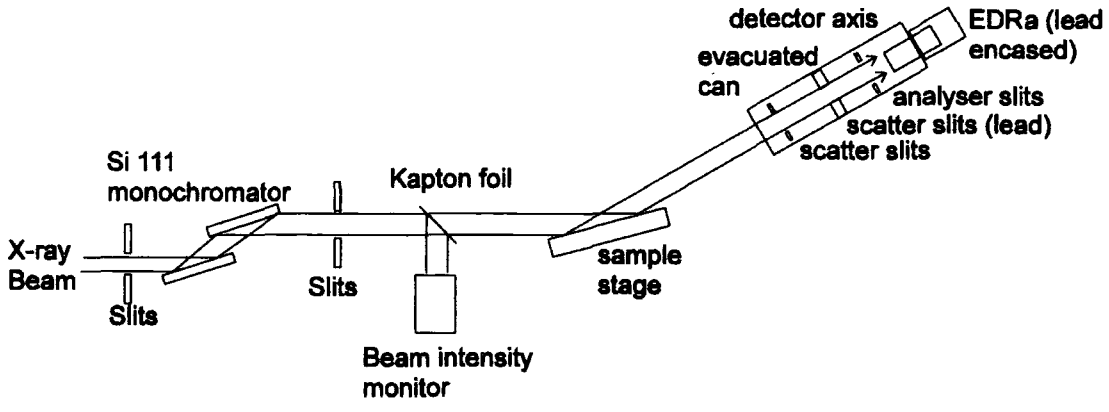

Fig 3.20 : Schematic diagram of Station 2.3.

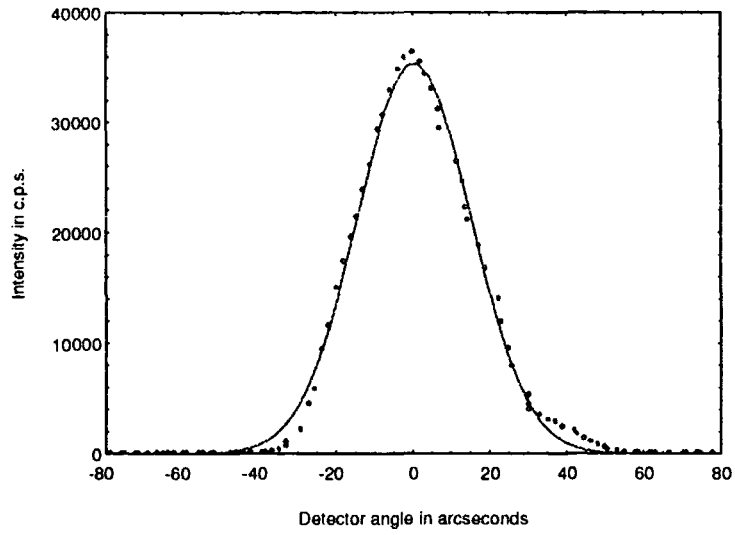

Fig 3.21 : Detector scan across the incident beam with no sample in place. The intensity is reduced to below saturation by the addition of a piece of Al

In these experiments, it is important to have the sample stage exactly flat and on the centre of rotation, and have the detector rotate about this point. The sample stage is aligned first by ensuring it is flat using a spirit level. The crosshairs of a telescope are then aligned on the top surface and it is rotated by 180° to check the surface still lies on the crosshairs. Any discrepancy is removed by altering the height of the sample on the goniometer, then repeating. The post-monochromator slits are set using shims to an accuracy of $\pm$ 1μm, and the table is moved vertically until the beam has been half cut. This ensures that the centre of rotation is now in the centre of the beam. The detector slits are now added, as well as the anti-scatter slits, by exposing x-ray sensitive yellow paper where the beam path is, fixing the telescope on this point, then closing the slits. The vacuum can is put around these slits and the detector shielded, then the detector axis is scanned and set to zero. Yellow paper is then used on the sample holder to mark out the beam tramlines, and the alignment procedure is complete. The sample is aligned for each scan by half cutting the beam with its surface, and checking the coupling on the sample and detector to ensure that the scan remains on the specular ridge. This is performed by moving the detector (2θ) to 1, 1.5, and 2° and scanning the sample through 0.5, 0.75 and 1° respectively, and setting the sample peak angle to half the detector angle. After this there are three possible types of scan - sample (θ),

sample and detector linked (θ-2θ), and detector only. The first two of these have been performed, and are described below.

3.5.2 : Types of scan : Specular

Specular reflectivity scans are performed by moving the detector and sample in coupled motion so that the detector sweeps at twice the rate of the sample (Fig 3.22). This means that the entrance and exit beams make an equal angle with the crystal surface at all times, and is equivalent to scanning q_z in reciprocal space, perpendicular to the surface. When the incident angle is low, below the critical angle, the beam is totally externally reflected and the intensity remains approximately constant. The position of the critical angle is determined by the electron density in the very near surface region, so its measurement allows a determination of this density. Beyond the critical angle, however, the beam penetrates into the crystal, and the intensity falls as a function of θ^{-4} for a non-absorbing, flat, interface. The presence of roughness at the surface or a change in composition reduces the specular intensity from the ideal and allows this apparent roughness to be measured to Å precision.

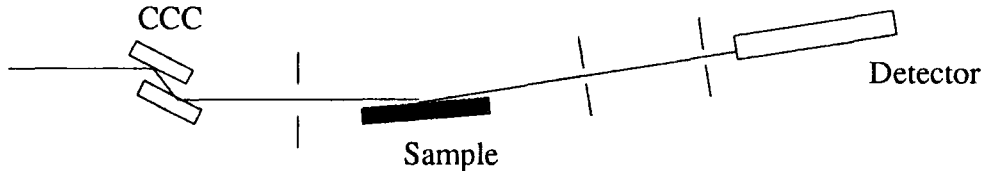

Fig 3.22 : Experimental arrangement for specular scans

One limitation of specular reflectivity is that diffuse scattering can contribute to the intensity measured at the detector. This effect can be removed by off-setting the sample angle by 0.1°, and taking a θ-2θ scan. This off-specular scan gives the forward diffuse scatter, so when it is removed from the specular scan, only true specular scatter remains. As has been discussed in Section 2.1, the apparent roughness obtained from specular scans cannot be resolved into roughness and compositional grading, so additional scans are necessary to characterise fully a surface or interface.

3.5.3 : Types of scan : Diffuse

Diffuse scatter scans are performed by fixing the position of the detector, and scanning the sample from 0 to 2θ (Fig 3.23), which is equivalent to scanning q_y in reciprocal space, parallel to the surface. The scatter reaches a peak called a Yoneda wing when $\theta = \theta_c$, where all the incident beam is in the plane of the surface of the crystal (Section 2.1.4). The intensity falls as the beam begins to penetrate, then rises up to the specular peak. A second Yoneda wing is obtained when the exit beam reaches its critical angle. The shape of the curve is determined by several inter-related parameters. These are the surface and interface roughness, both correlated (replicated from one layer to the next) and uncorrelated (not replicated), compositional grading error function (Σ_g), the lateral correlation length (ξ) and the fractal dimension (h).

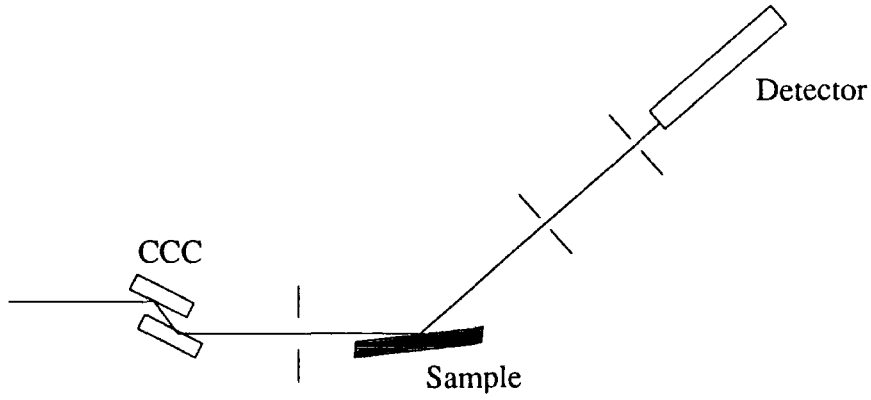

Fig 3.23 : Experimental arrangement for diffuse scans

A combination of specular and diffuse scans, therefore, allows the characterisation of the surface morphology. In the case of a graded layer, the apparent roughness will change with scattering vector, so taking and simulating transverse diffuse scans for two different scattering vectors allows a far more sensitive fit. In this study, these are generally at $2\theta = 1.2^\circ$ and 1.5°. As the diffuse scatter is far less intense than the specular, and spreads further in q_y, two scans comprise each diffuse plot. One is a sample scan from 0 to 2θ, with 72" steps and 10s count per point, and the other is over the specular peak with 1.8" steps and 2s count per point. These are combined to yield maximum information for minimum scanning time.

References

1. Tanner, B.K., *X-Ray Diffraction Topography*. 1st ed. International Series in the Science of the Solid State, ed. B. Pamplin. Vol. 10. 1976: Pergamon Press. 174.

2. Tanner, B.K., *Contrast of defects in X-ray diffraction topographs,* in *X-Ray and neutron dynamical diffraction : theory and applications*, A. Authier, *et al.*, Editor. 1996, Plenum Press: New York. p. 147-166.

3. Klapper, H., *X-ray diffraction topography : principles and techniques,* in *X-ray and neutron dynamical diffraction : theory and applications,* A. Authier, S. Lagomarsino, andB.K. Tanner, Editor. 1996, Plenum Press: New York. p. 137-146.

4. Franzosi, P., *X-ray Topography,* in *Handbook on Semiconductors,* S. Mahaian, Editor. 1994, Elsevier Science. p. 1032-1066.

5. Authier, A., *Dynamical theory of x-ray diffraction,* in *X-Ray and Neutron Dynamical Diffraction: Theory and Applications,* A. Authier, S. Lagomarsino, andB.K. Tanner, Editor. 1996, Plenum Press: New York. p. 1-30, 41-60.

6. Bowen, D.K. and S.T. Davies, *The double crystal x-ray camera at Daresbury Laboratory.* Nucl. Instr. and Meth., 1983. **208**: p. 725-729.

7. Bowen, D.K., *et al.*, *The x-ray topography station at Daresbury Laboratory.* Nucl. Instr. and Meth., 1982. **195**: p. 277-284.

8. Quinn, P.D., *Source performance.* 1995, CLRC.

9. Mason, R., *ESRF Beamline Handbook.* 1994, ESRF.

10. Baruchel, J., A. Draperi, and F. Zontone, *Present status of the topography and high-resolution diffraction beamline at the ESRF.* J.Phys.D:Appl. Phys., 1993. **26**: p. A9-A14.

11. Barrett, R., *et al.*, *The present status of the ESRF diffraction topography beamline : new experimental results.* J.Phys.D:Appl. Phys., 1995. **28**: p. 1-6.

12. Zontone, F., *Imagerie par diffraction ("topographie") a l'installation europeenne de rayonnement synchrotron ("ESRF"): ligne de lumiere, possibilites et premieres experiences.* 1995, L'Universite Joseph Fourier, Grenoble.

13. Baruchel, J., J. Hartwig, and F. Zontone, Synchrotron Radiat. News, 1994. **7**: p. 19.

14. Baruchel, J., *et al.*, Phys. Status Solidi, 1994. **141**: p. 59.

15. Hart, M., J.Crystal Growth, 1981. **55**: p. 409.

16. Hart, M., A.R.D. Rodrigues, and D.P. Siddons, *Adjustable resolution Bragg reflection systems.* Acta Cryst., 1984. **A40**: p. 502-507.

17. DuMond, J.W.M., *Theory of the use of more than two successive x-ray crystal reflections to obtain increased resolving power.* Phys. Rev., 1937. **52**: p. 872-883.

18. Nakayama, K., *et al.*, *Use of asymmetric dynamical diffraction of x-rays for multiple-crystal arrangements of the (+n,+n) setting.* Z. Naturforschung, 1973. **28a**: p. 632-638.

19. Runshen, L. and X. Shunsheng, *The dispersion phenomenon of double-crystal diffraction in certain (n,-n) settings.* J.Appl.Cryst., 1988. **21**: p. 902-904.

20. Buerger, M.J., *et al.*, ed. *International Tables for Crystallography*. 2nd ed. Vol. III. 1985, D. Reidel Publishing Company: Dordrecht, Holland.

21. Shunsheng, X. and L. Runshen, *The three-dimensional dynamic DuMond diagram for x-ray diffraction analysis of nearly perfect crystals*. J.Appl.Cryst., 1988. **21**: p. 213-217.

22. Shunsheng, X., C. Jingyi, and L. Runshen, *Analysis of single- and double-crystal spectrometers using three-dimensional DuMond diagrams and the high-precision measurement of the CuKa line profile*. J.Appl.Cryst., 1988. **21**: p. 218-223.

23. Schwarzschild, M.M., *Theory of the double x-ray spectrometer*. Phys. Rev., 1928. **32**: p. 162-171.

24. Ayers, J.E., *The measurement of threading dislocation densities in semiconductor crystals by x-ray diffraction*. J.Crystal Growth, 1994. **135**: p. 71-77.

25. Tanner, B.K., *High resolution x-ray diffraction and topography for crystal characterisation*. J.Crystal Growth, 1990. **99**: p. 1315-1323.

26. Tanner, B.K. and D.K. Bowen, *Advanced x-ray scattering techniques for the characterization of semiconducting materials*. J.Crystal Growth, 1993. **126**: p. 1-18.

27. Wie, C.R., *High resolution x-ray diffraction characterization of semiconductor structures*. Materials Science and Engineering, 1994. **R13**(1): p. 1-56.

28. Bond, W.L. and J. Andrus, Am. Mineralogist, 1952. **37**: p. 622.

29. Bonse, U. and E. Kappler, Z. Naturforschung, 1958. **13a**: p. 348.

30. Baruchel, J., *Neutron and X-ray topography*, in *Neutron and Synchrotron radiation for Condensed Matter Studies*, J. Baruchel, *et al.*, Editor. 1993, Springer-Verlag: Paris. p. 399-408.

31. Bowen, D.K., *X-ray topography of surface layers and epitaxial films*. Advances in X-ray Analysis, 1990. **33**: p. 13-23.

32. Franzosi, P., *Investigation of crystal defects in III-V heterostructures by X-ray topography and electron microscopy*. J.Crystal Growth, 1993. **126**: p. 109-124.

33. Mohling, W., *Versatility and limitations of double crystal reflection topography for dislocation imaging*. Cryst. Rev., 1989. **2**: p. 89-104.

34. Turnbull, A., *Relaxation in Epitaxial Layers of III-V Compounds*. 1992, University of Durham.

35. Hashizume, H., A. Iida, and K. Kohra, *A multiple crystal system for high strain-sensitivity x-ray topography and its applications*. Jpn. J. Appl. Phys., 1975. **14**(10): p. 1433-1441.

36. Meiran, E.S., *Industrial applications of crystal quality*, in *Characterisation of Crystal Growth Defects by X-Ray Methods*, B.K. Tanner and D.K. Bowen, Editor. 1979, Plenum Press: New York. p. 1-27.

37. Shulpina, I.L., *Microdefects investigated by x-ray topography*. J.Phys.D:Appl. Phys., 1993. **26**: p. A82-A85.

38. Barnett, S.J., *Stuctural Characterisation of Semi-insulating LEC Gallium Arsenide*. 1987, University of Durham.

39. Ishikawa, T., T. Kitano, and J. Matsui, *Synchrotron plane wave x-ray topography of GaAs with a separate (+,+) monochro-collimator.* Jpn. J. Appl. Phys., 1985. **24**(12): p. L968-L971.

40. Boettinger, W.J., *et al., Real time topography with x-ray image magnification.* Nucl. Instr. and Meth., 1982. **195**: p. 355-361.

41. Korytar, D., *et al. Monolithic devices for high resolution x-ray diffractometry and topography.* in *X-TOP'96.* 1996. Palermo.

42. Jenichen, B., R. Kohler, and W. Mohling, Phys. Status Solidi, 1985. **89**: p. 79.

43. Jenichen, B., R. Kohler, and W. Mohling, J. Phys. E, 1988. **21**: p. 1062.

44. Halfpenny, P.J., G.S. Green, and B.K. Tanner, *X-ray topography studies of the defect depth profile in processed silicon wafers.* J.Phys.D:Appl. Phys., 1993. **26**: p. A65-A68.

45. Loxley, N. and B.K. Tanner, *X-ray double crystal topography of processed silicon wafers.* Mater. Res. Soc. Symp. Proc., 1987. **82**: p. 215-220.

46. Barnett, S.J., *et al., In situ x-ray topography studies during the molecular beam epitaxy growth of InGaAs on (001) GaAs: effects of substrate dislocation distribution on strain relaxation.* J.Phys.D:Appl. Phys., 1995. **28**: p. A17-A22.

47. Fewster, P.F., *Combining high resolution x-ray difractometry and topography.* J.Appl.Cryst., 1991. **24**: p. 178-183.

48. Fewster, P.F., *X-ray analysis of thin films and multilayers.* Rep. Prog. Phys., 1996. **59**: p. 1339-1407.

49. Iida, A. and K. Kohra, *Separate measurements of dynamical and kinematical x-ray diffractions from silicon crystals with a triple crystal diffractometer.* Phys. Status Solidi, 1979. **51**: p. 533-542.

50. Fewster, P., *Reciprocal Space Mapping,* in *X-Ray and Neutron Dynamical Diffraction : Theory and Applications,* A. Authier, S. Lagomarsino, andB.K. Tanner, Editor. 1996, Plenum Press: New York. p. 269-288.

51. Loxley, N., *et al., High resolution X-ray diffractometry and topography of float-zone GaAs crystals grown in microgravity.* Advances in X-ray Analysis, 1995. **38**: p. 195-200.

52. Cockerton, S. and B.K. Tanner, Advances in X-ray Analysis, 1995. **38**: p. 371.

53. Loxley, N., *Flexible X-ray characterisation.* 1995, Bede Scientific.

54. Tanner, B.K., *et al., Grazing incidence x-ray measurement of interface roughness in sputtered Co/Cu multilayers.* Advances in X-ray Analysis, 1996. **40**.

55. Tang, C., *Station 2.3 - User manual.* 1996, Daresbury Laboratory.

56. Loxley, N., *The Bede EDRa.* 1996, Bede Scientific.

Chapter IV

Investigation of InP Substrates for use in Epitaxial Growth

4.1 : Introduction

InP is a III-V compound semiconductor of increasing significance in the electronic and optoelectronic industries. A recent survey in 1994 by the US Air Force Wright Laboratory [1] found that the world market was valued at $20 million (compared to $130 million for GaAs and $124 million for GaP). Over 80% of wafers produced were used in optoelectronic research or devices, while most of the remainder went to electronics applications.

InP is commonly used in heterostructures, where epitaxial multilayers are grown to have tailored electronic properties, a process known as bandgap engineering [2, 3]. InP based lasers, such as GaInAsP/InP have an operating range between 1.3μm and 1.55μm, which makes them suitable for use in low loss optical fibres for long haul telecommunications where minimum dispersion and loss occurs in the range 1.1μm to 1.6μm. Other electronics applications include heterojunction bipolar transistors, HBTs, (e.g. InGaAlAs/InP) and high electron mobility transistors (HEMT) like $Al_{0.48}In_{0.52}As/Ga_{0.47}In_{0.53}As/InP$ which offer low noise, higher gain and higher frequency performance than GaAs based devices. These materials are lattice-matched to InP, but higher frequencies can be obtained by using an increased In composition and hence strained layers.

In order to improve device yield and performance from InP based devices, research is being carried out on various aspects of wafer production. The work in this chapter was commissioned by Epitaxial Products International of Cardiff, who, in the 1994 survey, were the largest consumer of InP wafers in Europe. The issues that are being addressed are relevant to subsequent epilayer growth and the re-sale of original wafers. These include a comparison of wafers from different manufacturers, in terms of dislocation distribution, polishing process and misorientation angle. In addition, many

of the wafers provided were grown by the relatively new growth technique for this material, Vertical Gradient Freeze, discussed in Section 1.4. Issues which are still under discussion in VGF InP, include dislocation density and residual strain, both of which have been investigated here.

4.2 : Substrate Misorientation Angle

The importance of substrate misorientation (i.e. the offcut angle between surface and (100) planes) has been much discussed in the recent literature. It has been observed that a large increase in misorientation angle (e.g. 14°) towards the <110> direction leads to increased interfacial oxygen incorporation and hence interfacial roughness within superlattice structures grown by MOVPE, which causes reduced device performance [4]. MOCVD growth processes are also affected, as zinc incorporation studies in GaAs have shown [5]. The amount of zinc incorporated has been shown to depend on misorientation angle, with a minimum at 4° off (001).

Substrate misorientation has been shown to affect the ordering in GaInP by governing the density of [110] steps [6, 7], as well as the absence of twin boundaries [8]. Other effects on growth include uniformity and anisotropy of strain relaxation in InGaAs/GaAs [9, 10], island density in InP/GaAs [11] and terrace width in MOVPE of GaAs [12]. The misorientation of substrate material has been directly related to device performance. MOCVD grown InGaAs/InGaAsP/InGaP/GaAs quantum well laser diodes display high surface roughness when 2° misorientations are used [13]. MBE grown AlGaAs/GaAs heterostructures [14] and GaInP/AlInP double heterostructure lasers [15], however, show improved performance on off-axis materials.

The misorientation of substrates has been directly related to the presence of defects in epitaxial layers. Takagishi and colleagues at Sumitomo Electric Industries have investigated GaAs layers grown on GaAs substrates by MBE [16]. Elliptic-shaped surface defects which have a dislocation with a screw component at their centre were observed. It was noted that as the growth rate increased the defects diminished, disappearing at $4\mu mh^{-1}$, and were not observed for substrates oriented 2° off (100) towards the <110> direction. A similar defect dependence on growth rate, substrate

misorientation, and in addition growth temperature in epitaxial layers grown by MOCVD on InP substrates has been reported by Nakamura et al [17]. In this case "tear-drop-like" hillock (TLH) defects in InP and GaInAsP layers were seen if the growth temperature was less than 700°C, the growth rate above $0.3\mu mh^{-1}$ and the misorientation angle was above a (temperature and rate-dependent) critical angle. In general, the number of these TLHs was seen to correlate with the etch pit density, and they increased with decreasing temperature and higher growth rates. This was explained in terms of a model of absorbed atoms which are trapped at the intersection of the surface with the dislocation, whilst migrating to monolayer steps. If they move from the dislocation before another atom arrives, no TLHs are formed. If another atom joins it, three dimensional growth begins, and TLH defects are formed. If the growth rate is increased, atoms are more likely to be trapped, so TLHs increase. If the temperature increases, however, the atoms have the necessary energy to leave the dislocation, and the number of TLHs decreases. The defects appear to be very sensitive to the exact angle of misorientation, with a critical angle of 0.06° being measured when the growth rate is $1\mu mh^{-1}$ and the growth temperature is 625°C.

These experiments were repeated by Epitaxial Products International (EPI) using MCPWT wafers with nominal misorientations of 0.0, 0.05, 0.10, 0.15 and 0.2 degrees off-axis. A sample of Japanese Nippon Mining material (now Japan Energy) was also used as a control. No effects described above were observed on the MCPWT wafers, but growth on the Japanese sample agreed perfectly with predictions. The answer appeared to lie with the misorientation of the wafers, so a technique of measuring this angle accurately was required.

4.2.1 : Experimental Technique

In order to measure the misorientation angle of a substrate, it is necessary to combine knowledge of the specimen surface and the (001) planes. A novel technique has been devised, which utilises the ability of a Bede D3 diffractometer to move both detector and specimen out to high angles using only motor-driven action. This permits the combination of reflectivity and diffraction which has been used here. In essence, the exact position of the surface of a wafer can be determined by measurement of the

critical angle, as this is a constant for a given material at a known wavelength (Eq. 2.7). As the measured Bragg angle gives the position of the crystal planes, the two techniques combined can give the relative angle between the planes and the surface.

Experimentally, the D3 diffractometer is aligned as follows. The detector is positioned directly in the beam by scanning the direct beam while narrow detector slits are in place. A translation of the detector behind the slits allows the detector and slits to be aligned. These positions are then set to zero. The beam is half cut by the sample by an iterative process of rocking the sample and translating it into the beam. The sample tilt axis is scanned, and set to the position at which the transmitted intensity is a minimum, as this is when the crystal is vertical. A rotation of the sample about an axis normal to its surface should now give a constant signal. These positions are zeroed on the software. This is now a suitable arrangement for reflectivity. A θ-2θ coupled scan is performed, with the detector slits in place. A scan range from 0" to 2000" is sufficient. If the slits are then removed an 004 rocking curve of the sample can be taken by moving the sample and detector to the Bragg condition, and scanning the θ axis. As no re-calibration occurs between the reflectivity and diffraction measurements, the values obtained can be combined. Initially in these scans the incident beam lay along the $[0\bar{1}\bar{1}]$ crystal direction. The substrates were then rotated by 90° to look along the $[01\bar{1}]$ direction, and the scans were repeated.

The reflectivity scans obtained were simulated using Bede Scientific's commercial software REFS [18]. This gives an indication of the roughness, and allows the offset between the theoretical and measured critical angle to be obtained. This angle is equal to the offset of the crystal surface from the zero position, so the surface position is now known accurately. The difference between the measured Bragg angle (after the reflectivity correction) and that expected for planes parallel to the surface is therefore the misorientation angle. As the dominant error here is through simulation of the critical angle, the measurement can be made to an accuracy of less than 0.01°.

4.2.2 : Results and Analysis

An example of the results obtained is found in Fig 4.1, and a summary is given in Table 4.1.

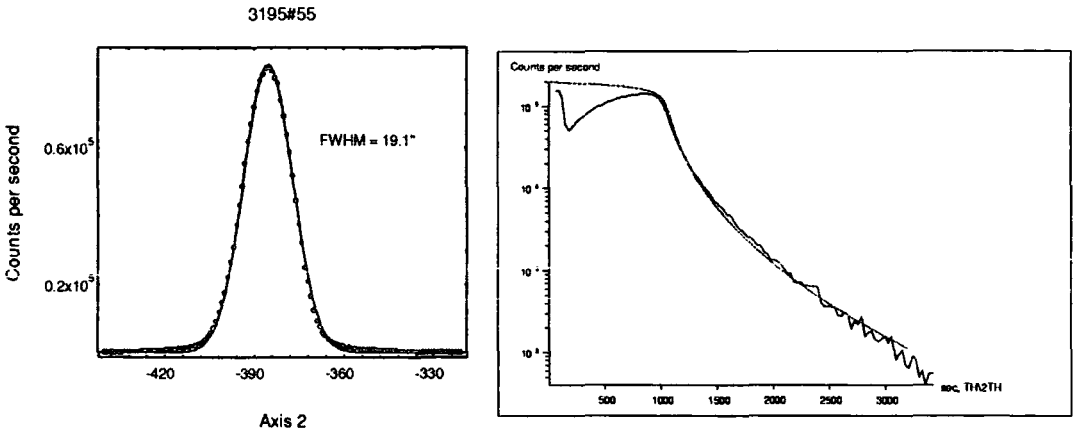

Fig 4.1 : The double axis rocking curve for sample 3195#55 (Nippon Mining material) is shown, which has been simulated by fitting to a Gaussian distribution. This gives a FWHM of 19.1 arc seconds. The specular reflectivity scan for this sample is shown on the right, which has been simulated using REFS to give a roughness of 0.55nm. The experimental scan is shifted to the right to allow for the misalignment of the sample with the holder.

Table 4.1 : Misorientation angles for InP substrates using combined reflectivity and diffraction. The nominal values are shown in brackets.

	3200#9 (0°)	**3202#21 (0.10°)**	**3195#55**
Company	MCPWT	MCPWT	Nippon Mining
FWHM (″)	28.8 ± 1.8 56.9 ± 3.4	15.8 ± 0.3 46.5 ± 5.6	19.5 ± 0.3 19.1 ± 0.3
Roughness (nm)	0.89	0.75	0.55
Misorientation along $[0\bar{1}\bar{1}]$ (degrees)	0.24	0.22	0.07
Misorientation along $[01\bar{1}]$ (degrees)	0.40	0.53	-0.01
Resultant Misorientation Angle (degrees)	0.47	0.57	0.08

Several differences are seen between the InP produced by MCPWT and Nippon Mining. The first is that the Nippon Mining material has a lower FWHM in both directions which probably means that the crystal has a lower tilt (i.e. dislocation) distribution than the others. For this crystal the planes are close to being on axis in

both directions, and the resultant misorientation is only 0.08°. The crystal is virtually on axis perpendicular to the major flat. The roughness of this sample is also less than that of the other two. If the two samples grown by MCPWT are compared it is easily seen that the difference in misorientation angle between the two samples is indeed 0.1° but that there is a considerable offset in this angle, amounting to 0.47°. This means that there is an error in the calibration of the saw being used to cleave the substrates, of nearly half a degree. The other points of interest are that the resultant angle along which the misorientation lies is at 63 and 71 degrees to the flat for 3200#9 and 3202#21 respectively. The resultant FWHM also lie roughly along these directions giving 63.8 and 49.1 arc seconds.

In order to validate further these conclusions, optical measurements on the samples were made at E.P.I., by etching away several planes, then measuring the angle of the step produced. These results were in excellent agreement with those above. As the critical misorientation angles of interest were less than 0.47°, this offset accounted for the failure to reproduce the TLH effects. As a consequence the cutting saw at MCPWT was recalibrated to zero.

4.2.3 : Alternative Measurement Techniques

A more conventional method of performing this experiment, where a Bede 150 double axis diffractometer and a rotation stage are sufficient, has also been employed. The axis of rotation needs to be normal to the sample surface, so a stage was designed, where the rotation plate is mounted directly onto the motor spindle. The holder for the rotation plate is made from one piece of metal, so that the vertical plate is at an angle of 90° ± 0.1° from the diffractometer base. The deviation of the plate from the vertical position on rotation was measured using a clock gauge. As the plate was rotated, a sinusoidal variation in plate position was noted, corresponding to the rotation axis being 0.25° from the surface normal. The direction of this deviation was noted, so that the results could be adjusted accordingly. An example of on-axis rotation is given in Fig 4.2.

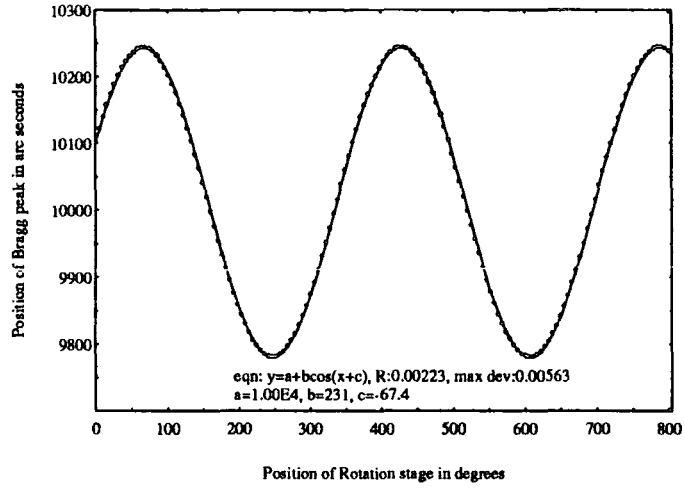

Fig 4.2 : An example of rotation from an on-axis sample of GaAs

In this technique the wafer is set to a symmetric 004 Bragg diffraction position, and an optimise routine is carried out [19]. This is based on the principle that if the diffracting plane is not parallel to the crystal surface, when the sample is rotated the normal precesses about the axis of rotation, so two Bragg peaks will be found. In order to move the planes normal to the diffracted beam, the sample should be placed at a rotation position half way between the two peaks. This is carried out through a simple algorithm [20] of finding a rotation angle, α, where a peak is registered, then continuing to rotate until the second peak is found. The rotation position half way between these is then located, and the sample scanned about θ for the peak position. For these measurements, the angle at which this peak was found was noted, then the sample was rotated through 180° and the new peak position was found. This gives the resultant misorientation angle. The samples tested previously were measured on this system, and gave the same values, within $\pm$ 0.04°. The error on this method is greater, as the way that the sample is mounted can contribute to the result, as no reliable surface position measurements are possible. This technique could be improved by using laser alignment on the sample face, as well as diffraction for measurement of the planes. The results on the second set of samples are shown in Table 4.2.

Table 4.2 : Misorientation angles measured by rotation method

Wafer Number	Manufacturer	Nominal Misorientation Angle (degrees)	Measured Misorientation Angle (degrees ± 0.04)
3231#1	JE	0.0	0.08
4020#6	JE	0.0	0.26
4028#2	JE	0.1	0.31
4029#2	JE	0.2	0.36
4023#4	MCPWT	0.0	0.11
3146#42	MCPWT/AT&T	0.0	0.12

This table shows that the companies investigated provide samples with the right trends in misorientation angle, but the angle tends to have a small offset, of the order of 0.1°, in the actual value. Many wafers come with half a degree quoted tolerance on the misorientation angle, so these are acceptable results. In particular, the MCPWT wafer was much closer to being on axis than previously. The lower accuracy of this technique, however, makes corrective action less viable, and highlights the advantages of the novel technique for misorientation measurement described earlier.

4.3 : White beam topography of InP single crystals

As discussed in Section 3.1, white beam topography is a non-destructive characterisation technique which allows the imaging of large areas. It has been extensively used in the characterisation of III-V wafers, including InP, as it potentially allows the whole crystal to be imaged, providing information on dislocation distributions and directions, twins, growth striations and precipitates [21-26].

4.3.1 : Whole Wafer Mapping at Daresbury Laboratory

As the distribution of defects within a wafer is known to be non-uniform, for comparison of growth techniques a dislocation map of the whole wafer is useful. Three aspects of the samples were considered in this study: the growth technique, manufacturer, and polishing process employed. Three samples were characterised at Daresbury Laboratory in this study, namely an MCPWT LEC wafer (4023#4), a JE LEC wafer which had been refinished (4020#6), and a MCPWT/AT&T VGF wafer (3146#42). The beam size was set using slits to be 13mmx30mm, so that most of the

wafer could be characterised in six topographs. The goniometer allowed manual movement of the sample by the amounts necessary to image the whole wafer. A wavelength of 1Å was chosen, which gives a value for μt of 2.3, i.e. conditions of anomalous transmission. The wafers were aligned with the major flat to the right when facing the beam, then tilted towards the source by the Bragg angle for the 220 reflection (13.94°). Four rotations were taken, but most of those shown here are from this geometrical arrangement. The goniometer base was set to twice the Bragg angle, so the film holder was mounted between the first and second axes, perpendicular to the x-ray beam, at a distance of about 15cm. This allowed sufficient shielding to be placed between the sample and film to ensure a clear image. In this case 25μm thick nuclear emulsions were used, which needed an exposure time of 12min, with the beam current being in the region of 250mA.

4.3.2 : MCPWT LEC InP Wafer

The white beam topograph of the LEC wafer is shown in Fig 4.3. As the anomalous transmission topograph is printed here in positive, areas which are dark are where the intensity is high and areas which are shown up white are dislocated regions. The major flat is marked. Around the edge of the wafer is a grey ring. This is purely due to absorption of the x-rays by the perspex holder, and has no other contrast significance. The magnification in this picture is low, to show the change in dislocation density between the edge of the crystal and the centre. It can be seen that the defects propagating from the edge of the wafer are mainly in the <110> directions, presumably along the {111} slip planes. They are being punched out from the wafer edge, as the density decreases from the edge inwards. The dislocation distribution near the edge of the wafer is shown more clearly in Figs 4.4 and 4.5, taken at positions A and B (Fig 4.3), where the high density at the edge of the wafer (~$6x10^4 cm^{-2}$) is seen to drop to that of high quality crystal nearer the centre, and the slip bands can be seen.

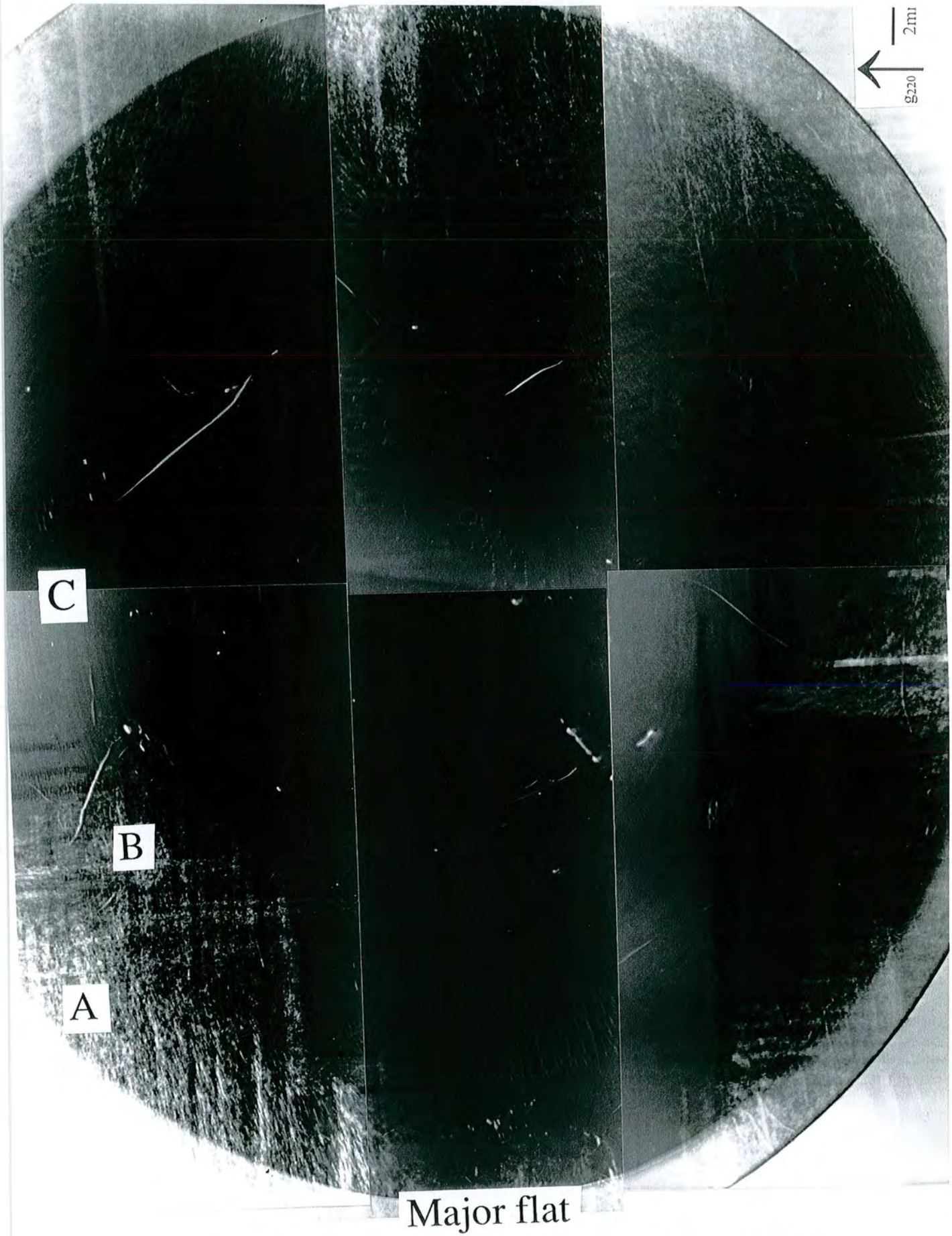

Fig 4.3 : Anomalous transmission topograph of an LEC InP wafer showing the dislocation distribution.

At the top of the topograph (Fig 4.3) it is possible to make out precipitates (C). These are probably structures based on the three elemental ingredients of the crystal, i.e. In, P and S. At the centre of the wafer, a collection of dots can be seen, which are dislocations generated at the seed, which have not been removed in the necking process (Fig 4.6). These are either dislocations present in the seed which propagate through the interface, or dislocations which relieve the stress generated at the interface by lattice misfit due to, for example, the seed being undoped while the melt is doped. To the right of these dislocations are a set of 'wiggly' dislocations, propagating in the <110> direction parallel to the major flat (Fig 4.7). When these are magnified, it can be seen that they are either spirals or loops on an inclined plane. These may be helical dislocations the structure of which is shown in Fig 4.8. These are formed by a dislocation being partly edge and partly screw in character and being pinned at A and B. If it moves in the plane ABC it is gliding as this plane contains the line and the Burgers vector. If motion occurs perpendicular to this plane it is climb, which is encouraged by an excess of vacancies at a particular temperature. Once climb starts, the dislocation lies on the surface of a cylinder where the axis is parallel to the Burgers vector, and glide is possible on this cylinder. The combination of glide and climb results in a spiral, which we see here.

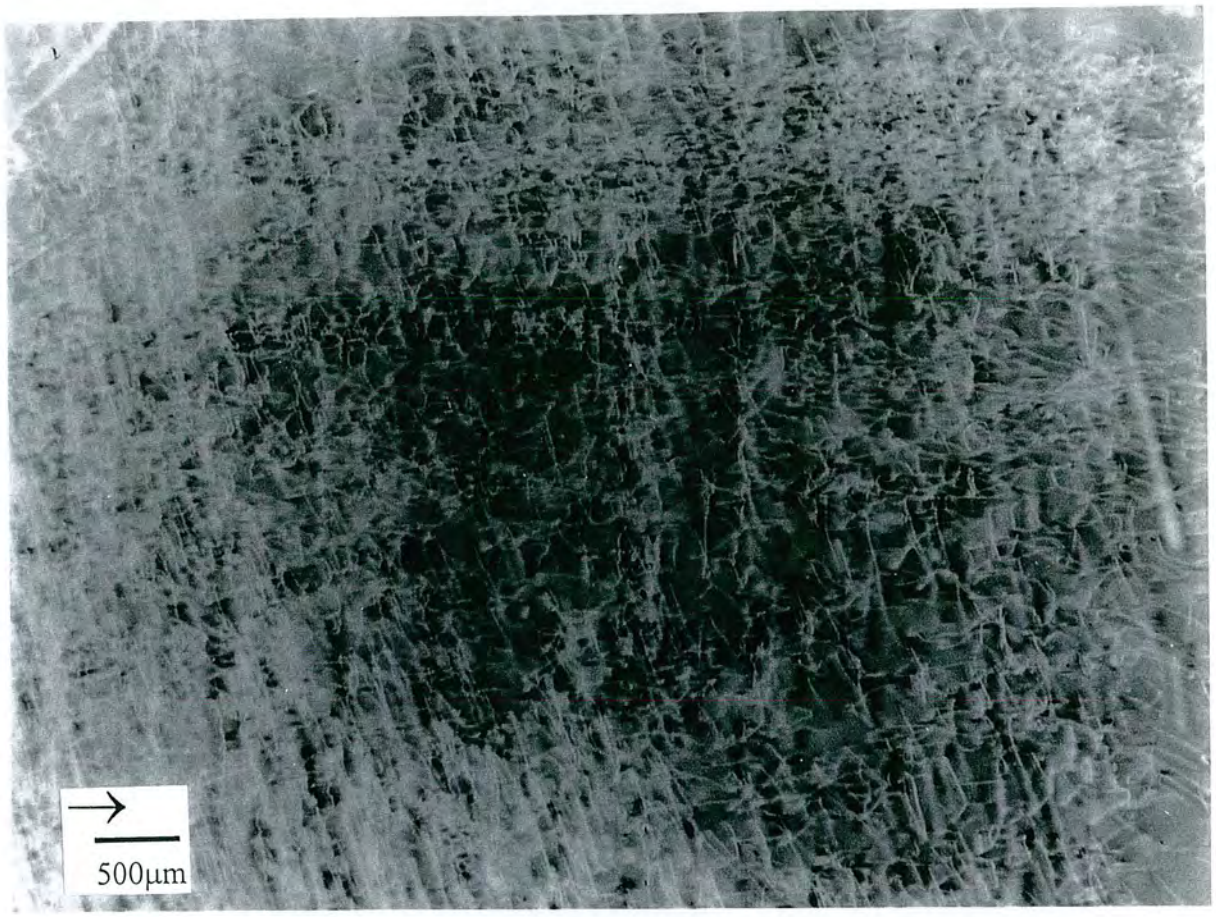

Fig 4.4 : Topograph of LEC wafer at A. The dislocation density is ~$6x10^4 cm^{-2}$.

Fig 4.5 : Topograph of LEC wafer at B, showing the fall in dislocation density.

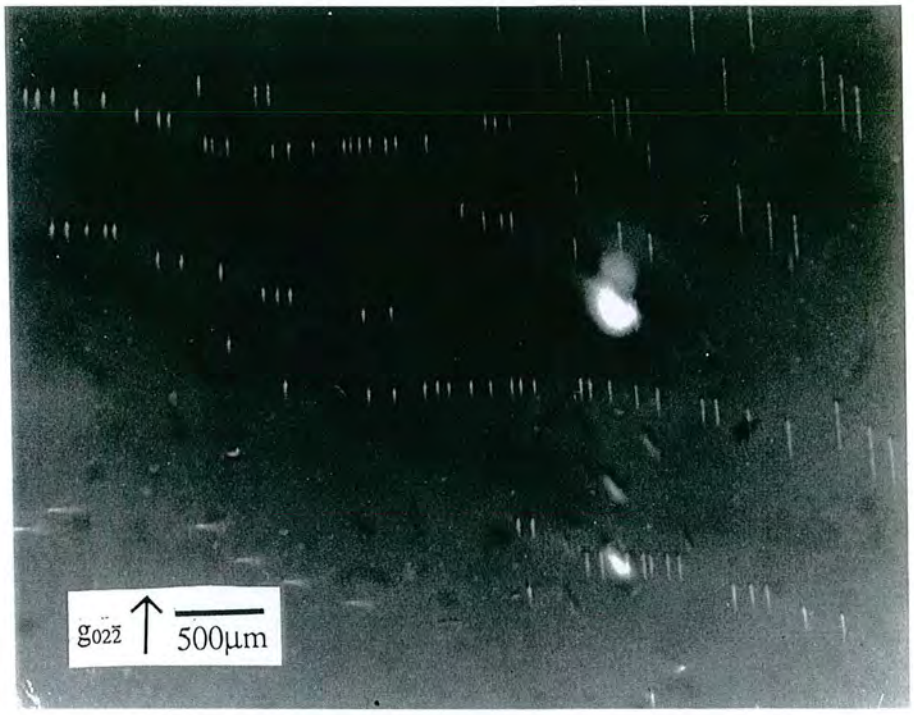

Fig 4.6 : Dislocations generated at the seed.

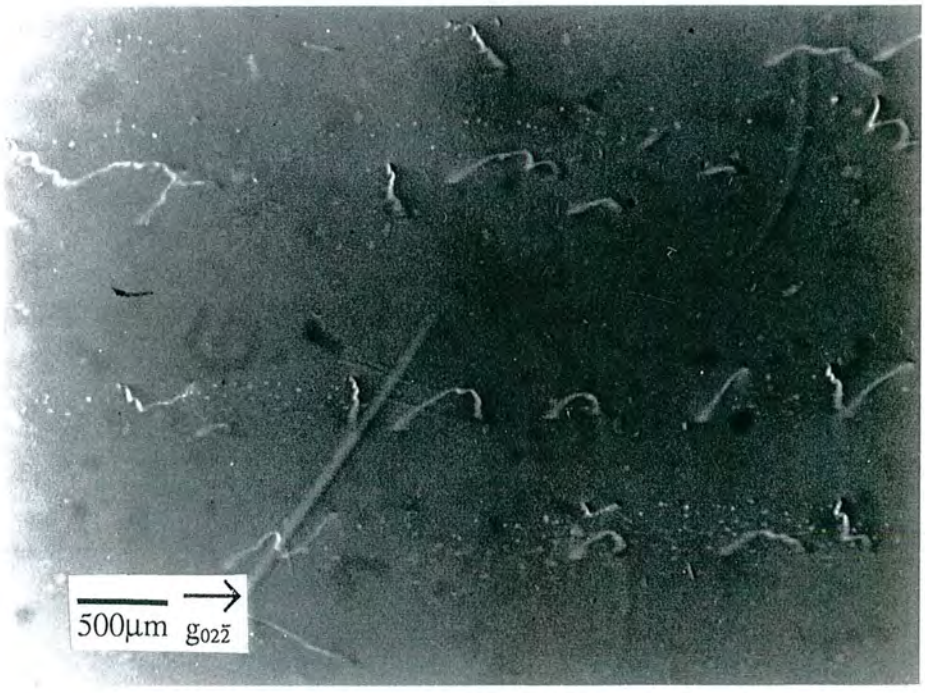

Fig 4.7 : Dislocations in LEC material.

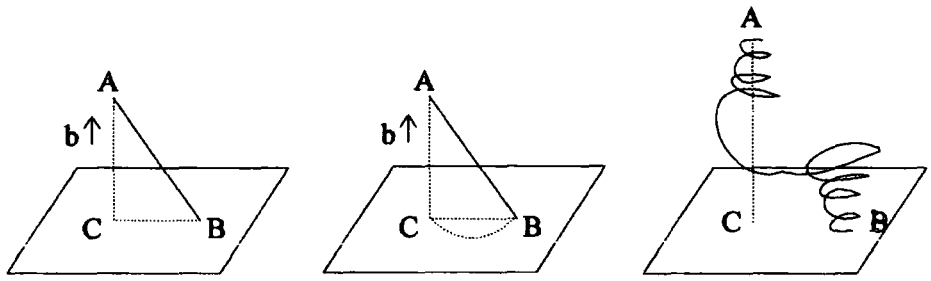

Fig 4.8 : Formation of a helical dislocation

Dots near the centre of the wafer are shown in Fig 4.9, where the dislocations must be parallel to **g** to image only the end of the dislocation. If a diffraction vector is used perpendicular to this, lines are expected, which are shown in Fig 4.10. This allows us to determine that the dislocations are lying in the <011> direction, perpendicular to the major flat. As this is in the plane of the wafer, dislocations are probably caused by radial stress from a non-planar solid/liquid interface.

Near the major flat there are some hollow precipitates, which are shown magnified in Fig 4.11. These may have been caused by bubbles of air in the melt, which have been incorporated into the wafer, then sliced open. Cockayne et al [27] have observed hollow precipitates previously in V-doped InP, which they identified using EDAX, as vanadium monophosphide with an InP centre. As these samples are S-doped, these could be indium sulphide precipitates. Franzosi et al [28], reported hollow precipitates which they attributed to gaseous inclusions. These could arise from chemical reactions between water vapour present in the boric oxide encapsulant, and molten InP, the products of which are then trapped within the growing crystal. The centre was again identified as being In and P based. In this case there is evidence for these hollow precipitates being due to gaseous inclusions as there is a dark area at the centre of the precipitate, surrounded by a lighter area of contrast. Another type of precipitate which has been identified are spherical precipitates (Fig 4.6) which have radial strain fields. This gives a characteristic image of two lobes separated by a line of no contrast which is perpendicular to the diffraction vector, as in this direction the atomic displacements are parallel to the Bragg planes. Oscillatory contrast is observed along some dislocations (Fig 4.12), which is probably due to the imaging of the intermediary image

rather than decoration by impurities but is confused by overlapping dislocation images and surface relaxation effects.

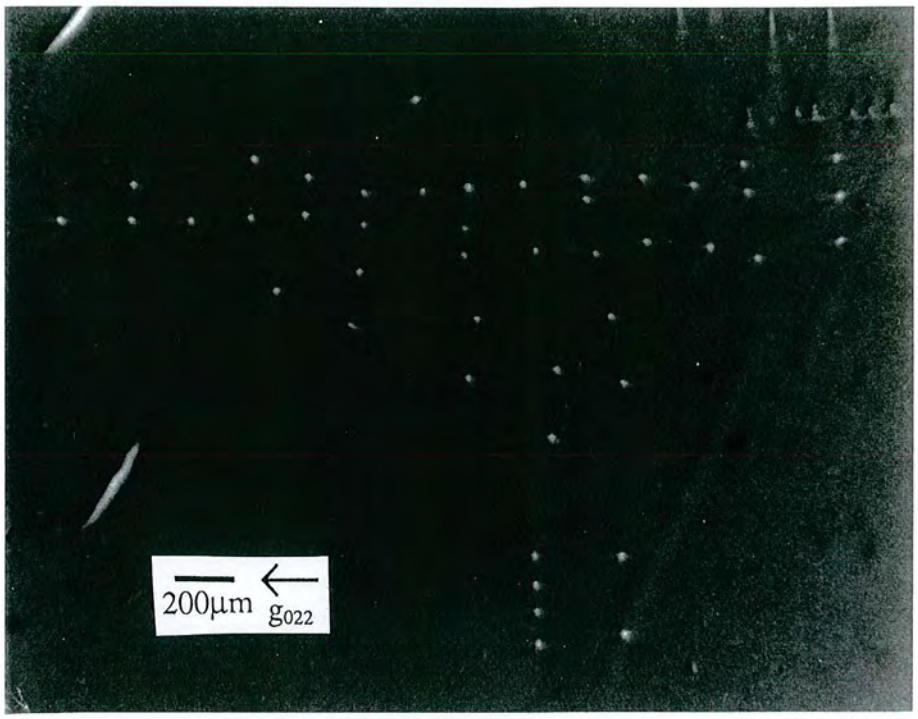

Fig 4.9 : Dislocations at centre of wafer imaged as dots.

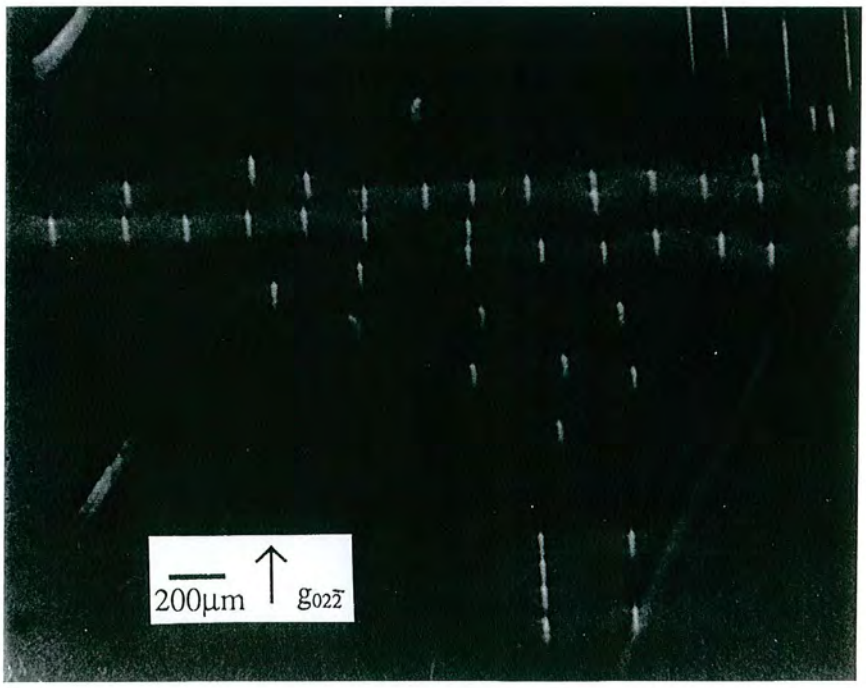

Fig 4.10 : Dislocations at centre of wafer imaged as lines.

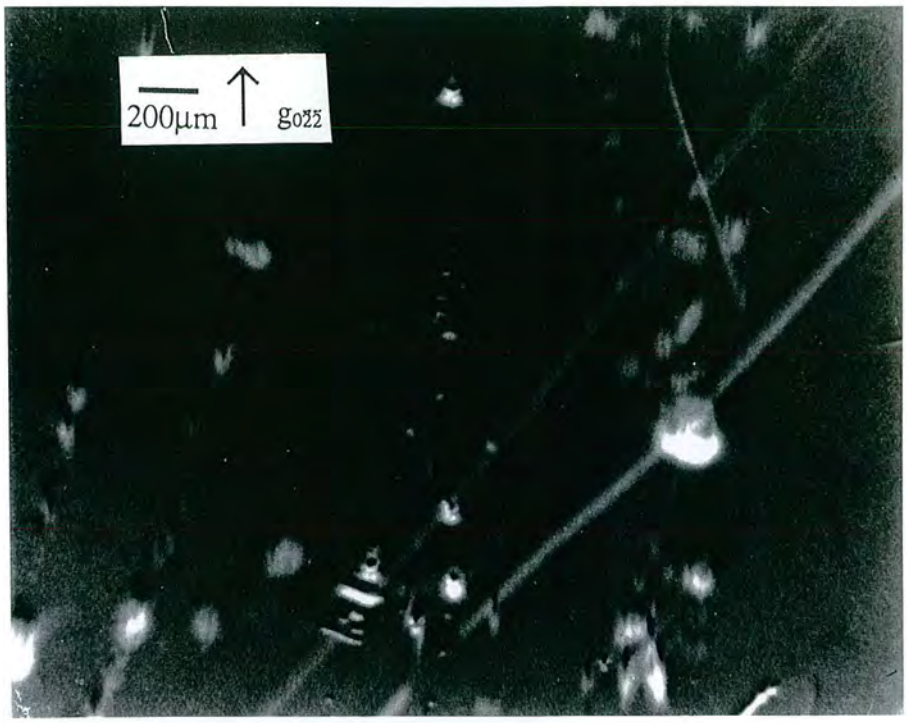

Fig 4.11 : Hollow precipitates in LEC InP near the major flat.

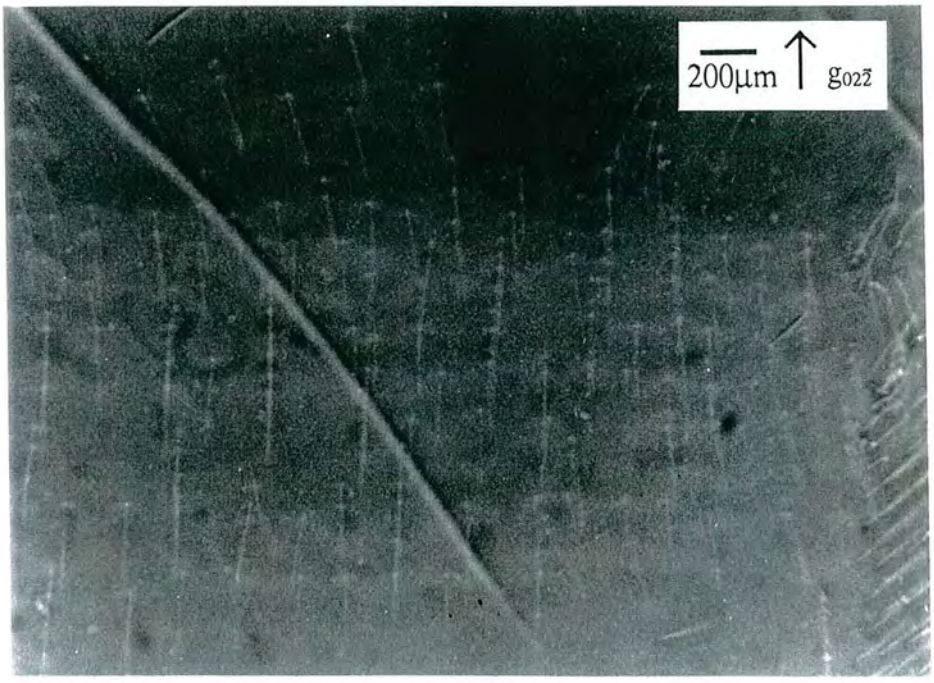

Fig 4.12 : Contrast changing along the length of a dislocation, probably due to the presence of intermediary images.

The last features which should be mentioned are the growth striations visible in the less dislocated regions of the topograph. These are caused by two complementary effects - firstly variations in dopant concentration due to curvature of the interface between the solid and the melt during growth and secondly the bands left from the rotation of the crucible. These are linked as the rotation speed of the crucible affects the shape of the interface. If no rotation is present, these growth bands exist with enhanced amplitude. The bands shown here are imaged due to the lattice parameter variations at these points, and double crystal topographs (in particular asymmetric reflections) are more sensitive to this feature. It is possible to take infra red photographs of these bands as the differential amount of sulphur present will cause contrast. These bands are regularly spaced, and show no evidence of being discontinued, then reformed elsewhere. This means that the growth rate was fairly constant, and that once the crystal was solidified it was not re-melted, as is often the case in LEC processes. The distance between these striations has been related to the growth and rotation rate by the formula [29],

[4.1] $$R = 60.d.\omega$$

where R is the pull rate in mm hr^{-1}, ω is the rotation rate in rev min^{-1} and d is the striation spacing in mm. As in an LEC process, the pull rate is about 8mm hr^{-1} and the rotation rate is several rev min^{-1}, a striation spacing of the order of a tenth of a mm is expected. In this case it is larger than this (~1mm), so only the dominant striations with the greatest variations in intensity are being imaged.

The features described here are largely growth related, and are particularly dependent on the growth temperature. The slip at the periphery of the wafer shows that the temperature gradient between crystal and ambient temperature was too great after growth, so that the CRSS was exceeded. These slip directions are chosen as they have the lowest critical stresses for this crystal system. The necking procedure is inefficient, as seed dislocations propagate to the melt. The presence of strong growth striations can be attributed to an inhomogeneity in the mixing process of the melt before and on solidification, due to an unoptimised interface shape and crucible rotation. These problems are typical of those encountered in growth by LEC, and although this wafer is certainly not as good as some produced by this method, the requirements of the

semiconductor industry to have a larger useful area on each wafer has provided the incentive to look at other growth techniques.

4.3.3 : JE Refinished LEC InP Wafer

A full wafer topograph of the refinished LEC crystal manufactured by Japan Energy is shown in Fig 4.13. It is clear that this wafer is of a much higher quality than that just discussed. Some slip dislocations (A) are visible propagating from the edge of the wafer, again in the <110> directions. These propagate less than 1cm into the wafer, so only some bands are seen beyond the limits set by the perspex holder. There are a few small defects, some of which are shown in Fig 4.14. Some growth striations are visible, but the contrast is very weak. The most striking aspect of the topograph is the considerable surface damage which crosses the wafer. These lines, with widths up to about 150μm are mostly directed perpendicular to the major flat, in a roughly linear manner, or form a random swirl formation. In the refinishing process, it is expected that the damage introduced by the first polish will have been removed, so only damage from the secondary polish should be visible. The macroscopic damage to the wafer looks as if it is due to particles of hard material being mixed in with the polish solution, which then grind parts from the sample. As the sample normally rotates during this process, the collection of random swirls is produced. The linear scratches must have been imposed subsequent to this, by, for example, inadequate care being taken when removing the wafer from the polishing machine. JE, therefore, have produced a high quality substrate where the dislocations are confined to the wafer edges, providing large regions of useful substrate. The subsequent polishing of the wafer by MCPWT has degraded the finish, and is far from an optimal process. More discussion on the polishing of the samples will be given in Section 4.7, where more sensitive techniques are employed to investigate this situation.

Fig 4.13 : Anomalous transmission topograph of JE wafer.

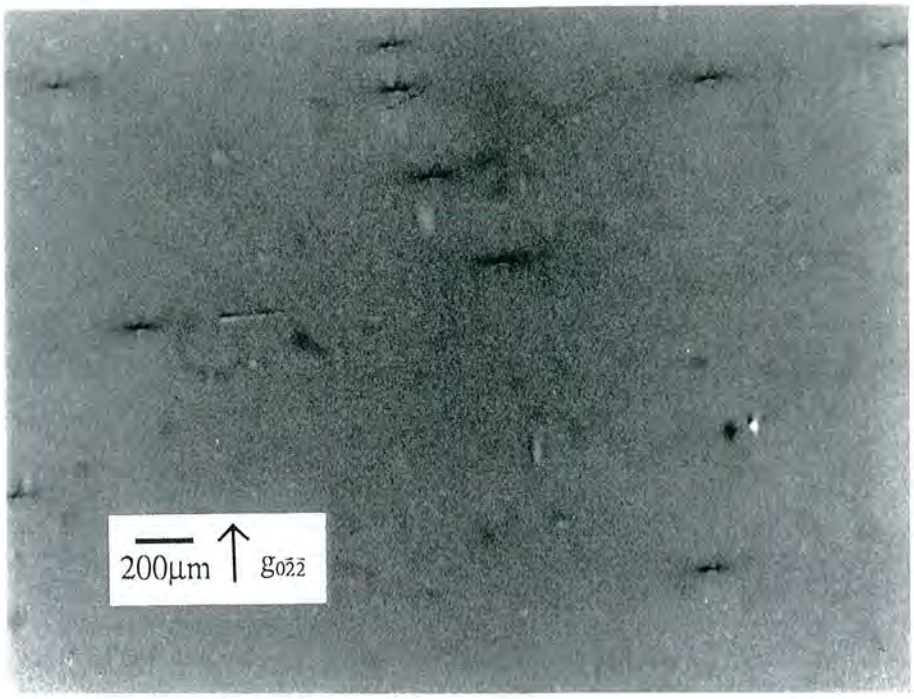

Fig 4.14 : Enlargements of defects found in JE InP wafer.

4.3.4 : MCPWT/AT&T VGF InP Wafer

Fig 4.15 shows a VGF wafer (3146#42) topographed under the same conditions as those discussed previously. It is clear that the wafer is of extremely high quality, and is virtually dislocation free. If the edges of the wafer are considered, where slip dislocations propagating from the edge have been observed in LEC crystals, no such defects are visible, which implies that the thermal gradient during the cooling process was much lower than in LEC. Very few precipitates are observed, and there are no growth striations. As this wafer is also S doped, this implies that a planar interface between the solid and the melt has been achieved, and any rotation which has been employed has been on-axis so dopants have been incorporated homogeneously. Several fine lines (A) dissect the wafer which are straight and lie along the <100> directions. As white beam topographs are relatively insensitive to twinning, it is thought that these may be twin boundaries, where the misorientation between the twins is small. As the In plane lies along the <110> direction perpendicular to the major flat, and the P plane lies parallel to the major flat, twin formation is more likely along these directions than along the <100>, although rotation twins may be possible. The low

dislocation density here is of great interest, and it was considered necessary to corroborate the results by investigating another wafer from the same boule, and other wafers from different boules. It was interesting to use the ESRF for this study as, although high energy topography results on germanium and silicon have been published [30], no studies on III-V compounds have been made until now.

4.3.5 : MCPWT/AT&T VGF InP Wafers at ESRF

Four samples were investigated at the ESRF, one of which was the sample above (3146#42), another which was three wafers apart from it in the boule (3146#45), and two from separate boules (3154#36 and 3145#38). The experimental arrangement for these measurements has been described in Section 3.1.6. In this case the wafers were wax mounted on a goniometer, and positioned in the white beam, at a slight angle to it. The image was taken directly behind the wafer, at a distance of 15cm, in Laue geometry. One problem encountered was the presence of high fluorescence which fogged the film and masked the images. This was reduced by decreasing the size of the beam and imaging an area of $7x21mm^2$. At least two parts of the wafers were imaged - near the middle and near the top of the wafer, where the minor flat was positioned downwards and the major flat to the left when facing the beam. For each part of the sample, two topographs were taken, with opposite tilts and a slight rotation, so that different crystal planes were imaged. All topographs were recorded on Kodak R films, with exposure times of 2s. The topographs were taken at 0.15Å or less, which corresponds to 82keV and a μt of 0.34, which avoids the indium edge at 0.44Å. Due to the high energy used, the images obtained are high order reflections.

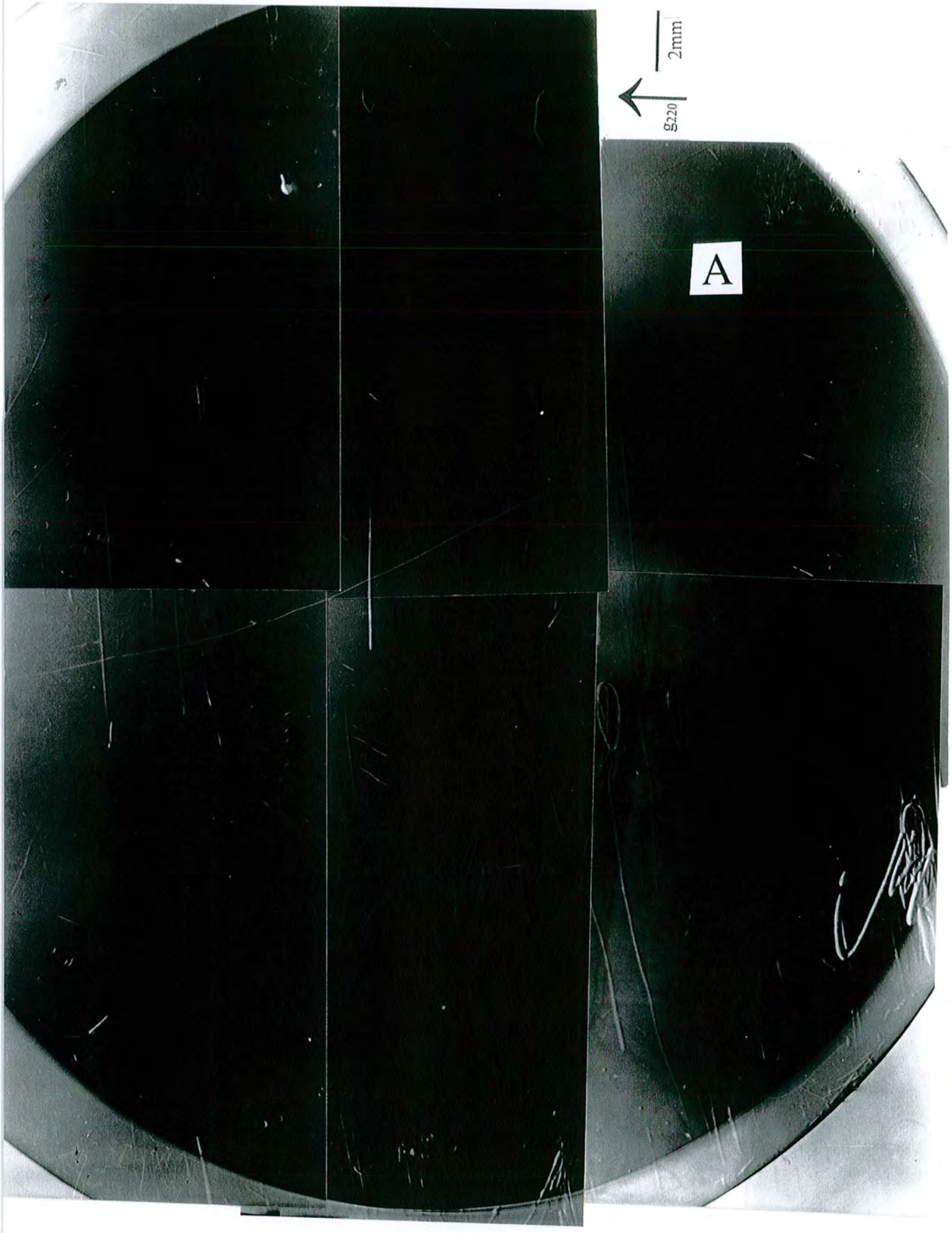

Fig 4.15 ; Anomalous transmission topograph of VGF wafer.

The sample investigated above, 3146#42, was again seen to have no dislocations in the areas being imaged, confirming the previous conclusions. The other wafer from the same boule, 3146#45, was also found to be dislocation and striation free, showing that the uniformity of the growth process is good. Although these two wafers are close together in the boule it is likely that a large fraction of the boule is dislocation free. Wafer number 3154#36 contained no imaged dislocations, and at the edge of the wafer Pendellosung fringes were observed. As these arise from the interference of the wave-fields from the two branches of the dispersion surface, and the coherence of these waves is destroyed by the presence of defects, this is a further confirmation that the crystal is highly perfect. The period of the fringes is found to be 120±30 μm, which are shown in the ($\bar{2}$ 0 22) reflection in Fig 4.16.

Only one VGF wafer was found to contain dislocations, which was number 3145#38. The dislocations are fairly evenly distributed across the wafer with a dislocation density of about 200cm^{-2}. Some slip was present in dislocations propagating perpendicular to the major flat, and some precipitates were imaged, but no growth bands were observed. The dislocations present were seen to disappear in the (1 $\bar{1}$ 13) reflection, which is imaged at about 0.1Å, and is contrasted with a ($\bar{2}$ 0 22) reflection in Fig 4.17. The extinction conditions for screw and edge dislocations are $\mathbf{g}.\mathbf{b} = 0$ and $\mathbf{g}.\mathbf{b} \times \mathbf{u}=0$ respectively, where **b** is the Burgers vector, **u** is the line direction and **g** is the diffraction vector. These have been used to give $\mathbf{b}=\pm a/2[110]$ so the Burgers vector is in the plane of the crystal surface. The projected length of the dislocation was measured and from the fact that dislocations propagate from one surface to the other, the angle of inclination of the dislocation is found to be 60°. The line direction is found to be $\mathbf{u}=[011]$ from the geometry of the diffraction condition, so the dislocations are identified as 60° mixed dislocations which lie in the {1 $\bar{1}$ 1} slip plane. This is consistent with their generation through slip.

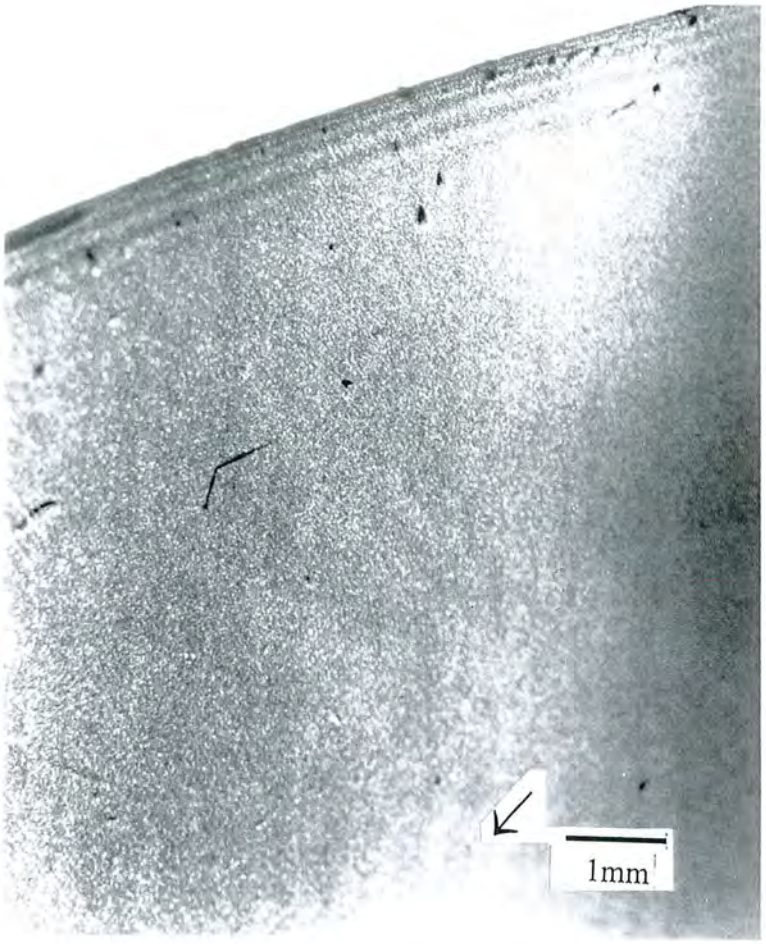

Fig 4.16 : Pendellosung fringes in VGF InP , taken at the ESRF.

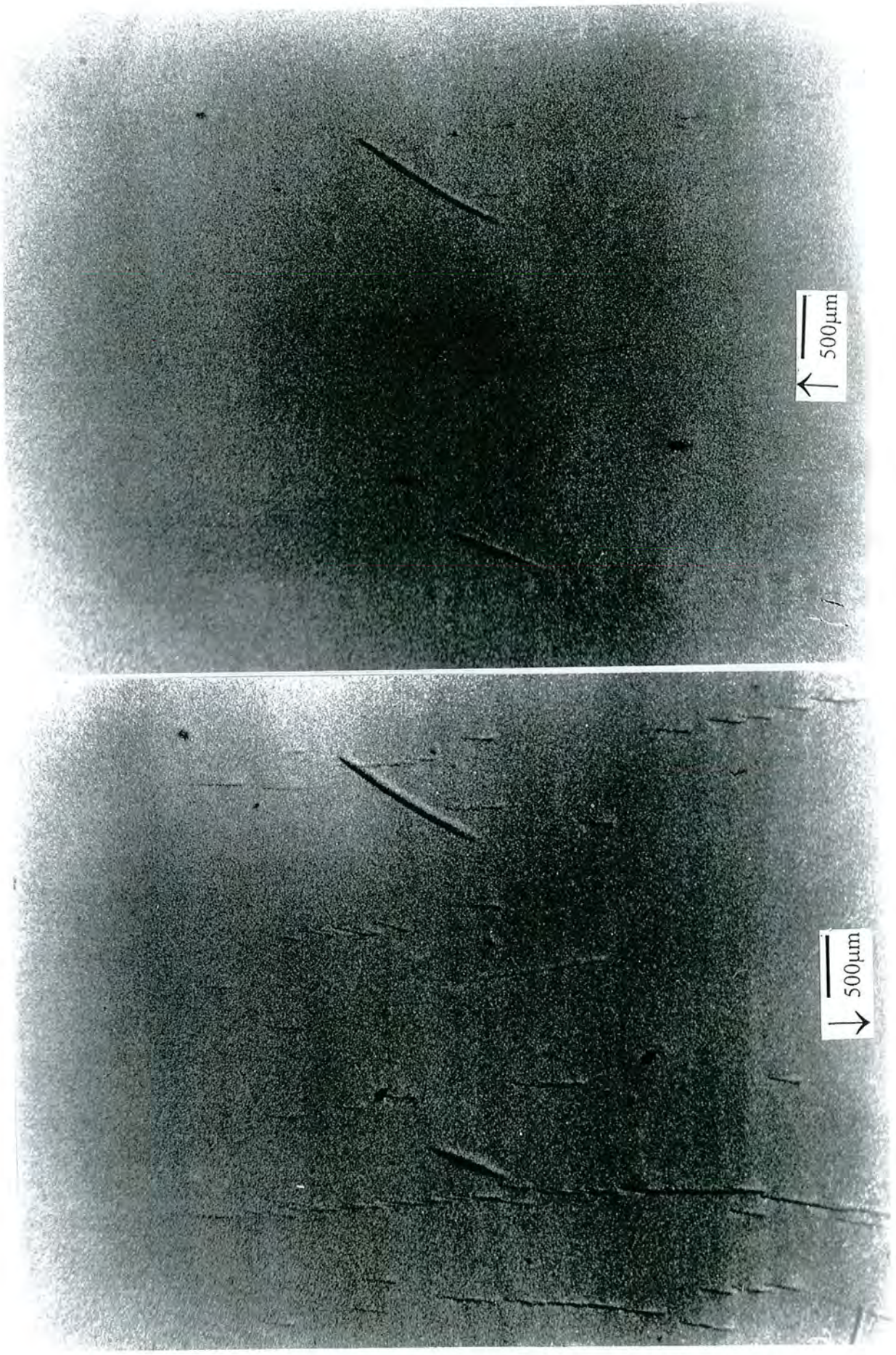

Fig 4.17 : Extinction condition for 60° mixed dislocations in VGF InP. Showing the $(1\bar{1}13)$ reflection (above) and $(\bar{2}022)$ reflection (below)

4.3.6 : Summary of Topographic Results

A summary of the features discussed for all the wafers is found in Table 4.3. We have seen that dislocations are regularly found in LEC grown crystals through their having large radial and axial temperature gradients. The radial gradient is demonstrated by the presence of slip dislocations emanating from the crystal periphery, and the axial gradient has caused climb. Dopant inhomogeneity due to crucible rotation rates and a non-planar interface structure will lead to non-uniform device performance, while the high dislocation density across the wafer makes over half of it unsuitable for device applications. The results on the JE wafer show that most of these difficulties can be overcome by a controlled growth process, where proper necking, rotation and temperature control occur. The presence of the slip dislocations at the edge of the wafer, however, seem impossible to eliminate.

Table 4.3 : Summary of comparison between LEC and VGF InP:S

	Dislocation Density cm^{-2}	Dislocation Distribution	b Direction	Dislocations from seed	Slip?	Precipit-ates?	Striations?
LEC 4023#4	$6x10^4 \rightarrow 0$	High at edge and centre, low in-between in some areas	From edge propagating in <110> directions.	Yes, visible in centre of wafer	On {111} planes	Yes, near edges	Yes, evenly distributed, contrast uneven
LEC (JE) 4020#6	$10^3 \rightarrow 0$	Only very near edge	From edge propagating in <110> directions.	x	On {111} planes	Few	Yes, weak contrast
VGF 3146#42	~0	-	-	x	x	Few	x
VGF 3146#45	~0	-	-	x	x	Few	x
VGF 3145#38	~200	Even	In surface	x	x	Few	x
VGF 3154#36	~0	-	-	x	x	Few	x

The use of the VGF technique has been shown to allow the production of dislocation free wafers, in a fairly reliable way. The use of independently controlled heaters has effectively allowed the latent heat of solidification at the interface to be counteracted, and a planar solid/liquid interface to be maintained throughout the growth process. As it is easier to control these parameters at a slow growth rate, it is likely that the wafers were grown at a rate less than 3mm hr^{-1}, which has obvious financial disadvantages.

The planar growth interface and controlled crucible rotation (if it was employed at all), have resulted in wafers with uniform dopant concentration, all of which are suitable for use in device applications. That the VGF process is not easy to control is shown by the fact that one of the wafers contains 60° mixed dislocations, with their Burgers vector in the surface plane. This implies that the radial temperature gradient was higher than the critical value, leading to dislocation generation. This could be caused by the growth rate being faster, so distorting the planar interface, or by the feedback system on the furnaces being too slow. The absence of striations implies that the latter is more likely. The dislocation density is still much lower than that at the edge of LEC wafers, and has the advantage that it is uniform across the sample. Of course, commercial wafers have been screened prior to sale, and there is no method of knowing how many wafers have been rejected due to the presence of twins, which is the most likely disadvantageous effect of this growth process. On the basis of this comparison, however, vertical gradient freeze appears to be a promising and lucrative growth technique of the future.

4.4 : Double Axis Topography

The advantages of using double axis topography have been discussed in Section 3.3. In this case, the aim was to measure the strain/curvature of the InP 2" wafers, which appeared unstrained in white beam topographical experiments. The experiments were performed at the SRS Daresbury Laboratory, on Station 7.6, using the experimental arrangement described in Section 3.3.1. The samples were mounted in the holder designed for transmission topography, which allowed them to be imaged in a strain-free environment. A wavelength of 0.53Å was chosen, with the topographs being taken in transmission. Both symmetric and asymmetric 220 topographs were taken. The asymmetric topographs are necessary for the growth strain normal to the crystal surface to be imaged. In most cases, the sample angle was scanned until the peak was incident on the detector. Several exposures were then made onto the same topograph, with a sample rotation of 5" or 10" between each exposure. For a few scans, the step sizes were made smaller so that a continuous image was obtained. Images were recorded on D2 or D4 film, with exposure times of up to 1 hour. The results of the curvature measurements are described in the next section, so only examples of the small step topographs will be given here.

Although striation contrast was observed in one sample under white beam conditions (Section 4.3), double axis topography is more sensitive to light swirl. An example of this is shown in Fig 4.18, where the bands of contrast can be seen emanating from the crystal centre. The spacing of these lines is 0.2mm, which is in excellent agreement with the tenth of a mm predicted from Equation 4.1, and emphasises the increased sensitivity of this diffraction geometry. It is also interesting to note that this sample, made by JE, shows signs of scratching. This implies that the surface damage seen in the refinished JE sample, 4020#6, is not entirely due to the repolishing process. Symmetric double axis topographs of this sample, Fig 4.19, also showed the dark defects seen in 4020#6, which are peculiar to this manufacturer.

An asymmetric topograph of sample 3145#38, the only VGF wafer found to contain much evidence of dislocations in the white beam studies, again shows an even distribution of dislocations (Fig 4.20). The slip planes can be seen, as can some precipitates. A dislocation-free VGF wafer is also shown, in Fig 4.21, which was previously imaged in a full wafer map under conditions of anomalous transmission. It was remarked from this topograph, that several fine lines crossed the surface of the wafer, which were attributed to possible twinning. From Fig 4.21 it is clear that the sample does indeed contain sharply tilted regions, which may correspond to twins.

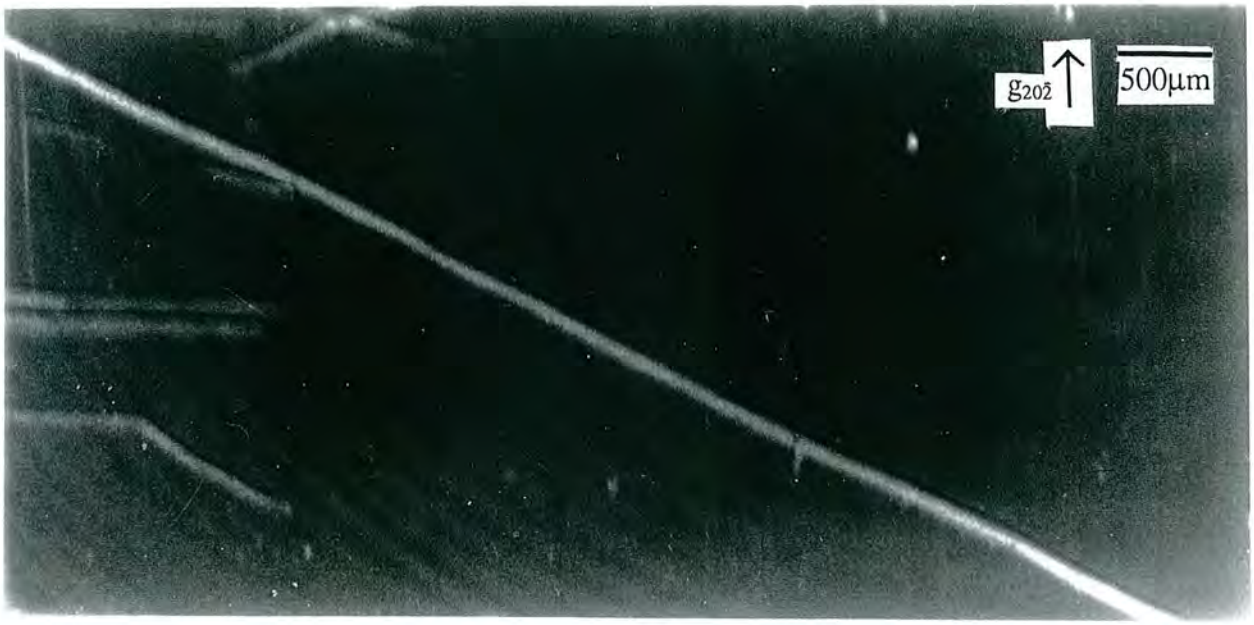

Fig 4.18 : Asymmetric double axis topograph of JE sample, 3231#1

Fig 4.19 : Dark defects in JE 3231#1. Symmetric double axis.

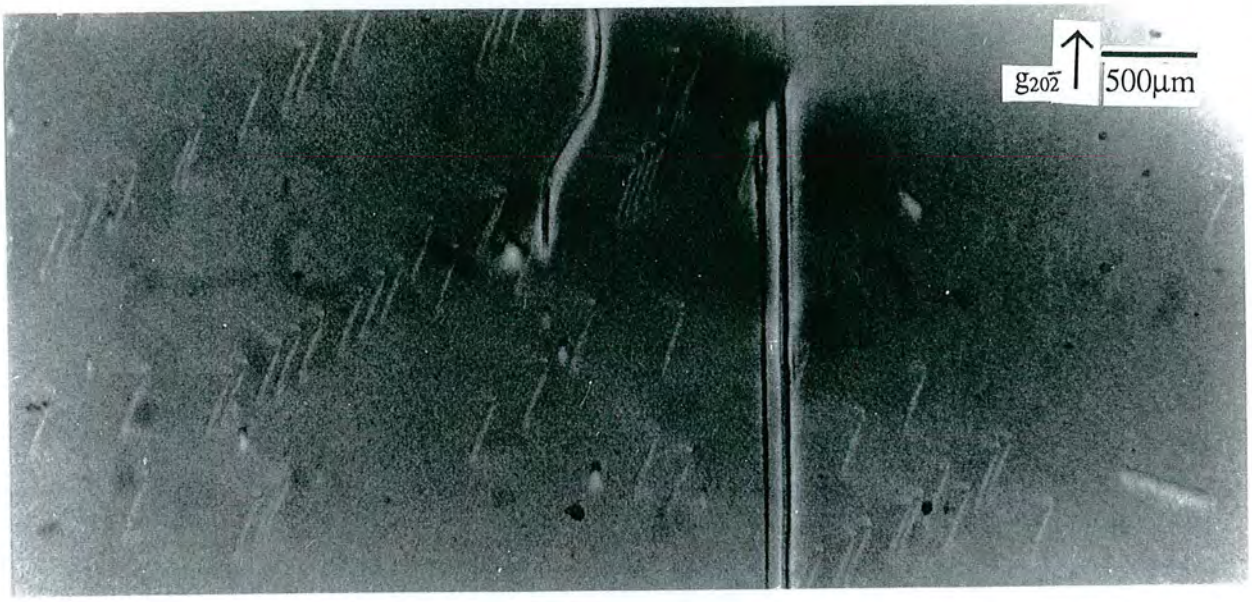

Fig 4.20 : Asymmetric double axis topograph from VGF 3145#38

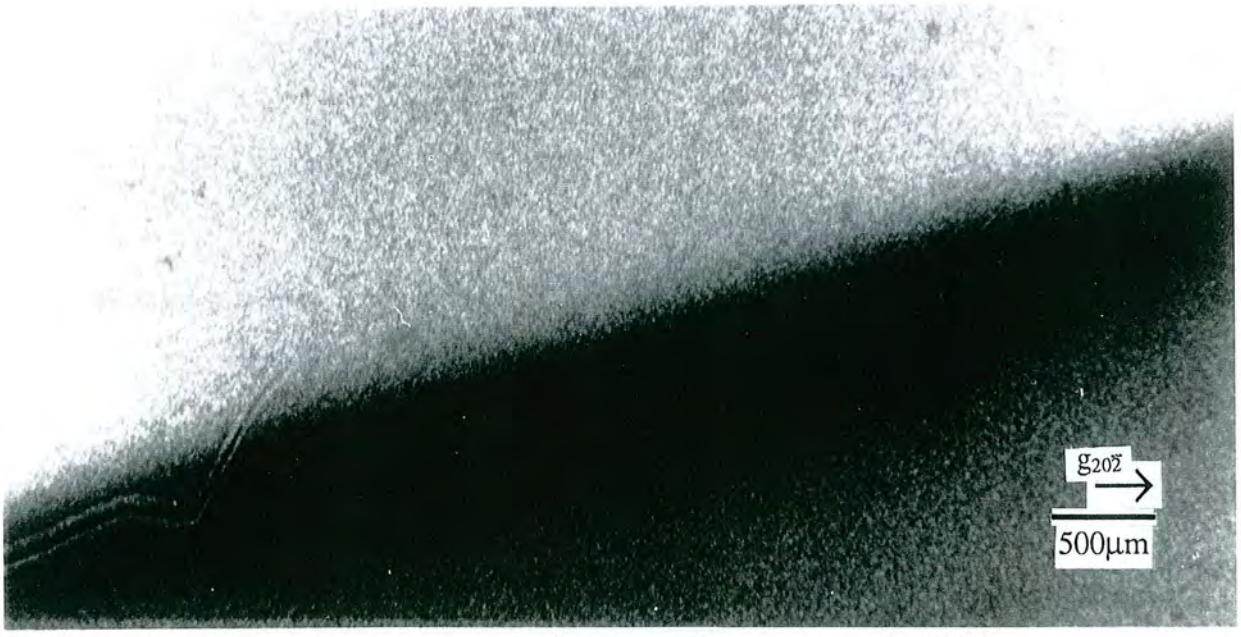

Fig 4.21 : Asymmetric topograph from sample 3146#42

4.5 : Comparison of Curvature of 2" LEC and VGF InP wafers

4.5.1 : Introduction

Wafer curvature can result from residual strain following the growth and cutting/polishing process of semiconductor wafers. The shape of the strain distribution can give information on dislocation distributions, and damage due to flats being sawed. A flat crystal is the goal for epitaxy, as it allows undistorted, uniform layers to be deposited on the surface. One method of quantifying the curvature within a sample is the radius of curvature, which is of the order of 1km for a perfect dynamical crystal, and decreases down to less than a metre for bent kinematical crystals [31]. This curvature affects the structure factor that is measured, and hence all the diffraction processes. The problem of wafer curvature in diffraction techniques has recently been approached, by the introduction of curved monochromators which expand the divergence of a lab source so that all of a curved wafer can be imaged, e.g. by topography [32, 33]. In this study two techniques, double axis diffraction and topography, have been employed to measure curvature of 2" InP wafers, and the results have been compared. Similar work has recently been reported as a novel technique strain-mapping technique at X-Top '96 [34]. If the radius of curvature measurements are described in terms of strain, a curvature of 10m represents a strain ($\delta d/d$) of 3.10^{-4} and one of 30m gives 1.10^{-4}, compared to 3.10^{-6} for a radius of curvature of 1km.

4.5.2 : Double axis diffraction mapping

As has been described previously, one of the techniques of double axis diffraction is to map a wafer by mounting it on an X-Y stage then looping the scan to repeat it at different positions on the sample. One of the advantages of this is that in a loop, the effect of backlash on the motors is eliminated, and the absolute position of a peak is kept constant throughout the scan. This enables the movement of a diffraction peak to be mapped, as it shifts due to wafer curvature. The accuracy on the XY movement of the stage is 0.05mm, while the precision on the stepping motors is 0.2". In this study, the wafer was scanned over an area of about $18mm^2$, which was the limit of reliable movement on the stage using a surface symmetric 004 reflection. This was taken from

near the centre of the wafer. The samples could be rotated manually without re-mounting, and were positioned initially with the major flat horizontal and the minor flat to the right. A beam size of 1x1mm was used, and step sizes were 3mm in each direction, so a total of 49 scans are represented in each plot. As the scans are only sensitive to curvature in the plane of the diffraction vector, the sample was rotated by 90° and the scans repeated, so that curvature in two orthogonal directions could be calculated. The peak position is mapped relative to the position at the centre of the wafer, as these are not absolute lattice parameter measurements, and only relative values are meaningful.

The surface can be visualised as made up of sections of wafer tilted with respect to each other. By rotating the sample through an angle α the position of the beam on the surface is changed by a distance x. The radius of curvature, R, is thus given by x/α.

4.5.3 : Double Axis Topography

The advantage of strain mapping using double axis topography is that the sample can be mounted strain free, so that curvature measured is inherent to the crystal. These measurements were performed at Station 7.6. at Daresbury Laboratory using the 333 reflection from a Si (111) monochromator crystal at 0.53Å. Topographs were taken in transmission using the $20\bar{2}$ asymmetric reflection, from near the centre of the wafer, so components of curvature both parallel and perpendicular to the major flat are present. An area of $4x8mm^2$ was imaged in each case, on D4 film or low resolution Kodak dental film. The exposure times were about 5 min for each diffracted stripe, then the crystal was rotated by 5 or 10 arc seconds and the film was re-exposed. This gives a two dimensional striped topograph [35]. As a rotation of α leads to a diffracted beam a distance x away on the film, and no magnifications are involved, this is analogous to the double axis case and $R=x/\alpha$. The distance between the stripes was measured by enlarging through a microscope and averaging over the magnified images.

4.5.4 : Discussion of Results

In order to check that the results produced by the X-Y scans were mapping wafer curvature rather than any systematic instrument errors, the same area of wafer 3154#36

was mapped for four crystal rotations, and the variations in peak position (in arc seconds) are shown in Fig 4.22. It can be seen that the two equivalent scans in part a) and c) yield the same pattern of variation, with a similar range of values, both increasing in angle towards the bottom left hand corner of the plot. The two scans in b) and d) also correspond exceedingly well, with both the shape and values on the profile agreeing, to within ± 10" for a given point. These results confirm the stability of the system, and make measurements c) and d) unnecessary in future scans. Additional information which is obtained in these scans is the variation in FWHM across the wafers. These are shown in Fig 4.23, for wafer 3154#36.

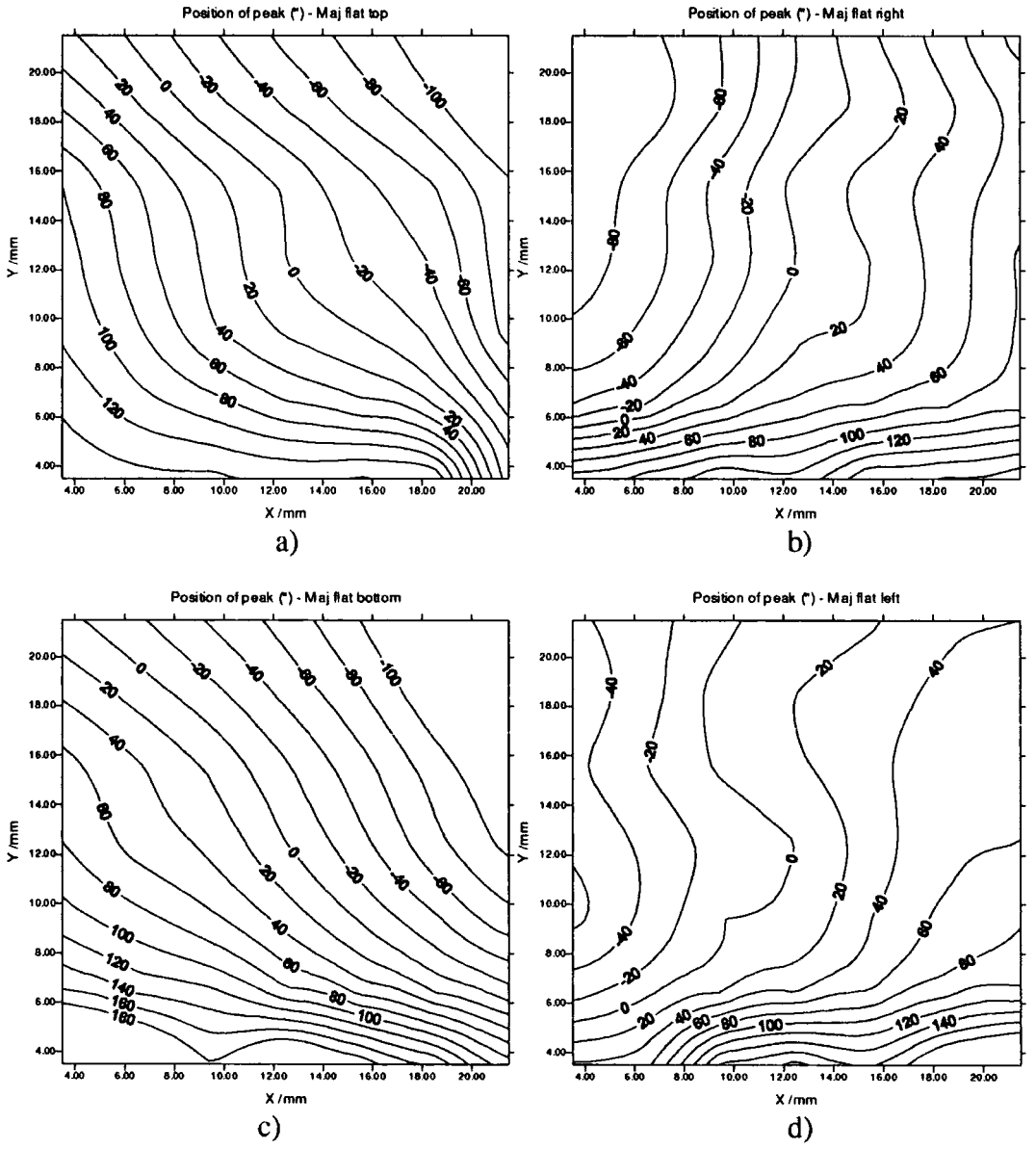

Fig 4.22 : Scans for sample 3154#36, showing the position of the Bragg peak relative to the centre of the wafer. These are shown for the four rotations of the wafer.

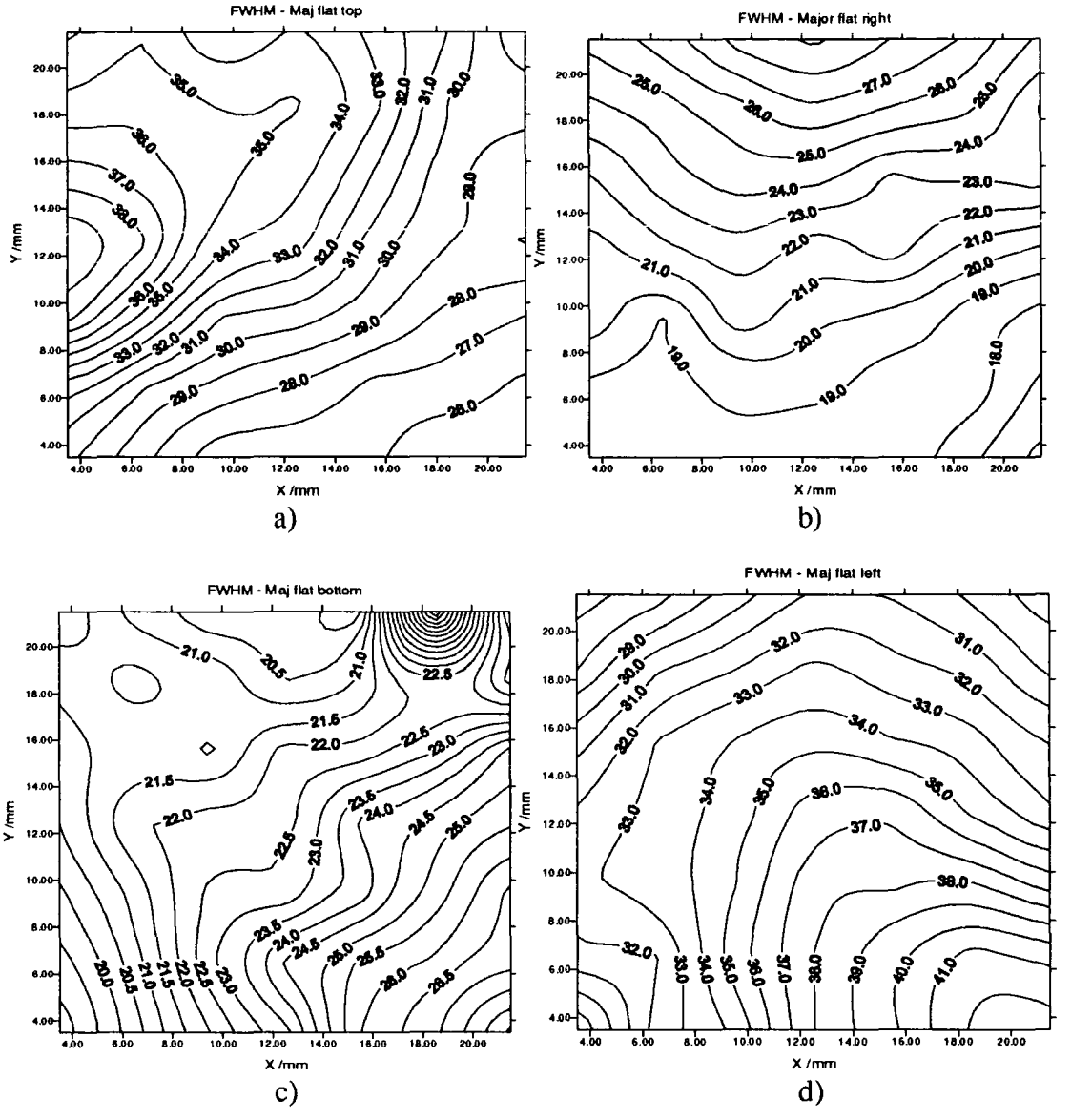

Fig 4.23 : FWHM scans for sample 3154#36 for four rotations of the wafer.

In the case of the major flat being at the top or bottom of the crystal (a) and c)), good agreement is obtained in the FWHM scans, with the FWHM decreasing away from the flat in both cases. There is a disparity in the values obtained, which can be attributed to a combination of a slight tilt between the two cases, and the sample not being exactly aligned with the flat horizontal, as this was done by hand rather than with a mechanised rotation stage. The variation which is obtained in part b) shows a different pattern, which is reasonable, as misorientation measurements on these wafers (Section 4.2) found that the FWHM is orientation dependent. The correlation between this scan and the one in d) is not as clear as in the case of a) and c), but the FWHM does increase away from the minor flat in both cases, with a spread in values of about 10". In this

sample we can see that there is no relationship between the position of the Bragg peak and the width measured, which means that the peak broadening is being caused by more than just wafer curvature, such as precipitates, dislocations in this region, or tilt domains which are independent of the general curvature trend. An example of a situation where the two correspond very well is shown in Fig 4.24, where a region of rapid change at high x values becomes gently sloping and fairly uniform at the centre of the wafer.

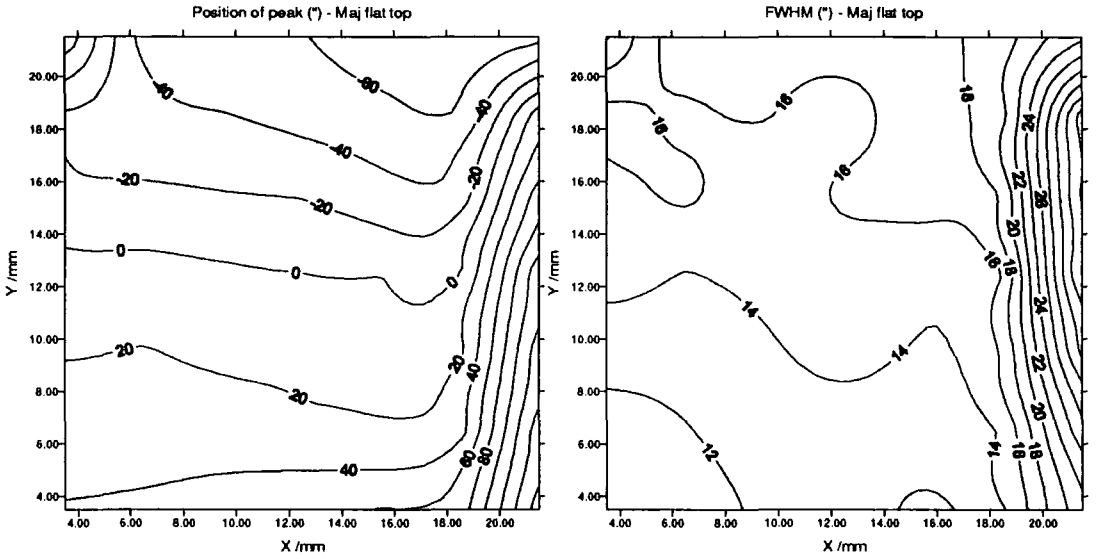

Fig 4.24 : Relationship between a) peak position and b) FWHM for sample 4029#2

Another example where the FWHM and peak position correspond well is shown in Fig 4.25. It should be noted that a similar range of values of FWHM are measured, with both varying from the mid teens to high twenties. A symmetry in the wafer exists as, in the Bragg peak scans, the peak position varies from negative values in the $[00\bar{1}]$ direction to positive ones in the [001] direction in both cases. The same curvature is also seen in the scans from the sample only three wafers lower in the boule, as would be expected, shown in Fig 4.26. In this latter case, however, the FWHM map shows a hillocky formation which may be due to the presence of precipitates or cracks in the wafer, which mask the gradual effect of curvature. The values of FWHM for both these wafers are the same in the two crystallographic directions, implying that the wafers are again uniform.

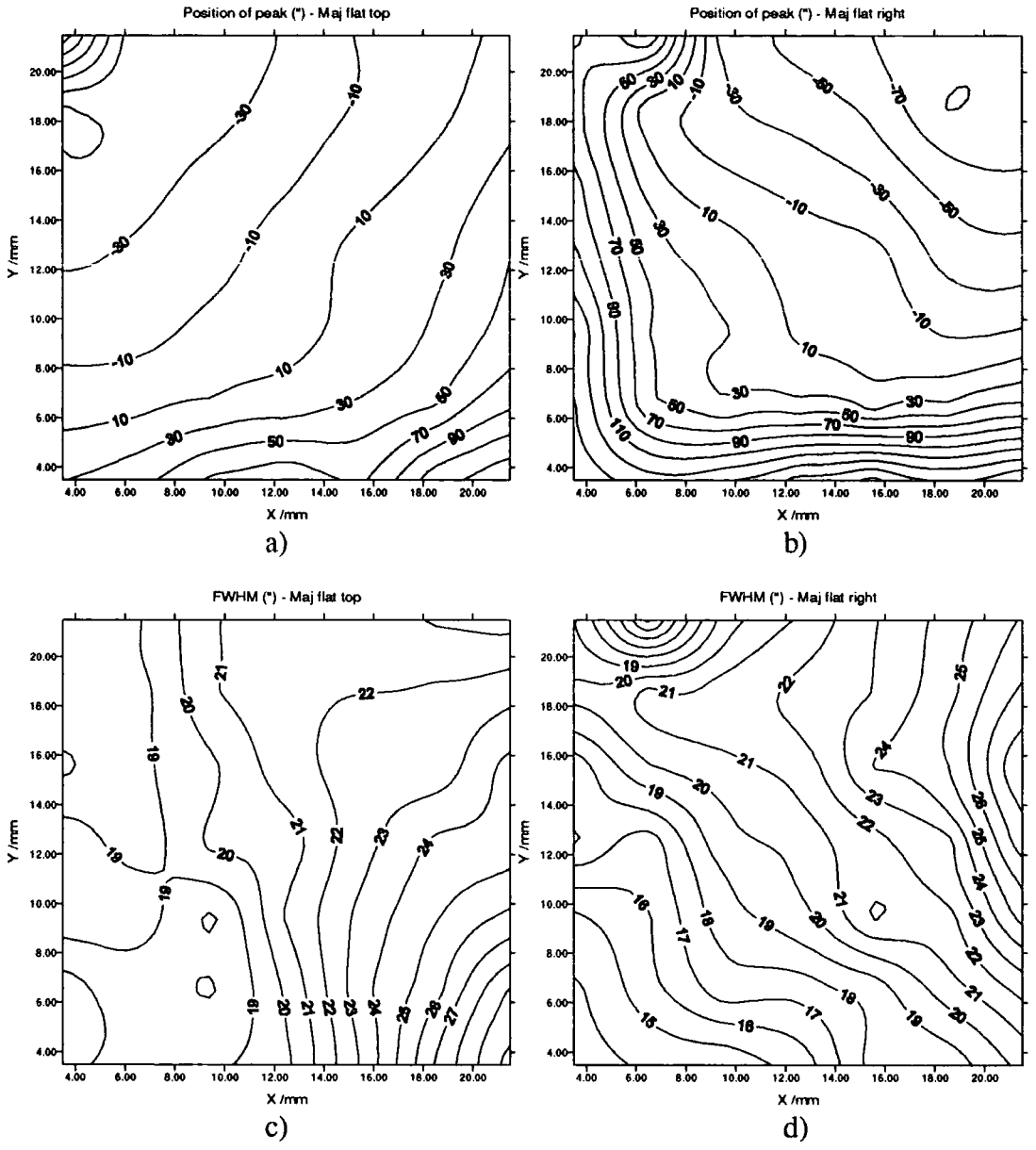

Fig 4.25 : Bragg position and FWHM maps for 3146#45

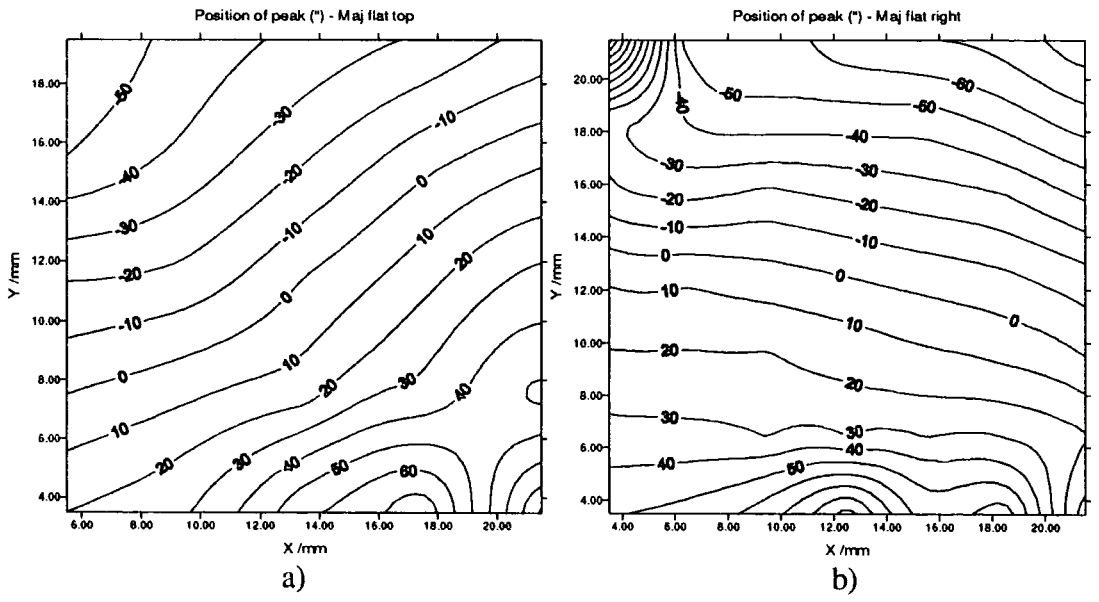

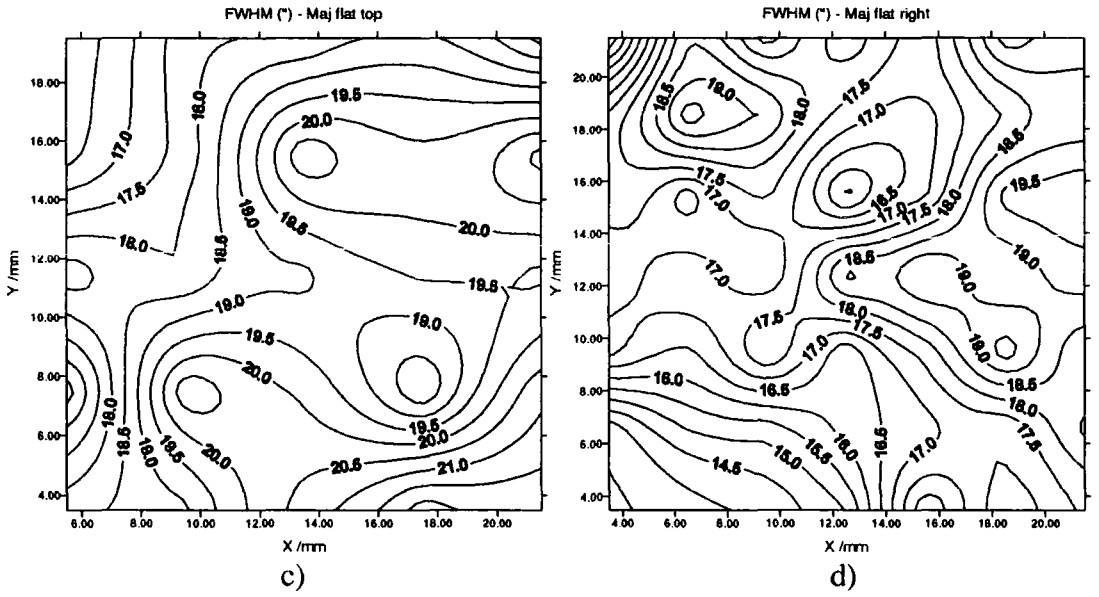

Fig 4.26 : Bragg position and FWHM maps for 3146#42

As topographic techniques have been employed as well as diffraction, the last example of this type of scan is shown together with the corresponding photograph of the curvature, in Figs 4.27 and 4.28. In this case, the scans of Bragg peak position look very similar, although when the major flat is at the top of the wafer there are two zero positions. This means that the wafer is basically a u shape, with one side of the u being steeper than the other. The other positional scan shows a gently-varying curvature. Lattice orientation has been linked to dislocation distributions in the past [36], and in this case, the uneven FWHM distribution implies that there is a variation in wafer quality across the scanned area. This is confirmed by inspection of the topograph where the dislocations can be seen, arranged in groups between small areas of perfect crystal.

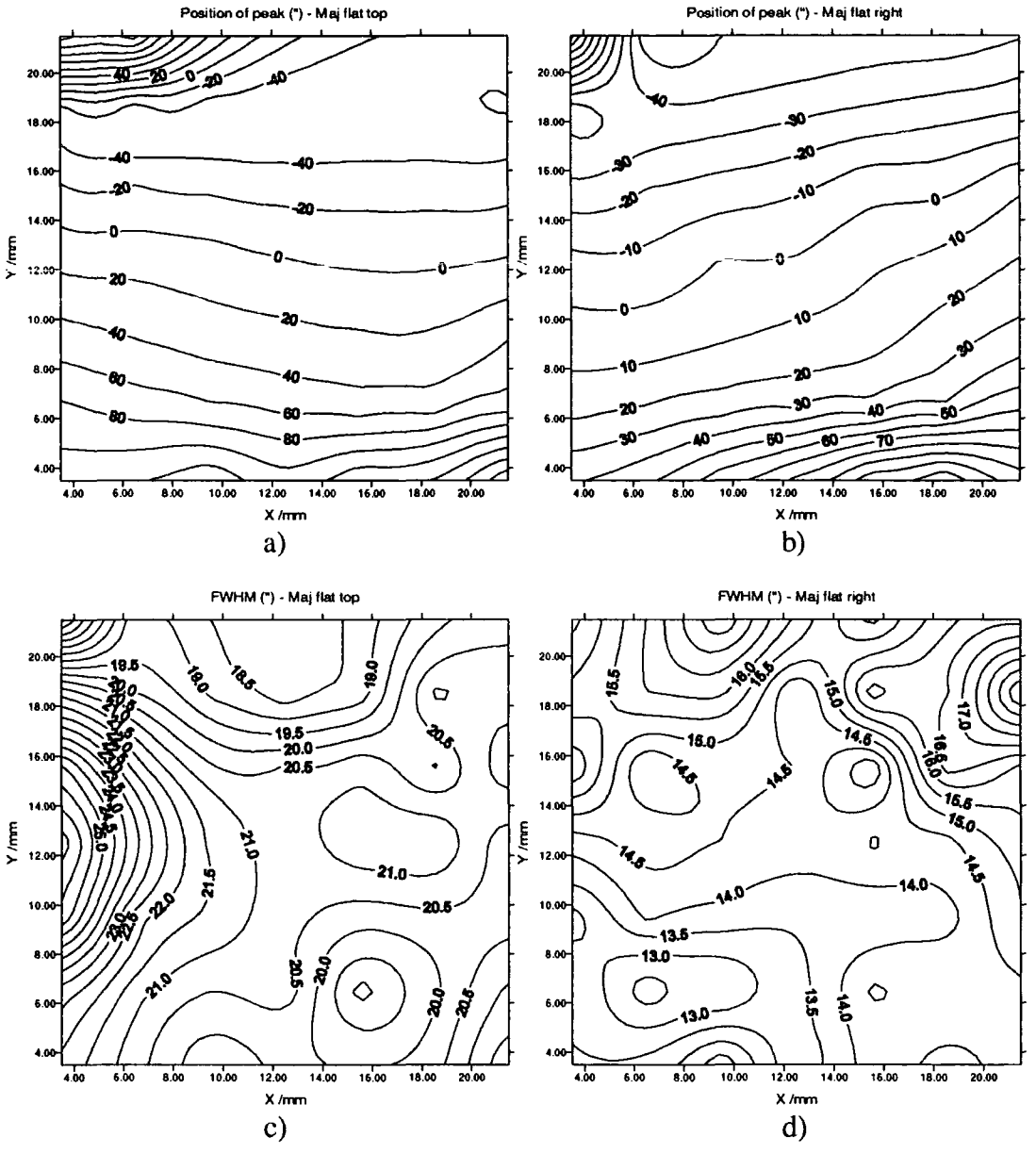

Fig 4.27 : Position maps and FWHM for 4028#2

The diffraction pattern shows uniform variations in position, and hence curvature across an area of 18x18mm^2. This is replicated in the topograph where evenly spaced lines of contrast are seen, across an area of 4x9mm^2. These lines of contrast are seen to lie perpendicular to the dislocations, so that the line of dislocations is on an inclined plane. The radii of curvature measured from the topographs are summarised in Table 4.4. Only the resultant curvature is measured in this technique.

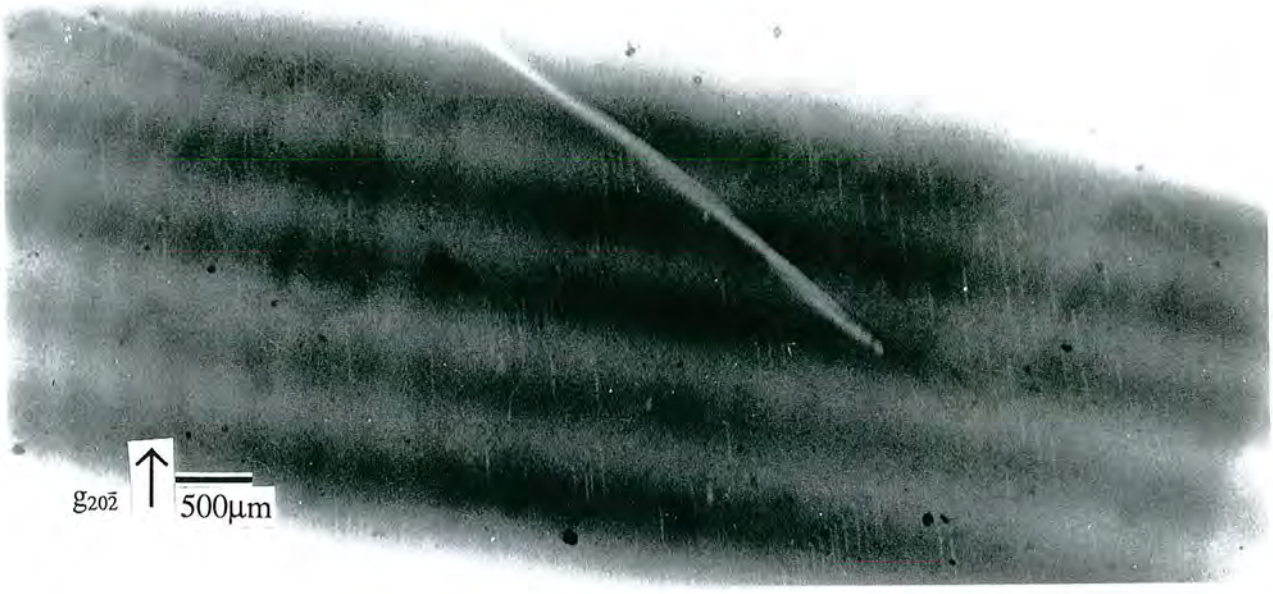

Fig 4.28 : $20\bar{2}$ asymmetric transmission topograph of 4028#2, taken at five sample positions, with a separation of 5" between each exposure. Note the images of individual dislocations.

Table 4.4 : Radii of curvature calculated from diffraction and topography

Sample Number	Growth Technique	Position of major flat in diffraction scan	Radius of Curvature from diffraction /m	Radius of Curvature from topography /m
4028#2	LEC	top right	13.9 ± 0.5 20.9	10.4 ± 1.0
3231#1	LEC			10.7 ± 0.9
3154#36	VGF	top right	14.1 17.5	16.5 ± 5.4
4029#2	LEC	top	21.2	19.8 ± 4.2
3146#42	VGF	top right	29.6 20.3	20.6 ± 5.5
3145#38	VGF			27.7 ± 1.7
3146#45	VGF	top right	26.0 18.4	31.0 ± 6.0

It can be seen that similar values are obtained for the two techniques, and that the samples vary between having a radius of curvature of 10m and 31m. The error bars which are quoted are roughly the same for the diffraction scans, but vary greatly for the topography, depending on how many clear stripes were imaged. For this reason, the

errors have been quoted individually, and vary from less than 1m up to 6m. The two samples which are near to each other in the boule (3146#42 and #45), have very similar radii of curvature in the two orthogonal directions which provides evidence of consistency. Quite a range of curvatures are represented here, and there is no clear trend. If the values from diffraction are averaged for the LEC and VGF wafers, they give 18.7m for the former and 21.0m for the latter, compared with the equivalent averages from topography of 13.6m and 24.0m. Both of these give a higher value of curvature, and therefore a less strained wafer, under the VGF technique. As only two of the samples, 4028#2 and 3145#38, were observed to contain dislocations, it is hard to relate the radius of curvature to dislocation density within the wafer.

It is possible to conclude that on average VGF growth produces a wafer which is less strained than with LEC. The FWHM of the LEC crystals was in general smaller than in the VGF, which is reasonable if it is considered that the JE wafers used here are of exceedingly high quality at the crystal centre, as seen in Section 4.3, which is where the scans were taken. Both LEC and VGF were capable of providing uniformly curved wafers, with a corresponding FWHM profile. Both techniques also provided examples of the FWHM being dominated by crystal imperfections so deviating from the curvature pattern. The curvature and residual strain in these wafers could be investigated using triple axis diffraction techniques. In particular, an XY plot of θ-2θ (mapping only strains) and θ (mapping only tilts) through an analyser crystal compared to a topograph taken at the same point would be of great interest.

4.6 : Triple Axis Diffraction Measurements

The topography results described in sections 4.3 and 4.4 have shown that there is a variation in the dislocation distribution within the InP wafers, which is dependent on the growth technique employed. Further information can be obtained by mapping a small part of the sample in reciprocal space, using a triple axis scan. In this way, contributions to the x-ray diffracted intensity can be resolved into those due to dilations within the lattice, and those due to tilted regions of the lattice. The theory behind a triple axis scan, and experimental conditions, have been discussed in Section 3.4. As

changing the angle of incidence allows the depth of crystal sampled to be varied, both symmetric 004 reflections and asymmetric 224 reflections have been employed.

4.6.1 : Symmetric 004 Space Mapping

The symmetric 004 scans were taken on a Bede D3 diffractometer with a duMond monochromator using the symmetrically cut channels. This gives an angular divergence of 5 arc seconds and a wavelength dispersion of $\delta\lambda/\lambda = 5.5\text{x}10^{-5}$. A four reflection 111 Si analyser crystal was used. The wavelength was $\text{CuK}\alpha_1$ which gives an intrinsic 004 rocking curve minimum of 6.7" for InP. Scans were taken by incrementing the value of 2θ (the sample and detector axis coupled in a ration of 2:1) and scanning θ (the sample axis). Step sizes varied between 2" and 8", with an average count time of 2s per point. For all the scans, the crystals were positioned with the beam incident along the $<01\bar{1}>$ direction. The scans were transformed into reciprocal space using the convention of Iiada and Kohra [37], outlined in Section 3.4.1, using the Bede Contour program. This automatically places the highest point in the scan onto the position (0,0) in the plot. The contours have been gridded within the Golden Software Surfer plotting package.

The 004 reciprocal space maps are shown in Figs 4.29, 4.30 and 4.31. In all cases, the contours are natural logarithms, so in terms of counts per second they represent 1, 2.72, 7.39, 20.09 etc. As the background is quite high in these scans (in excess of 1c.p.s.), the minimum contour plotted in all cases is 2.72 c.p.s.. Although some information on the diffuse scatter is lost, this is inevitable with high background. The high background is attributed to air scatter which is coming over the analyser crystal, rather than through it [38]. As the volume of reciprocal space scanned varied between samples, all the plots (with the exception of 3146#42) are shown with the same scale on the axes, with one unit corresponding to half an inch. This facilitates comparison between the level of scatter on each map.

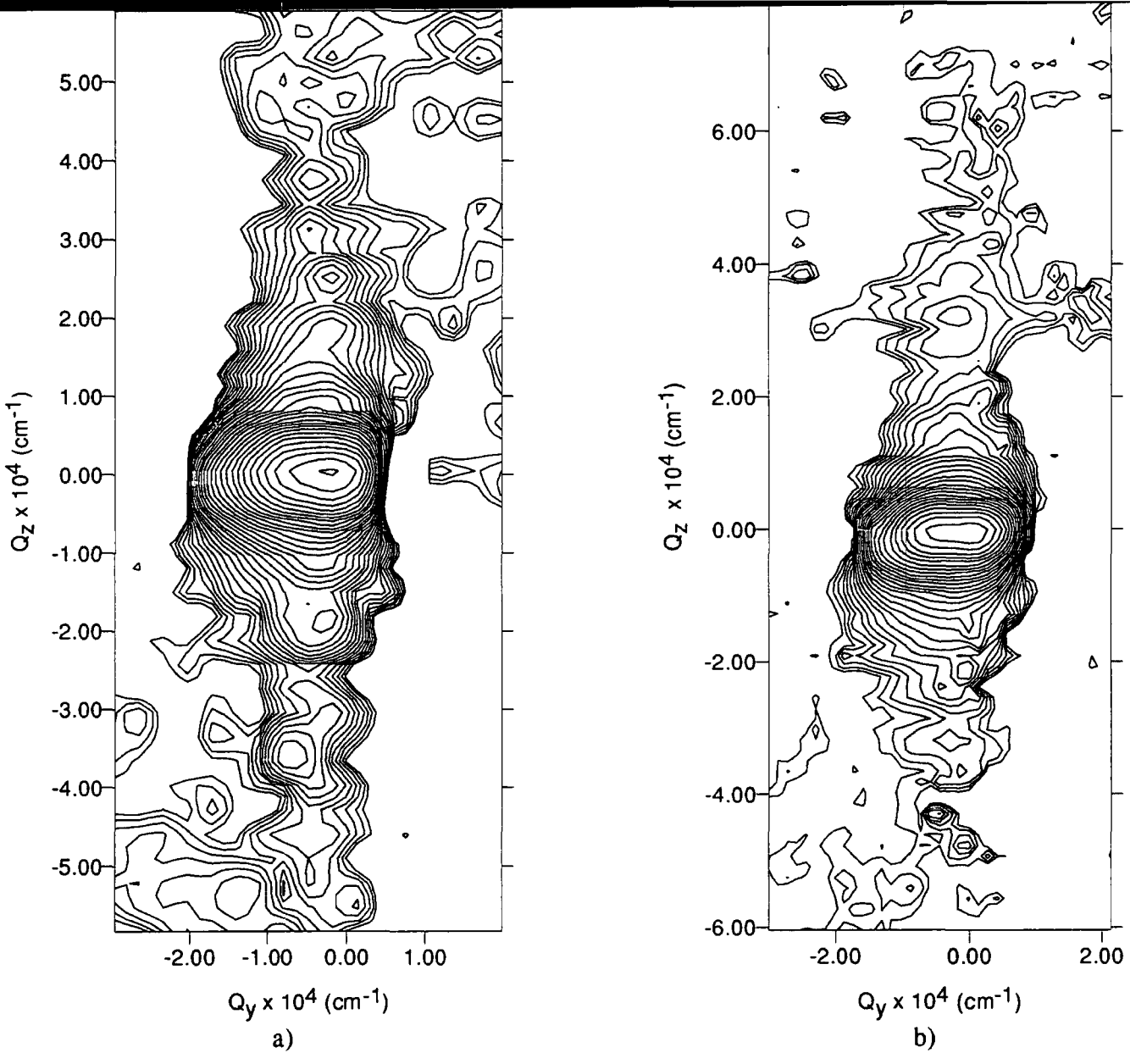

Fig 4.29 : Symmetric reciprocal lattice maps of a) 4023#4 - MCPWT LEC and b) 3146#42 - MCPWT/AT&T

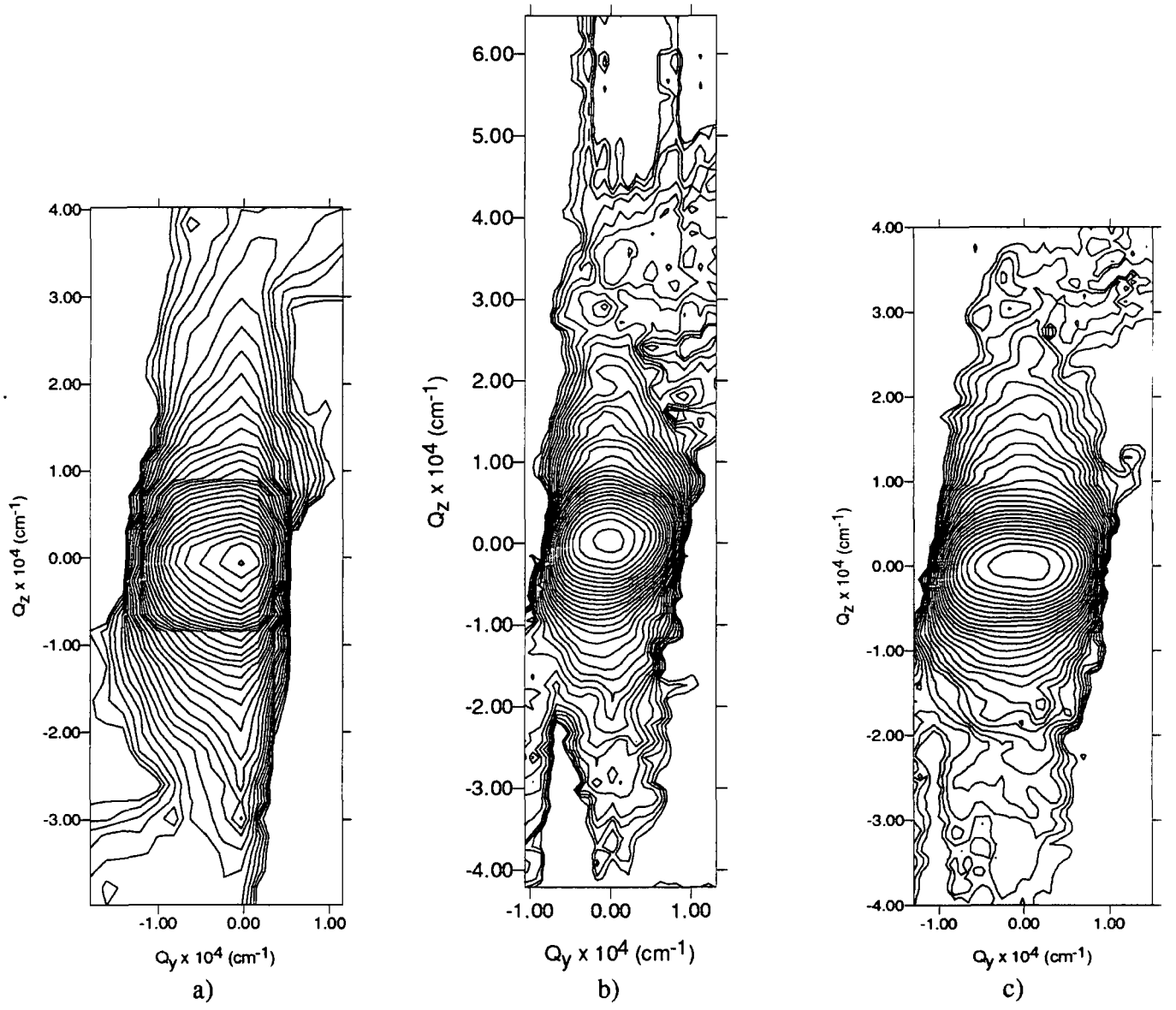

Fig 4.30 : Symmetric reciprocal lattice maps - a) 4020#6 - JE LEC, b) 4047#5 - AXT VGF, c) 3145#38 - MCPWT/AT&T

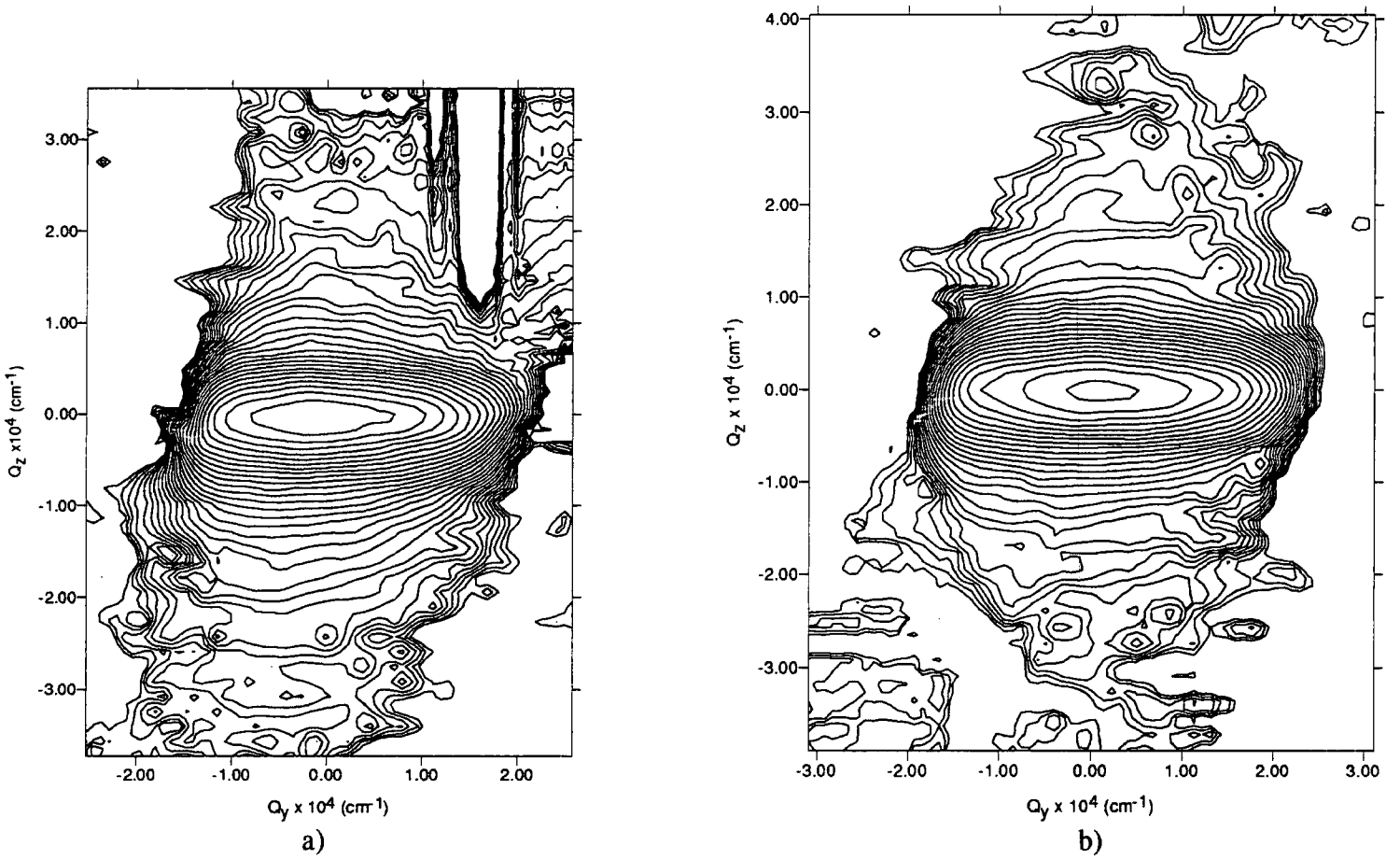

Fig 4.31 : Symmetric reciprocal space maps - a) 3146#45 - MCPWT/AT&T VGF, b) 3154#36 - MCPWT/AT&T VGF

Several features are similar in all the space maps. The level of diffuse scatter is generally low, and the dynamical diffraction surface streak can be seen in all cases. No pronounced monochromator or analyser streaks are evident, although a slight monochromator streak is sometimes visible. The data presented is unsmoothed, so some fluctuations at low count rates are seen. All the scans are symmetric about $Q_z = 0$, so there are no resolvable compressive or tensile strains in the InP lattices. Very similar values of FWHM in the Q_z direction are obtained for all samples, which is discussed in full in Section 4.7. Variations in the symmetry about $Q_y = 0$ are present, and will be discussed below.

Two of the samples, in Fig 4.30 b) and c) give a very symmetric distribution about $Q_y=0$, which corresponds to tilt distributions. There is no preferred tilt direction in these cases, and the absence of an asymmetry in the tilt confirms the system alignment. A slight asymmetry is observed for scans in Figs 4.29b), 4.31a) and b). The most obvious examples of a tilt q-dependence are shown in Fig 4.29a) and 4.30a). In both these cases the tilts are mainly distributed on the low Q_y side, corresponding to smaller incident angles. It should be noted that the two samples which display the strongest tilt asymmetry are both grown by LEC, the only two representatives of this technique in this particular study. Let us now compare the maps in terms of the growth technique and manufacturer involved.

The only two LEC samples, as already mentioned, are 4020#6 and 4023#4. The first of these is manufactured by Japan Energy (JE), and was shown in the topography sections to contain some dislocations at the periphery of the wafer, and some dark defects. The sample has been repolished, and shows evidence of large scale scratches. Despite the asymmetry in tilt to the low angle side, the Bragg peak is narrow in this sample, and quite a sharp dynamical streak is present. The other LEC sample, 4023#4, manufactured by MCPWT, also contains some dislocations (from topographical results), and has both a larger Q_y FWHM and a greater spread in diffuse scatter around the lattice point than the JE sample. As these two samples contain a significant number of dislocations the tilt effect may be caused by dislocations within the crystal, whose strain perpendicular to the surface is not resolved in the scans. It may also be caused

by the sample being figured, with most of the sample diffracting at a high-angle tilt position. Specular scans from reflectivity analysis provide more information, as discussed in Section 4.7.

All the other samples shown were grown using VGF. The first, Fig 4.30b) is manufactured by AXT, and shows a spherical distribution of intensity around the 004 reciprocal lattice point. The scatter is not extensive, and a dynamical streak is still visible. In fact the scatter in the Q_y direction extends over a smaller region of reciprocal space than in any other sample. All the other crystals were manufactured by MCPWT/AT&T, using the VGF technique. It is hard to compare the extent of the dynamical streak as not all of the scatter is imaged. An obvious difference in the tilt component is present, however. All the samples show an oval peak, with the scattering being dominated by tilts. In the case of 3145#38 and 3146#42, the scattering extends over a similar range as in the LEC samples, but with no marked asymmetry in the tilt distribution. Sample 3145#38 has been shown to contain some dislocations, and has a fractionally higher strain distribution than 3146#42, which is virtually dislocation free. The largest difference is shown in samples 3146#45 and 3154#36, which demonstrate a large tilt component, and little dynamical streak. The absence of data in one section of the graph of 3146#45 is attributed to a software error, as a row of zeros were collected in the data. No dislocations have been observed in these two samples with high tilt components, and one (3146#45) even comes from the same boule as a much lower tilt sample (3146#42). The presence of a large tilt component in the absence of any imaged dislocations may be due to the polishing process, a discussion of which forms Section 4.7. As surface effects may be attributable for the patterns shown here, asymmetric scans, which are more sensitive to kinematical scattering from the top surface were employed.

4.6.2 : Asymmetric 224 space mapping

The asymmetric 224 scans were taken using the Bede 200 Diffractometer, as described in Section 3.4.4. A Ge 111 monochromator crystal was used, together with a four bounce 220 symmetrically cut Si analyser crystal. $CuK\alpha_1$ radiation was used, which gives an angular divergence of 16" and a wavelength dispersion of 3×10^{-4}. The

measurements were taken by stepping the angle of the analyser crystal and sample coupled, and scanning the sample (θ) axis. A geometry of glancing incidence was used, which gives an incident angle of less than 5°. The beam was incident along the $<0\bar{1}1>$ direction. If the extinction and absorption lengths within the crystal are calculated, the values in Table 4.5 are obtained.

Table 4.5 : Factors dominating penetration depth

	004	**224**
Extinction Depth /μm	8.0	10.1
Absorption Depth /μm	9.6	1.5

The extinction depth in this case is determined by the dynamical formula given in Section 2.3.4, and the absorption from the kinematical case, in Section 2.2.3. Whereas in the 004 case the depths are similar, with extinction determining the depth penetrated at the rocking curve maximum, the 224 reflection is dominated by absorption effects, with the x-rays penetrating to only 1.5μm.

The asymmetric scans are shown in Figs 4.32-36. These have been converted to reciprocal space using Bede's Contour for Windows (β test), and the integral plotting package. In this case the maximum peak intensity has not been positioned at zero. The colour scale is shown, where the bands are logarithmic, and are the same for each plot. They have been plotted within a square of 10 x 10 in order to scale them in the same way.

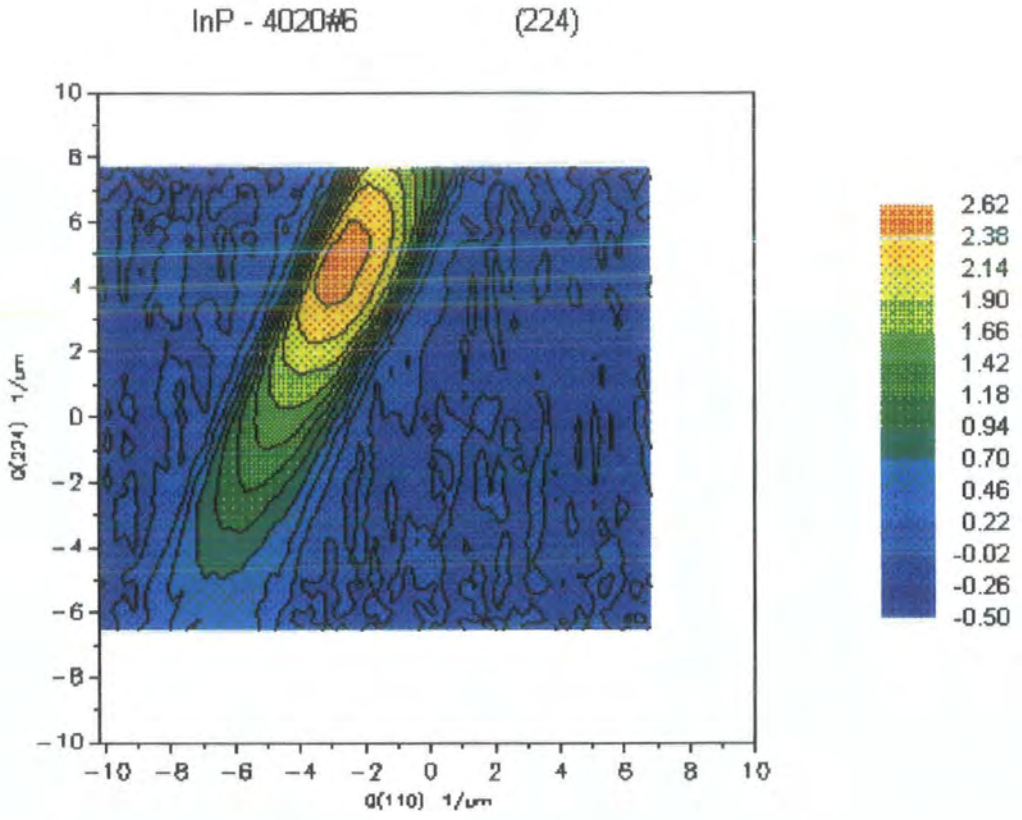

Fig 4.32 : Asymmetric scan for 4020#6

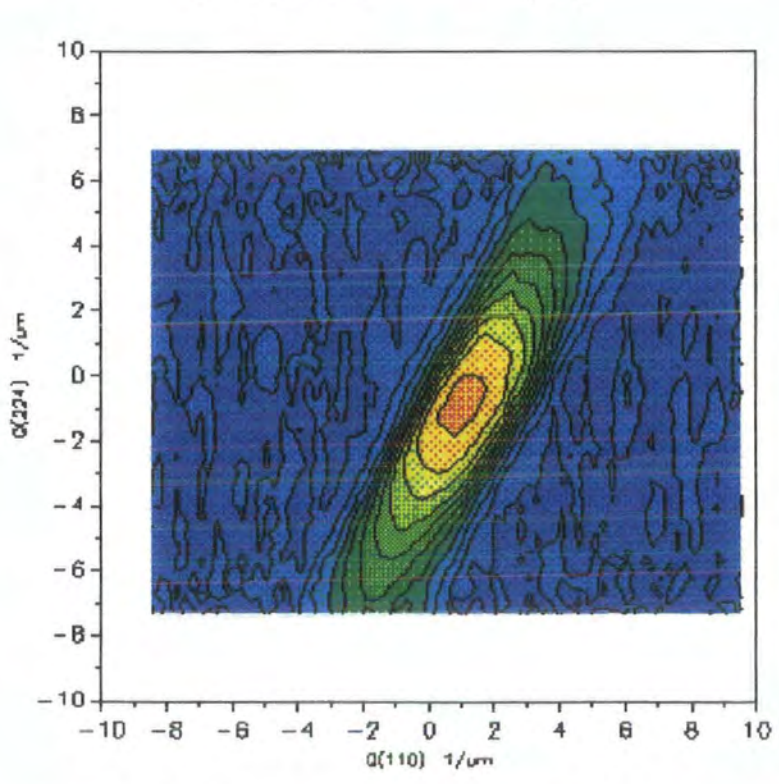

Fig 4.33 : Asymmetric scan for 3154#36

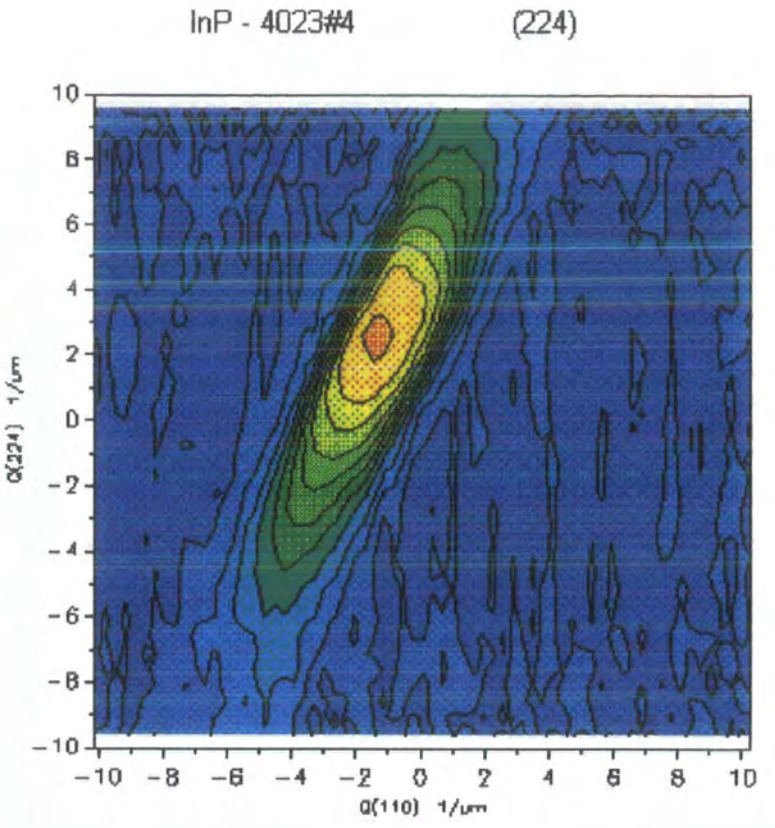

Fig 4.34 : Asymmetric scan for 4023#4

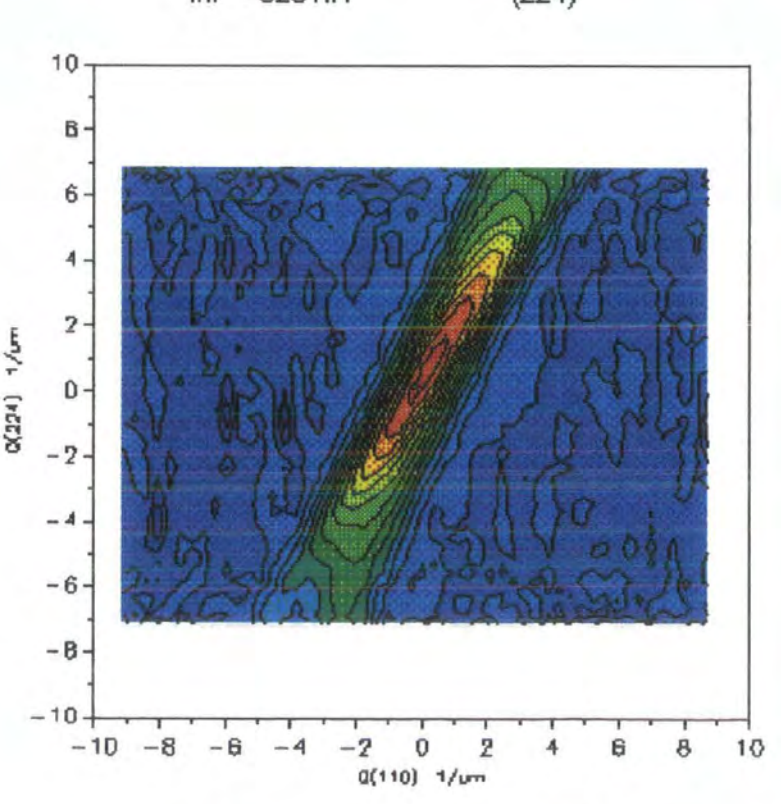

Fig 4.35 : Asymmetric scan for 3231#1

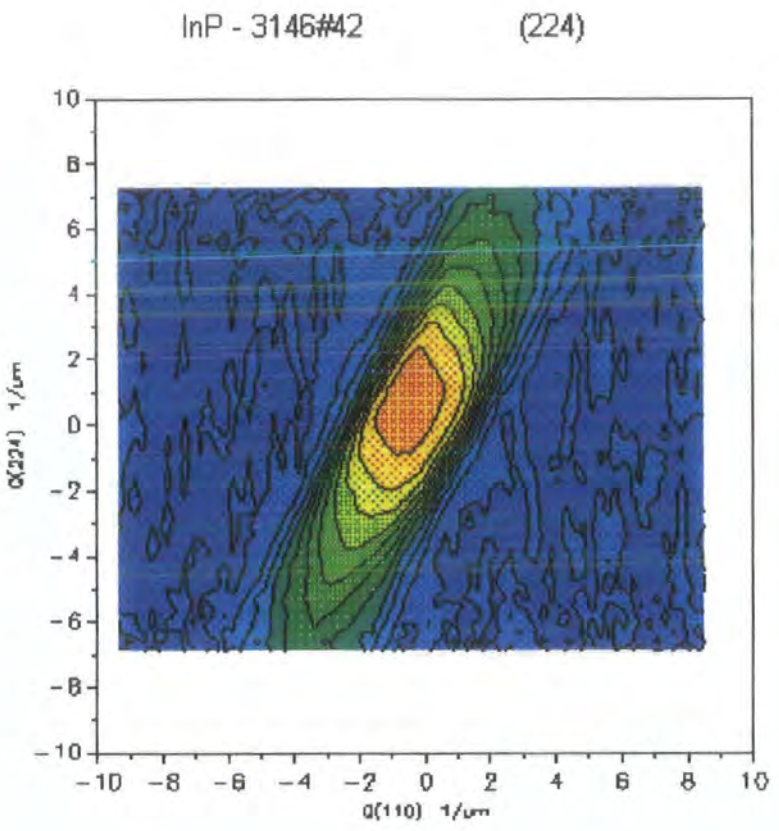

Fig 4.36 : Asymmetric scan for 3146#42

A similar amount of diffuse scatter is seen in each map, with a slight increase for sample 3231#1. They all show a strong dynamical streak, which extends to the edge of reciprocal space sampled. It is interesting to note that the tilt asymmetry noted in the symmetric scans is also present here, with samples 4020#6, 4023#4 being quite strongly asymmetric, 3154#36 and 3146#42 being very slightly asymmetric and the previously unscanned 3231#1 being symmetric. In addition, where the tilt distribution tended to be highest on the low Q_y side in the symmetric case, it is now noted to be on the high Q_y side. This is simply explained by the geometry of diffraction. In the symmetric case the x-ray beam was incident along $<0\bar{1}1>$ but in the symmetric case it was in the opposite direction, along the $<0\bar{1}\bar{1}>$. This is further evidence to suggest that the tilts observed here are real rather than artefacts of the experimental arrangement.

The tilt distribution varies between samples, with the lowest being observed in 3231#1. This sample, grown by LEC, gives the highest diffracted intensity, and an extremely

low tilt distribution. The tilt asymmetry is obviously not peculiar to LEC wafers as this is symmetric. This emphasises the quality of JE wafers, as the narrowest peaks are found in both the symmetric and asymmetric cases. The repolished JE sample, 4020#6, shows a larger tilt distribution in the asymmetric case, which is believed to be related to surface damage introduced in the refinishing process.

4.7 : Polishing Studies Using Triple Axis Diffraction and Grazing Incidence X-Ray Scattering

4.7.1 : Introduction to Polishing

In all advanced semiconductor processing, the quality of substrate material is of crucial importance and through large investment in crystal growth technology there has been an impressive fall in defect density with time. However, the polishing of wafers for epitaxy remains a closely guarded art. Vendors provide data on flatness and a qualitative measure in terms of haze visible optically after etching, but non-destructive techniques for incoming quality assurance are far from universally established.

There are several reasons for polishing substrates, which depend on the final use of the material. When the semiconductor is sawed after growth deep structural defects are introduced, which are removed in the lapping process. Lapping involves a plate being placed on top of the sample and depressed while rotating. As a suspension of particles is introduced in between plate and sample, segments of substrate are ripped out, so removing the majority of large-scale damage, but introducing more superficial damage. The action of polishing is to remove the (lesser) damage introduced by lapping and produce a damage free, flat, specular surface. By preferentially etching crystal planes, polishing may be used to study the defect structure of semiconductors, as dislocations produce etch pits at the point of intersection with the surface. There are two components to most polishing techniques used currently, i.e. mechanical and chemical. Mechanical polishing is a fracture process where the surface is in contact with a fluid suspension of small particles which are highly resistant to deformation, such as diamond or alumina. This leads to flat surfaces, but with a large amount of sub-surface

damage. Chemical polishes such as bromine in methanol (Br_2/MeOH) produce a surface which is damage-free but often not flat [39]. As photolithographic processes require a substrate flat enough to keep optical projection in focus at all points of the wafer surface [40], wafer flatness is becoming increasingly important as device dimensions decrease. A combined technique of chemo-mechanical polishing is therefore frequently employed.

A typical polishing process for InP is shown in Fig 4.37, where a Br_2/MeOH polish is being used [41, 42]. The InP wafer is in contact with a polishing pad saturated with the chemical polish. An oxidation reaction occurs at the etching surface in which bromine is depleted. The rate of reaction, therefore, is limited by the rate of diffusion of bromine to the reaction area. If the etch were free, the finished surface would be the same as initially. In a chemo-mechanical polisher, however, the crystal is mounted on a block which is in motion over the pad. Polishing, therefore, occurs due to contact between the substrate and pad causing turbulence at the high points on the surface. This means bromine can reach the area easily and the etch rate increases. Also, hydrodynamic forces are greatest at the contact points, so an increase in the viscosity of the polishing medium results. This causes an increase in frictional forces, and hence in temperature which leads to higher diffusion rates and faster polishing. High points, therefore, are preferentially etched and a flat surface is produced. In this case the pad is the only mechanical abrasive. Non-contact polishing methods are possible, where the sample is suspended on a layer of etch solution above a rotating polish pad [43, 44], but traditional contact rotary polishing is more common in mass production.

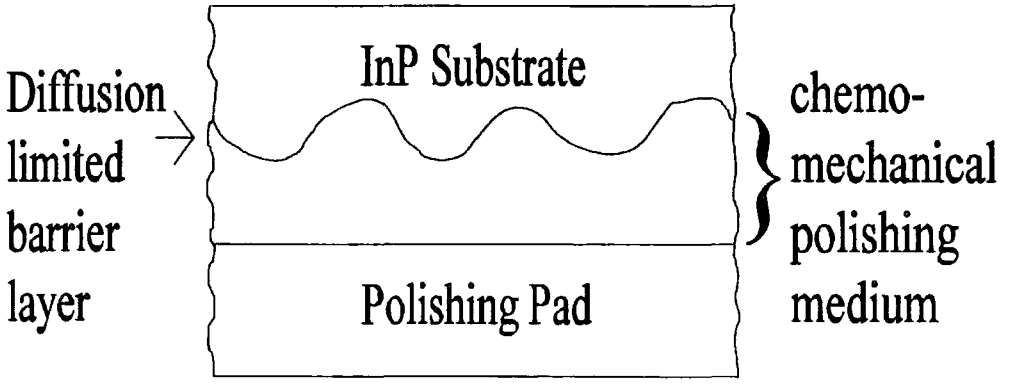

Fig 4.37 : A schematic diagram of the mechanochemical polishing process

Polishing techniques for InP have not as yet been fully optimised and several unwelcome effects can occur. These include orange-peel effect which is maybe due to inhomogeneities in the polishing process over a surface [45]. Circles emanating from the core can result from dopant inhomogeneity, as this leads to differential polishing rates [46]. An uneven distribution of mounting wax results in mounted wafers being strained, leading to local elastic deformation when the wafers are removed. All these, together with surface and sub-surface damage to the crystal structure, make the investigation of polishing effects useful to the semiconductor industry. This is reflected in the number of techniques which have been employed, such as x-ray topography [47], optical techniques [46], photoluminescence [48], grazing incidence diffraction (GIXD) [49], inclined Bragg plane x-ray diffraction (IBXD) [49] as well as the high resolution x-ray diffraction (HRXRD) and grazing incidence x-ray scattering (GIXS) described here .

HRXRD has been proved to be sensitive to different polishing methods by study of the diffuse scatter generated by crystal imperfections and surface roughness. Matyi and colleagues at the University of Wisconsin used absolute lattice parameter measurements [49] and triple axis x-ray diffractometry [50] to show changes in GaAs surface structure polished under differing conditions of speed and pressure. The effects of polishing can be seen in Fig 4.38. A mechanically lapped sample is shown in Fig 4.38a) where the intense diffuse scatter associated with this process is visible. The same substrate is then polished with bromine methanol solution giving the reciprocal space map in Fig 4.38b). The reduction in diffuse scatter is clearly visible. Although the differences in maps between different polishing techniques are less obvious, quantitative results show clear trends, which will be demonstrated here.

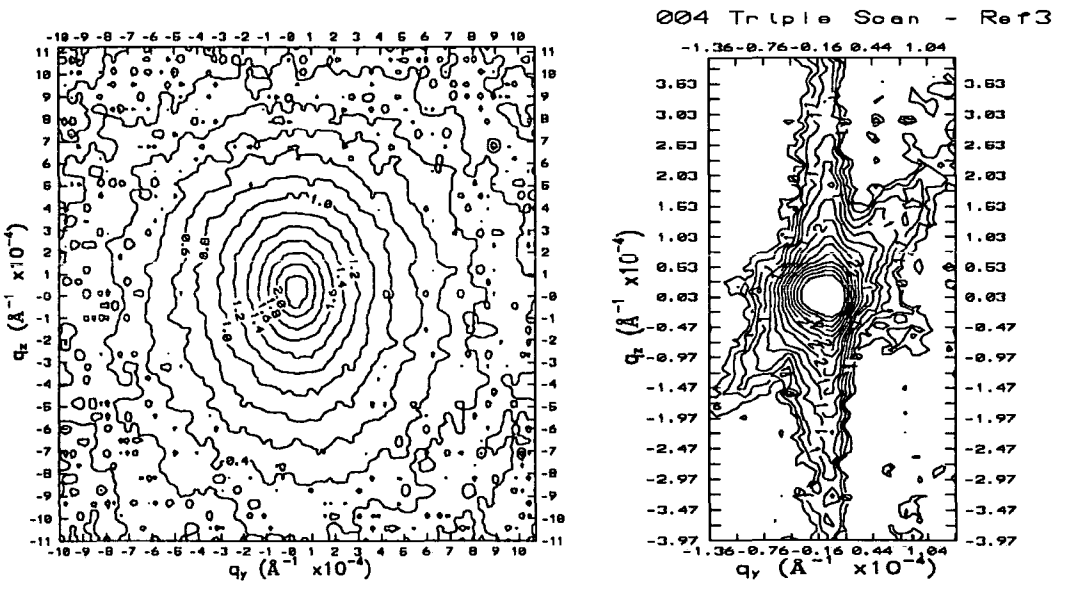

Fig 4.38 : Reciprocal space maps of (a) a lapped and (b) a bromine methanol polished GaAs substrate. The lines shown are equi-intensity contours on a logarithmic scale. The axes are q_y and q_z in units of $Å^{-1}$ x 10^{-4}, which are orthogonal directions in reciprocal space and perpendicular and parallel to the reciprocal lattice vector respectively. Data taken by I.Pape (U. of Durham).

4.7.2 : InP Triple Axis Diffraction

Triple axis diffraction is useful in this study as it allows us to separate the effect of crystal tilts and dilations, as has been described in Section 3.4. In this case, triple axis scans were taken on a Bede D3 diffractometer for the 004 reflections, and a D200 diffractometer for the 224 reflections, and the data obtained has been fitted to Gaussians to obtain the FWHM. The full width at fiftieth maximum (FW1/50M) has been measured directly. The errors on these FWHM are taken as the difference between the Gaussian fitted and the experimental curve at half the peak height. This means that an asymmetric peak will yield a larger error bar, as will a scan with poor counting statistics. The intrinsic FWHM value for the 004 scan is 6.7" and for the 224 scan is 17.8"(allowing for the different diffraction geometry of the two instruments). Visually the reciprocal space maps, shown in Section 4.5, are similar, but when the values obtained by this process are plotted, clear trends are obtained. In the diagrams below, the FWHM in the θ direction (corresponding to lattice tilts) is plotted along the

x axis, and the FWHM in the θ-2θ direction (corresponding to lattice dilations) is plotted along the y axis. Each cross represents a separate sample, and they are identified by the letters shown in Table 4.6.

Table 4.6 : The samples represented in Figs 4.39 and 4.40

A	LEC Refinished wafer - 4020#6	JE
B	VGF - 4047#5	AXT
C	VGF - 3145#38	MCPWT/AT+T
D	LEC - 4023#4	MCPWT
E	VGF - 3146#42	MCPWT/AT+T
F	VGF - 3154#36	MCPWT/AT+T
G	VGF - 3146#45	MCPWT/AT+T
H	LEC Standard wafer - 3231#1	JE

Fig 4.39 shows the FWHM and FW1/50M of the θ and θ-2θ scans using the surface symmetric 004 reflection. It can be seen that the value of FWHM and FW1/50M in the θ direction varies significantly, by up to a factor of six, whereas the values for the θ-2θ scans, stay constant within the error bars of the experiment. This shows that polishing affects the distribution of tilts, but leaves the distribution of the strain component normal to the surface constant. It can be seen that the two crystals from the same boule E and G have different values of θ FWHM and FW1/50M. These were only three wafers apart in the boule so the differences between them are largely due to the lapping and polishing procedures, rather than from the crystal perfection. Two growth techniques are represented here, as samples A, D and H are grown by LEC and the others by VGF. As both fit the trend, it can be inferred that the technique is independent of growth conditions. Sample A was manufactured by Japan Energy (JE), which gives the lowest tilt distribution. Although this sample is LEC, topographs (Section 4.3) showed a low dislocation distribution, but large scratches. As the beam footprint is about 1mm x 2mm, the x-rays see the areas of good quality but not the scratches. Sample B is made by AXT who produce good quality VGF GaAs crystals, so were expected to manufacture VGF InP quite well. All the others (C-G) are made by MCPWT or MCPWT in connection with AT+T. The values for the FW1/50M, which are sensitive to the tails of the Bragg peak, follow the same trends as the FWHM.

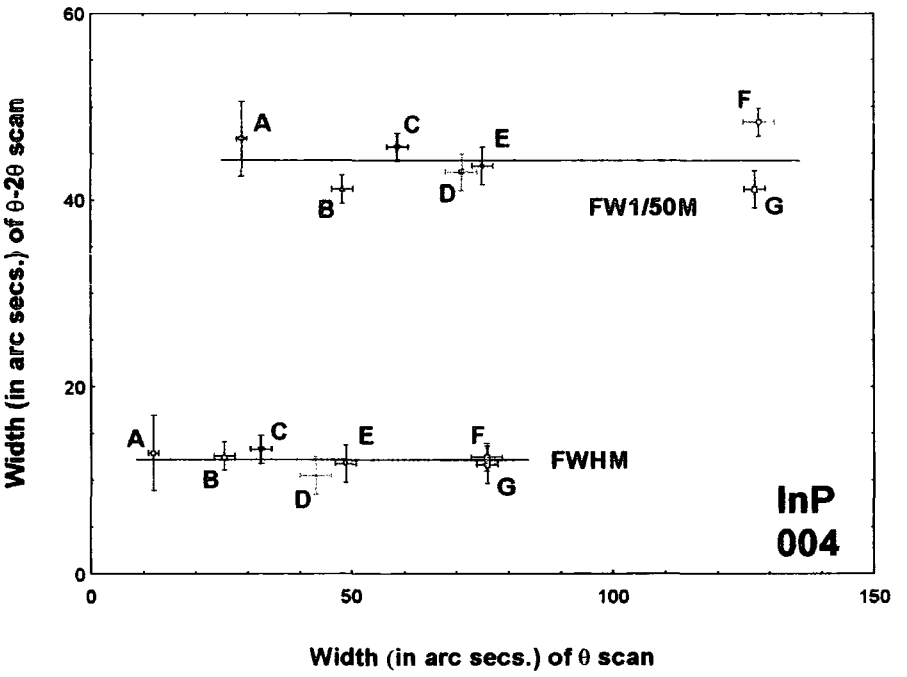

Fig 4.39 : FWHM and FW1/50M for the θ and θ-2θ scans from the samples studied for the 004 surface symmetric reflection.

The 224 reflections are sensitive to both in-plane and out-of-plane strains and also probe a smaller depth below the surface than the 004 reflections. If the extinction depths and absorption lengths perpendicular to the crystal surface are calculated, the 004 reflection is seen to be extinction limited, with a depth of 8.0μm, while in the asymmetric 224 case, the penetration is dominated by absorption, with a depth of 1.5μm. This makes the 224 scans far more sensitive to surface effects. Fig 4.40 shows the data for these asymmetric reflections. It can be seen that in this case there are variations in both tilt and strain between the samples. The sample with the lowest tilt is H, which is again a JE sample, which was not available for measurement in the symmetric case. It should be noted that the θ-2θ FWHM and FW1/50M values of the two InP samples which differ from the rest show the largest distribution of tilts, which implies that the constancy of the in-plane strain distribution cannot be guaranteed to hold over a wide range of polishing conditions.

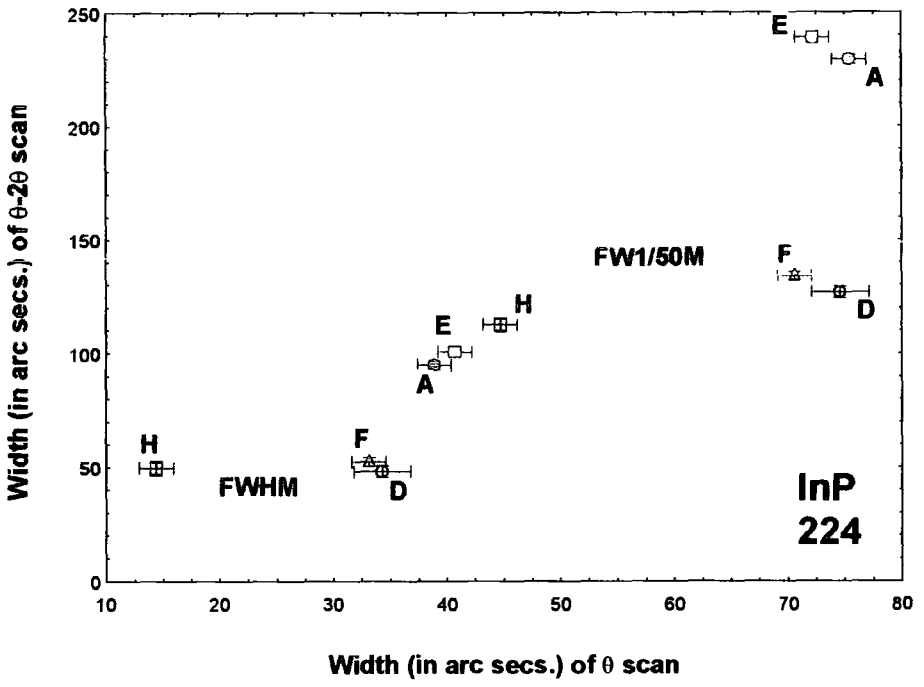

Fig 4.40 : FWHM and FW1/50M for the θ and θ-2θ scans from the samples studied for the 224 surface asymmetric reflection with grazing incidence.

The absence of strain and the presence of a distribution of tilts in the near surface layer could be interpreted in one of two ways. A possible model could be of low angle boundaries consisting of rows of edge dislocations between small mosaic blocks of otherwise perfect material. For low dislocation density, such boundaries give rise only to tilt and have no associated long range strains. These edge dislocations would presumably propagate by fast climb and correspond to relaxed microcracks extending from the surface into the material being polished. The asymmetric X-ray data show that within the top micron of material there is a change in the strain distribution as well as the tilt as a result of polishing technique. As this is not evident in the symmetric scans, this implies a change in lattice parameter parallel to the surface in the very near surface region, which would be consistent with the microcracks being forced open by debris at the surface. As the probe depth of the two reflections differs, the measured tilt distribution averaged over these depths may well differ. For example, the sample of InP which has been repolished, labelled A, has the lowest tilt distribution measured in

the symmetric reflection, but one of the highest tilt and strain distributions from the asymmetric reflection.

The second model which could give rise only to a tilt distribution is one of material removed by the abrasive being redeposited epitaxially in unstrained mosaic blocks. While there is evidence from transmission electron microscopy and X-ray reflectivity for a redeposited surface layer, it is only a few nanometres in thickness and even if epitaxial would not give sufficient signal averaged over the micrometre length scale of the X-ray experiments here. However, the two processes are not incompatible and propagation of microcracks beneath the abrasive particles, followed by subsequent removal and partial redeposition is still consistent with the X-ray diffraction data. No information is available on the InP polishing processes used in this study, but successful chemical polishes for InP include one part HCl with one part HNO_3, or 0.4N solution of $FeCl_3$ in HCl [39]. However, companies such as Logitech regularly use bromine moderated by methanol and ethylene glycol in order to achieve surface flatness below 10 nm. Complementary studies on GaAs crystals polished by different methods show that bromine based polishes provide a large distribution of tilts [51], which is in agreement with the observations made here.

This study, together with the independent work of I.Pape [52] on GaAs, has shown that high resolution triple axis diffraction can be used to assess the polishing of compound semiconductors by separating the effects of lattice tilts and dilations. As the variations were confined to the θ direction for symmetric scans, a single specimen-only scan in the triple axis geometry provides a powerful and rapid method for incoming wafer screening prior to growth of epitaxial layers.

4.7.3 : InP Grazing Incidence X-Ray Scattering

As the polishing procedure has been observed to affect the near surface and slightly deeper part of the crystal differently, the use of grazing incidence x-ray scattering should yield more information on the polishing process. This would also allow the results of the two techniques to be compared, which is in itself a useful and novel

exercise. Reflectivity experiments on the same samples were therefore performed at Daresbury Laboratory, as described in Section 3.5.

The two types of scan performed were specular and diffuse scans (Section 3.5), which are shown here with the simulations to the data (Section 2.1). A specular scan of InP is shown in Fig 4.41, where the circles are the experimental data, and the line is the simulation. The increase in scatter visible above 4300" is characteristic of the presence of a surface layer with a density different from that of the substrate. In this particular case, a satisfactory fit could only be obtained by inclusion of two layers, with slightly differing densities. As In_2O_3 is denser than InP, having a density of 7.179 gcm^{-3} compared to 4.787 gcm^{-3}, these layers have been modelled as being mixtures of InP and In_2O_3. A substrate roughness of 5 Å was used, together with a 5.2Å layer of $InP_{(0.25)}In_2O_{3\ (0.75)}$ with a roughness of 2.7Å. This was capped by a 23.2Å layer of material only slightly denser than InP, with composition $InP_{(0.92)}In_2O_{3\ (0.08)}$. This layer has a roughness of 7.9Å. Fig 4.42 shows two diffuse scans taken at $2\theta = 1.2°$ and 1.5° and fitted using layer thickness and the effective roughness σ_{spec} determined from the specular reflectivity fit of Fig 4.41.

As seen in Table 4.7, the top surface effective roughness is dominated by compositional grading. The bottom interface between the oxide and pure InP was modelled with only compositional grading. The fractal parameter, h, used in Fig 4.42 is 0.5 and the lateral correlation length, ξ, is 700 Å. These are determined by fitting the shape and the Yoneda wing heights at the two angles. Fig 4.42 is plotted on a linear scale to show the sensitivity of the fit, and the same data are shown again in Fig 4.43 on a logarithmic scale. Here it can be seen that the specular peak is quite well fitted in the simulation provided that the specular peak is broadened in the simulation by increasing the beam divergence. As the data was taken at a synchrotron, the beam divergence is in reality very low, but this is equivalent to increasing the curvature of the sample. It can be seen, however, that the simulation loses its accuracy at the base of the specular peak. Simple figuring would lead to a Gaussian distribution of increased FWHM, so this indicates that more than one roughness length scale is present. The concentration of intensity under the specular peak can arise from different length scales of figuring or a very long correlation length component in the roughness. These two merge into one

another when the correlation length component is of the order of the X-ray coherence length.

Table 4.7 : Parameters used in the simulations.

		4047#5	3145#38	4023#4	3231#1	4020#6
h		0.7	0.5	0.5		
ξ in Å		75	450	700		
Substrate	Σ_g in Å	0.4	1.5	5		
	σ_{spec} in Å	0.4	1.5	5	6	2.5
1st Layer	Composition : InP	0.78	0.73	0.25	0.63	0.42
	: In_2O_3	0.22	0.27	0.75	0.37	0.58
	Thickness in Å	26.4	28.8	5.2	35	35.2
	σ_u in Å	5.2	1.58	0		
	σ_c in Å	0	0	1		
	Σ_g in Å	6.8	6.4	2.5		
	σ_{spec} in Å	8.6	6.65	2.7	5.65	7.2
2nd layer	Composition : InP			0.92		
	: In_2O_3			0.08		
	Thickness in Å			23.2		
	σ_u in Å			0		
	σ_c in Å			1.75		
	Σ_g in Å			7.7		
	σ_{spec} in Å			7.9		

The other samples could be fitted with a single oxide layer at the surface. An example is shown in Fig 4.44, where the bulk material (0.4Å roughness) is capped with a 26Å thick $InP_{(0.78)}In_2O_{3\ (0.22)}$ layer. The diffuse scans (Fig 4.45) show an increase in scatter at very low angle which is not replicated on the high angle side of the specular peak. We suggest this is an artefact from a geometrical source, probably a bending of the sample at the edge. The fractal parameter in this case is 0.7, and the correlation length is extremely short, at 75 Å. As a result of the short correlation length, the diffuse scatter is confined to higher q_y values, resulting in higher Yoneda wings and lower intensity close to the specular ridge. The fits to the third sample, 3145#38, shown in Figs 4.46 and 4.47 are very similar, with a layer of 29 Å thickness, whose roughness is largely from grading, but partly from uncorrelated roughness. This again has a fractal parameter of 0.5, but the correlation length lies between the other two, at 450 Å.

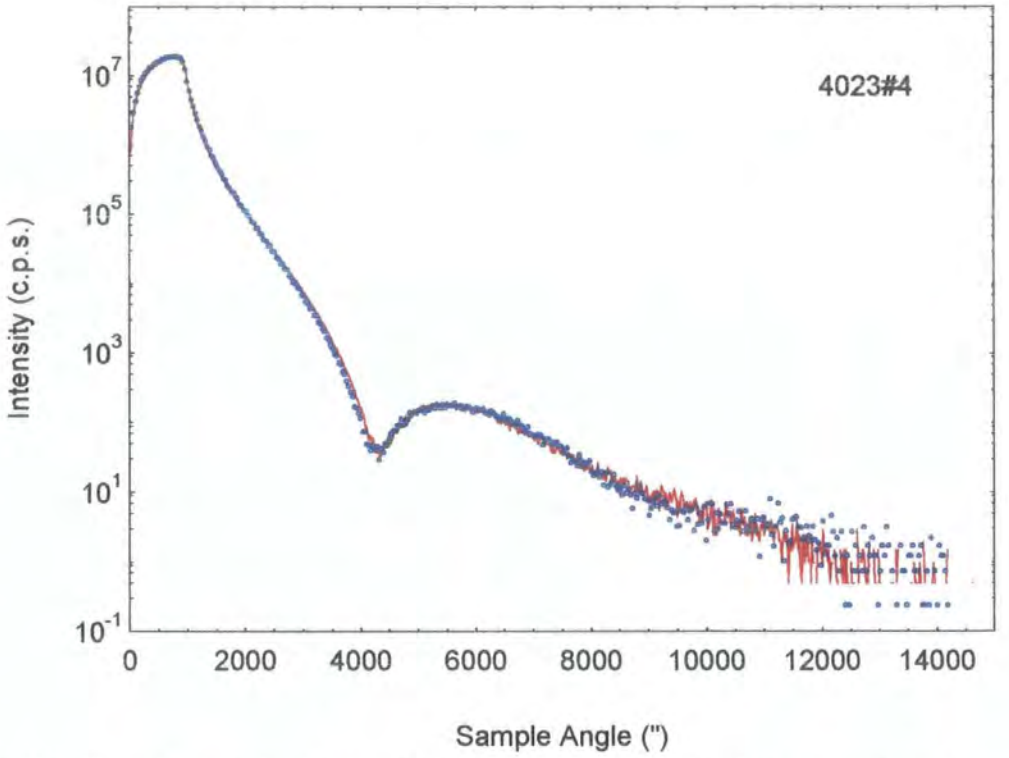

Fig 4.41 : Experimental (points) and simulated (solid curve) of the specular reflectivity

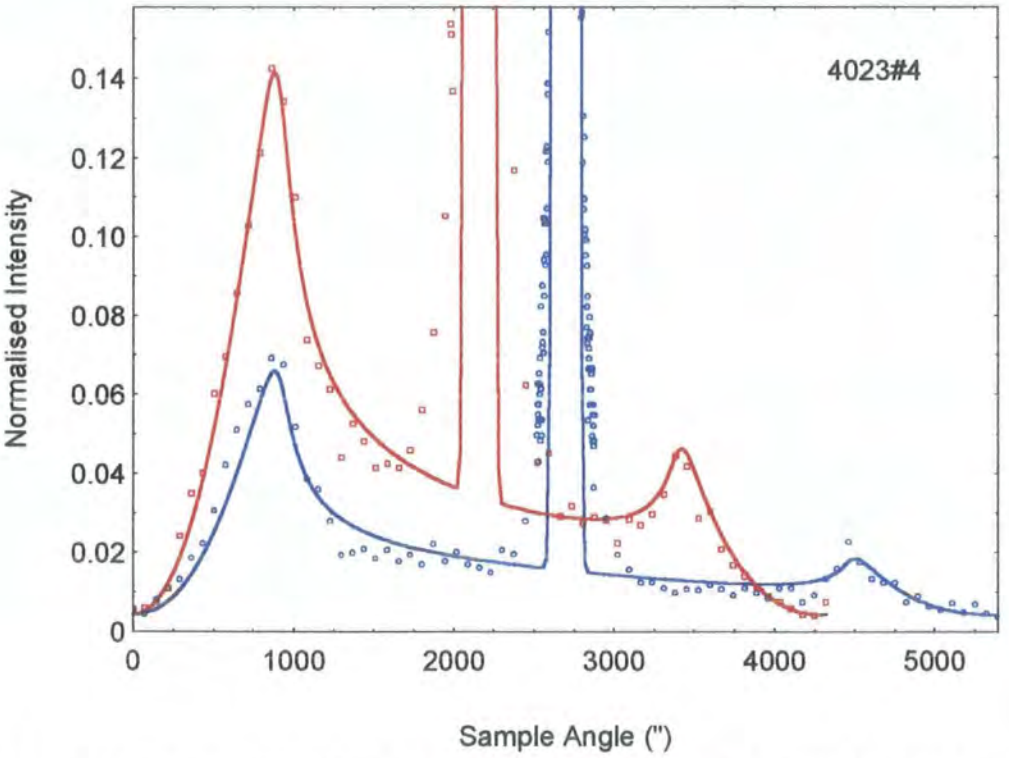

Fig 4.42 : Specimen-only diffuse scans for different scattering angles from the same sample as in Fig 4.41. Points are experimental data and solid lines are the best-fit simulations.

The specular scans of the standard and refinished sample are shown in Figs 4.48 and 4.49. A similar thickness of oxide layer is obtained in both cases, but the composition is changed, with the refinished wafer having a more dense surface layer. The substrate roughness is reduced on refinishing, but this may well be due to grading effects.

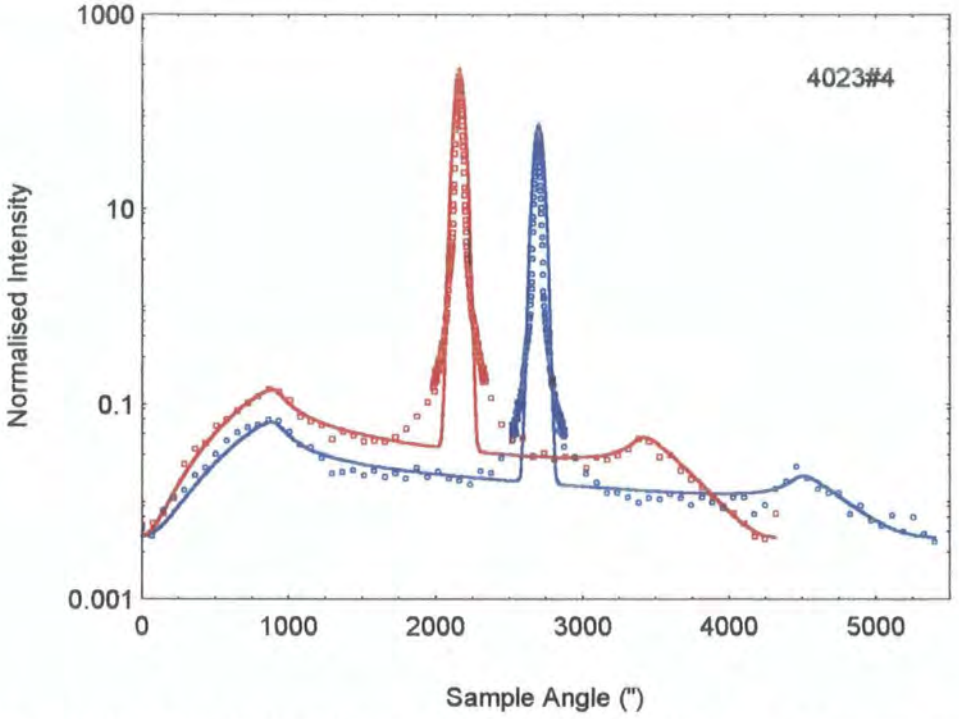

Fig 4.43 : Data of Fig 4.42 plotted on a logarithmic scale to show the presence of the tails in the specular peak.

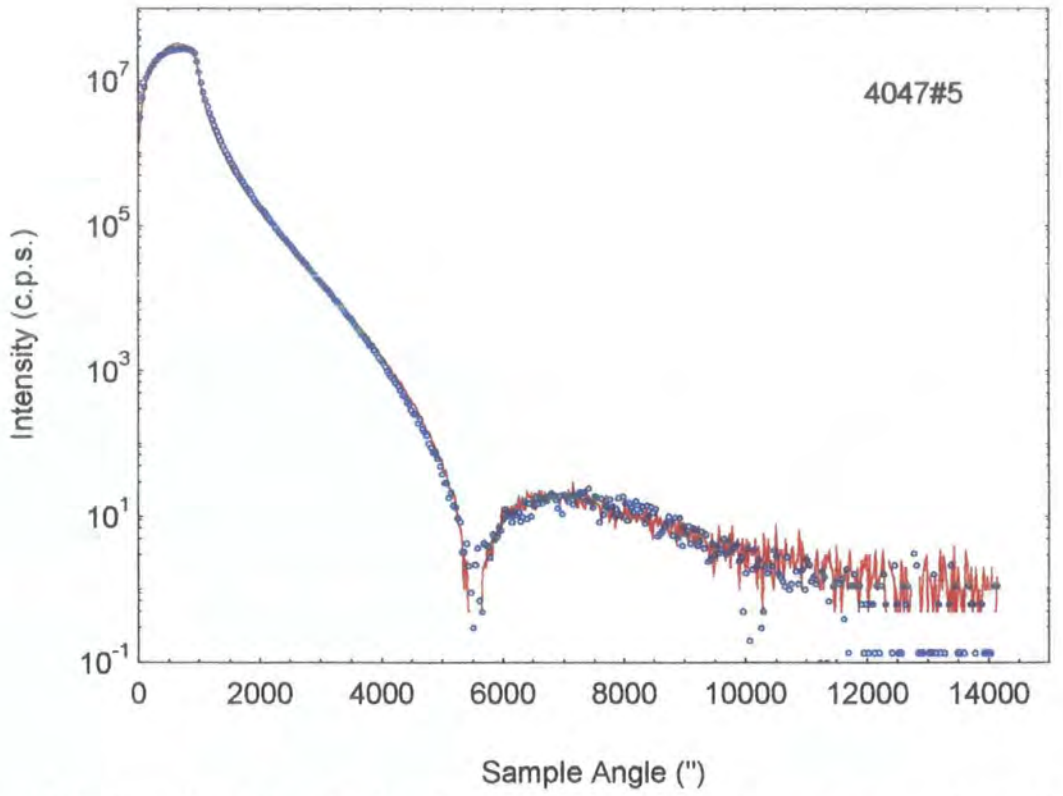

Fig 4.44 : Specular reflectivity data (points) fitted to a simulation using a single graded oxide layer at the surface

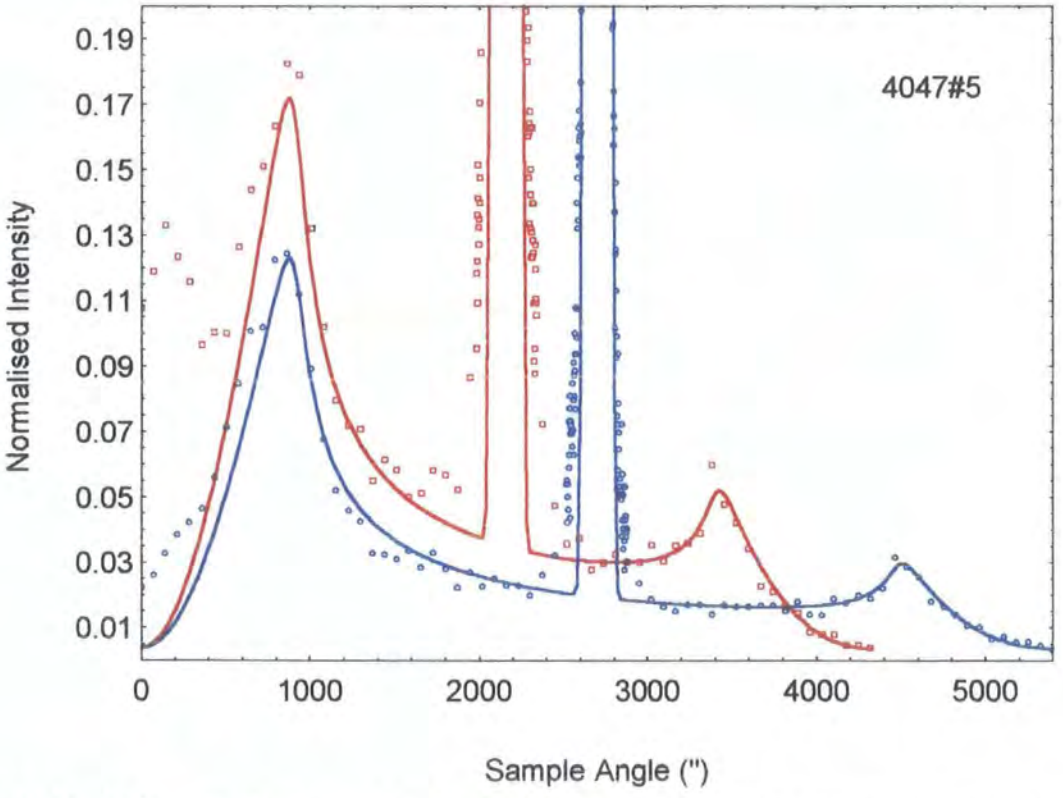

Fig 4.45 : Diffuse scatter (points) and simulations (solid lines) for the same sample as in Fig 4.44.

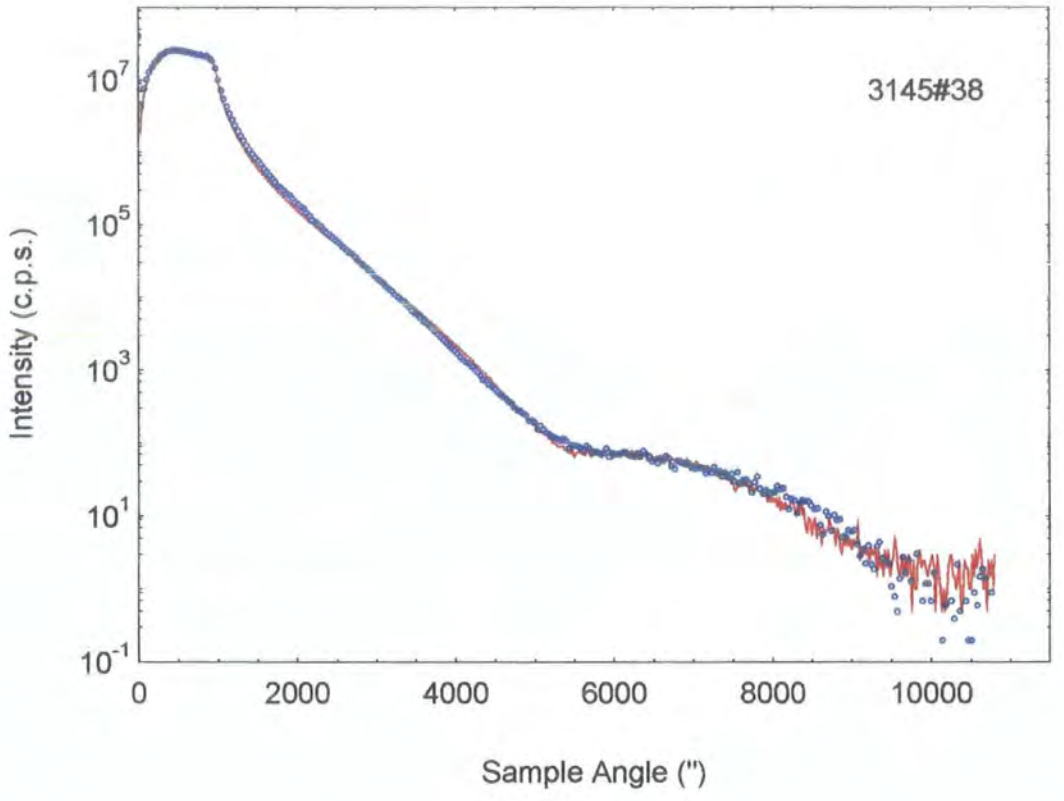

Fig 4.46 : Specular scan of a sample with a single oxide layer

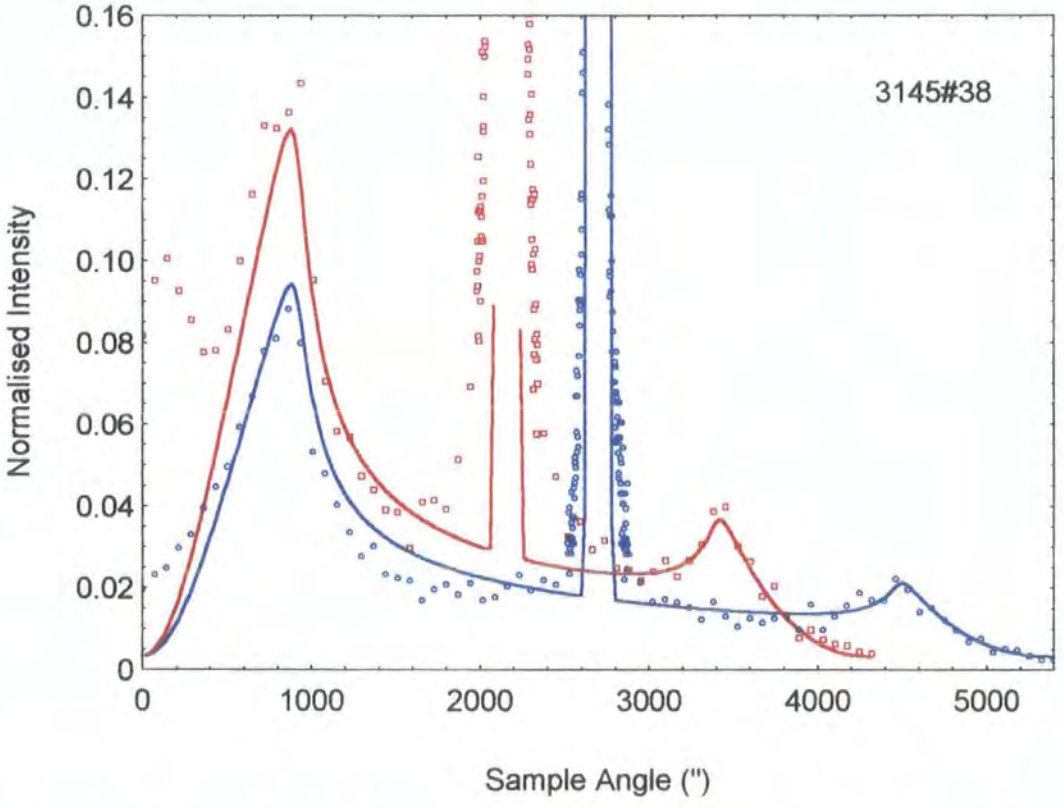

Fig 4.47 : Diffuse scans with simulation corresponding to the specular in Fig 4.46.

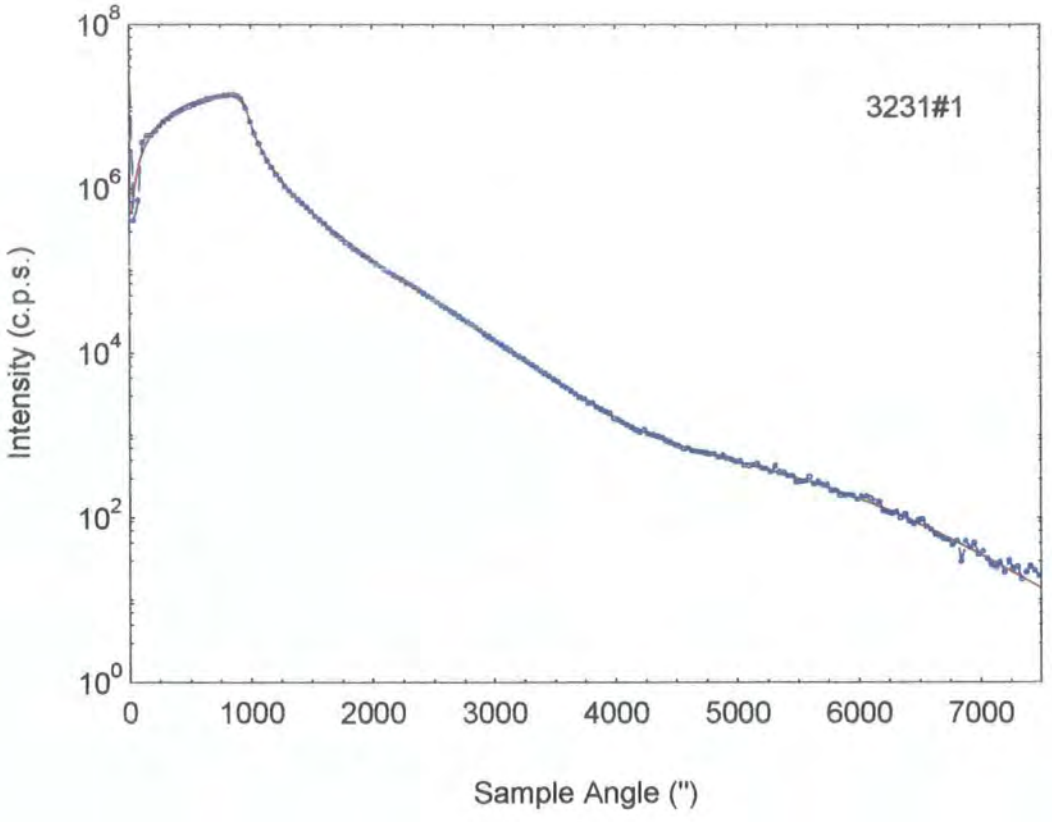

Fig 4.48 : Specular reflectivity data (points) and simulation (solid line) for the wafer type which was subsequently refinished.

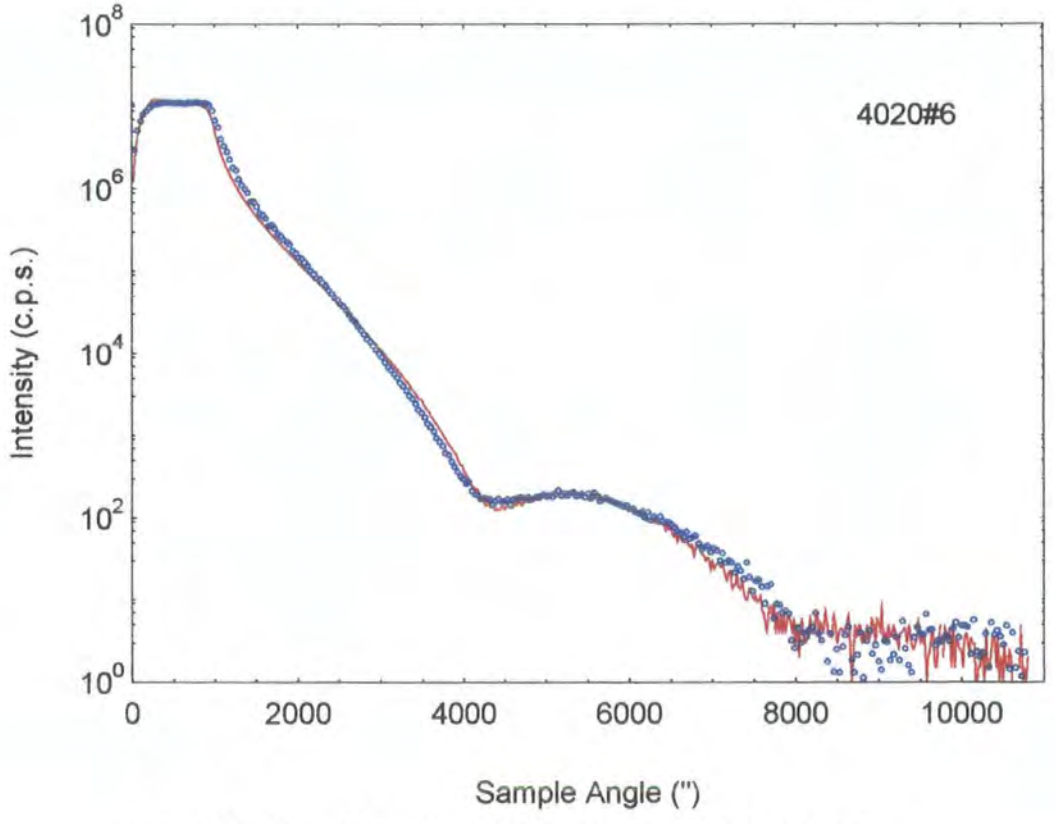

Fig 4.49 : Specular reflectivity for the wafer after refinishing

All samples had a specular FWHM significantly above that of the instrumental resolution, indicating that they were all figured. Very good fits to Gaussian distributions were found (Fig 4.50) with FWHM varying between 24" and 34". These scans were taken at $2\theta = 1.5°$, so the specular peak should lie at 2700". The maximum deviation from this value is 7", which means that the specular scans are still well aligned at this value of 2θ. It proved impossible to make a satisfactory fit of the diffuse scatter from sample 4020#6. The central section of the transverse scan for this sample, shown in Fig 4.51, is composed of three Gaussians. The FWHM of these peaks are shown to be very similar, so the crystal morphology is uniform across the sample, but there are three areas within the beam footprint which are tilted with respect to each other. From the relative intensities we can deduce the proportion of the sample which is tilted in a particular direction. In this case, the part of the sample with the lowest FWHM is aligned with respect to the incident beam. The three peaks are approximately equally spaced, giving a symmetric surface with tilt angle 20".

If this is compared with the asymmetric triple axis diffraction data, 4020#6 gives a 224 FWHM of 41" in the θ direction and 101" in the θ-2θ direction, which is the largest for any sample studied. This is in agreement with the large tilts which we identify here. However, in the symmetric 004 diffraction data we obtain the lowest tilt distribution for this sample, which corresponds to the low individual FWHM of the three tilt regions measured. The high resolution diffraction experiments were performed with a beam width of about 1mm by 1 mm, giving a footprint in the 224 reflection of 12 mm by 1 mm. This is comparable with the footprint of the beam in the grazing incidence experiments, where the 0.1 mm by 4 mm beam is projected to 20 mm by 4 mm in the region close to the specular peak. On the other hand, for the 004 high angle diffraction measurement, the footprint is only 2 mm by 1 mm. This suggests that the scale of the figuring is between 1 mm and 1 cm, the 004 diffraction data coming from just one of the tilted regions.

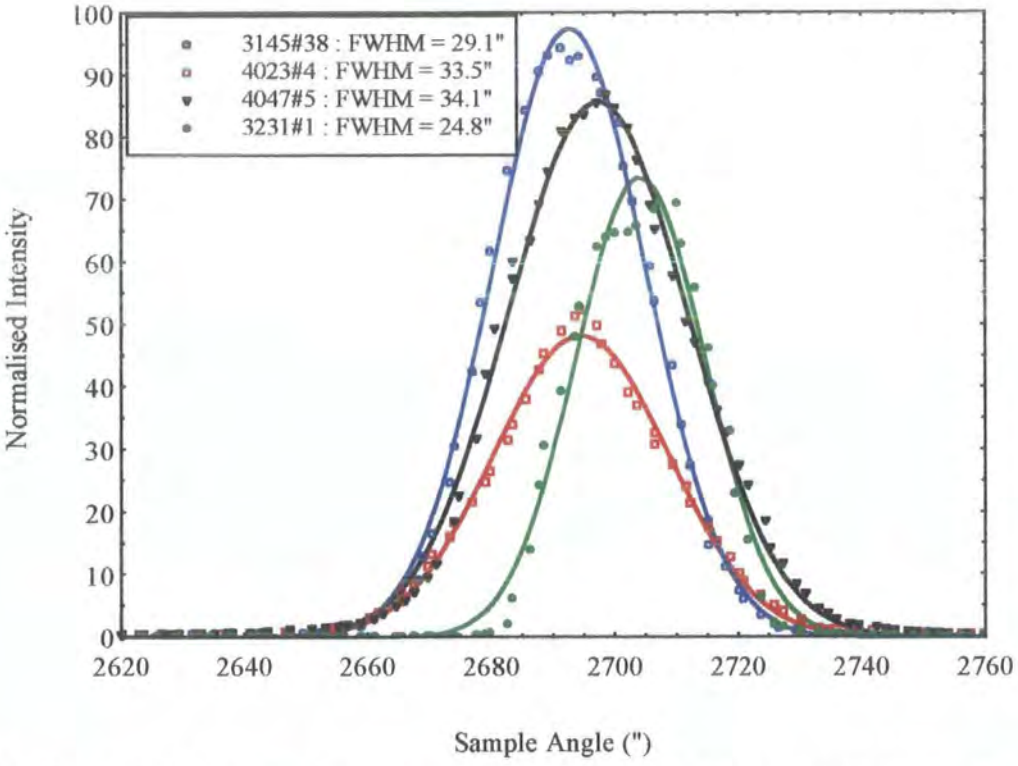

Fig 4.50 : Central section of specimen-only scans showing the Gaussian distribution of the specular peak shape

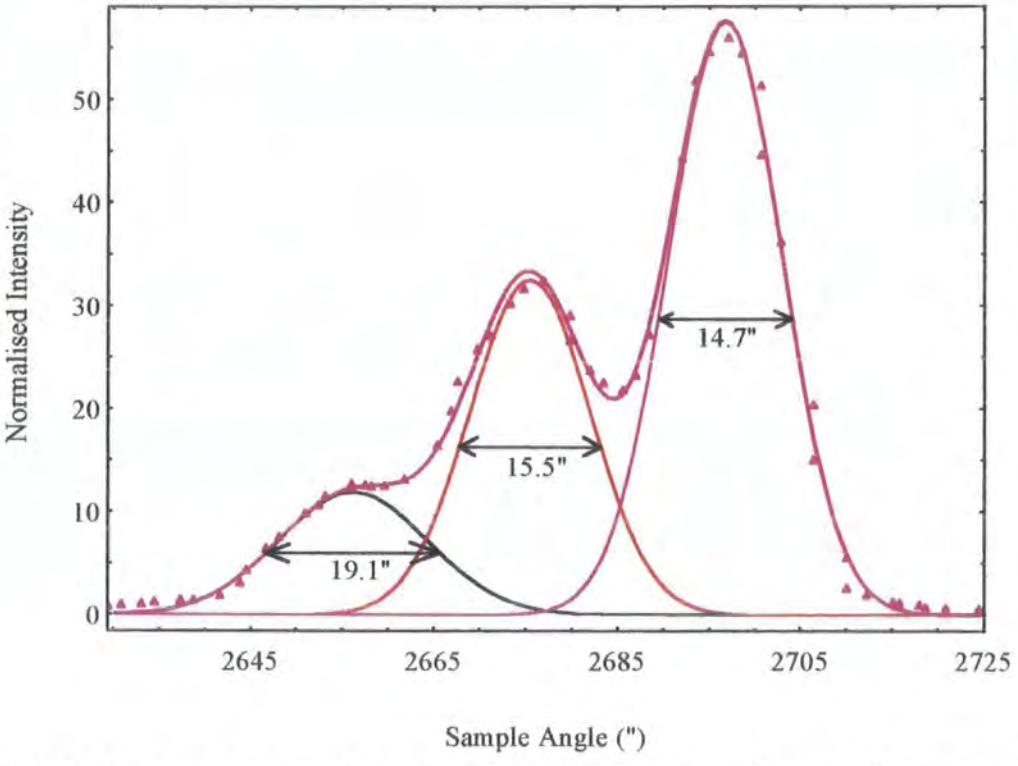

Fig 4.51 : Specular profile of sample 4020#6 fitted to three Gaussian distributions. The line through the points is the sum of the Gaussians.

If the three peaks are taken together, giving one broad peak, and the asymmetric diffraction FWHM are plotted against the specular peak FWHM in the grazing incidence diffuse scans, we find a linear relationship for the three samples for which full data are available (Fig 4.52). This linear relationship between the lattice tilt distribution measured by diffraction and the surface tilt measured by reflectivity provides support for our model of tilted mosaic blocks at the surface.

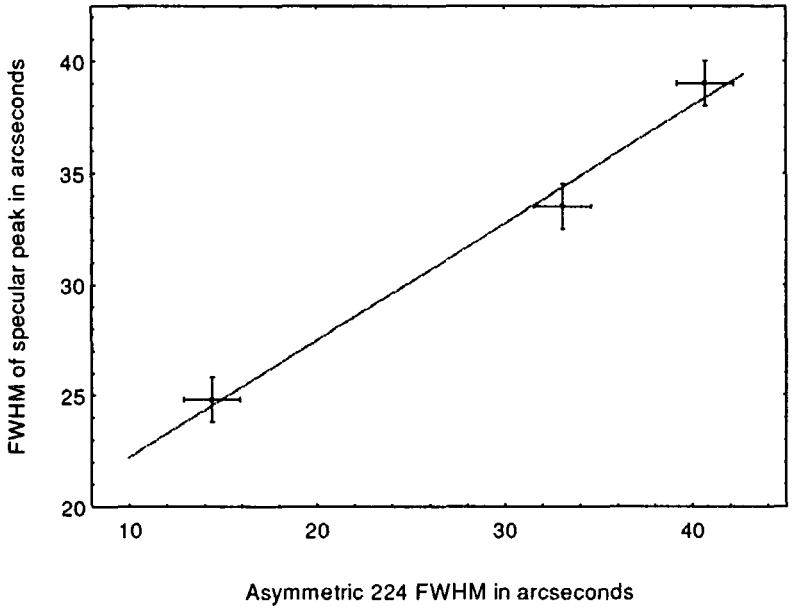

Fig 4.52 : FWHM of specular reflectivity peak versus FWHM in asymmetric diffraction

All the data shown here have been fitted assuming a dense top surface layer, with thickness of approximately 30Å. This layer may in part be due to the polishing procedures used, as some polishes aim to form an oxide layer in order to stop etching down microcracks, which gives rise to large tilt distributions. Alternatively, as these crystals have not been stored in a clean-room environment since manufacture, this layer may have developed subsequently to polishing. Different polishes result in a spread of top surface density, varying between $5.31 gcm^{-3}$ and $6.17 gcm^{-3}$ for the single layer oxides. The critical angle in the specular scan was found to match that of bulk InP in all cases, but in the diffuse scans, a density of $0.9\rho_{InP}$ was needed to fit the position of the Yoneda wings. This discrepancy may be a feature of the grading, present in all surface layers. The correlation lengths which are observed are fairly short, and at less than $0.07\mu m$ are probably smaller than the size of any particles used in polishing. The surface roughness is small, varying between 5.2Å and 1 Å, and decreases as the correlation length increases.

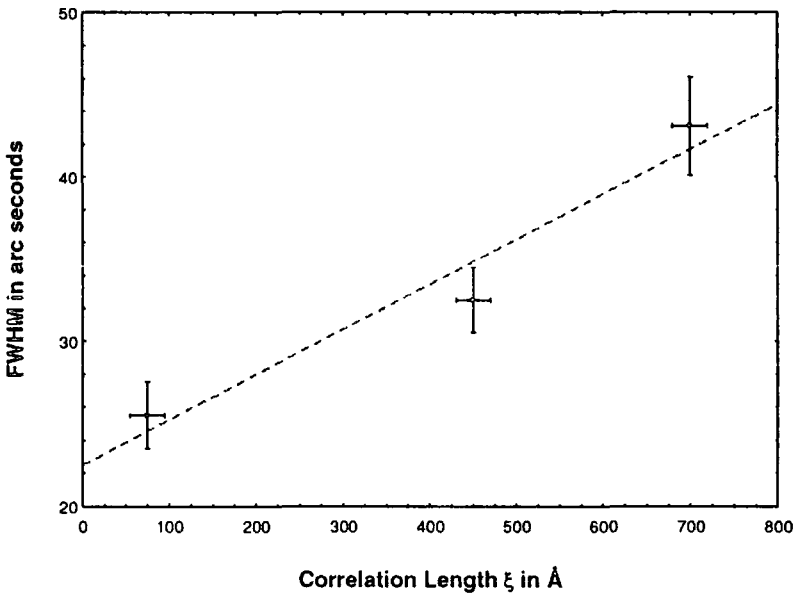

Fig 4.53 : FWHM of the specimen-only 004 diffraction scans versus correlation length

For the relatively short correlation lengths being used here, the simulations are not highly sensitive to h, and no trends in fractal parameter can be observed when they are compared with the diffraction data. For the three samples for which the grazing incidence diffuse scatter data could be simulated, a linear relation was found between the correlation length ξ and the FWHM in the specimen-only 004 triple axis diffraction scans (Fig 4.53). Although the diffuse scans of the remaining two samples cannot be fitted, their shape indicates a low correlation length. As these samples had very small FWHM in the diffraction scans, the trend in Fig 4.53 is confirmed.

4.7.4 : Conclusions on Polishing

In this section evidence has been given for a tilted mosaic block model for the surface of polished InP. Diffraction data has shown a system where there is little change in dilations on polishing, but a large variation in tilts. If this is described in terms of blocks it means that mosaic blocks of perfect crystal are being separated by microcracks, which are being enlarged by the action of bromine or other reactants in the polish. On polishing, these blocks are being physically rotated, as the specular part of the diffuse scan in 4020#6 shows. It is possible, therefore, for a sample which has a low FWHM to give a wide specular peak in a diffuse reflectivity scan. A relationship between the surface morphology of the crystal observed by reflectivity and the near surface tilt distribution seen in diffraction has been observed. The connection between

short correlation length and small tilt distribution measured from the 004 symmetric reflection probably arises through the relatively large depth sensitivity of this reflection. The short correlation lengths could correspond to a high density of microcracks confined to the very near surface region. All the samples have been simulated using a top surface layer of about 30 Å which has been modelled as a lighter than bulk oxide layer. Thin surface layers have been observed in polishing studies before. Choi et al observed a thin graphite layer when polishing diamond films by thermomechanical methods [53], and Sakata et al observed a 40 Å thick surface layer on mechanochemically polished (100) silicon surfaces, which corresponded to a density 90% of that of the native oxide [54]. This paper also compares well with the grading of density at the interface and surface observed here, as the roughnessess which they were measuring assuming discrete densities gave them values consistently greater than those measured by optical techniques. As some of their observed roughness would have been due to grading, this is predictable. Experimentally it has been shown that a single specimen only scan can be used in triple axis mode to allow a quick comparison of polishing damage in crystals. Although more points are required to verify the relationship between grazing incidence reflectivity data and asymmetric triple axis scans, the data shown here imply that analysis of the specular part of a diffuse reflectivity scan allows the same surface tilt information to be obtained as an asymmetric triple axis diffraction scan.

4.8 : Conclusions

In this chapter, the growth and polishing of InP wafers has been discussed. The wafers produced by various manufacturers in Japan, Europe and America have been compared. For LEC grown wafers, those produced by JE were found to be superior in terms of dislocation density to those manufactured by MCPWT. JE provided wafers which contained a large area of dislocation-free material, and narrow rocking curve widths. The samples showed evidence of surface scratches, however, both before and after refinishing, and the refinished sample was heavily figured. Misorientation measurements on JE wafers found them to be close to on-axis, while those from MCPWT were found to have an offset angle of almost half a degree.

VGF growth techniques were found to be effective in reducing the dislocation density down to virtually zero in all but one sample investigated. In this sample, 60^0 mixed dislocations were observed, with Burgers vector in the plane of the wafer. In addition, no growth striations were observed in VGF wafers, and the average residual strain over the samples was slightly lower than that in LEC wafers. It can be concluded that VGF has the ability to provide InP wafers of extremely high crystalline perfection, presumably due to the low thermal gradients during growth.

Using grazing incidence x-ray scattering, a grading in electron density on the surface of InP wafers has been identified. This has been attributed to the presence of an oxide layer approximately 30Å thick. A large variation in tilt distributions has been observed between samples, which has been attributed to the polishing process, and in particular to the action of bromine in etching down microcracks. A surface model of an array of edge dislocations between areas of near perfect crystal has been developed, and justified using symmetric and asymmetric triple axis diffraction data.

In addition to the information obtained on InP substrates, this chapter has included some novel x-ray experimental and analysis work. The ESRF has been used for the first time to obtain topographs of III-V semiconductor materials. A new and highly accurate technique has been proposed for the routine assessment of the misorientation angle of semiconductor wafers. A procedure of Bragg angle XY mapping to assess residual strains within wafers has been employed, and been found to agree with that obtained from topographical measurements. Sample only triple axis scans have been shown to be suitable for the routine assessment of substrate polishing, and a relationship between asymmetric diffraction FWHM and reflectivity specular peak FWHM has been observed. Finally, diffuse reflectivity scans at two incident angles have been fitted to the same parameters as the specular scan, using the DWBA, and including a graded layer.

References

1. Meyer, M., *InP Market Survey*. Compound Semiconductors, 1995. 1(1): p. 20-21.

2. Razeghi, M., *LP-MOCVD growth, characterisation and application of InP material,* in *Indium Phosphide: Crystal Growth and Characterization,* R.K. Willardson and A.C. Beer, Editor. 1990, Academic Press, Inc.: New York. p. 243-351.

3. Hashemi, M.M. and U.K. Mishra, *Unipolar InP-Based Transistors,* in *High Speed Heterostructure Devices,* R.A. Kiehl and T.C.L.G. Sollner, Editor. 1994, Academic Press, Inc.: New York. p. 157-213.

4. Redwing, J.M., *et al., The effect of controlled impurity incorporation on interfacial roughness in GaAs/$Al_xGa_{1-x}As$ superlattice structures grown by metalorganic vapor phase epitaxy.* J.Crystal Growth, 1994. **145**: p. 792-798.

5. Anders, M.J., P.R. Hageman, and L.J. Giling, *Misorientation dependence of zinc incorporation in GaAs.* J.Crystal Growth, 1994. **142**: p. 292-297.

6. Su, L.C., *et al., Order/disorder heterostructure in $Ga_{0.5}In_{0.5}P$ with deltaE$_g$=160meV.* J.Crystal Growth, 1994. **145**: p. 140-146.

7. Murata, H., *et al., Surface photoabsorption study of the effect of substrate misorientation on ordering in GaInP.* Appl.Phys.Lett., 1996. **68**(16): p. 2237-2239.

8. Su, L.C., I.H. Ho, and G.B. Stringfellow, *Control of ordering in $Ga_{0.5}In_{0.5}P$ using growth temperature.* J.Appl.Phys., 1994. **76**(6): p. 3520-3525.

9. Werner, P., *et al., Stress releasing mechanisms in $In_{0.2}Ga_{0.8}As$ layers grown on misoriented GaAs [001] substrate.* Appl.Phys.Lett., 1993. **62**(22): p. 2798-2900.

10. Goldman, R.S., H.H. Wieder, and K.L. Kavanagh, *Correlation of anisotropic strain relaxation with substrate misorientation direction at InGaAs/GaAs(001) interfaces.* Appl.Phys.Lett., 1995. **67**(3): p. 344-346.

11. Sopanen, M., H. Lipsanen, and J. Ahopelto, *Self-organized InP islands on (100) GaAs by metalorganic vapour phase epitaxy.* Appl.Phys.Lett., 1995. **67**(25): p. 3768-3770.

12. Shinohara, M., *et al., Behaviour and mechanism of wide terrace formation during metalorganic vapour phase epitaxy of GaAs and related materials.* J.Crystal Growth, 1994. **145**: p. 113-119.

13. Bhattacharya, A., *et al., Interface structures of InGaAs/InGaAsP/InGaP quantum well laser diodes grown by metalorganic chemical vapor deposition on GaAs substrates.* Appl.Phys.Lett., 1996. **68**(16): p. 2240-2242.

14. Chand, N., *Growth of high quality AlGaAs/GaAs heterostructures by molecular beam epitaxy for photonic and electronic device applications.* Thin Solid Films, 1993. **231**: p. 143-157.

15. Kishino, K., *et al., Gas source molecular beam epitaxial growth and characterisation of 600-660nm GaInP/AlInP double-heterostructure lasers.* Thin Solid Films, 1993. **231**: p. 173-189.

16. Takagishi, S., H. Yao, and H. Mori, *Origin and formation mechanism of elliptic-shaped surface defect on GaAs layers grown by molecular beam epitaxy.* J.Crystal Growth, 1993. **129**: p. 443-448.

17. Nakamura, M., *et al., Effect of substrate misorientation on tear-drop-like hillock densities in InP and GaInAsP grown by metalorganic chemical vapor deposition.* J.Crystal Growth, 1993. **129**: p. 456-464.

18. Wormington, M., D.K. Bowen, and B.K. Tanner, *Principles and performance of a PC-based program for simulation of grazing incidence x-ray reflectivity profiles.* Mater. Res. Soc. Symp. Proc., 1992. **238**: p. 119.

19. Loxley, N., *DCC Control Software.* 1993, Bede Scientific Instruments Ltd.

20. Loxley, N., *et al., New algorithms for rapid full-wafer mapping by high resolution double axis diffraction.* 1994.

21. Monberg, E.M., *et al., The growth and characterisation of large size, high quality, InP single crystals.* J. Electrochem. Soc., 1988. **135**(2): p. 500-503.

22. Farges, J.P., C. Schiller, and W.J. Bartels, *Growth of large diameter dislocation-free Indium Phosphide ingots.* J.Crystal Growth, 1987. **83**: p. 159-166.

23. Coquille, R., *et al., Growth of low-dislocation semi-insulating InP(Fe,Ga).* J.Crystal Growth, 1987. **83**: p. 167-173.

24. Naukkarinen, K., *et al., An Examination of Defects in InP single crystals grown by the Liquid-Encapsulated Czochralski Technique using Synchrotron X-ray Topography.* J.Crystal Growth, 1983. **64**: p. 485-491.

25. Haji, L., *et al., X-ray Topography and TEM studies of (Ga,Fe)-Double-Doped LEC Grown InP crystals.* J.Crystal Growth, 1987. **82**: p. 487-494.

26. Katsui, A. and S.-i. Tohno, *LEC Growth and Characterisation of Ga Doped InP Crystals.* J.Crystal Growth, 1986. **74**: p. 221-224.

27. Cockayne, B., *et al., The identification of precipitates in V-doped InP single crystals.* J.Crystal Growth, 1984. **69**: p. 610-612.

28. Franzosi, P., *et al., Inclusion-like defects in Czochralski grown InP single crystals.* J.Crystal Growth, 1984. **69**: p. 388-398.

29. Hofmann, D., *et al., Model-based directional solidification of semiconductor materials by the VGF-technique using multi-zone cold wall furnace technology.* Materials Science and Engineering, 1993. **A173**: p. 67-71.

30. Barrett, R., *et al.*, J.Phys.D:Appl. Phys., 1995. **28**: p. A250-5.

31. Kato, N., *Statistical theory of dynamical diffraction in crystals,* in *X-Ray and Neutron Dynamical Diffraction: Theory and Applications,* A. Authier, S. Lagomarsino, andB.K. Tanner, Editor. 1996, Plenum Press: New York.

32. Jenichen, B., R. Kohler, and W. Mohling, Phys. Status Solidi, 1985. **89**: p. 79.

33. Jenichen, B., R. Kohler, and W. Mohling, J. Phys. E, 1988. **21**: p. 1062.

34. Ferrari, C., D. Korytar, and J. Kumar, *Study of residual strains in wafer crystals by means of Bragg angle mapping.* Il Nuovo Cimento, 1997. **in press**.

35. Hashizume, H., A. Iida, and K. Kohra, *A multiple crystal system for high strain-sensitivity x-ray topography and its applications.* Jpn. J. Appl. Phys., 1975. **14**(10): p. 1433-1441.

36. Kitano, T., J. Matsui, and T. Ishikawa, *X-ray topography of lattice distortions in LEC-grown GaAs single crystals.* Jpn. J. Appl. Phys., 1985. **24**(12): p. L948-950.

37. Iida, A. and K. Kohra, *Separate measurements of dynamical and kinematical x-ray diffractions from silicon crystals with a triple crystal diffractometer.* Phys. Status Solidi, 1979. **51**: p. 533-542.

38. Hudson, J.M., *Specular and Diffuse X-Ray Scattering Studies from Surfaces and Interfaces.* 1994, University of Durham.

39. Tuck, B., *The chemical polishing of semiconductors.* J.Mat.Sci., 1975. **10**: p. 321-339.

40. Tuppen, C.G. and B.H. Conen, *Ultra-flat InP substrates produced using a chemo-mechanical polishing technique.* J.Crystal Growth, 1987. **80**: p. 459-462.

41. Chin, B.H. and K.L. Lee, *Bromine/Methanol polishing of <100> InP.* J. Electrochem. Soc., 1990. **137**(2): p. 663-666.

42. Chin, B.H. and K.L. Barlow, *Bromine/Methanol polishing of <100> InP substrates.* J. Electrochem. Soc., 1988. **135**(12): p. 3120-3125.

43. Gormley, J.V., M.J. Manfra, and A.R. Calawa, *Hydroplane polishing of semiconductor crystals.* Rev. Sci. Instrum., 1981. **52**(8): p. 1256-1259.

44. Hamaguchi, T., *et al.*, *Hydrostatic float polishing for wafer preparation.* Rev. Sci. Instrum., 1984. **55**(11): p. 1867-1868.

45. Reisman, A. and R. Rohr, J. Electrochem. Soc., 1964. **111**: p. 1425.

46. Laczik, Z., G.R. Booker, and A. Mowbray, *Comparison of surface polishing techniques used for InP wafers.* J.Crystal Growth, 1995. **153**: p. 1-5.

47. Guinier, A. and J. Tennevin, *Sur deux Variantes de la methode de laue et leurs Applications.* Acta Cryst., 1949. **2**: p. 133-138.

48. Laczik, Z., G.R. Booker, and A. Mowbray, *Assessment of residual subsurface polishing damage in InP wafers by photoluminescence.* J.Crystal Growth, 1996. **158**: p. 37-42.

49. Wang, V.S. and R.J. Matyi, *X-ray Diffraction Observation of Surface Damage in Chemo-Mechanical Polished Gallium Arsenide.* J. Electrochem. Soc., 1992. **21**(1): p. 23-31.

50. Wang, V.S. and R.J. Matyi, *Triple crystal x-ray diffraction analysis of chemical-mechanical polished gallium arsenide.* J.Appl.Phys., 1992. **72**(11): p. 5158-5164.

51. Moore, C.D., I. Pape, and B.K. Tanner, *Triple axis X-ray diffraction study of polishing damage in III-V semiconductors.* Il Nuovo Cimento, 1996 (in press).

52. Pape, I., . in preparation, University of Durham.

53. Choi, S.K., *et al.*, *Surface characterisation of diamond films polished by thermomechanical polishing method.* Thin Solid Films, 1996. **279**: p. 110-114.

54. Sakata, O., A.Y. Nikulin, and H. Hashizume, *X-ray evaluation of microroughness of mechanochemically polished silicon surfaces.* Jpn. J. Appl. Phys., 1993. **32**(2, 4B): p. L616-L619.

Chapter V

Doping in VGF GaAs Substrates

5.1 : Importance of doping

The role of dislocations in device performance has been much debated in the scientific literature (see Section 1.3), and although it is difficult to separate the effects of dislocations themselves and the potentially electrically active point defects and impurities which they attract, a low dislocation density is generally thought to be advantageous. Dislocations arise from thermal stresses during growth and impurities such as point defects and vacancies. It is reasonable, therefore, that the issue of dislocation reduction should be approached from both a metallurgical and electronic point of view. One last aspect of doping is also of vital importance - doping with elements with a different valency changes the electronic structure of a material. This allows its conduction properties to be altered from semi-insulating to metallic, and also from n to p-type. In this chapter the mechanisms by which dopants affect dislocation and electronic structure will be reviewed, followed by some topographical results on the effect of Si and Zn doping in Vertical Gradient Freeze (VGF) GaAs.

Dislocations can be divided into two categories - those which are non-stoichiometric, i.e. caused by the relative proportions of atoms present, and those which are stoichiometric, which includes those from thermal stresses. In the former case, the dislocation generation mechanism is believed to involve point defects, i.e. Ga and As vacancies, coalescing into vacancy clusters [1]. These clusters form discs "sandwiched" between layers of atoms, which collapse, and lead to dislocation climb through absorbing point defects. The way of reducing these defects, therefore, is to change the concentration of vacancies present in the material. In the second, stoichiometric, case, it is easier to approach the problem from a metallurgical point of view, and attempt to reduce the yield stress by inserting impurities which have a different atomic size, so compensating for the strain between the dislocation and crystal lattice.

5.2 Effect of doping in GaAs

5.2.1 : Isovalent Doping

A dislocation present in a crystal lattice will have either a compressive or a tensile strain. For example, in an edge dislocation, the strain will be compressive where the extra set of planes has been inserted. In the same way, the presence of an atom with a larger or smaller radius than that of the bulk will also impose a strain on the lattice. It has frequently been remarked that dislocations and impurities are often found together in a crystal. Once the two are together, there is a resistance to slip of the dislocation, as, if the dislocation was removed, there would be a net increase in strain. This process is therefore known as "pinning", or impurity hardening, and is analogous to the formation of an alloy for greater tensile strength. A schematic of the way in which this interaction occurs for an edge dislocation is shown in Fig 5.1.

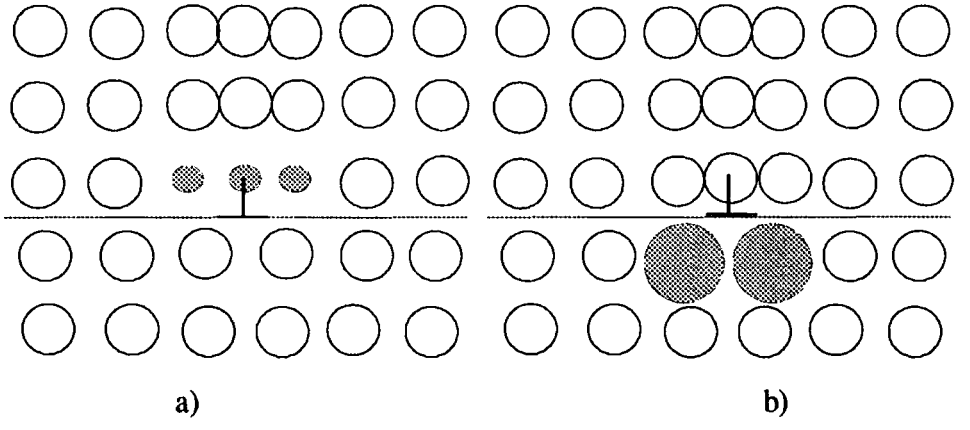

Fig 5.1 : Showing how the addition of impurities can compensate for the strain of an edge dislocation by a) tensile forces, and b) compressive forces.

The most common isovalent dopant used in GaAs is In, which is a group 3 element with an atomic number of 49 (compared to 31 in Ga and 33 in As). In LEC GaAs, a reduction in dislocation density from 10^4-$10^5 cm^{-2}$ in undoped material to dislocation free is possible by In doping with 10^{20} atoms cm^{-3} [2], where in general 90% of the In is incorporated onto the Ga sites [3]. Although a potential factor of three increase in the CRSS can be obtained through In doping, levels have to be carefully chosen, as

excessive doping leads to stressed and tetragonally distorted material which can cause misfit dislocations in epitaxial films [4].

5.2.2 : p-type Doping

Acceptors which are used in GaAs include C, Mg, Zn, Mn, and Cu [5], but the most commonly used is Zn, as it acts as a shallow impurity with a high solubility and an activation energy between 0.024 and 0.031 eV [6]. Experiments on LEC and HB GaAs have shown that the dislocation density actually increases when p-doping GaAs [2, 7-9]. Firstly, it has been noted that the dislocation density and carrier concentration is dependent on the stoichiometry of the melt, as this alters the relative proportions of the Ga and As vacancies. These vacancies can either condense into dislocations, or attract dislocations already present, depending on their charge state, and that of the dislocations. Both vacancies and dislocations (due to their unsaturated dangling bonds) have energy levels within the bandgap, so their charge state is determined by the position of the Fermi level, shown in Fig 5.2.

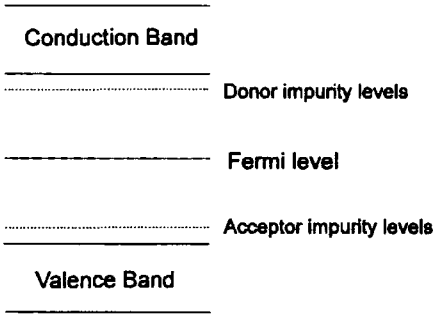

Fig 5.2 : Electronic band structure

In the case of GaAs the critical vacancy is V_{Ga}, which has an acceptor level near the middle of the energy gap. When the material is undoped, the Fermi level (E_F) is dependent on the stoichiometry of the crystal. The addition of p-type donors moves the Fermi energy down towards the valence band so the number of neutral Ga vacancies increases, and the dislocation density increases. This change in charge, together with that of the dislocations, appears to result in little pinning and formation of significant numbers of dislocations.

The dislocation density in HB GaAs in one study [9] was seen to increase from an undoped level of $10^3 cm^{-2}$ to above $10^5 cm^{-2}$ for a Zn dopant concentration of $10^{18} cm^{-3}$. Another aspect of dislocation suppression is that of the dislocation velocity. Dislocation motion is thought to be dependent on the charge state of dislocation kinks, so a change in E_F can decrease their yield stress and increase their speed. This process occurs with p-doping until the concentration of impurities is sufficient to introduce hardening effects, when the dislocation velocity falls. P-type impurities have, in particular, been observed to increase the mobility of 60° dislocations with a particular sign (α) [2].

5.2.3 : n-type Doping

Donors used in GaAs crystals include Si, S, Se, Te and Sn. Silicon is interesting as a dopant because of its amphoteric behaviour in this case. When GaAs is grown from a melt with stoichiometric composition, Si goes onto the Ga sites and acts as a shallow donor, with activation energy between 0.002 and 0.0058eV. If it is grown from solution with a low As vapour pressure, the Si sits instead on the As site and becomes an acceptor with energy in the range 0.025 to 0.030eV [6]. As the crystals dealt with in this study are grown from the melt, only the first of these will be considered here.

When a donor is added to the crystal, the Fermi energy increases, and there is an increase in the number of negatively charged acceptor-type defects, fewer ionised deep donor levels, and fewer neutral Ga vacancies. This leads to a lower probability of vacancies forming into dislocations, so a lower dislocation density is produced. In addition, the mobilities of all types of dislocations (α and β) are reduced [2].

Although the action of Si has been noted to improve LEC GaAs crystals [10] without causing precipitation, there are problems with the doping being accompanied by boron incorporation, which is an isovalent impurity with respect to Ga. As this comes from a reaction with the B_2O_3 encapsulant, this effect can be removed by using HB techniques instead, which are preferred for the production of GaAs:Si wafers. Si doping at levels of $\sim 10^{17} cm^{-3}$, therefore, allows the production of n-type, dislocation free LEC GaAs crystals [7].

Some examples of dislocation densities in GaAs crystals grown by LEC and HB with different dopants have been given here, but as yet there has been no systematic comparison of effects of doping in VGF GaAs. As these wafers have been subjected to a much lower temperature gradient during growth, it is expected that many of the dislocations present will be due to vacancy concentrations, rather than thermal stress. It is therefore of interest to see if VGF material can combine the required electrical characteristics with a lower defect density than formerly obtained.

5.3 : Topographical Comparison of Dopants

All the white beam topographs shown here were taken at Daresbury Laboratory on Station 7.6, using the $02\bar{2}$ reflection in transmission with λ=0.75Å. The area sampled in each exposure was approximately 1cm vertically by 2cm horizontally using D2 film. At least six of these were taken for each sample, mapping a different area of the wafer each time. In addition, small area white beam Laue topographs imaging a large number of reflections were taken at two places on each sample, but due to the necessity of using low-resolution film, none of these are shown here. The dislocation densities obtained from these topographs, however, are in agreement with those presented. Four wafers were investigated, three manufactured by AXT, and one by MCP. The AXT wafers represented one each of undoped, n-type and p-type, while the MCP wafer was n-type. Each one will be treated in turn, with an example of a typical dislocation structure and a sketch of the variation in dislocation density across the wafer.

5.3.1 : AXT GaAs:Un 5154#2

Fig 5.3 shows a topograph from an undoped VGF GaAs wafer. The CRSS theory of Jordan et al [11] predicts a six-fold reduction in dislocation density in VGF compared to LEC, with totally dislocation-free regions, but an average EPD of ~1000cm^{-2} was measured. In this case, we can see that dislocations are present, with an average density of 900cm^{-2} across each 1x2cm^2 topograph. The values over individual square centimetres varied between 600 and 1200cm^{-2}. All the topographs gave the same dislocation density, as is represented in Fig 5.4, so the density is uniform across the

wafer. As Jordan has suggested, the presence of dislocations in excess of those predicted from thermal stress factors is evidence for a secondary mechanism of dislocation generation which is dependent on the number and charge of vacancies. It is also evidence for temperature gradients being lower than in LEC growth, as there are no high dislocation density regions at the edges(as seen in the work of Barnett et al [12]).

The cell walls are oriented in the <011> directions, although less cell structure is present than in LEC wafers [12]. There is little tilt between cells and the cell sizes average $4mm^2$. No striations are visible, as would be expected in an undoped sample. Some dislocation loops are imaged, which probably arise due to the intersection and recombination of two dislocations with the same slip vector. This wafer is only the second from the seed, so is likely to be inferior to many in the boule, which emphasises the high quality of wafers produced by the VGF technique.

The uniform dislocation density seen above should be compared with that of LEC GaAs wafers investigated in the 1980's. In many cases, a characteristic "W" shaped distribution of defects was observed, with a four-fold symmetry [3, 12]. The highest dislocation densities were observed at the edge of the wafer, which decrease away from the wafer periphery, but rise again at the centre.

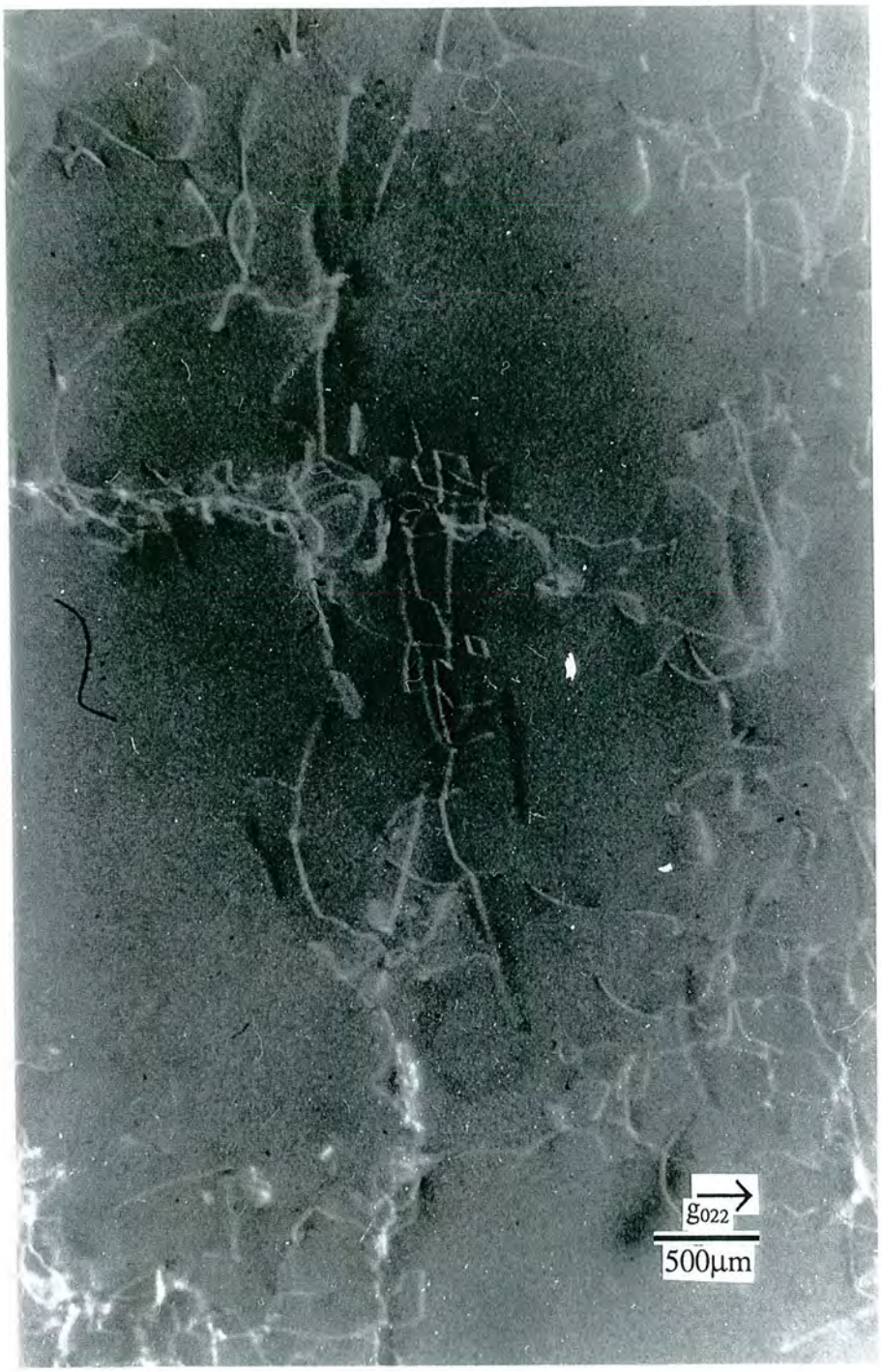

Fig 5.3 : Anomalous transmission topograph of AXT VGF GaAs:Un, 5154#2

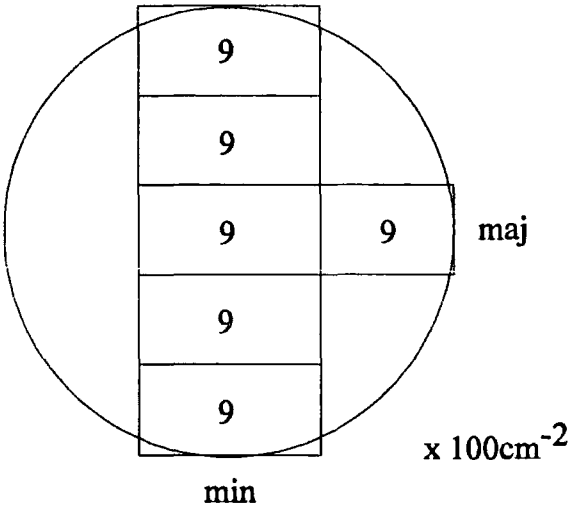

Fig 5.4 : Variation in dislocation density for AXT VGF GaAs:Un

5.3.2 : AXT GaAs:Zn 5155#4

The wafer in Fig 5.5 is again taken from near the seed in the boule, but this time the dislocation density is higher. The cell structure is not very pronounced, with dislocation-free areas being in the region of $2mm^2$. Small dots within the tangles of dislocations may be As precipitates formed through having an As-rich melt. Again, some dislocation loops are visible, and no striations are present, so the dopant was fairly uniformly spread. If the dislocation distribution across the whole wafer is considered (Fig 5.6), it can be seen that the crystal is fairly uniform, with a slightly lower dislocation density at the edges of the wafer. The density varies between 500 and $1600cm^{-2}$, and apart from at the very top of the wafer, is always higher than in the undoped material.

We can conclude, therefore, that the effect of p-type doping in VGF wafers is the same as that in LEC and HB. As the initial dislocation density in the undoped material is lower than that in LEC material, it is reasonable that the density of dislocations measured is less than that in LEC GaAs:Zn. The average increase in dislocation density on doping is a factor of 1.4, which is small compared to the two orders of magnitude seen previously. As the initial VGF wafer presumably contained fewer Ga vacancies than in LEC wafers, there are fewer vacancies to change their charge state when the Fermi energy decreases. The effect on the measured dislocation density would, therefore, be less than in poorer wafers.

Fig 5.5 : Topograph of AXT GaAs:Zn, 5155#4

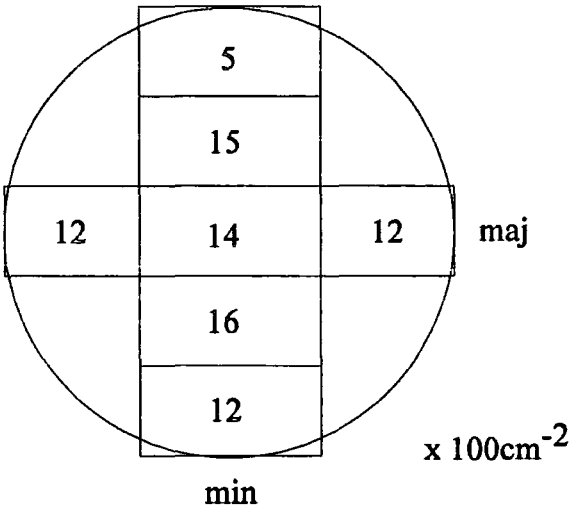

Fig 5.6 : Dislocation distribution in AXT GaAs:Zn

5.3.3 : AXT GaAs:Si 5118#72

This wafer, 5118#72, is virtually dislocation-free, as can be seen in Fig 5.7, which is shown at the same magnification as the previous topographs. The only dislocations visible in the wafer are those shown under high magnification in Fig 5.8, where there is evidence of slip along the <011> direction. The position in the wafer from which this topograph was taken is shown in Fig 5.9. In this wafer, therefore, the doping has been effective in removing virtually all the dislocations present in the undoped wafer.

The topographs again show the expected trend in dislocation density. As the Fermi energy moves towards the conduction band in this n-type wafer, the charges on the vacancies and dislocations have altered so that the vacancies are unlikely to collapse, while the dislocations are pinned by the vacancies present. Of course, Si has the added advantage of having a small radius compared to Ga and As (Z=14), so it can combine electronic effects with effective pinning. The presence of the few slip dislocations implies that a slightly higher level of doping is needed.

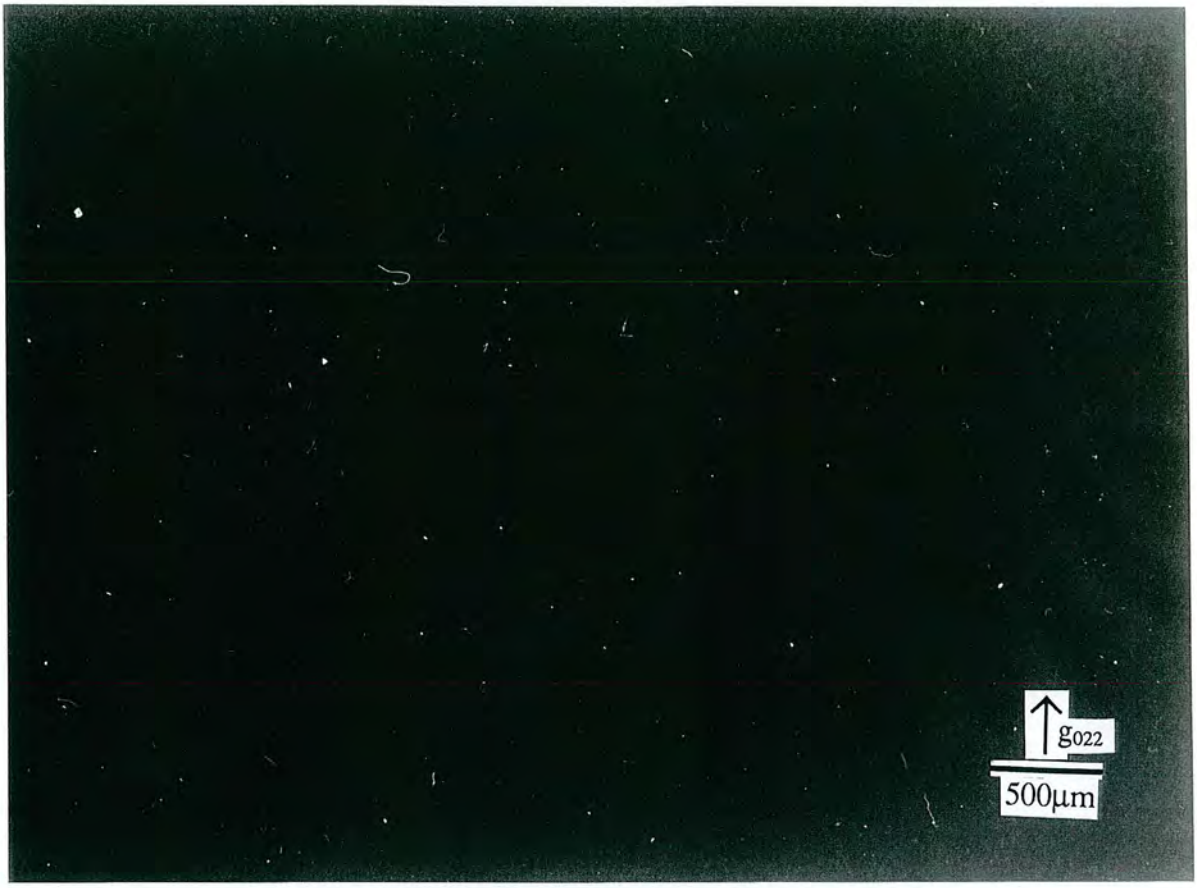

Fig 5.7 : A dislocation-free wafer of AXT GaAs:Si

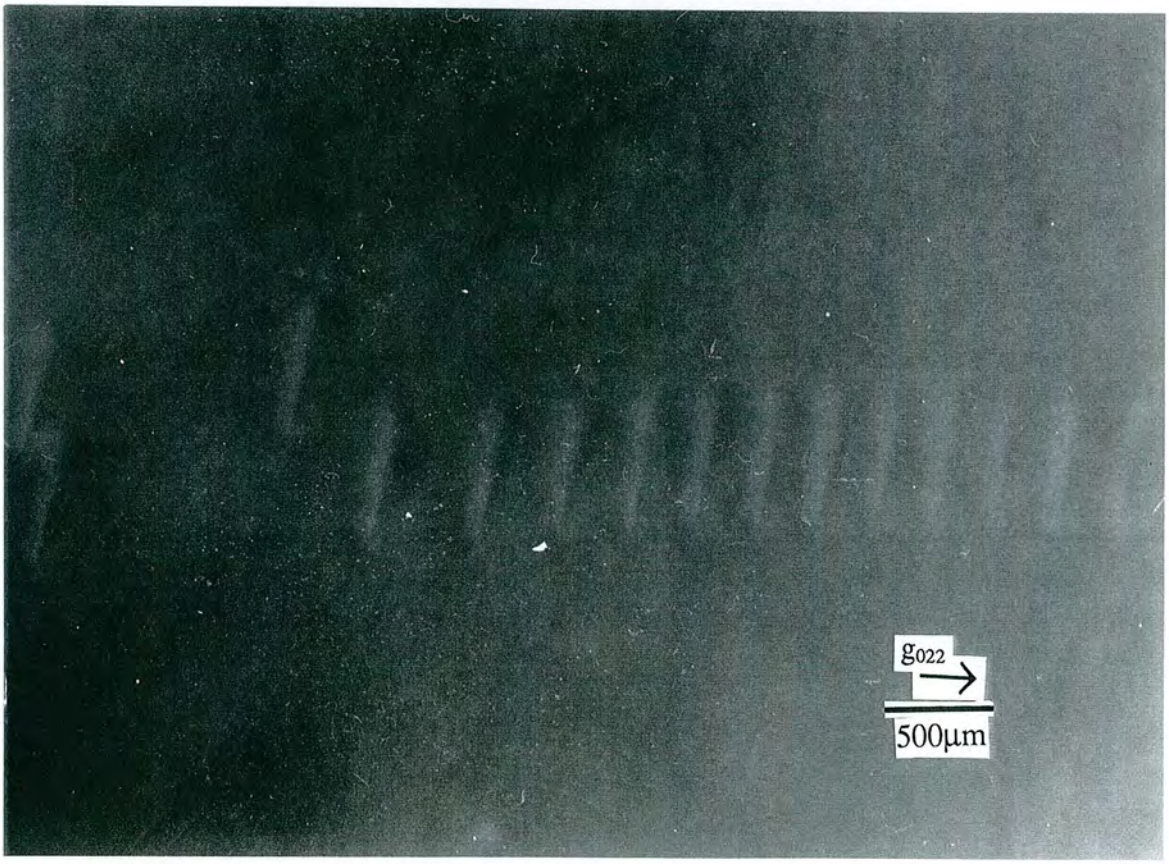

Fig 5.8 : Slip dislocations in AXT GaAs:Si near the wafer periphery

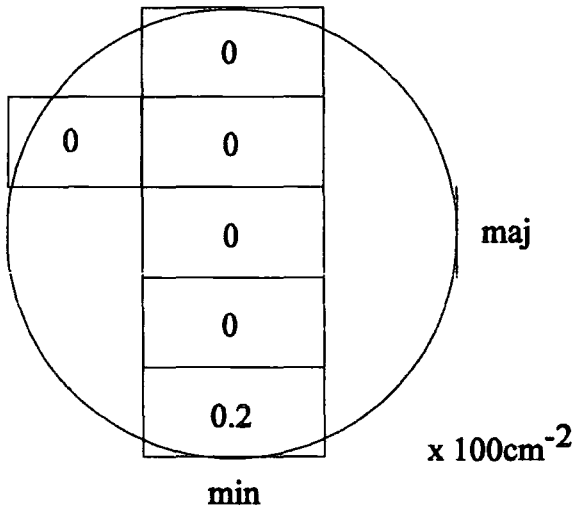

Fig 5.9 : Dislocation distribution in AXT GaAs:Si

5.3.4 : MCP GaAs:Si 4207#66

Dislocations are visible in this Si doped wafer, although no real cell structure is present. There are areas of several mm^2 with virtually no dislocations, rising to $430cm^{-2}$ in the centre. Fig 5.10 shows a topograph from near the centre of the wafer, where two images are seen for each dislocation. This may be due to the presence of two reflections, but it is more likely due to the film not having been perpendicular to the diffracted beam, leading to slightly displaced images on the two surfaces of the film. There is little tilt in the wafer, and some dislocation loops can be seen. More loops are shown in Fig 5.11, which is taken from near the edge of the wafer. In this topograph some dark defects are imaged, lying parallel to the major flat. The sketched wafer map is shown in Fig 5.12, where the decrease from the centre to the edge of the wafer can be seen. There is also increased dislocation density along the <001> direction. This is not quite as pronounced in the other quadrants, as supplementary topographs have shown, although higher levels of surface damage exist on the left hand side of the wafer (as imaged).

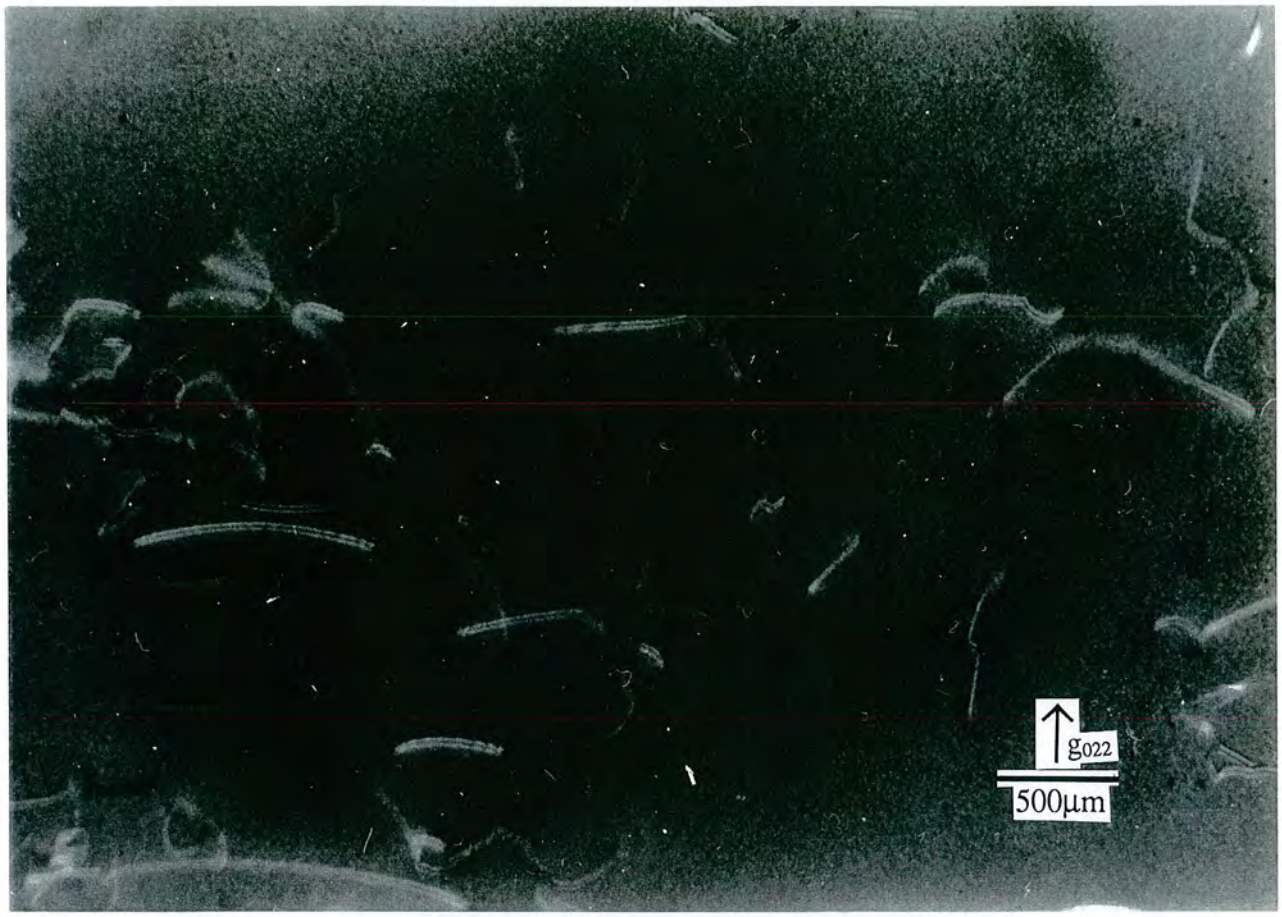

Fig 5.10 : Topograph from the centre of MCP Ga:Si

Fig 5.11 : Topograph from the edge of MCP GaAs:Si wafer

The presence of dislocations in this wafer shows that the doping level used is insufficient to pin, and slow down, all the dislocations present. The non-uniform distribution has been observed before in VGF GaAs wafers where the centre and four quadrants were seen to contain low numbers of dislocations [13]. In that case, the wafers used were grown by AXT, who have obviously improved their growth process in the last year or so.

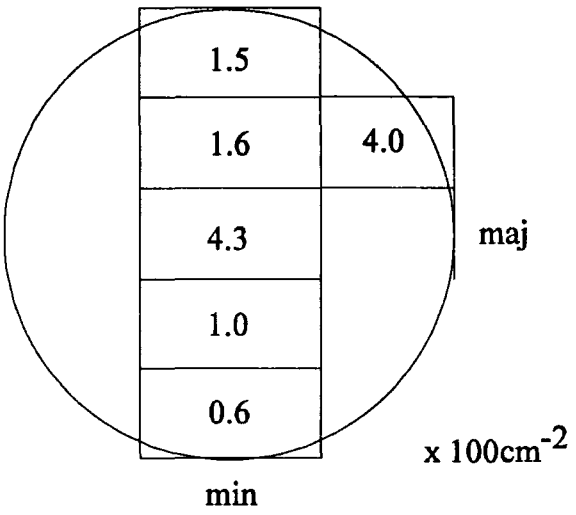

Fig 5.12 : Variation in dislocation density in a MCP GaAs:Si wafer

Several factors could contribute to this measured distribution. The high number of dislocations at the centre are probably propagating from the seed, so that many remain even in doped material. The increased dislocation density in the corner may simply be due to the projection of the {111} planes, along which slip occurs most easily, being along the <011> direction in a (100) wafer. MCP, therefore, have not as yet successfully optimised their growth/doping procedure in VGF GaAs.

6.4 : Summary

The action of dopants in VGF GaAs has been shown to be the same as that in LEC and HB GaAs. The lower thermal stresses involved have resulted in undoped material with uniform dislocation densities in the region of 900cm^{-2}. The introduction of p-type and n-type dopants to these wafers has been achieved uniformly (as no striations were imaged), with the Zn doping resulting in an increased dislocation density, between 500 and 1600cm^{-2}. The addition of Si has been shown to enable the dislocation density to

be reduced to near-zero levels, although in one case, densities of up to 430cm^{-2} remained.

References

1. Henderson, B., *Defects in Crystalline Solids*. 1972, London: Edward Arnold.

2. Sumino, K., *Dislocations in GaAs crystals*, in *Defects and Properties of Semiconductors: Defect Engineering*, J. Chikawa, K. Sumino, andK. Wada, Editor. 1987, KTK Scientific Publishers: Tokyo. p. 3-24.

3. Barrett, D.L., *et al.*, *Low dislocation, semi-insulating In-doped GaAs crystals*. J.Crystal Growth, 1984. **70**: p. 179-184.

4. Jordan, A.S., E.M. Monberg, and J.E. Clemans, *A comparison of reducing the dislocation densities in GaAs grown by the vertical gradient freeze and liquid-encapsulated Czochralski techniques*. J.Appl.Phys., 1993. **73**(1): p. 477-479.

5. Wilson, R.G., *Impurity densities and the redistribution of Fe and Cr in LEC GaAs*, in *Gallium Arsenide and Related Compounds, 1981*, T. Sugano, Editor. 1981, The Institute of Physics Conference Series: Oiso, Japan. p. 1-6.

6. Milnes, A.G., *Deep Impurities in Semiconductors*. 1973, New York: John Wiley & Sons.

7. Aoyama, T., *et al. Control of dislocation density in GaAs grown from the melt; effects of isoelectronic doping*. in *Gallium Arsenide and Related Compounds*. 1985. Karuizawa, Japan: Institute of Physics Conference Series.

8. Fugimoto, I., *et al. Analysis of lattice location of doped impurities in GaAs by the x-ray quasi-forbidden reflection (XFR) method*. in *Gallium Arsenide and Related Compounds*. 1985. Karuizawa, Japan: Institute of Physics Conference Series.

9. Lagowski, J., *et al. On the dislocation density in melt-grown GaAs*. in *Semi-Insulating III-V Materials*. 1984. Kah-nee-ta: Shive Publishing Ltd.

10. Frigerio, G., *et al.*, *Dislocations and microdefects in LEC-grown silicon-doped gallium arsenide crystals*. J.Crystal Growth, 1990. **99**: p. 685-691.

11. Jordan, A.S., E.M. Monberg, and J.E. Clemans, *Thermal stress theory of dislocation reduction in the vertical gradient freeze (VGF) growth of GaAs and InP*. J.Crystal Growth, 1993. **128**: p. 444-450.

12. Barnett, S.J., *Stuctural Characterisation of Semi-insulating LEC Gallium Arsenide*. 1987, University of Durham.

13. Barnett, S.J., *et al.*, *In situ x-ray topography studies during the molecular beam epitaxy growth of InGaAs on (001) GaAs: effects of substrate dislocation distribution on strain relaxation*. J.Phys.D:Appl. Phys., 1995. **28**: p. A17-A22.

Chapter VI

IMP Grown Epitaxial Layers of $Hg_{1-x}Mn_xTe$

6.1 : Introduction

Mercury manganese telluride (MMT) belongs to a class of semiconductor known as diluted magnetic semiconductors (DMS) or, alternatively, semi-magnetic semiconductors (SMSC's). These are materials of great scientific interest because of their unique magnetic and magneto-optical properties. The basic properties of DMS and MMT in particular are discussed below.

6.1.1 : Diluted Magnetic Semiconductors

A DMS [1] is a solid solution of a magnetic ion in a non-magnetic compound semiconductor lattice. Most research work so far has been focussed on II-VI materials [2, 3], although recent work has included other structures, such as III-V and IV-VI semiconductors. The most common substitution which is made, is to replace a fraction of the A^{II} cations in a material $A^{II}B^{VI}$ by Mn^{2+} double positive ions, although Fe^{3+} ions are now in common use. Examples of this include $Cd_{1-x}Mn_xSe$, $Cd_{1-x}Mn_xTe$, $Zn_{1-x}Mn_xTe$, $Hg_{1-x}Mn_xTe$ and $Cd_{1-x}Fe_xSe$. They are interesting because, in the absence of a magnetic field, they act in a similar manner to their non-magnetic counterparts, like $Hg_{1-x}Cd_xTe$, but in the presence of an applied magnetic field their properties are very different. One of their unique features is that exchange interactions occur: these consist of d-d exchange interactions between Mn ions, which are normally antiferromagnetic, and s,p-d exchange interactions between conduction electrons and Mn ions, which are normally ferromagnetic. The g-factor which determines the amount of the Zeeman splitting in an applied field is enhanced, leading to a large Zeeman effect and Faraday rotation.

6.1.2 : Magnetic Manganese Ions

The most common magnetic ion used in these substitutions is Mn^{2+}, which has 5 parallel aligned spins in the 3d orbital. As Hund's rule has described, this system is stable, and a large amount of energy is required to add a spin in the opposite direction. In this way Mn^{2+} resembles a group II ion. Due to the fact that the $4s^2$ energy is lower than that of the $3d^5$ shell, Mn has a remarkable property in II-VI semiconductors: it acts as neither a donor nor an acceptor, which is a further advantage. High concentrations of this ion can be incorporated without destroying the crystallographic quality and structure of the host semiconductor. The bandgap follows a linear relationship with Mn concentration (increasing Mn widens the bandgap). If Hg is the ion replaced, a narrow band gap DMS is produced, and if Cd is replaced, a wide band gap DMS is formed. The dependence of the band gap on magnetic ion concentration enables the tuning of a material for a particular wavelength.

The magnetic ion concentration is also important in the fabrication of DMS, due to the dual nature of the growth of MnTe. MnTe has two phases, zinc blende and nickel arsenide. As II-VI materials form covalent bonds in a zinc blende or würtzite structure, a similar structure is required in the MnTe incorporated in the DMS compound. Unfortunately, MnTe tends to crystallise in the nickel arsenide structure. The two structures are shown in Fig 6.1. This imposes a limit over the range of values of x which can be obtained, as for example $Hg_{1-x}Mn_xSe$ will only form in the zinc blende structure in the range $0<x<0.38$.

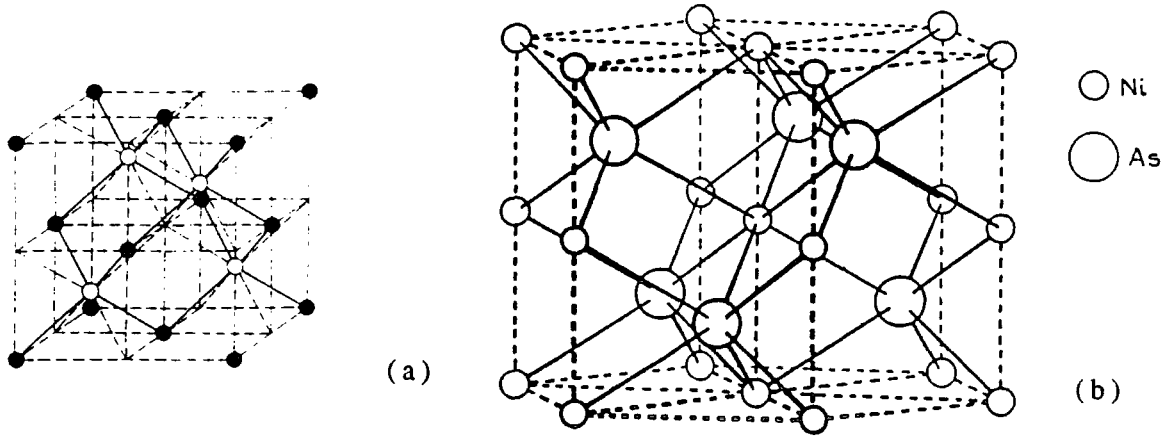

Fig 6.1 : Crystalline structures of MnTe: a) zinc blende, b) nickel arsenide

The inclusion of magnetic ions into a material changes the lattice parameter, which can be calculated using Vegard's Law. This law states that the lattice parameter in a system $A_{1-x}B_xC$ varies linearly between that of AC and BC, as x varies between 0 and 1. In the case of MMT, when the linear plot of measured lattice parameter against magnetic ion mole fraction is extrapolated out to x = 1, the lattice parameter of MnTe in its zinc blende structure can be obtained. As the graphs converge for various DMS, it can be concluded that the structures are indeed pseudobinary alloys of MnTe and another compound such as HgTe.

The magnetic properties of the material also depend on the manganese fraction. At low temperatures a change from paramagnetic to antiferromagnetic behaviour is observed, as the Mn ions interact in clusters. The temperature at which this occurs is dependent on x, with larger x leading to higher temperatures. A spin glass phase is also observed. The electrical and magnetic behaviour of $Hg_{1-x}Mn_xTe$ thin films is being researched within the University of Durham [4, 5], and the aim of this work is to provide the complementary structural information to form the basis for the interpretation of magnetic results.

6.1.3 : The DMS $Hg_{1-x}Mn_xTe$

Mercury manganese telluride is an important diluted magnetic semiconductor for several reasons. It can be grown over a large range of x, between 0 and 0.75 with the required zinc blende structure, which is higher than most II-VI alternatives, and up to x=0.35 only one MnTe phase is present. Another interesting property is due to the fact that HgTe is a semi-metal with a negative band gap (~-300meV). Varying the Mn fraction from 0 to 1, therefore, results in an energy gap range of -0.3eV to 3.2 eV (room temperature, zero magnetic field). The band gap opens at about x = 0.07 (4.2K), which provides suitable wavelengths for device applications.

Commercial $Hg_{1-x}Mn_xTe$ infrared detectors are available where tuning of the bandgap has been possible, but only at liquid helium temperatures [6]. A possibility is that this temperature could be increased to liquid nitrogen temperatures by the use of superlattices. This fuels the interest in epitaxially grown material, as well as the bulk

material more commonly studied. Other devices which have been proposed include magneto-optical isolators (due to the large Faraday rotation), x-ray detectors, infrared LEDs and injection lasers [7].

6.2 : Sample Growth Conditions

The samples investigated in this study were all grown using the IMP process described in Section 1.5, by S. Oktik at the University of Durham. The MOVPE reactor used has been described in papers by Clifton and Funaki[Clifton, 1990 #191; Funaki, 1993 #192]. The precursors used were

- DIPTe - di-isopropyl telluride
- TCMn - tricarbonyl methylcyclopentadienyl
- DMCd - dimethylcadmium
- DMZn - dimethylzinc

In all cases a buffer layer of 0.1μm ZnTe was deposited to ensure that the CdTe grew in the (100) direction, followed by 1μm CdTe. The growth conditions used are summarised in Table 8.1. DIPTe was used as a precursor instead of diethyl telluride as it allows growth at lower temperatures. This reduces outdiffusion from the substrate and reduces stresses due to the differential contraction of substrate and layer on cooling. Before growth the GaAs substrates were degreased in trichloroethane, rinsed in de-ionized water, etched in sulphuric acid/hydrogen peroxide/water, then rinsed and dried.

Table 6.1 : Growth conditions for $Hg_xMn_{1-x}Te$ by IMP

Substrate	CdTe buffered (100) GaAs
Substrate Temperature	370-410°C
TCMn Bubbler Temperature Carrier Gas Flow Rate	75°C 400cc/min
DIPTe Bubbler Temperature Carrier Gas Flow Rate	15°C 75-600cc/min
Mercury Boat Temperature	215°C 230°C (T=410°C)

These conditions resulted in layers with thicknesses between a fraction of a micron and several microns. The nominal compositions varied between zero manganese and 30%.

The surface morphology of the samples was in general poor, and included some which were rough and powdery, and some which appeared hazy. In most cases x-ray measurements were made on the samples prior to the magnetic and transport measurements, and within six months of being grown.

6.3 : Uniformity Measurements

6.3.1 : Experimental Technique

The importance of the compositional changes across a sample, in particular with regard to the magnetic ion concentration has been discussed in Section 6.1. In order to measure these changes, wafer mapping using double axis diffraction was performed. In this case the Bede 150 diffractometer was used, with a GaAs (100) reference wafer, and an X-Y translation stage. This gives a positional accuracy of 0.05mm. Initially, the Bragg peak for the GaAs reflection was found, and axis X then axis Y was scanned in order to determine the size of the crystal and hence the scan range. For each point on the sample, two looped scans were performed - one containing the GaAs substrate peak, and one the CdTe and MMT peaks. In order to gain sufficient intensity, a beam size of $1x1mm^2$ was used, so large steps between scans were reasonable. In most cases, a 2 or 3mm step was used, giving a total of between 50 and 80 scans per sample. Ideally, each scan would include both the substrate and layer peaks, but as the range between them is great, over 20,000 arc seconds for the 004 peaks using CoKα radiation, this is not practical. A small step size of 1 or 2" is required for the narrow GaAs peak, while large step sizes of 20" are acceptable for the layer peaks. In addition, tests on the micrometer tangent arm drive in this diffractometer showed that it was not linear over this range of movement, so any deductions about lattice parameters would be invalid. Two loop scans were performed, without moving the sample, therefore, one containing the substrate peak, and one the layers.

The first piece of information which is extracted from the scans is the position and FWHM of all peaks. We know that the lattice parameter for CdTe is 6.477Å (see Table 6.2), so the 004 Bragg angle for $CoK\alpha_1$ is 33.53°. If the difference in angle between the CdTe and MMT peaks is added to this value, the Bragg angle of MMT is

obtained. Using Bragg's Law (Eq 2.2.4) the lattice parameter is calculated. The lattice parameter, a, is related to the manganese fraction, x, by Vegard's Law, which gives,

[6.1] $$a = 6.462\text{-}0.128x.$$

The difference in peak positions can therefore be used to map the Mn composition across the sample. It should be noted that in this approach the layers are assumed to be totally relaxed, as any residual strain will move the relative peak positions. This assumption is discussed at length in Section 6.4, and is found to be valid in most cases. The FWHM of all the layers (and substrate) can be plotted against position directly, and is a good indication of the crystalline perfection of the materials.

In order to make some estimates of layer thickness the integrated intensities from the GaAs substrate are compared before and after layer growth. The integrated intensity scattered from a substrate crystal is measured, using exactly the same diffraction conditions as for the grown-on material. In particular, the beam size and power rating on the generator need to be kept constant after this calibration, as well as the distance between detector and sample. In order to obtain a reliable value for this intensity, the substrate material was remounted and tilt optimised several times during the period over which measurements were taken, so that any variation in alignment or generator power would be identified. Using settings of 40kV and 30mA on the generator, the integrated intensity from the GaAs substrate material was found to be 450,000 ± 20,000. The total thickness of the layer can be deduced from this, as the intensity of an x-ray beam is known to decay as

[6.2] $$\frac{I(t)}{I(0)} = e^{\frac{-2\mu t}{\sin\theta_B}}$$

where I(t) and I(0) are the diffracted and incident beams respectively, θ_B is the substrate Bragg angle, and μt is sum of the product of absorption coefficient and thickness for all the layers in the material [8]. It should be noted that the absorption coefficient is dependent on the manganese fraction present, so this must be included in the calculations. The constants which have been used all through this chapter to analyse the diffraction data were taken from the International Tables for Crystallography [9], or were calculated from data therein.

Table 6.2 : Atomic parameters used in this study

Element	Atomic Number	Atomic Weight u	μ/ρ (Cokα_1) cm^2g^{-1}
Mn	25	54.94	412.8
Zn	30	65.38	92.8
Cd	48	112.41	337.7
Te	52	127.60	406.0
Hg	80	200.59	311.4

Table 6.3 : Further parameters used in this study

Compound	μ/ρ (Cokα_1) cm^2g^{-1}	Density gcm^{-3}	Lattice Parameter, a in Å	Absorption Coefficient, μ cm^{-1}
CdTe	373.2	5.867	6.477	2189.5644
ZnTe	291.4	5.645	6.101	1644.9530
HgTe	348.7	8.078	6.462	2816.7986
MnTe	408.2	4.771	6.334	2585.5388
$Hg_{1-x}Mn_xTe$	348.7+59.5x	[8.3]	6.462-0.128x	(348.7+59.5 x)*[8.3.2]

The density of MMT, equation [6.3], is given by,

[6.3] $$\text{Density}_{MMT} = \frac{4M_{Te} + 4(xM_{Mn} + (1-x)M_{Hg}).10^{-6}}{N_0(6.462 - 0.128x)^3.10^{-30}}$$

in gcm^{-3}. The value of μt obtained experimentally, therefore, is the summation given below.

[6.4] $$\mu t_{expt} = \sum_j \mu_j t_j$$

where j is the number of layers. Unfortunately, only the total μt can be obtained by this technique. In order to give an estimate for the thickness of the MMT layer, a buffer layer of 1μm CdTe and 0.1μm ZnTe has been assumed. It should therefore be emphasised that all thicknesses quoted are an estimate only, their accuracy depending on the validity of this assumption.

It was noted that the peak position migrated during a sequence of scans, even if the lattice parameter remained unchanged. This is related to the curvature of the sample, and is the reason why the peak position values for composition measurements had to be made relative to a peak of known lattice parameter.

6.3.2 : Compositional Variations

MMT layers grown epitaxially by DAG (Direct Alloy Growth) have been shown to produce compositional variations of more than 1% mm^{-1} across a sample surface [10]. Some IMP samples give a gradient as low as 0.03%mm^{-1} under certain growth conditions [11]. The samples investigated here showed variations (averaged across a sample) of between 0.3%mm^{-1} and 2.8%mm^{-1}. Examples of low and high variation are shown in Fig 6.2. Although the composition fluctuates in a), there is no strong gradient across the wafer.

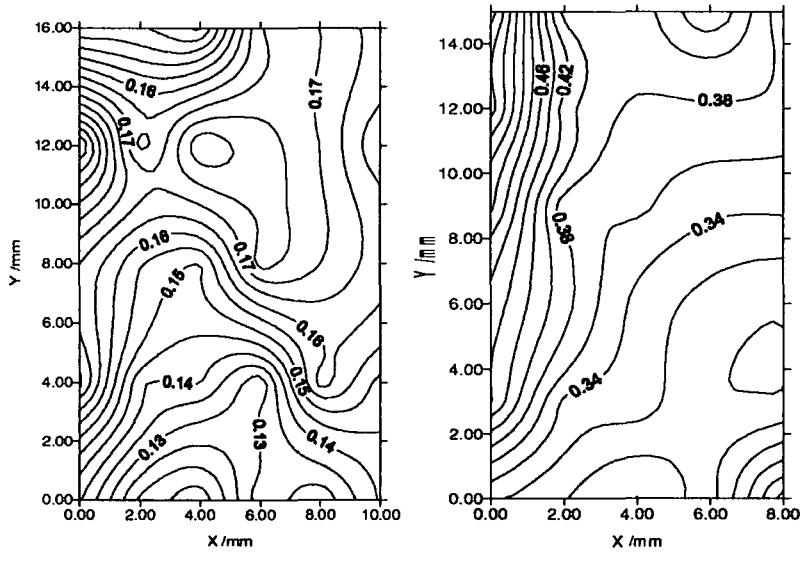

Fig 6.2 : Compositional changes across a) MMT26 and b) MMT24

Models for the gas flow within a MOVPE reactor during DAG show that large compositional changes are inevitable, as the pyrolysis rate ratio (TCMn/DIPTe) increases along the gas flow direction. This can be suppressed by increasing the total flow rate through the reactor or by using lower susceptor temperatures. Alternatively, IMP growth exploits conditions where only one of the constituent binaries is grown at a time. Under metal rich conditions, growth variations along the susceptor are determined by the pyrolysis profile of the DIPTe during both HgTe and MnTe growth, and the total thickness ratio of HgTe to MnTe becomes constant. This should result in a more uniform layer, as has been seen here.

The consistency with which good quality IMP layers were produced was, unfortunately, poor, and many of the samples produced CdTe and MMT peaks which were unresolvable, indicating a degree of polycrystallinity in the layers. In addition, in cases where the MMT layer was far thicker than the CdTe, the CdTe peak disappeared into the flank of the MMT rocking curve, so no composition measurements could be made. A summary of five samples where the peaks were clearly defined is given in Table 6.4. One point to note is that a larger concentration of Mn seems to be associated with a greater change in composition.

Table 6.4 : Compositional changes across MMT

Sample	Max change along x %mm^{-1}	Max change along y %mm^{-1}	Average Mn fraction
MMT12	0.7	1.6	0.21
MMT17	0.5	0.4	0.13
MMT18b	0.0	0.8	0.16
MMT24	2.0	0.7	0.39
MMT26	0.1	0.25	0.14

6.3.3 : Variations in FWHM

The largest variation in MMT FWHM across a sample was 600" (75"mm^{-1}), while the smallest was 160" (16"mm^{-1}). The variation in FWHM of the GaAs peak was small, of the order of 1" across a sample. There is no solid evidence to suggest that the FWHM variations in the substrate are being propagated through to the layers, although some similarities in pattern can be seen (for example Fig 6.3).

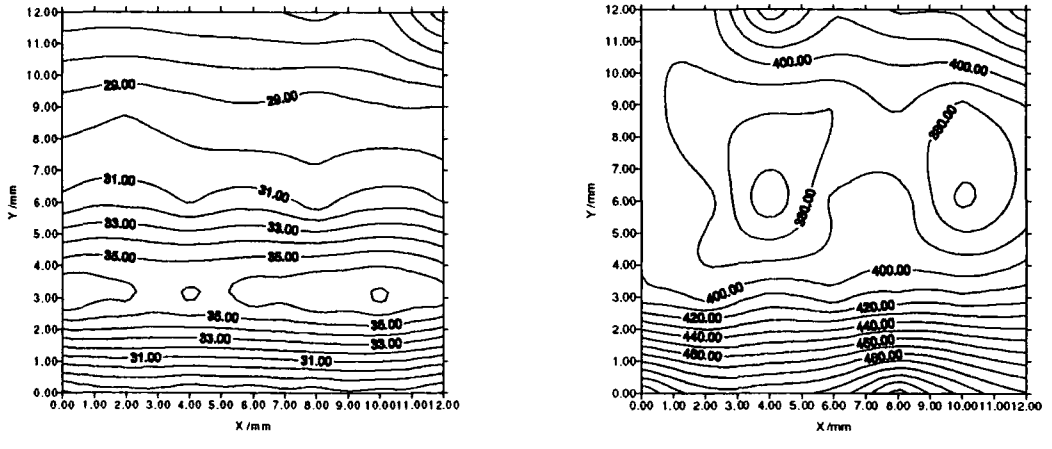

a) b)

Fig 6.3 : FWHM plots of MMT18a for a) GaAs substrate and b) MMT layer

The variation in FWHM can be related to several parameters, such as the dislocation density, compositional changes with depth, and increased strain due to lattice mismatch as x varies. The fact that the FWHM of MMT varies across the sample implies a lack of crystallographic uniformity, of the same order of magnitude as that in DAG crystals. The possible source of this lack of uniformity is discussed later.

6.3.4 : Variations in Thickness

The layers described here had thicknesses varying between 0.5μm and 2.5μm, but layers were grown up to 6μm. The variations in thickness, shown in Table 6.5, are very similar for all the samples, with the exception of MMT18b, which had a variation of only 0.04μm mm^{-1}. Where a clear linear gradient in concentration was observed, it was in the direction of gas flow, decreasing in thickness down the susceptor. An example of this is given in Fig 6.4, where the gas flow was from top to bottom. This has been observed previously in IMP grown layers, and is attributed to the depletion of precursor partial pressures [12].

Table 6.5: Thickness variations

Sample	Thickness gradient μm mm^{-1}
MMT17	0.1
MMT24	0.1
MMT12	0.08
MMT26	0.1
MMT18b	0.04

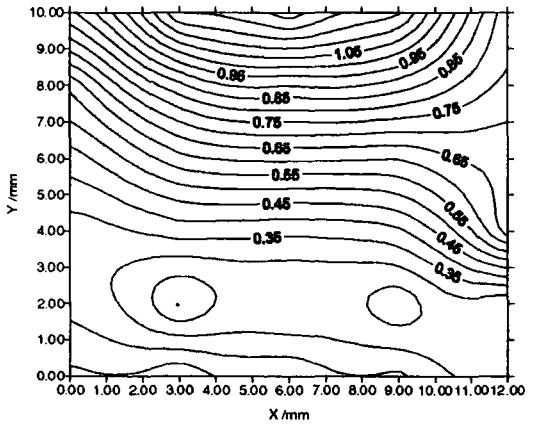

Fig 6.4: Thickness variations in MMT12

6.3.4 : Discussion

The most striking relationship on viewing the XY maps is the correlation between the manganese fraction and the FWHM of MMT observed. An example of this correlation is shown in Fig 6.5, where the contour lines follow the same pattern across the wafer. If all the data points for which both x and MMT FWHM are available are plotted on the same graph, we obtain Fig 6.6 where a linear increase in FWHM with Mn fraction is observed, even though there is some spread of points. Fewer data points are available for high manganese content, but the trend is still observed. This relationship implies that the crystalline perfection of the layer is directly related to the amount of Mn incorporated into the lattice. Of course, some component of this broadening in rocking curve will be due to the increased lattice mismatch, but this accounts for less than 10" of the increase across the whole range. The simulated rocking curve width for HgTe is 32", which is very similar to the intercept of 30" obtained.

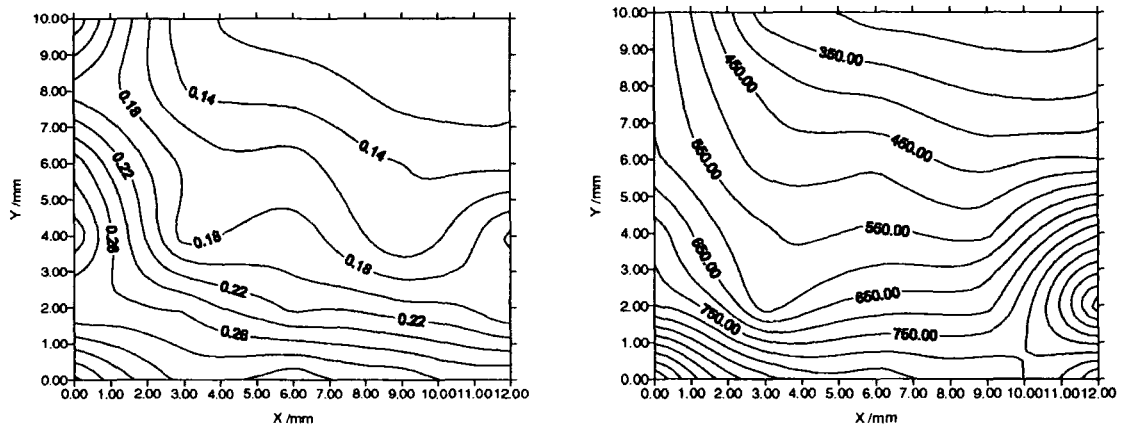

a) b)

Fig 6.5: Correlation observed between a) Mn fraction and b) MMT FWHM for MMT12

In order to test this relationship, pseudo-triple axis data, which is discussed and described later, is shown in Fig 6.7. The FWHM plotted corresponds to the tilt component of the rocking curve, and each circle is in this case a separate MMT sample. A linear relationship is again obtained, although with fewer data points. As these points just represent tilts and not sample strains, it is reasonable to suppose that the increase in FWHM is due to an increase in dislocation density at high x.

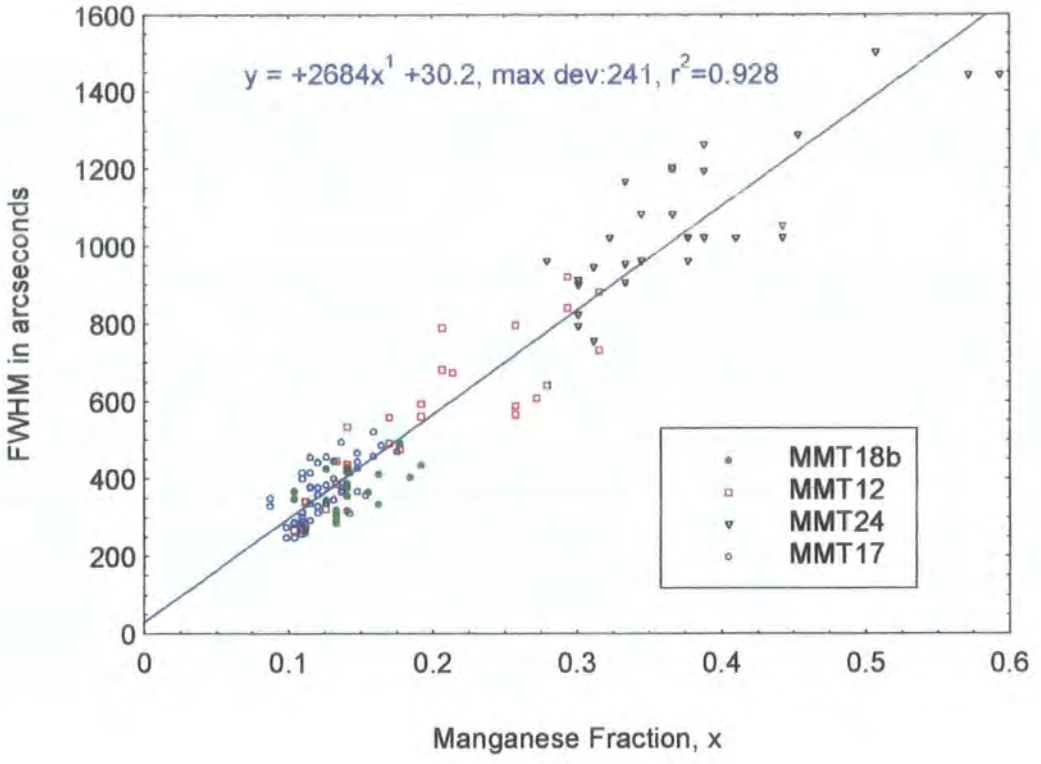

Fig 6.6: Relationship between Mn fraction and FWHM

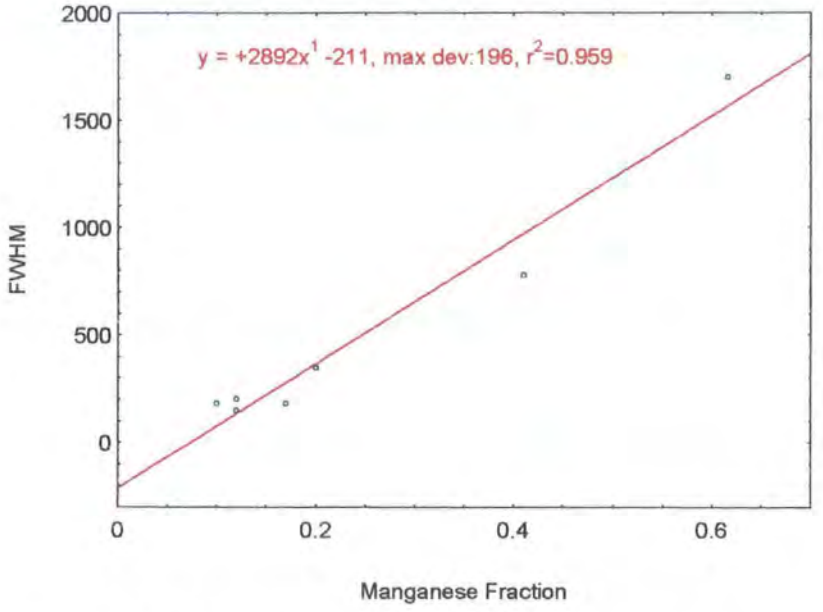

Fig 6.7: Additional data taken through analyser slits

There are several factors which may contribute to an increase in dislocation density with high x. One of these may be the diffusion co-efficient of precipitates varying with x, which means that precipitates formed during growth persist at high x. Very recent

TEM studies by Jones et al [13] at the University of Birmingham, investigated the presence and movement of point defects in IMP grown $Cd_xHg_{1-x}Te$ (CMT), using MOCVD. Using a 4-6μm CdTe buffer layer on GaAs, they observed that the microstructure obtained depended on x. With high x, small dislocation loops or precipitates were observed throughout the CMT layer, except close to the CdTe buffer. In particular, small defects were formed in the middle of the HgTe layers, as well as HgTe precipitates. They concluded that dislocation loops formed during interdiffusion persist under high x conditions.

Without a detailed study of the dislocation distribution in the layers, it is difficult to determine whether this effect accounts for the trend observed. Dislocations in MMT grown by DAG have been investigated using TEM by Funaki et al [14], where dislocation densities of $10^9 cm^{-2}$ were observed. When MMT was grown onto CdTe buffer layers, the dislocations were seen to spread into the MMT, with a hexagonal shaped misfit dislocation array. The diffusion of Hg was also discussed as affecting the distribution of dislocations and enhancing the generation of threading dislocations into the layers. It was also remarked that the crystal quality depends on the layer thickness. A reasonable alternative/complementary explanation, therefore, may be that the FWHM is really sensitive to layer thickness, and this in turn is proportional to the layer composition.

The dependence of the FWHM on layer thickness in MMT has been investigated for DAG samples by Hallam et al [15]. When data for CdTe on GaAs, MMT on CdZnTe (CZT) and MMT on GaAs was combined with that of Brown et al [16] for CdTe on GaAs a linear relationship between FWHM and 1/thickness was obtained. Thicknesses used were between 0.7μm and 12.5μm. Only one point on this graph represents the current system in this study, however, and that lay well below the average line (and represents DAG not IMP growth). That this relationship is viable for ternary compounds can be shown from data in the paper of Bernardi et al [17] investigating LPE $Hg_{1-x}Cd_xTe$. In this case thicknesses out to 20μm have been measured, and the graph of FWHM against 1/t (although not plotted in the paper) gives a good fit to a straight line.

The data obtained here have been plotted as FWHM against 1/t in Fig 6.8. It can be seen that no linear relationship is observed, although a general conclusion that smaller FWHM are observed for thicker layers is clear. The difficulties in the thickness measurements are clearly illustrated, as a thick CdTe buffer layer would affect the results substantially. It is not necessarily true that the 1/t trend should be observed here. The IMP process differs from other techniques in the way that dislocations will propagate from an interface, composed as it is of lots of interfaces. The thickness of the layers grown and the amount of diffusion between layers will affect the dislocation density, as well as misfit dislocations propagating from the substrate or buffer. In fact, other authors have reported increased dislocation density and FWHM on changing from DAG to IMP systems [18], emphasising the fundamental differences in dislocation generation and propagation.

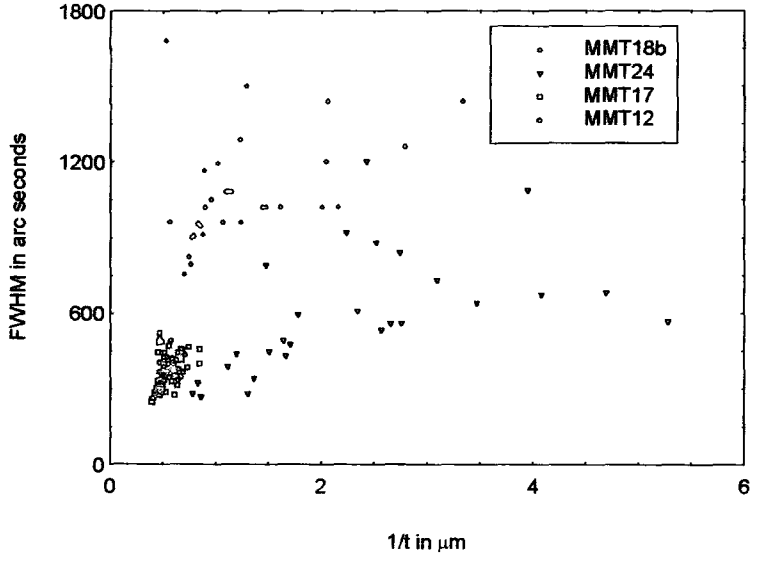

Fig 6.8: Crystalline perfection varying with inverse thickness

It has been suggested that the decrease in crystal perfection with manganese fraction is due to the dependence of x on the layer thickness. As can be seen in Fig 6.9, there is no firm trend, but layers with a high manganese fraction tend to be thin. The values of thickness for MMT24 are likely to be overestimated, as a strong CdTe peak is seen in diffraction scans. The reduction in thickness with increased Mn fraction has been observed previously, with DAG layers, where it was attributed to the slower growth rates necessary to produce high x layers. This is also applicable in the case of IMP. It may also be related to the presence of concentration gradients perpendicular to the

surface, where the top layers tend to display a higher concentration of Mn. This will be discussed later.

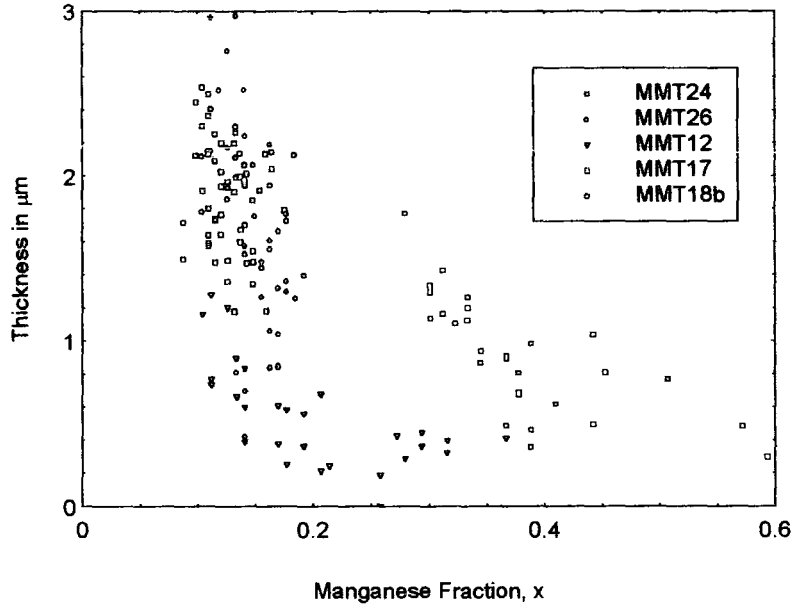

Fig 6.9: Relationship between layer thickness and Mn fraction

6.4 : Strain Investigations

In a system with such large mismatches as CdTe on GaAs, it is likely that the layer is almost completely relaxed. Relaxation is defined as,

[6.5] $$R = \frac{a_l - a_o}{a_r - a_o} ,$$

where a_l is the layer lattice parameter measured, a_o is the substrate lattice parameter and a_r is the relaxed layer lattice parameter. As relaxation affects the lattice parameter, it can be measured using x-ray diffraction, which has been performed in a number of publications [19-22]. In order to measure the in-plane and out-of-plane relaxation it is necessary to use at least one symmetric and one asymmetric reflection. The addition of further asymmetric reflections allows the effects of layer/substrate tilt to be removed.

6.4.1 : Double Axis Diffraction

In MMT, the buffer layer is supposed to relieve the stresses caused by the lattice mismatch through the formation of misfit dislocations. The MMT layer is therefore well matched to the buffer layer below, and the effect of relaxation is small in terms of

the movement of the Bragg peak. A further complication in this system is that a change in concentration will have the same effect as the addition of some residual strain. Without the knowledge of the precise relaxation at an exact point on the sample, therefore, the accurate manganese concentration cannot be calculated.

In order to gain an estimate of the relaxation, four scans were performed on the D200 on sample MMT24, believed to have a relatively thin MMT layer. The D200 was used as the micrometers were found to be uniform across the 30,000 arc second range necessary. An 004 double axis symmetric scan was followed by a 115 asymmetric with grazing incidence, both of which included the substrate peak as well as the layer peaks. The sample was then rotated about the surface normal, by 90^0, and the scans were repeated. These scans were then simulated using RADS, which, as it gives a dynamical simulation only, gives much narrower peaks than those obtained in reality. The position of the peaks is the important quantity, however. The experimental scans and simulations are shown in Figs 6.10 and 6.11.

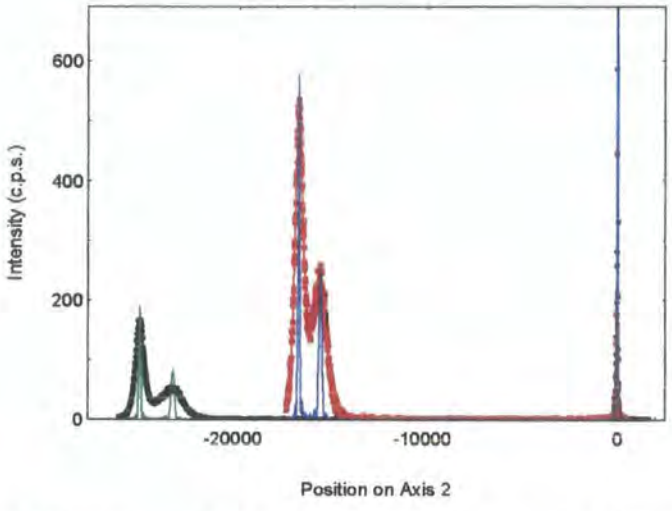

Fig 6.10 : 004 and 115 scans and simulations for MMT24

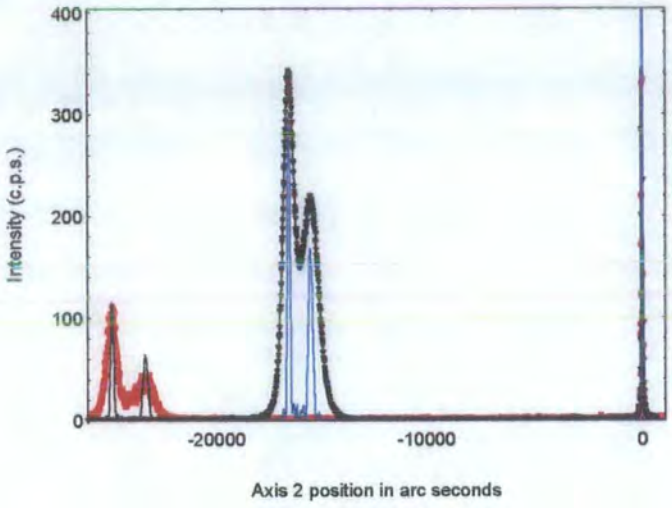

Fig 6.11 : 004 and 115 scans and simulations of MMT24 after rotation through 90°

In these scans the CdTe peak is on the far left and the MMT near to it on the right. The tallest peak on the far right is GaAs. The scans have been shifted to position the GaAs peaks all at the origin. The scans with the larger range and lower intensity correspond to the 115 reflection.

In both 004 scans the CdTe is simulated as being 98.8% relaxed, i.e. normal to the surface, while in the 115 scans it is 98.4% relaxed. Both of these carry a fitting error of less than 0.05%, which comes from the accuracy to which the peak position can be measured. The relaxation in-plane is slightly less than that out-of-plane, but as both 115 scans yield the same value, it is symmetric in-plane. This situation is known as tetragonal distortion.

For the MMT scans, the layers can be simulated either as fully relaxed, with a higher manganese fraction, or slightly strained with a lower one. Taking the first of these options gives $x = 0.30 \pm 0.01$, with the error being due to the width of the peak. As this value is returned for both the symmetric and asymmetric scans, there is no reason to conclude that the layers are strained. In fact, if the relaxation of MMT varied between 0% and 100% on the almost fully relaxed CdTe buffer layer, a peak shift (for the 004 reflection) of only 420" would be observed. As the FWHM of both the CdTe and MMT peak is in excess of this value, the sensitivity of this measurement is severely hampered by the wide tilt distribution. When these scans are simulated within Bede Scientific's CAP program, which automatically performs the simulations shown above,

Mn fractions of 0.292 and 0.288 are obtained, with a relaxation of 99.3%. These values are within the errors of the values quoted above.

The effect of tilts masking the lattice parameter in the MMT layer can be removed by performing scans in triple axis mode, i.e. through an analyser crystal. As has been described in Section 3.4, this technique allows reciprocal space mapping, where changes in lattice parameter, i.e. changes in composition or strain are mapped along the q_z direction, while tilts between blocks of crystal are mapped along q_y. One problem with II-VI epitaxial layers in general, and MMT in particular, is that the intensity obtained from a reflection is relatively low. This makes triple axis scanning difficult as the intensity is further reduced by the addition of an analyser crystal. This can be compensated for by using fewer analyser (and/or monochromator) reflections, by using an analyser slit to provide a wider acceptance angle than is available from analyser crystals, or by increasing the source intensity. In this case, although slit defined laboratory triple axis diffraction was performed, it was found to be far more advantageous to exploit the intensity combined with the resolution of a synchrotron source.

6.4.2 : Triple Axis Reciprocal Space Mapping

Triple axis diffraction scans were performed at Daresbury Laboratory on Station 2.3, using the experimental arrangement described in Section 3.5.1. Scans were performed by stepping θ-2θ and scanning θ. Count times were in the region of 1s per point, and step sizes of 0.1° were used with finer scans being added around features of interest. A program was written in Turbo Pascal, which normalises the data for the beam monitor, and converts to reciprocal space. Where asymmetric reflections are employed, the co-ordinates are adjusted appropriately so as to to rotate the axes. They have then been gridded and mapped within the Golden Software Surfer package. The minimum contour shown on each map is equivalent to 1 c.p.s., and the contours are natural logarithms in steps of 0.25, so represent countrates of 1, 1.28, 1.65...etc. The peak count is typically in the region of 36,000 c.p.s.

Two samples were chosen for initial investigations, as one had a thick MMT layer in the region of 6μm and the other had a thin layer of less than 1μm. Scans around the 004 and 115 reciprocal lattice point, with the latter being in grazing incidence, were taken. The scans for the thick layer are shown in Figs 6.12 and 13.

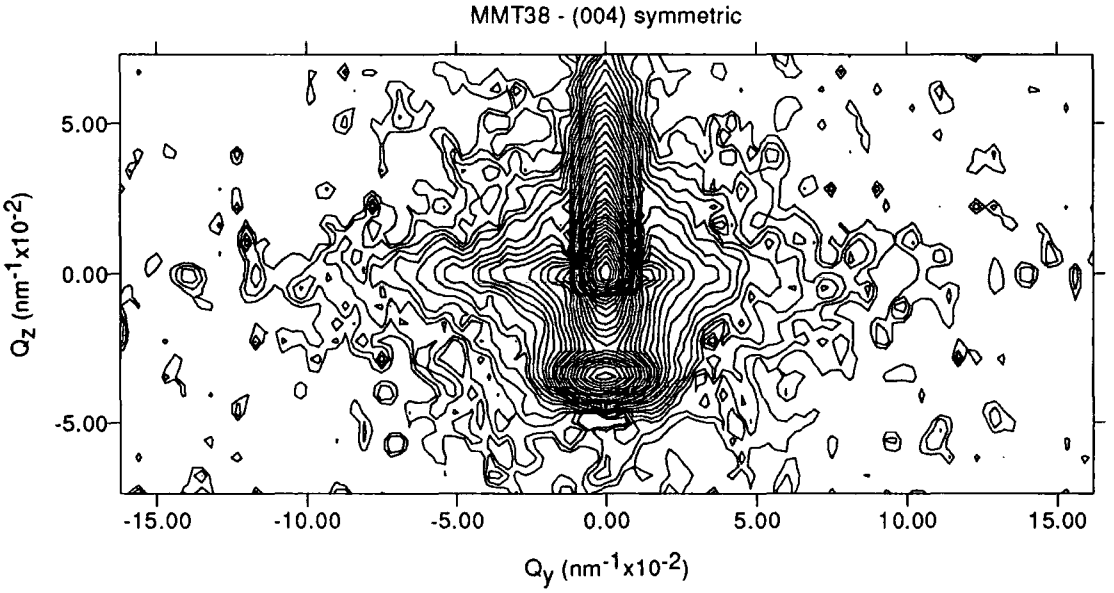

Fig 6.12 : Symmetric scan for thick MMT layer

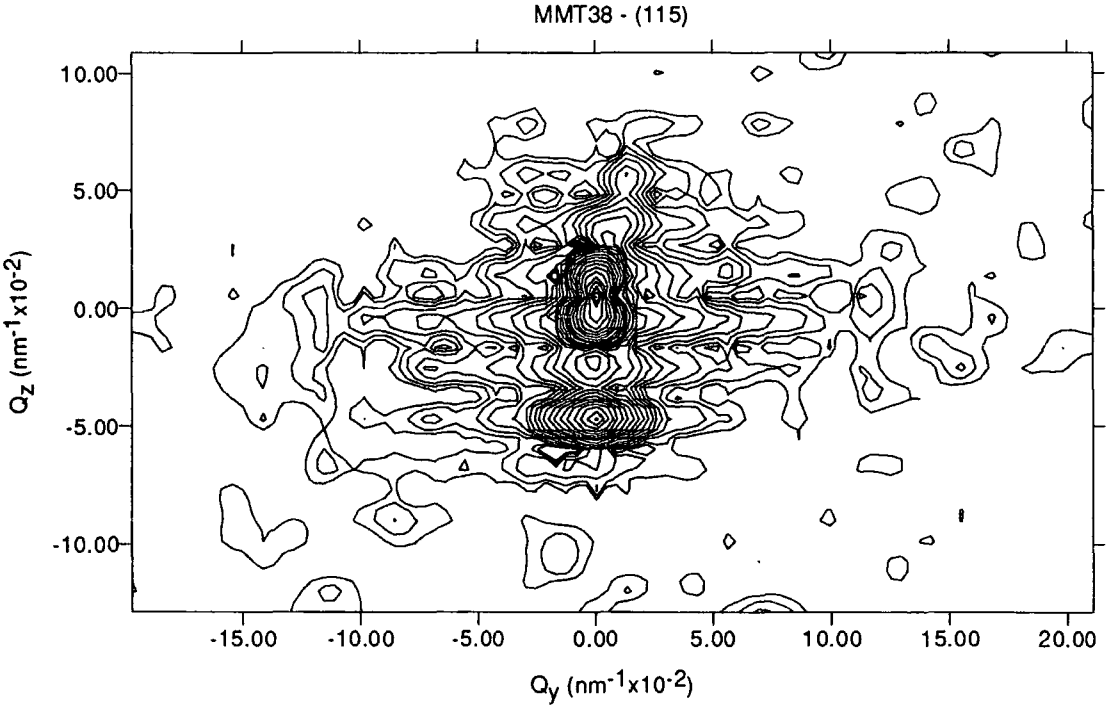

Fig 6.13 : Asymmetric scan for thick MMT layer

In a surface-symmetric scan, the x-rays are only sensitive to the lattice parameter perpendicular to the surface. In the reciprocal space map, shown in Fig 6.12, the

spread in intensity along q_z corresponds to a change in this lattice parameter. In all these scans, MMT is the upper peak and CdTe is the lower peak. In MMT38, the MMT peak shows a triangle-shaped distribution of intensity which has been observed frequently in II-VI semiconductors [23]. The greatest diffuse scattering is seen around the peak position, which corresponds to a manganese fraction of 0.17. The scattering is symmetric about $q_y = 0$, demonstrating a uniform tilt distribution. The CdTe peak is symmetric in the q_z direction but is dominated by tilts. The MMT peak shows a wide tail towards high q_z. As the peak on the low q_z side is extremely sharp, this corresponds to a peak lattice parameter of 6.440Å and a gradient towards lower lattice parameters. This could correspond to two cases. Firstly, the lattice parameter could be changing due to a strain gradient within the layer, i.e. a highly strained interface with a relaxed surface. Secondly, a gradient in composition, i.e. Mn fraction, with depth through the layer would cause a broadening along q_z. In this case, the broadening is towards a higher Mn fraction. The extent of the diffuse scattering decreases with higher x, yielding the triangle-like pattern in reciprocal space shown here.

The broadening due to strain and compositional changes can be separated by the use of an asymmetric reflection, due to the difference in angle between the surface normal and q_z direction. This is illustrated in Fig 6.14 for both the symmetric and asymmetric case. The line $\gamma = 1$ represents the direction of broadening where the layer is fully lattice matched with the substrate, and $\gamma = 0$ is where the layer is fully relaxed, as shown in Fig 6.15. Heinke et al [23-25] have developed a model for the separation of strain and compositional changes based on the "relaxation line". In this formalism, the direction of broadening of the peak allows the strain and composition parameters to be separated. The directions of broadening which they have assumed are shown in Fig 6.16. Therefore an asymmetric triple axis map can resolve the composition/strain ambiguity. The angle at which these lines lie with respect to $\gamma = 1$ is shown as α, where

[6.6] $$\alpha = \arctan(D_i^{-1} \tan \varphi)$$

and φ is the inclination angle of the lattice planes. D_i is a material constant given by

[6.7] $$D_i = -\frac{\varepsilon_\perp}{\varepsilon_{||}}$$

where $\varepsilon_\perp$ and $\varepsilon_{||}$ are the vertical and lateral strains in the unit cell.

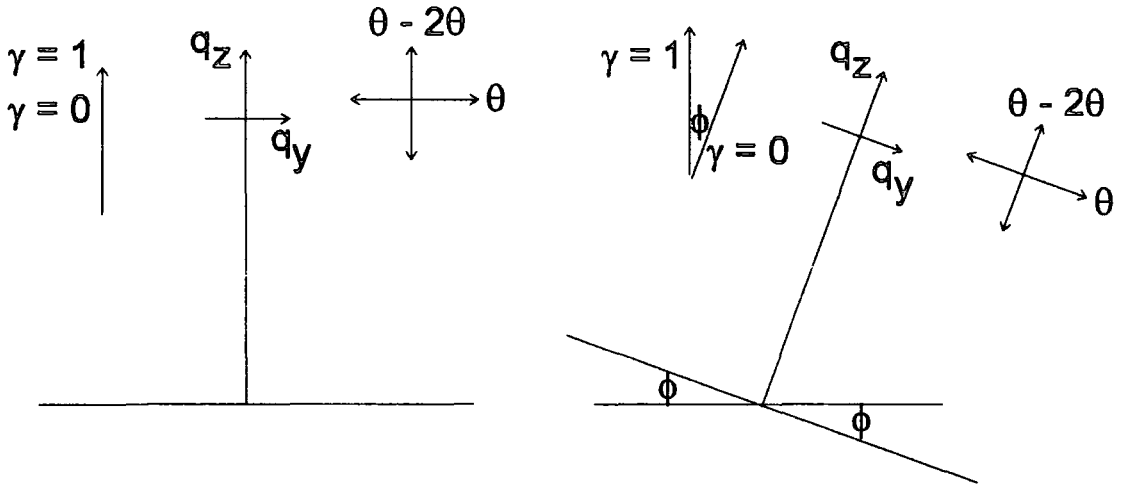

Fig 6.14 : Direction of reciprocal lattice point broadening in symmetric and asymmetric case

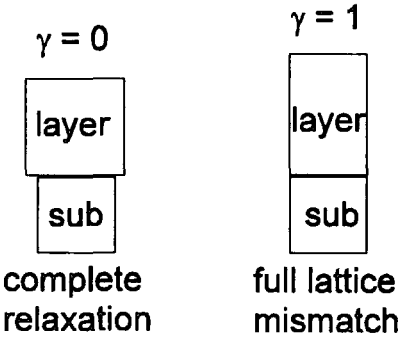

Fig 6.15 : Relaxation of epitaxial layers

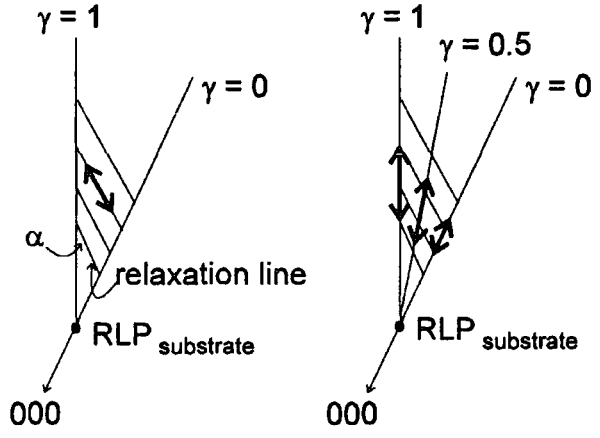

a) b)

Fig 6.16 : Broadening in reciprocal space due to a) strain gradient and b) concentration gradient

Fig 6.13 shows the asymmetric scan of MMT 38. It can be seen that the peaks again lie on $q_y = 0$, so the layer is fully relaxed. A symmetric pattern of diffuse scatter is seen, with the CdTe peak being dominated by tilts once again. There is little tail in the MMT peak, but the peak itself appears broader in the q_z than q_y direction. The indications are that the MMT layer is fully relaxed, with a smaller variation in composition. The value of the peak position corresponds to $x = 0.20$. As the asymmetric scan is more surface sensitive than the symmetric the layer must increase in manganese concentration towards the surface, but with the steepest gradient being near the interface region. Fits to this model will be given later. There is slight evidence for some strain at very high Mn compositions ($x \approx 0.5$), but the levels of scattering are fairly low.

The thick layer of MMT, therefore, is fully relaxed with a grading in composition which goes from low x at the CdTe/MMT interface to high x near the surface. As thicker layers of MMT are more likely to be relaxed than thin ones, a thin layer, MMT36, will be discussed next.

The symmetric scan of MMT36 is shown in Fig 6.17. In this case the layer is sufficiently thin for the ZnTe buffer layer (top peak) to be visible. Simulations through θ-2θ (shown in Fig 6.18) give the position of this peak to lie at that of $Zn_{0.7}Mn_{0.3}Te$. As the layers of ZnTe and MnTe should be separated by a 1μm layer of CdTe, it is likely that this may instead be a strained layer of ZnTe. A fit with the same degree of accuracy as that in Fig 6.18 is obtained for a layer of ZnTe with 85% relaxation. For the CdTe and MMT peaks, the diffuse scatter is more pronounced and extends further in reciprocal space than in the thick layer, particularly in the case of the CdTe peak. This implies that the layer is more tilted and strained than that in MMT38. The MMT peak again shows a strong gradient towards high q_z, with simulations yielding a peak value of $x = 0.14$.

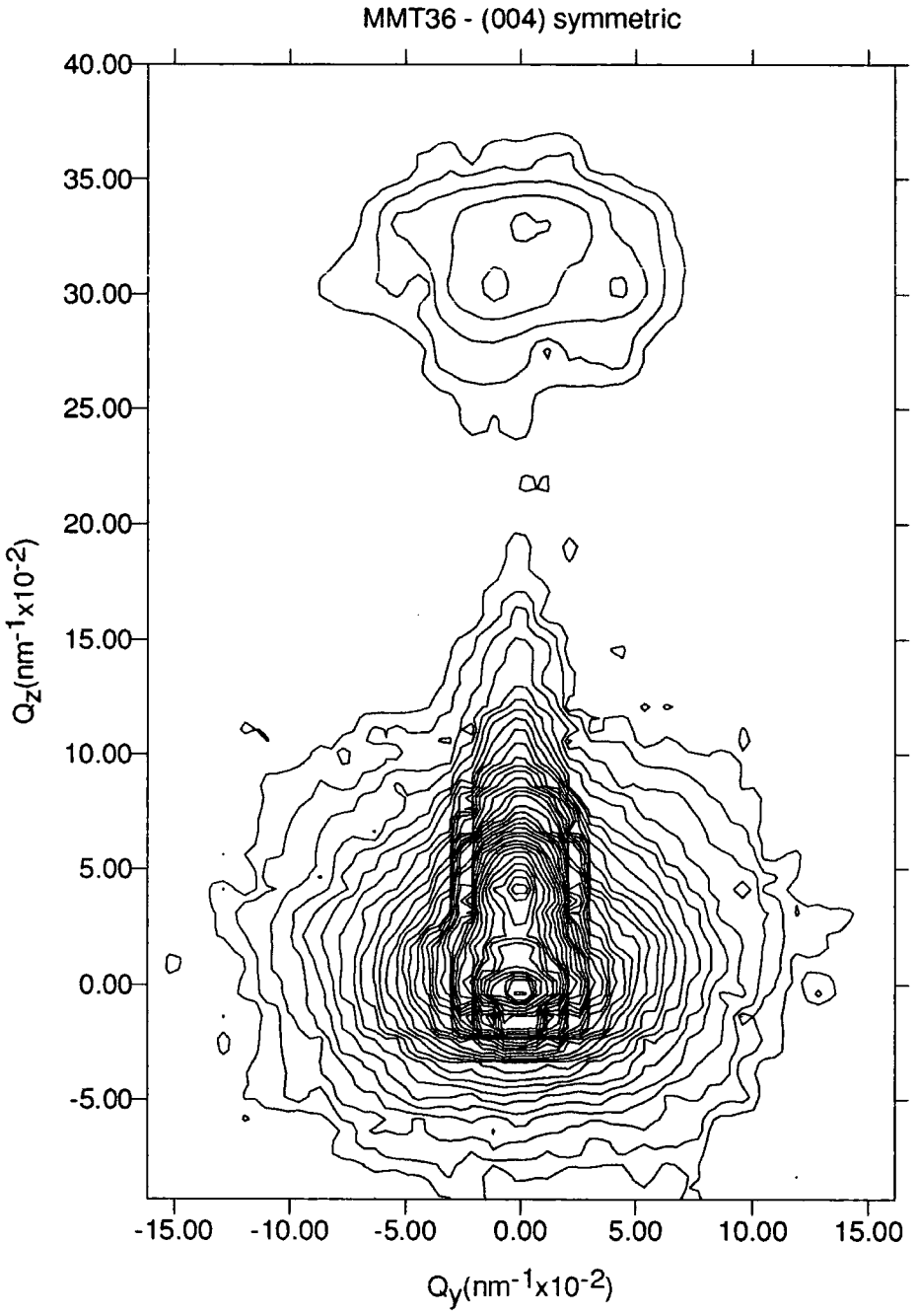

Fig 6.17 : Symmetric scan for thin MMT layer

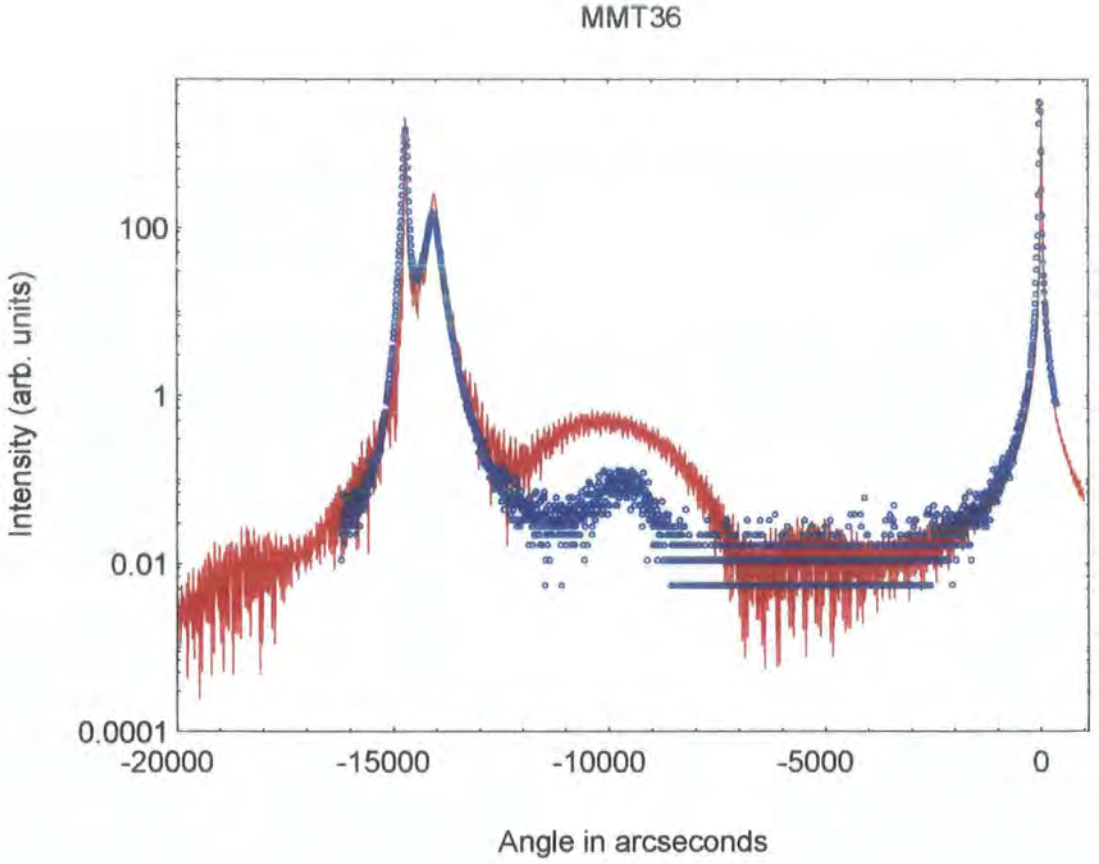

Fig 6.18 : Simulation of 004 θ-2θ scan for MMT36

The asymmetric MMT36 scan is shown in Fig 6.19. The lines for $\gamma = 0$ (fully relaxed) and $\gamma = 1$ (fully strained) have been included. It can be seen that the diffuse scatter is again extensive, but this time it is asymmetric about $q_y = 0$. The CdTe peak is fairly symmetric but the MMT has two peaks, one which lies along $\gamma = 0$, and the other along $\gamma = 1$. The extended gradient above the MMT peak is seen to be shifted, so that it lies along the dotted line. This line corresponds to $\gamma = 0.77$. As the reciprocal lattice point is broadened along a direction which lies from the substrate peak along one of the γ lines, the relaxation line model dictates that the layer is of constant γ, with variations in x. As this is the thinnest layer produced for this study, and hence the one most likely to show strain effects, all the other layers can be assumed to have gradients in concentration only, and will be simulated as such.

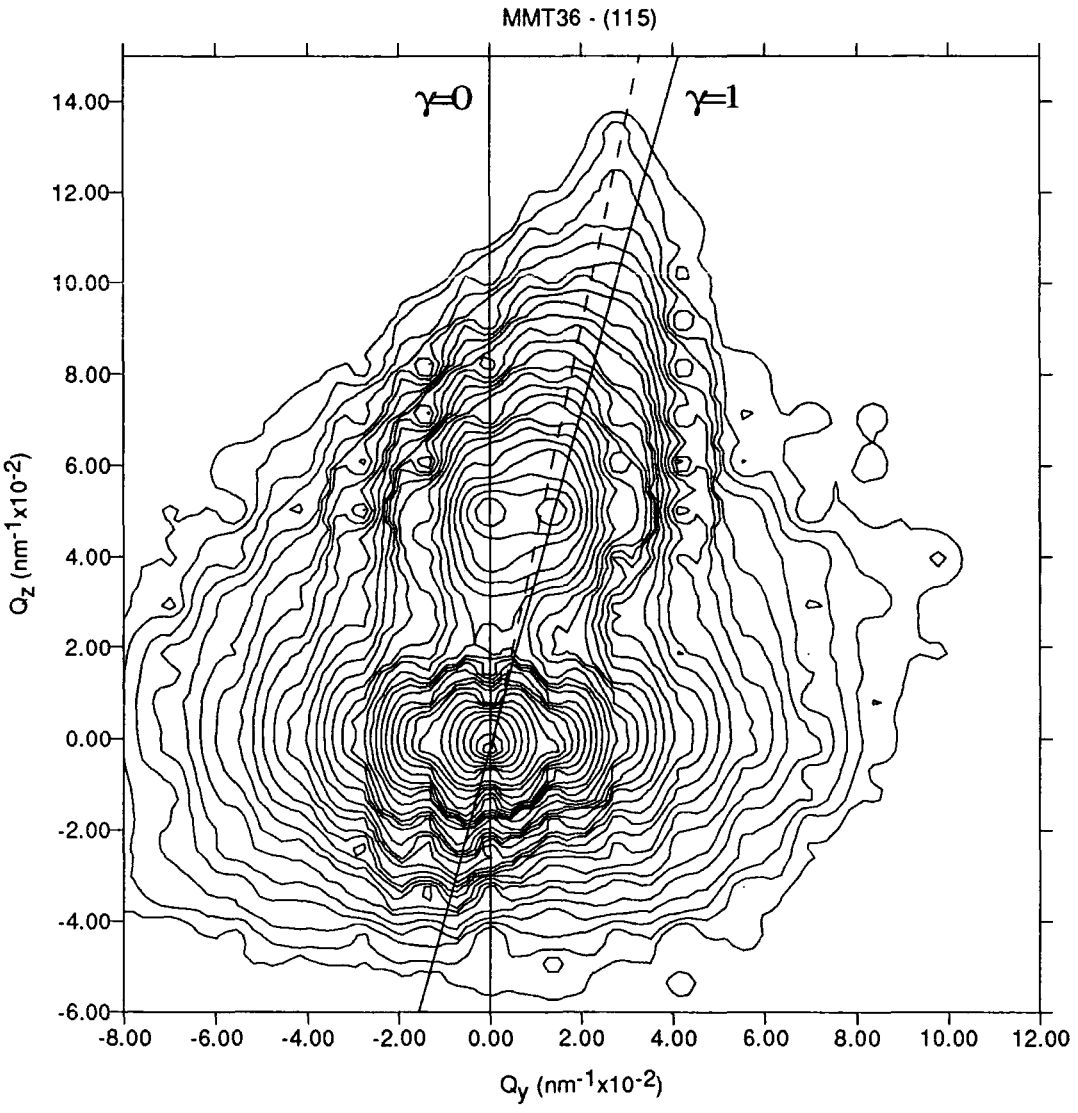

Fig 6.19 : Asymmetric scan for thin MMT layer

6.5 : Compositional Grading

6.5.1 : Depth Dependence of Mn Fraction

The vertical profile of IMP grown layers has been studied by several authors. Depth profiling has been performed using specular HeNe laser reflectance [12], infrared transmittance spectra and secondary ion mass spectrometry (SIMS) [18] and energy-dispersive x-ray spectroscopy (EDXS) [26]. Although the depth uniformity in II-VI IMP samples was found to be superior to that in DAG, some non-uniformity was observed in the case of MOCVD HgCdTe/CdTe/ZnTe/GaAs [12] and LPE HgCdTe/CdTe [17].

As depth uniformity is required, as well as lateral uniformity for device applications, it is important to ascertain whether the gradients observed here can be related to the sample growth conditions. Two samples with very differing compositions are shown in Figs 6.20 and 21. The first is a layer with a manganese concentration of only 8%. The grading is clearly seen at high q_z but the pseudopeaks are probably artefacts of the scan parameters, as are the ripples along the side of the peak. The second shows a layer with a very high Mn concentration, of 64%. Although at first glance the grading appears to be less than in MMT18b, looking at the diffuse scatter implies that this is not the case. The greatest diffuse scatter is located about the q_z value between the two peaks, so areas of sample with this lattice parameter must be present. If the sample was purely $x = 0.64$, the map would appear more as two discrete circles, with only some overlap. If a scan is taken through θ-2θ, a hump between the two peaks is visible, so another peak at $x = 0.25$ is present, and variations in composition are present.

In the IMP process, fluctuations in composition with depth must be linked either with instabilities in the growth period of one or both layers, or with the diffusion between layers occuring in a preferential direction. If the effect is due to the former, the uniformity should deteriorate with increasing thickness of the unstable layer. In order to compare the amount of grading present, detailed simulations are necessary.

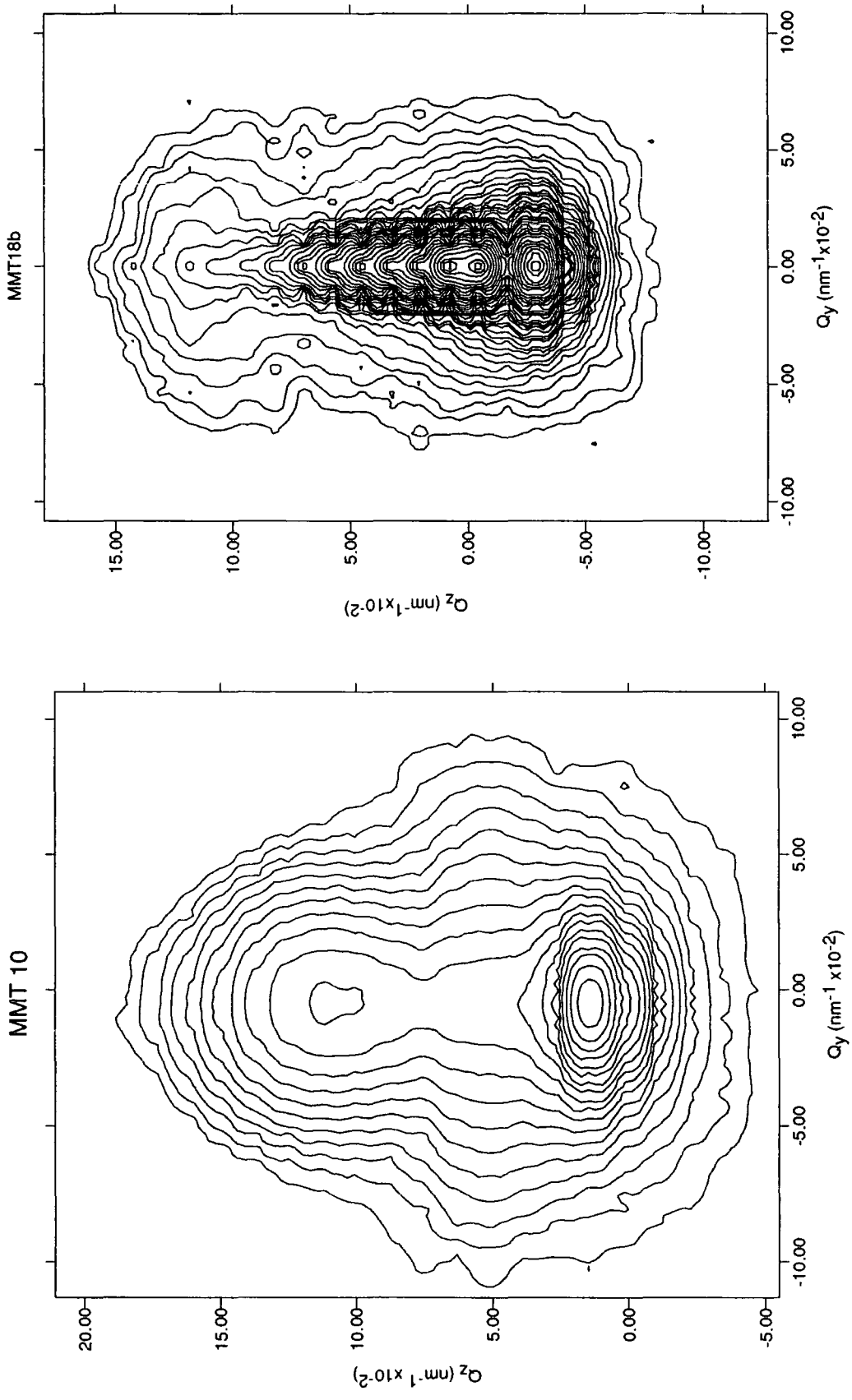

Fig 6.20 (top) and 21(bottom): Reciprocal space maps of sample with low Mn fraction (top) and high Mn fraction (bottom)

Simulations of θ-2θ scans (Figs 6.22-26) taken at Station 2.3 at the SRS at Daresbury Laboratory were performed using RADS and the material parameters given in Section 6.3. The beam intensities have been adjusted for the decrease in beam intensity during the scan, and are given in arbitrary units. In all cases the circles are the experimental data points and the lines are the simulations. As the intensity from some peaks caused saturation of the detector, an absorber was often placed before the sample. The simulations have included a 0.1μm layer of ZnTe and a 1μm layer of CdTe so only the thickness of the MMT peak has been adjusted to give the relative heights in the simulation. In some cases grading between the CdTe and HgTe has been included, but most of them just contain grading within the MMT layer.

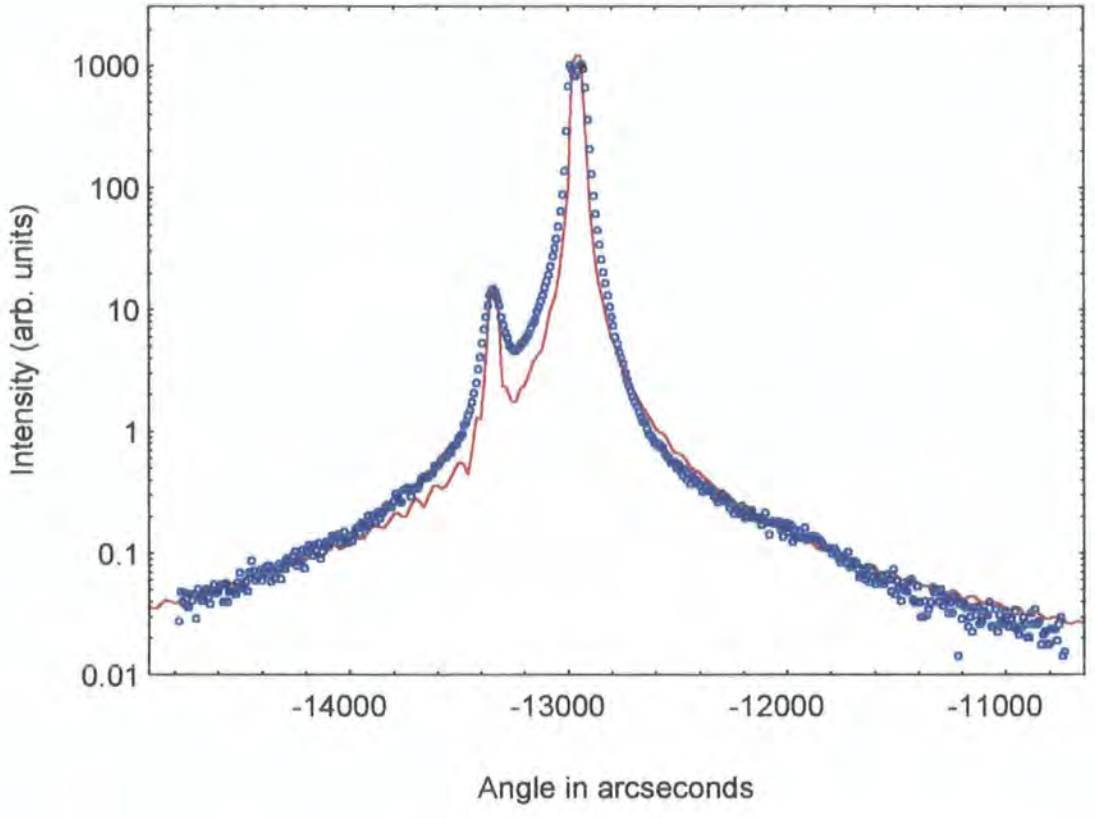

Fig 6.22 : MMT38a.

Fig 6.22 shows a sample on which a great deal of transport and electrical data has been performed, as it is n-type. The peaks are extremely narrow compared to other samples (187" CdTe, 161" MMT), and there is no evidence for grading. A dynamical simulation, together with sample curvature (to broaden the simulated peaks) provides a good fit. Although there is a slight rise in intensity around -12000", this is too small to

simulate. The high intensity between the two peaks compared to the simulation is probably due to some diffusion between the HgTe and CdTe layers, but the layer is predominantly of x = 0.103.

In contrast, a scan and simulation displaying clear grading is shown in Fig 6.23. The CdTe peak is still narrow, but the MMT peak shows asymmetric broadening, and an additional peak at about -11000". The grading has been simulated by dividing the layer up into a series of lamellae, with composition steps of x = 0.05 (or in cases of low grading 0.01). The thickness of these lamellae has then been adjusted during simulations, so the peak x, for example, corresponds to a large proportion of the sample thickness. As the layer is represented as a series of ten or twenty lamellae, some intensity fluctuations corresponding to the individual lamellae remain.

Although this sample is the same as that in Fig 6.20, a different part of the sample is investigated. There is grading from the CdTe buffer to the HgTe layer, and very little Mn is incorporated at the peak position. The incorporation of more Mn leads to the broad shoulder, followed by another wide peak, which is simulated as being cubic MnTe. This implies that the Mn has not diffused successfully through this sample, leading to a low Mn content MMT layer, and MnTe clumps, These are probably near the surface, as the presence of CdHgTe implies that the low x peak position is near the interface.

A sample with far less grading (out to x = 0.35) is shown in Fig 6.24. There is no evidence for a MnTe peak, and the higher scatter on the high angle side compared to the low is due to the ZnTe content in the material. The peak x is at 0.12. The next two simulations, in Figs 6.25 and 26 have higher Mn fractions, with x = 0.19 and x = 0.413. It is interesting to note that as the Mn composition increases, the CdTe peak broadens so the fit is not as good. This is probably due to the increased misfit between the layers leading to a higher dislocation density, and hence strain in the CdTe. Both these samples show grading behaviour, right out to MnTe, although no MnTe peak is visible.

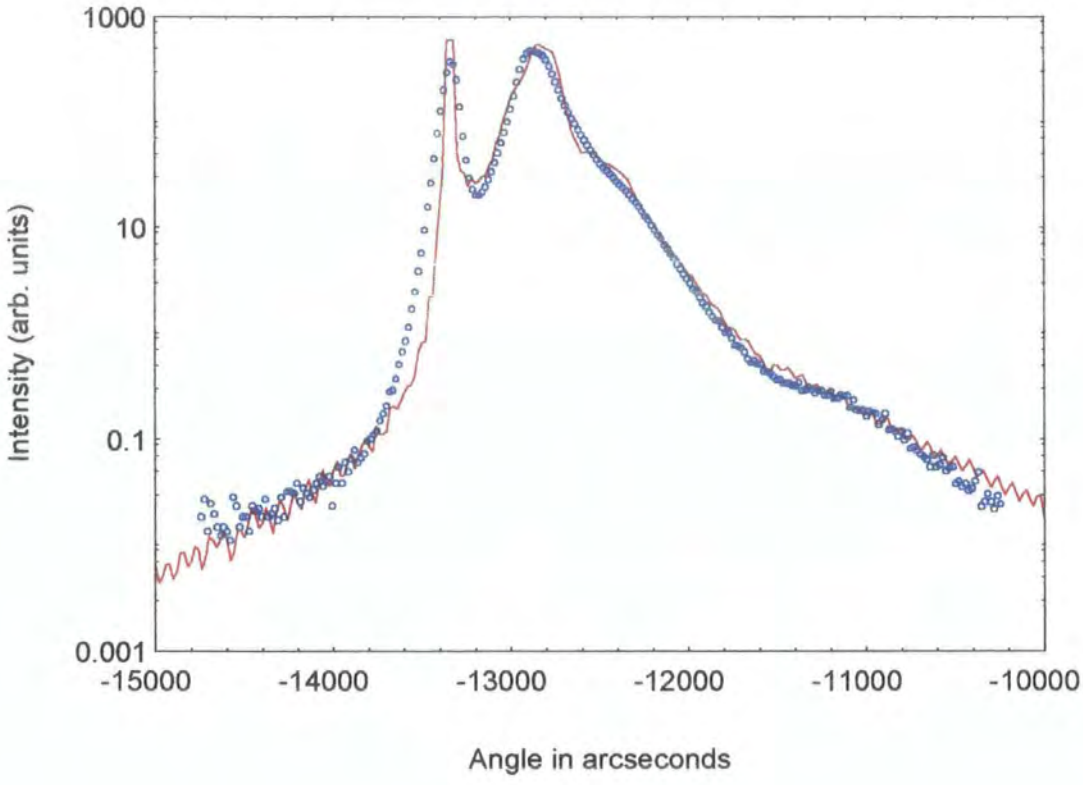

Fig 6.23 : MMT18b

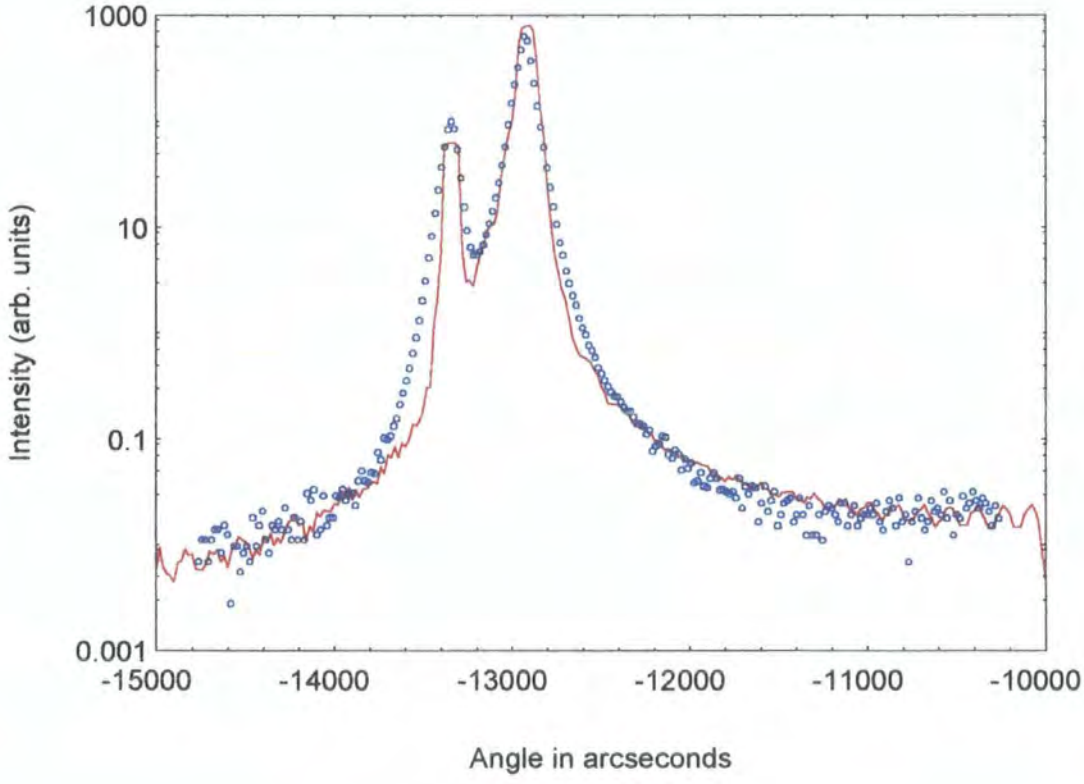

Fig 6.24 : MMT39a

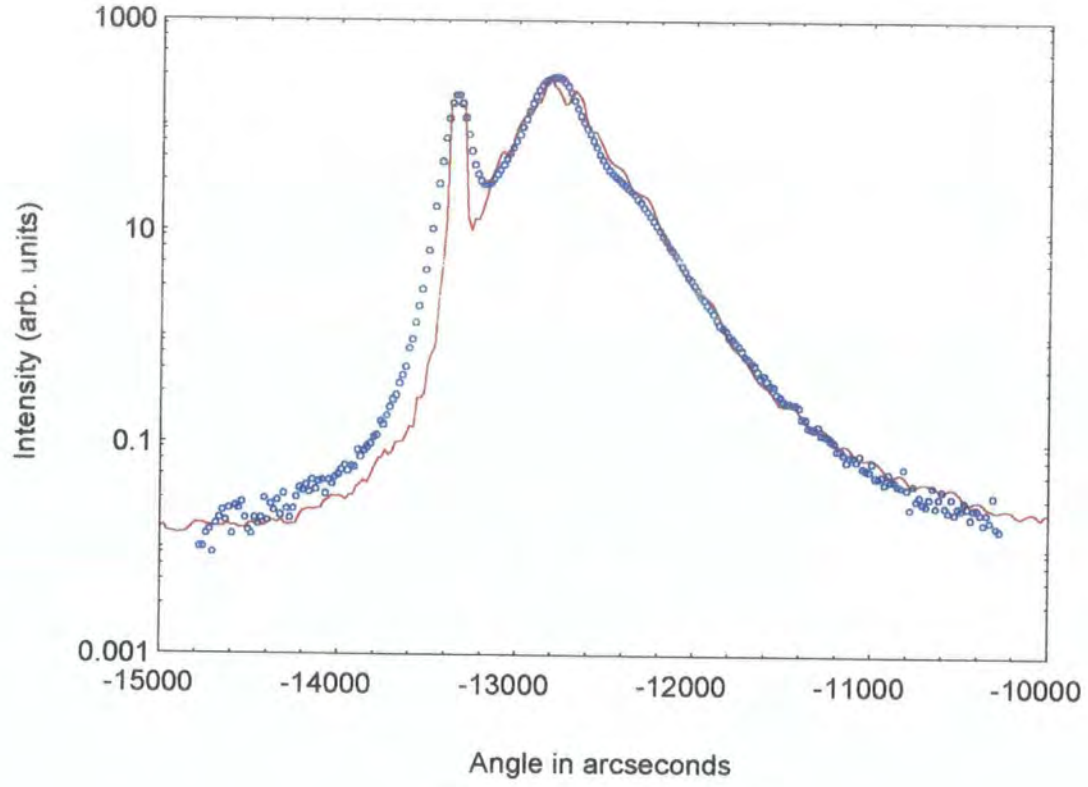

Fig 6.25 : MMT18a

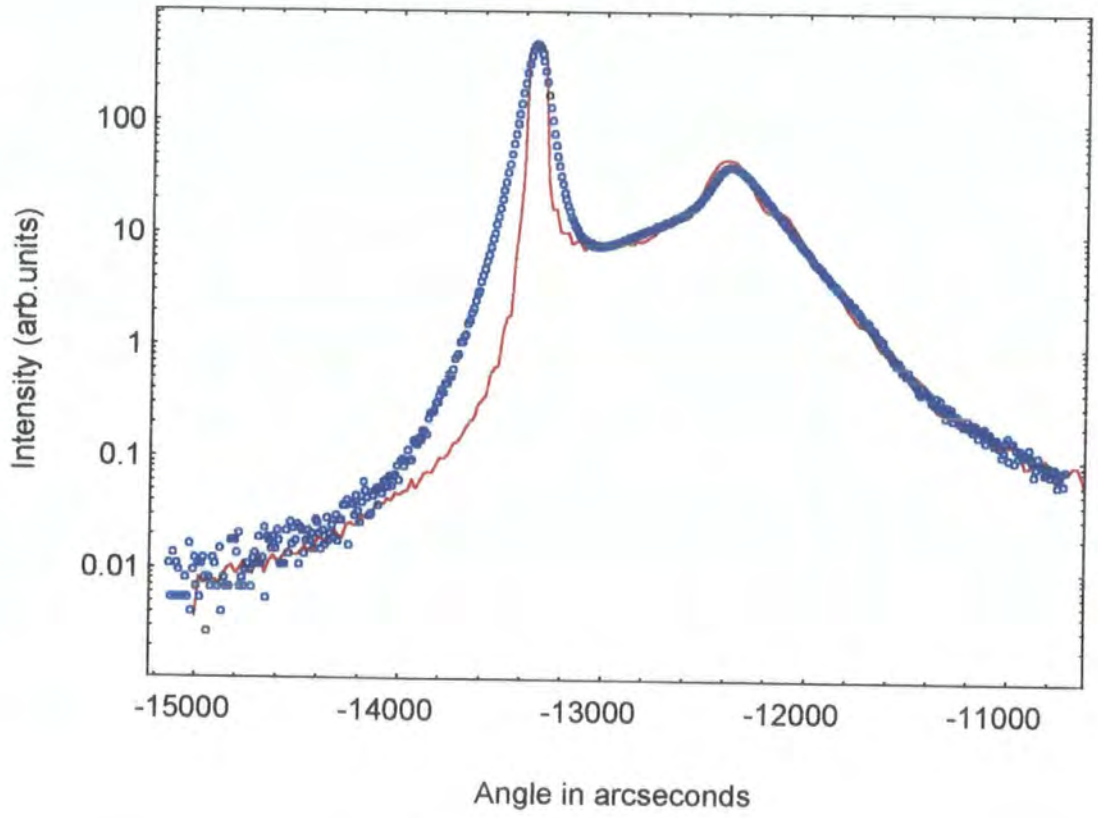

Fig 6.26 : MMT37

The grading parameters used in these scans, and others are shown in Fig 6.27. For each lamella, the manganese fraction has been plotted at the central position, so the lines do not go through the origin. The total thickness of the layer has been scaled to 5μm, so the gradients of manganese change with depth can be compared. The very top surface has been removed, due to the presence of small amounts of MnTe. A sample with a layer of one composition (such as x = 0.10), gives a horizontal line, while layers with large changes show a large gradient. It can be seen that as the peak fraction of Mn present in the sample increases, it is more likely that a large fluctuation in composition will occur. Up to x = 0.12, therefore, uniform growth can be obtained, but above this it becomes difficult.

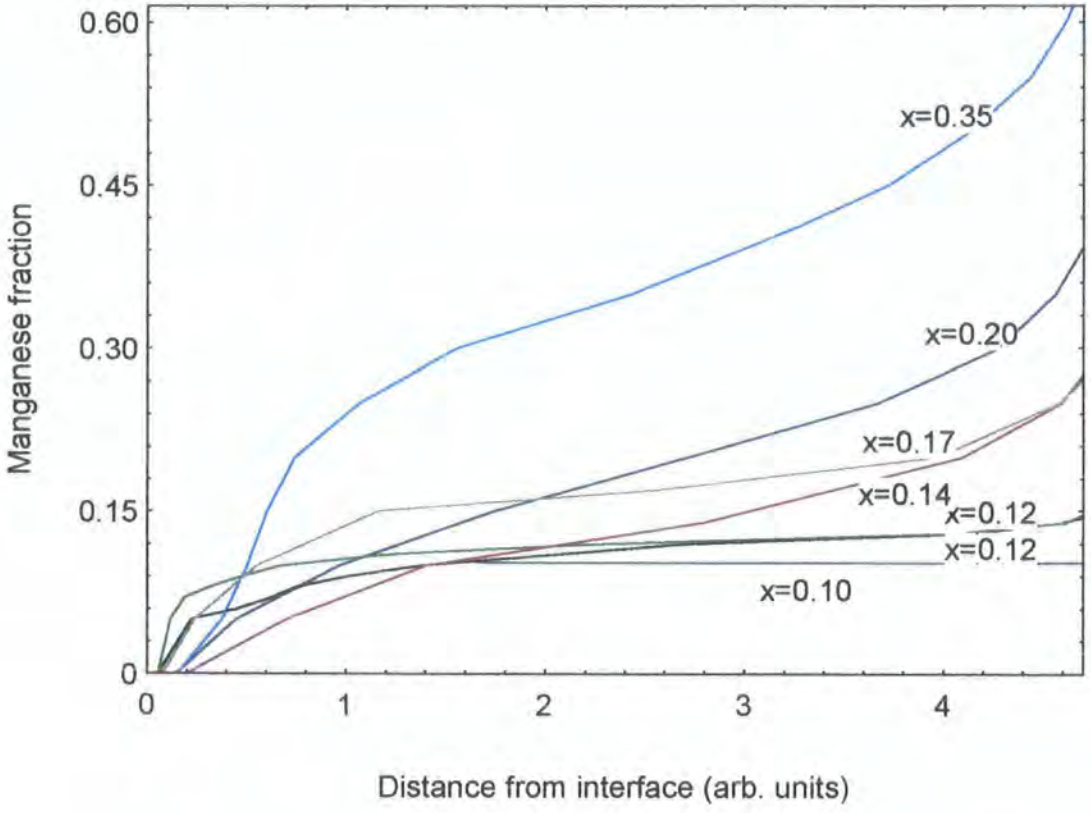

Fig 6.27 : Dependence of grading on x

Irvine et al [12], in their studies of nonuniform HgCdTe/CdTe/ZnTe/GaAs attributed fluctuations to changes in the DIPTe partial pressure (used for both CdTe and HgTe layers). This was due to condensation in the feed line, and was reduced by lowering the bubbler temperature. In the case of IMP grown MMT [27], the room temperature vapour pressure of TCMn is low, so the TCMn bubbler is heated to 75°C to obtain

sufficient precursor vapour pressure. This is compared to a temperature of 15°C for the DIPTe bubbler. The high temperature of the TCMn and the relationship between amount of MnTe deposited and nonuniformity, implies that this is an analogous situation, and that the fault lies with the TCMn precursor.

As well as compositional grading in the layers, the presence of MnTe is unexpected for the IMP growth process. The presence of clumps of cubic MnTe (or, more rigorously Mn doped Te) had, however, been postulated by Horsfall et al [28] due to anomalous magnetic and magneto-transport behaviour in some samples. They observed saturation in their Hall Effect measurements and anomalies in the magnetoresistance, as well as magnetic ordering at room temperature. All these could imply the presence of clumps of MnTe in the sample.

6.5.2 : Investigation of "MnTe" clumps

A clear MnTe peak is seen in Fig 6.28, where the simulated peaks are to show the positions expected for relaxed layers of CdTe, MMT and MnTe. The scan is double axis with open detector, so the peaks are broadened by lattice tilts. In this case, as in MMT18b, the Mn fraction in MMT is low, at x = 0.04. The MnTe peak was visible right across the sample, with a FWHM varying between 380" and 580", as shown in Fig 6.29. As has already been seen, the peak is far less evident through an analyser crystal, implying that the layer is highly tilted, and of poor crystallinity, as would be expected.

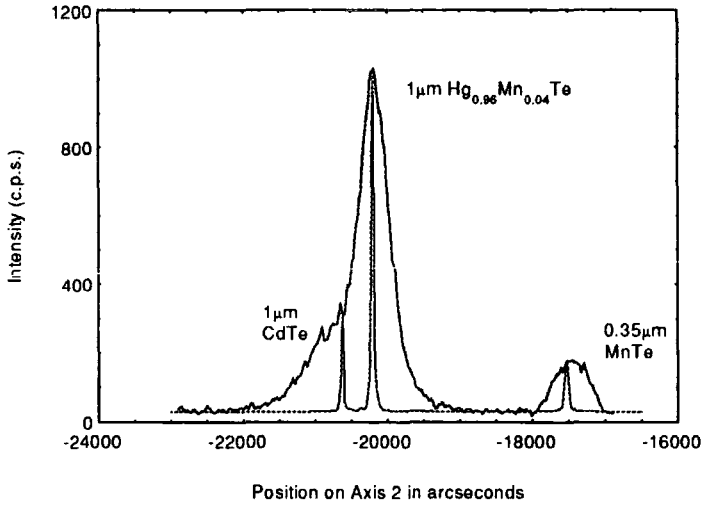

Fig 6.28 : Presence of a MnTe peak in MMT18a

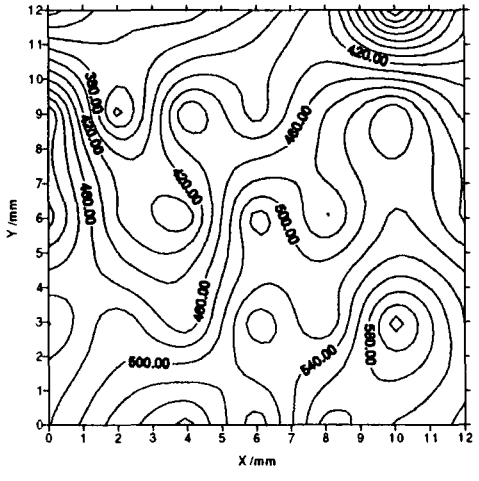

Fig 6.29: Variation of MnTe FWHM across sample

The two samples where the presence of MnTe was predicted were MMT38a and MMT16. The former has already been shown to have a uniform composition and no noticeable MnTe peak. Despite extensive scanning of the appropriate region in reciprocal space, no peak was obtained. When MMT16 was scanned in double axis mode, the profile shown in Fig 6.30 was obtained. The large peak has its centre at that expected for CdTe which, as the motors are encoded, has significance. There is no resolvable MMT peak, and the small peak on the right is near that of MnTe. This small peak has a FWHM of approximately 35" and was seen again on removing and remounting the sample, but only in some places on the sample. The line is a simulation for MnTe on GaAs with a CdTe buffer, with all layers fully relaxed. The theoretical width at this wavelength is 40" if MMT is present and 56" if not.

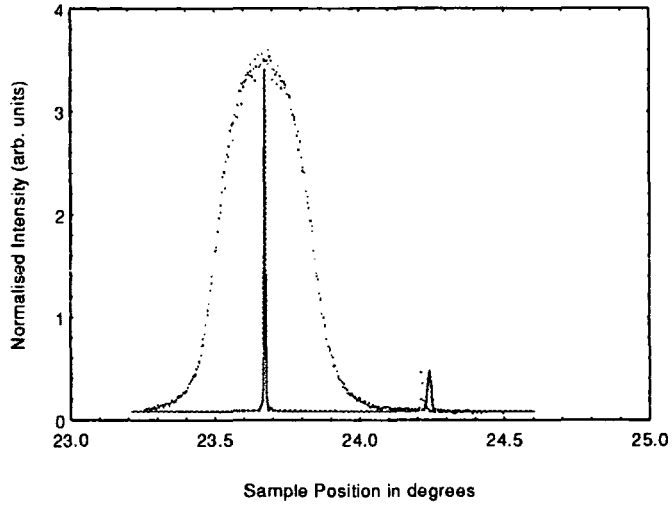

Fig 6.30: Wide buffer peak and narrow "MnTe" peak

It is clear that the narrow peak has a lattice parameter very similar to that of MnTe, but two problems are present in identifying it as such. Firstly, the absence of a resolved MMT peak makes the sample unusual, as does the extreme width of the CdTe peak. Secondly, in an epitaxial system, the layer is unlikely to have a FWHM less than that of the substrate, as dislocations and tilts in the substrate are replicated in the layer. In the case of MMT18a this was not a problem, and the MnTe did appear to be an epitaxial layer. In the case of MMT16, however, the layer cannot be epitaxial, and would have to be small clumps of material nucleating in 3D islands, where the bonding to each other was far stronger than that to the substrate. The first of these problems can be addressed by performing triple axis diffraction, which should separate the MMT and CdTe peaks. Two series of scans were taken at 1.3 Å then combined, one at the position for CdTe and one where the fine peak was present, which allowed the latter to have a smaller step size. The resultant map is shown in Fig 6.31.

The reciprocal space map shows that there is no crystalline MMT present, only a heavily tilted and strained CdTe buffer layer, which has an almost symmetric scatter distribution. The sharp peak seen at $Q_z \approx 11$ would lie at $Q_z = 13.5$ if it corresponded to the peak seen in the double axis scan, assuming that the centre of the CdTe peak was identified correctly. In an attempt to confirm the position of this "MnTe" peak, an asymmetric 115 map was made, again in two sections. The area corresponding to the "MnTe" peak produced nothing above background noise, and the CdTe peak is shown

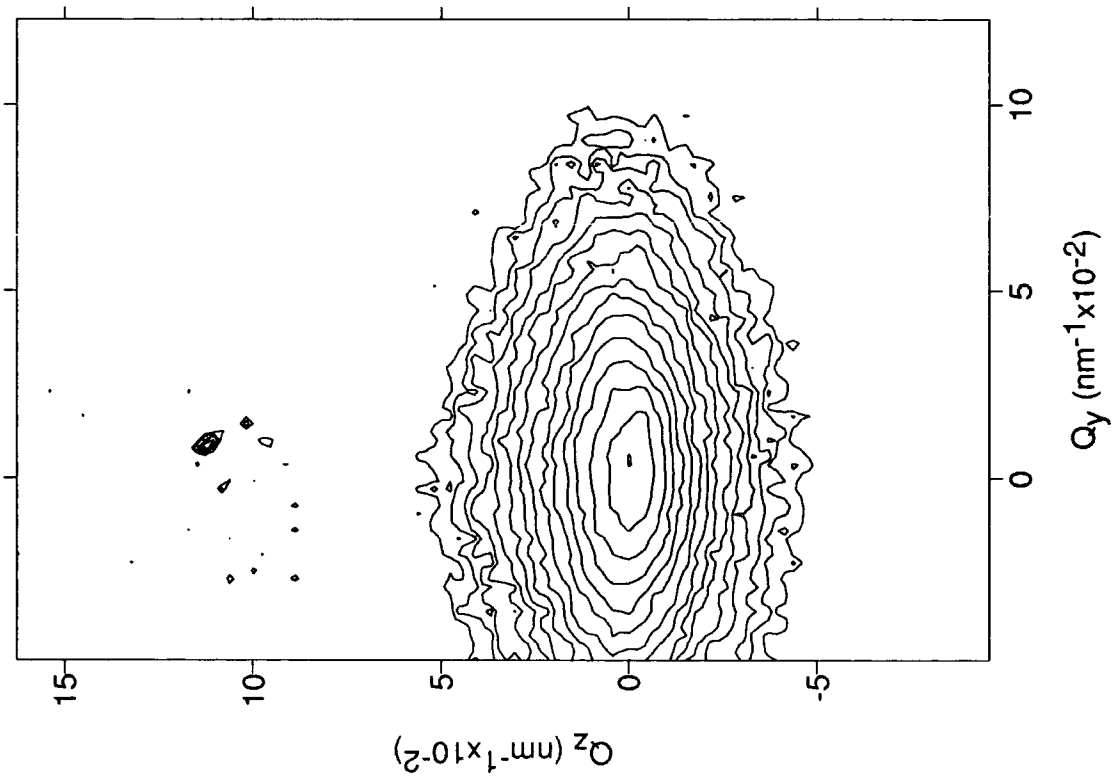

Fig 6.31 : Reciprocal space map of MMT16

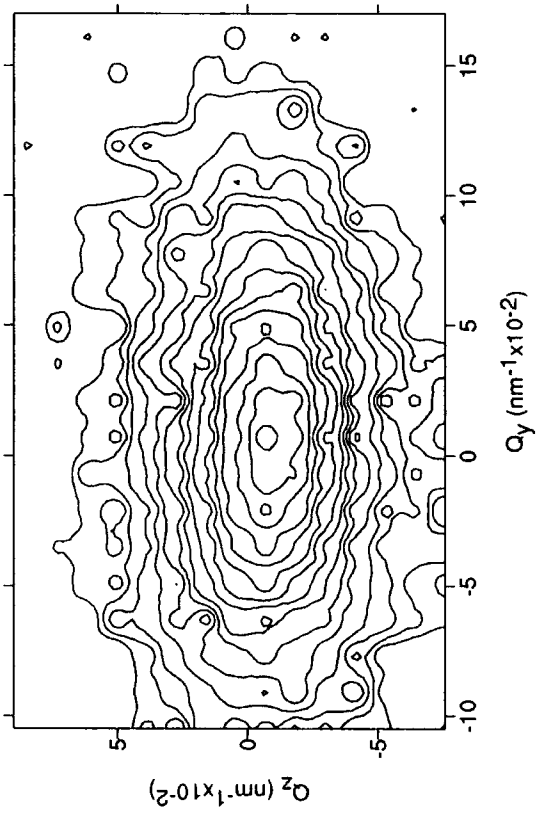

Fig 6.32 : Asymmetric 115 space map of MMT16

in Fig 6.32. Only one other sample, MMT28, was found to have a similar broad buffer layer and no MMT peak. The breadth of the buffer layer may be related to the ZnTe layer present. X-ray diffraction work on ZnTe/CdTe buffer layers [12] found a linear relationship between thickness of ZnTe layer and FWHM of the CdTe peak, with thicker layers causing an increased dislocation density in the CdTe. No ZnTe peaks were observed in either sample, however, and the FWHM in both directions are summarised in Table 6.6.

Table 6.6 : FWHM values for the two samples with a wide buffer and no crystalline MMT layer

Sample	θ-2θ FWHM (")	θ FWHM (")
MMT16	821 ± 138	2164 ± 100
MMT28	707 ± 68	6834 ± 100

It is clear that if the buffer layer is very strained, and hugely tilted, as in the case of these two samples, crystalline growth of MMT cannot occur. As electrical and magnetic measurements indicate the presence of MMT, it must be concluded that growth has proceded in a polycrystalline manner. The polycrystallinity of the intermediate layer leads credence to the idea that any MnTe deposited has developed in a non-epitaxial way, with only small clusters of MnTe diffracting in a crystalline manner.

In summary, in crystalline samples, the presence of MnTe appears to be linked to a low Mn concentration ($x \leq 0.1$), and gives a shallow and broad peak. This is consistent with the MnTe starting to form an epitaxial layer on the surface, instead of diffusing into the bulk material. In samples where growth has proceded in a polycrystalline manner, small clusters of partially strained MnTe may form, which produce sharp, low intensity peaks.

6.6 : Dislocation Density and Mosaic Block Size

6.6.1 : Dislocation densities from XRD FWHM

Pseudo triple axis scans were taken on Station 2.3 at Daresbury Laboratory, using the experimental arrangement described in Section 3.5.1. A range of samples were studied, all grown by IMP, with nominal thicknesses varying between less than 1μm and 6μm. For each sample a θ-2θ scan was performed, some of which have been shown together with simulations in the last section. The detector and sample were put to the peak position for CdTe and then for MMT, then the detector was held fixed and θ scans rocking just the sample were performed. The peaks obtained were fitted to Gaussian distributions, to extract the FWHM values. The error bars are taken as the difference between the Gaussian fit and the actual data at the FWHM position. These, together with some details on the samples, are shown in Table 6.7, while an example of a Gaussian fit is shown in Fig 6.33 The average x values have been taken from simulations of the θ-2θ scans. The integrated intensities of the Gaussian fits were calculated, and are tabulated as a ratio of integrated intensity MMT/CdTe.

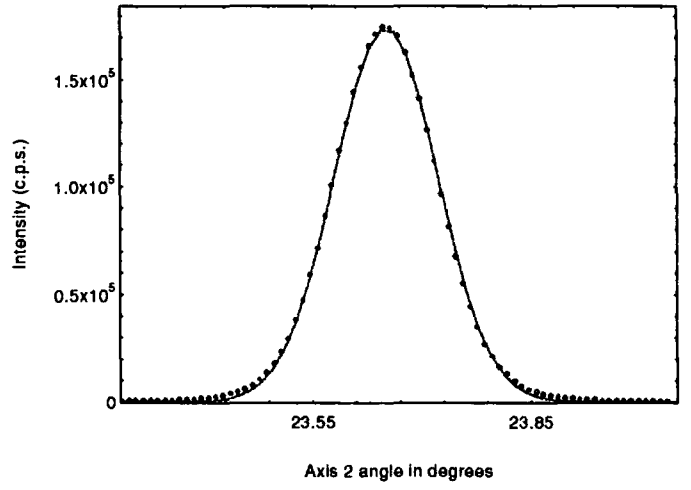

Fig 6.33 : A Gaussian fit to the θ scan for MMT18a - CdTe peak. The circles are experimental points and the line is the fit

Table 6.7 : Growth and triple axis FWHM for an assortment of MMT layers

Sample	MMT 10	MMT 18a	MMT 18b	MMT 35	MMT 37	MMT 38a	MMT 39a
Average x	0.25 0.70	0.20	0.00	0.12	0.41	0.17	0.12
Growth Time	1h55	2h20	2h20	5h45	1h10	5h45	1h45
No. Cycles	100	100	100	300	60	300	100
Ratio of Int Int	0.108 0.100	3.76	3.33	35.9	0.285	72.2	6.47
θ-2θ FWHM CdTe	215 ± 4	228 ± 15	188 ± 18	134 ± 62	222 ± 21	187 ± 12	182 ± 20
θ-2θ FWHM MMT	688 ± 4	577 ± 43	291 ± 148	202 ± 10	803 ± 159	161 ± 6	195 ± 35
θ FWHM CdTe	761 ± 4	599 ± 4	423 ± 7	530 ± 4	562 ± 14	416 ± 29	430 ± 11
θ FWHM MMT	1702 ± 278 1403 ± 4	348 ± 4	327 ± 4	150 ± 7	779 ± 9	181 ± 20	202 ± 2
Disl Density CdTe cm^{-2}	$1.44.10^9$	$8.93.10^8$	$4.45.10^8$	$6.99.10^8$	$7.86.10^8$	$4.30.10^8$	$4.60.10^8$
Disl Density MMT cm^{-2}	$7.32.10^9$ $5.06.10^9$	$3.05.10^8$	$2.67.10^8$	$5.66.10^7$	$1.54.10^9$	$8.25.10^7$	$1.03.10^8$

The measured FWHM in rocking curves has been related to dislocation density in a number of ways. The most commonly used of these is the model by Gay et al [29], where the dislocation density, D, is related to the FWHM β, by the expression,

[6.8] $$D = \frac{(\beta^2 - B^2)}{9b_{tilt}^{\ 2}},$$

where B is the intrinsic rocking curve FWHM and b_{tilt} is the component of the Burgers vector which leads to sample tilts. In using this formula, therefore, it is assumed that the presence of dislocations leads only to tilts and not to strains within the layer. As the FWHM used are taken through an analyser crystal, this criterion can be met, even if the assumption is not physically correct. In this case $b_{tilt} = a_o/2$, where a_o is the lattice

parameter. The effect of the intrinsic rocking curve is extremely small, with it being 16.5" for CdTe and 15-17" for MMT (depending on x), compared to measured FWHM well in excess of 100". The dislocation densities calculated are shown in Table 6.8, and range between 4.10^8 and 1.10^9 cm^{-2} for CdTe and 6.10^7 and 7.10^9 cm^{-2} for MMT. Dislocation densities from TEM studies on epitaxial MMT reported previously [30] were in the range 10^9 cm^{-2}, which is in excellent agreement with the data presented here.

With the exception of very high x samples (x= 0.41 and x=0.70) the dislocation density in the CdTe buffer is higher than that in the MMT layer, which means that the buffer layer is effective in matching the layer to the substrate. For very high x, however, a higher dislocation density is seen, which may be due to the difficulties of growing high x samples in the zinc blende structure, or may be due to the layers being so thin, as has been discussed previously. It has also been observed that in these samples the amount of grading is high. In this case, the propagation of dislocations from the CdTe buffer into the MMT layer is more likely. The relationship between dislocation density and layer thickness has been much debated, and has been discussed for high mismatch II-VI systems in reference [31]. In order to relate the dislocation densities measured here to layer thicknesses, simulations of the ratio of the integrated intensities for MMT and CdTe peaks for various layer thicknesses have been made. An exponential dependence of integrated intensity ratio with thickness was obtained (beyond the critical thickness), and was used to transform the ratios given in the table into thicknesses.

When thickness is plotted against FWHM and dislocation density, the relationships shown in Fig 6.34 are obtained. Each point represents a different sample, apart from the two highest points, which are obtained from two peaks in the same sample. The fall in dislocation density with thickness is similar to that reported on other materials, with thin layers having a high density which falls away to near constant levels for layers in excess of 1.5μm. This behaviour is consistent with a layer having a critical thickness less than 0.25μm.

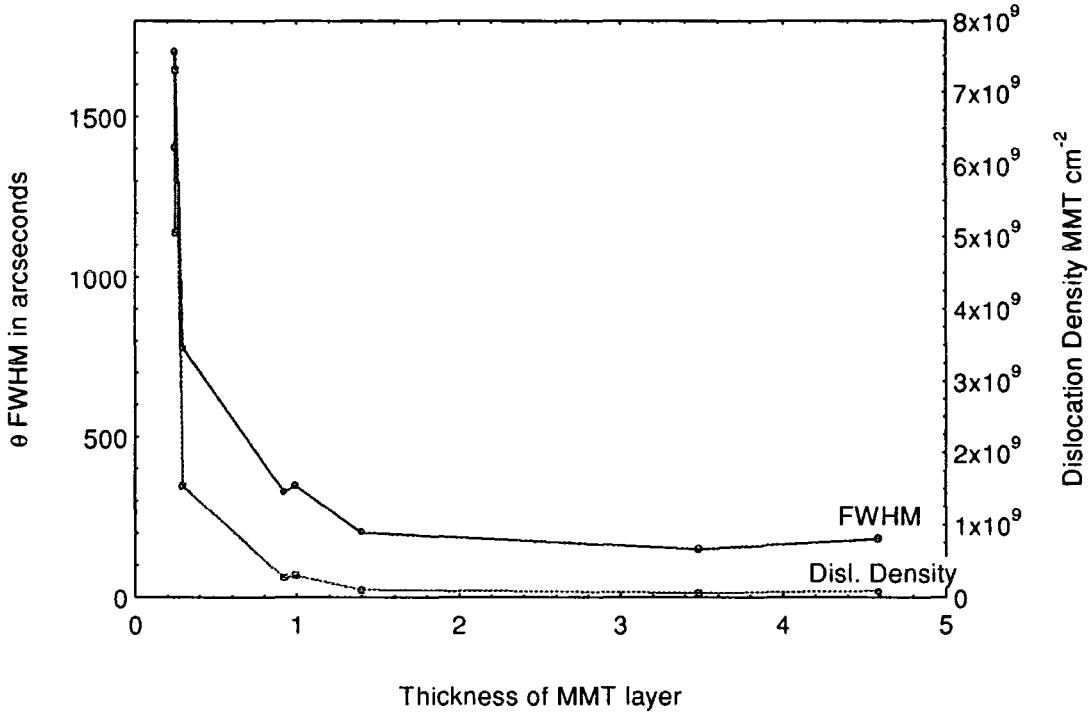

Fig 6.34 : Variation of dislocation density and FWHM with layer thickness

6.6.2 : Scattering volumes using topography

Another method of obtaining the size of blocks which scatter coherently is via x-ray topography. This potentially allows the whole wafer to be imaged, although individual dislocations are not expected to be imaged in samples with such a high dislocation density as MMT. Hudson [32] performed topography on DAG and IMP grown MMT layers, using radiation from a Cu sealed tube, and asymmetric 224 reflections for reasonable area imaging. Examples of these are shown in Figs 6.35 and 36. The DAG sample shows the presence of sub grains with dimensions in the range 130 ± 5μm. These are evenly spread out across the sample, and it was concluded that they were due to misoriented grains with little internal strain. The IMP sample studied, which was 5μm thick, gave no subgrain structure, and a large proportion of the sample was imaged. The uniformity of the IMP layers investigated in this study is less than that in the samples initially grown by Funaki [27], (as has been shown from the XY maps), and the FWHM are several hundred arc seconds wide. In order to compare the layer structure with that of higher quality IMP layers, double crystal topography was performed on Station 7.6 at the SRS, Daresbury Laboratory.

The experimental arrangement has been described in Section 3.3. A strain-relieved Si (111) monochromator crystal was used, in a (+n,+m) configuration. Both symmetric and asymmetric reflections were employed, usually at wavelengths near to the Mn absorption edge, 1.896Å, in order to sensitise the measurements to variations in Mn composition. The Bragg reflection from the sample was first found using an EDR detector, and the peak was scanned. The sample was moved to the position on the peak required, and the photographic film was placed over the detector head in order to take the topograph. In most cases, dental or D4 film was employed, as individual dislocations could not be imaged due to their high density, and these gave exposure times of up to half an hour, depending on the reflection and position on the rocking curve of the topograph chosen.

Topographs taken at the top and side of the Bragg peak (at the half maximum position) are shown in Figs 6.37 a) and b). As the angular precision on the motors was questionable (the FWHM was found to be 22"), the side of the peak was found from the measured intensity, rather than the angular position. For each position, a band of width ~700μm diffracts strongly, with some smaller blocks being visible. The size of the small areas which diffract coherently is about 25μm, in each case. The lower beam divergence at the synchrotron, therefore, allows these small blocks to be identified. On rotating the sample to the half maximum position, most of the areas which diffracted before no longer diffract. This implies that there is a large misorientation between the diffracting blocks, and that the sample is curved. The curvature on the sample can be seen in Fig 6.38, where the stripes correspond to sample rotations of 20". Several topographs have been superimposed to create this picture.

An asymmetric 224 reflection topograph, taken with grazing incidence, is shown in Fig 6.39. This looks very similar to the one taken by Hudson, in Fig 6.36. The topograph is taken on the high angle flank of the rocking curve. About half of the sample is imaged, with the other half coming into diffraction condition on the opposite side of the rocking curve. An attempt was made to map the Mn content across the wafer by moving the wavelength through the Mn absorption edge and viewing the change in the topograph on a video screen. Unfortunately the change in the contrast

was insufficient to make the comparison of topographs on either side of the edge useful.

Although the dislocation density within these layers is too great to image individual dislocations, the formation of small blocks of crystal which diffract coherently is confirmed. In these IMP layers the block size is about 25μm, which is far less than that measured in DAG layers. Good coverage of the sample is obtained even in Bragg symmetric geometry, although large misorientations exist between blocks. When topographs from different samples are compared, similar coverage is obtained.

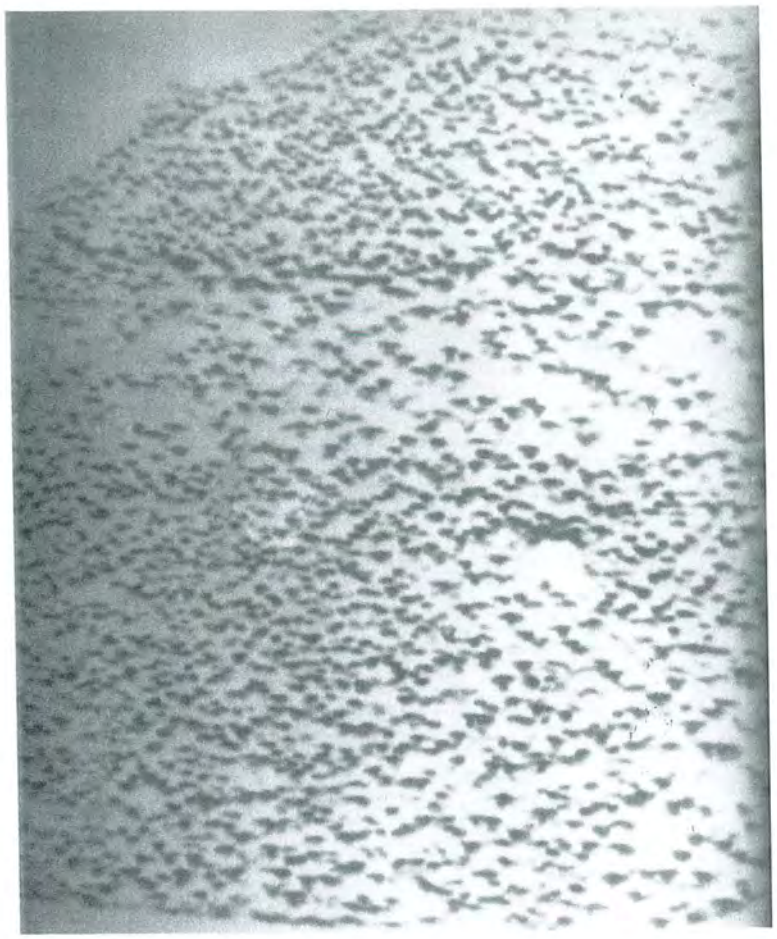

Fig 6.35 : 224 asymmetric reflection topograph for a DAG sample.

Magnification x 4.5. Courtesy of J.Hudson.

Fig 6.36 : 224 asymmetric reflection topograph for an IMP sample.

Magnification x 4.5. Courtesy of J.Hudson

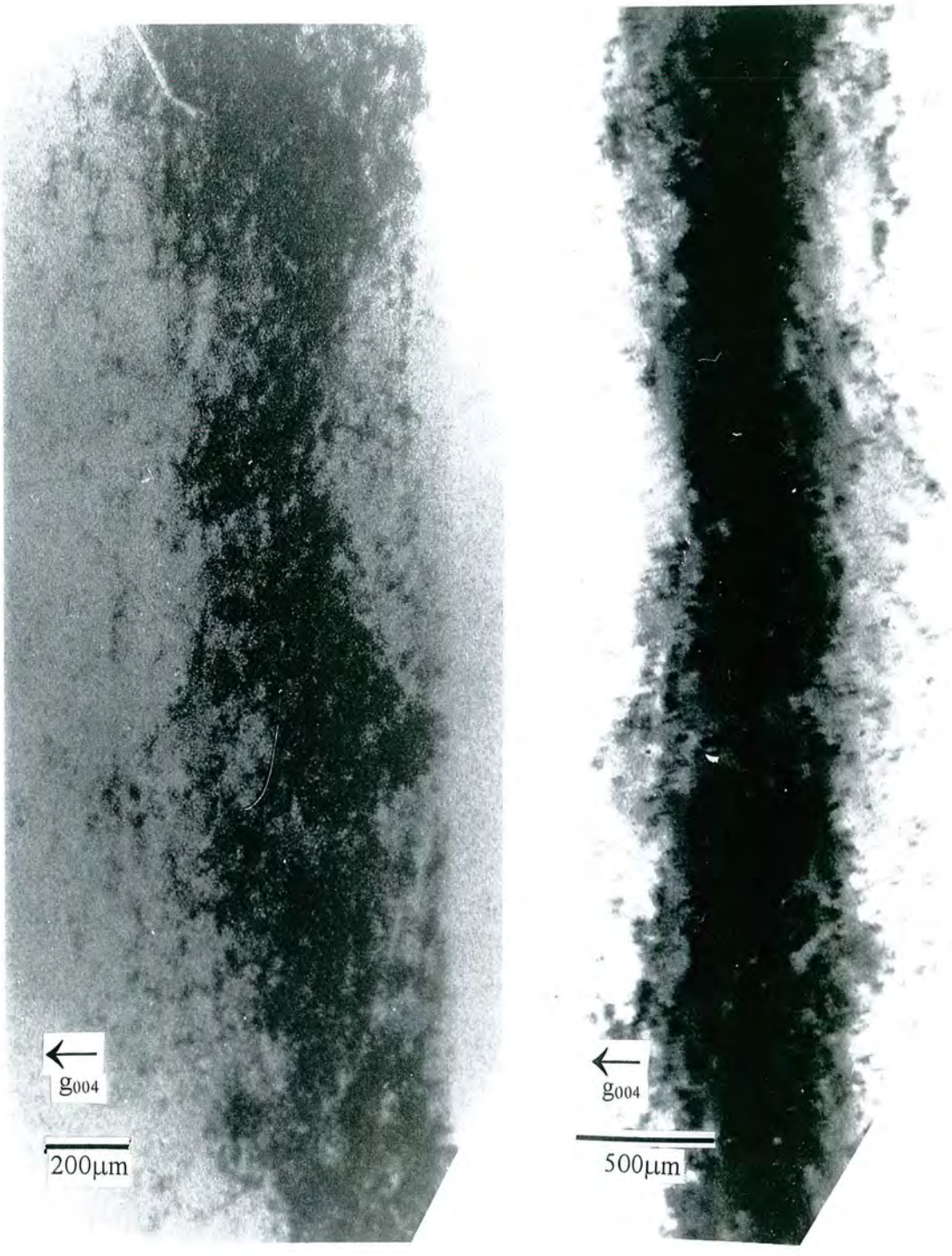

a) b)

Fig 6.37 : 004 reflection topographs of MMT36, taken at a) the Bragg peak and b) the high angle Bragg side

Fig 6.38 : Superimposed 004 topographs for MMT36

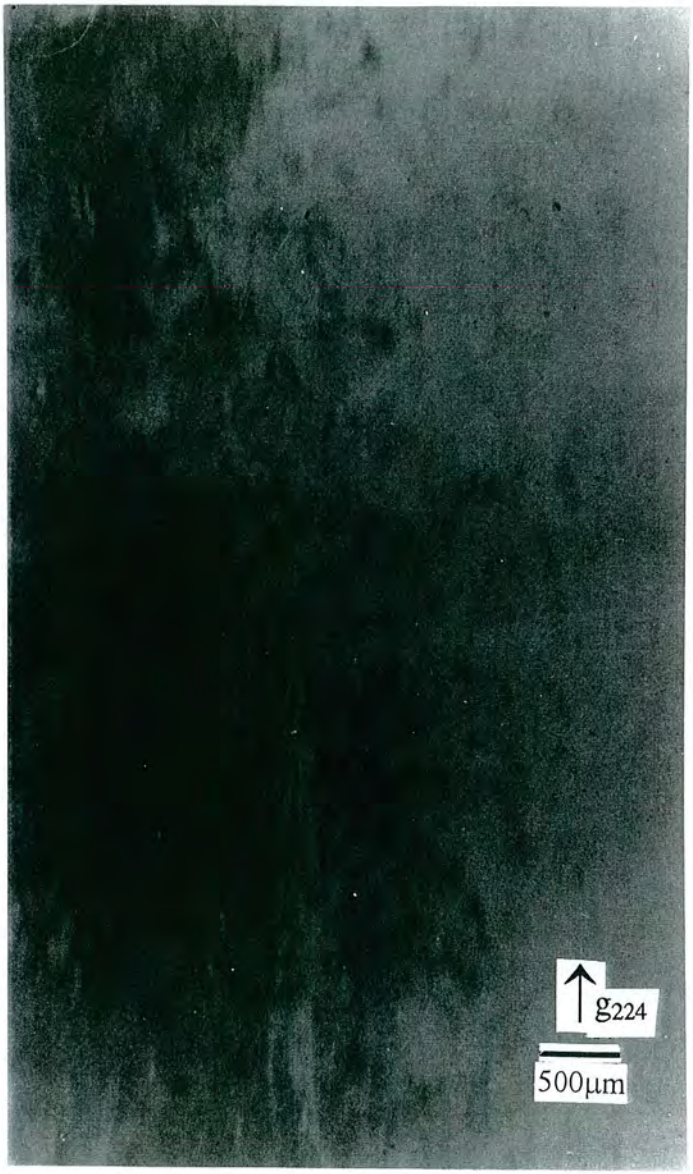

Fig 6.39 : 224 asymmetric topograph for MMT39 - high angle side

6.7 : Conclusions

The crystallographic structure of MMT layers grown by IMP has been investigated using x-ray diffraction techniques. The variation in composition, thickness and perfection has been mapped across wafers, showing the growth technique to be capable of providing layers of good uniformity, with compositional changes as low as $0.3\%mm^{-1}$. A correlation between crystal perfection and manganese fraction was observed, and has been attributed to thin layers having higher Mn fraction, and the diffusion co-efficient of precipitates varying with x, hence affecting the dislocation density.

Strain investigations have found the CdTe buffer layer to be 99% relaxed, and the MMT layer to be completely relaxed in all but the thinnest samples. The uniformity of layers perpendicular to the surface has been found to be poor, and simulations have been made of diffraction scans using a model of increasing Mn concentration towards the sample surface. Increased grading has been observed in high x samples. In addition, both epitaxial and clumps of MnTe have been identified on the surface of samples with low x content in the MMT peak, so providing a possible explanation of anomalous transport and magnetic data.

The dislocation densities within the MMT and CdTe layers have been calculated from the rocking curve widths (through an analyser crystal), giving values in the range 10^7-$10^9 cm^{-2}$. The dislocation density is seen to fall with increasing layer thickness. The presence of mosaic blocks within the crystal has been confirmed by x-ray synchrotron topography, where the minimum resolved block size was 25μm.

The IMP growth of MMT, therefore, has been found to present various difficulties to the crystal grower. The uniformity and crystal perfection of layers falls short of that predicted, although improvements have been observed over DAG layers. In particular, the factors governing the thickness of individual layers grown, and the in-diffusion of elements need to be more carefully controlled.

References

1. Furdyna, J.K., *Diluted Magnetic Semiconductors.* J.Appl.Phys., 1988. **64**(4): p. R29-R58.

2. Giriat, W. and J.K. Furdyna, *Crystal structure, composition, and materials preparation of diluted magnetic semiconductors,* in *Diluted Magnetic Semiconductors,* J.K. Furdyna and J. Kossut, Editor. 1988, Academic Press: San Diego. p. 1-34.

3. Jain, M. and J.L. Robins, *Material preparation, crystal structure and energy gap of diluted magnetic semiconductors,* in *Diluted Magnetic Semiconductors,* M. Jain, Editor. 1991, World Scientific: Singapore. p. 1-46.

4. Horsfall, A.B., *et al., Electrical measurements of $Hg_{1-x}Mn_xTe$ films grown by metalorganic vapour phase epitaxy.* J.Crystal Growth, 1996. **159**: p. 1085-1089.

5. Horsfall, A.B., *Characterisation of Epitaxial $Hg_{1-x}Mn_xTe$ Films.* in progress, University of Durham.

6. Rogalski, A., *Semiconductor infrared detectors.* Optical Engineering, 1994. **33**(5): p. 1392-1412.

7. Pain, G.N., *Device application of $Hg_{1-x-y}Cd_xMn_yTe$ (0<x,y>1),* in *Diluted Magnetic Semiconductors,* M. Jain, Editor. 1991, World Scientific: Singapore. p. 563-585.

8. Hallam, T.D., *The Characterisation of Epitaxial Layers of the Dilute Magnetic Semiconductor $Hg_{1-x}Mn_xTe$.* 1995, University of Durham.

9. Buerger, M.J., *et al.*, ed. *International Tables for Crystallography.* 2nd ed. Vol. III. 1985, D. Reidel Publishing Company: Dordrecht, Holland.

10. Tanner, B.K., *et al., High resolution x-ray diffraction of $Hg_{1-x}Mn_xTe$ epitaxial films.* Mater. Res. Soc. Symp. Proc., 1993. **280**: p. 635-640.

11. Hallam, T.D., *et al., Uniformity in (Hg,Mn)Te films grown by metal organic vapour phase epitaxy.* J.Crystal Growth, 1995. **146**: p. 604-609.

12. Irvine, S.J.C., J. Bajaj, and H.O. Sankur, *Complete in situ laser monitoring of MOCVD HgCdTe/CdTe/ZnTe growth onto GaAs substrates.* J.Crystal Growth, 1992. **124**: p. 654-663.

13. Jones, I.P., *et al., Precipitation and migration of point defects in MOCVD $Cd_xHg_{1-x}Te$.* J.Crystal Growth, 1996. **159**: p. 1096-1099.

14. Funaki, M., *et al., The MOVPE growth and characterisation of $Hg_{1-x}Mn_xTe$.* Semicond. Sci. & Technol., 1993. **8**: p. S200.

15. Hallam, T.D., *et al., X-ray scattering and topography studies of $Hg_{1-x}Mn_xTe$ epitaxial films.* J.Phys.D:Appl. Phys., 1993. **26**: p. A161-A166.

16. Brown, G.T., *et al.*, Electrochem. Soc. Symp. Proc., 1989. **89-5**: p. 171.

17. Bernardi, S., *et al., Structural characterisation of $Hg_{0.78}Cd_{0.22}Te/CdTe$ LPE heterostructures grown from Te solutions.* J.Crystal Growth, 1991. **113**: p. 53-60.

18. Shinenaka, K., *et al.*, *$Hg_{1-x}Cd_xTe$ epitaxial layers grown by low mercury partial pressure metalorganic vapor deposition and extended defect characterisation.* J.Crystal Growth, 1992. **117**: p. 37-43.

19. Hornstra, J. and W.J. Bartels, *Determination of the lattice constant of epitaxial layers of III-V compounds.* J.Crystal Growth, 1978. **44**: p. 513-317.

20. Bartels, W.J. and W. Nijman, *X-ray double-crystal diffractometry of $Ga_{1-x}Al_xAs$ epitaxial layers.* J.Crystal Growth, 1978. **44**: p. 518-525.

21. Tanner, B.K., *et al.*, *Measurement of aluminium concentration in epitaxial layers of $Al_xGa_{1-x}As$ on GaAs by double axis x-ray diffractometry.* Appl.Phys.Lett., 1991. **59**: p. 2272.

22. Turnbull, A., *Relaxation in Epitaxial Layers of III-V Compounds.* 1992, University of Durham.

23. Heinke, H., *et al.*, *Relaxation and mosaicity profiles in epitaxial layers studied by high resolution x-ray diffraction.* J.Crystal Growth, 1994. **135**: p. 41-52.

24. Heinke, H., *et al.*, *Unusual strain in homoepitaxial CdTe(001) layers grown by molecular beam epitaxy.* J.Crystal Growth, 1994. **135**: p. 53-60.

25. Heinke, H., *et al.*, *Application of the model of the relaxation line in reciprocal space to II-VI heterostructures.* J.Phys.D:Appl. Phys., 1995. **28**: p. A104-A108.

26. Utke, I., *et al.*, *Non-abruptness of heterointerfaces during LPE growth of (Hg,Cd)Te on (Cd,Zn)Te and Cd(Te,Se) substrates.* J.Crystal Growth, 1996. **162**: p. 126-134.

27. Funaki, M., *et al.*, *Epitaxial growth of (Hg,Mn)Te by the interdiffused multilayer process.* Appl.Phys.Lett., 1993. **62**(23): p. 2983-2985.

28. Horsfall, A.B., . 1996.

29. Gay, P., P.B. Hirsch, and A. Kelly, Acta. Metall., 1953. **1**: p. 315.

30. Tatsuoka, H., K. Durose, and M. Funaki, *Misfit dislocation arrangements at $(Hg_xMn_{1-x})Te/CdTe$ and $(Hg_xMn_{1-x})Te/CdZnTe$ heterointerfaces on (001), (-1-1-1)B and (-1-1-2)B substrates.* J.Crystal Growth, 1994. **145**: p. 589-595.

31. Port, R.I., *Structural defects in MOVPE grown CdTe/GaAs.* 1995, University of Durham.

32. Hudson, J.M., *Specular and Diffuse X-Ray Scattering Studies from Surfaces and Interfaces.* 1994, University of Durham.

Chapter VII

Investigation of Space-Grown Crystals

7.1 : Motivation for Space Experiments

It is only in recent years that space technology has advanced to the stage where experiments in microgravity have been viable. Before the advent of orbiting space stations and rockets, the longest period of microgravity sustainable was several seconds whilst in free-fall - which is obviously not a good condition for the complex process of crystal growth. Although the perfection of space-grown crystals has been noted on several occasions to be better than that on earth [1-3], the huge overheads involved will never make this a viable growth condition for commercial semiconductor wafers. Growth in microgravity, however, allows the separation of several artefacts of growth, aiding the improvement of earth-grown crystal methods [4].

There are four ways in which gravity acts on crystal growth. These are
i) the weight of a crystal acts to deform it
ii) hydrostatic pressure has a destabilising effect on float-zone growth
iii) sedimentation of heavy particles causes concentration gradients in the crystal, and
iv) buoyancy in the melt leads to convective transport.

The first of these matters chiefly where there are connections to an inertial system, such as at the crucible wall. This deformation is only a problem for gravity in excess of 1G, and de-wetting phenomena could potentially eliminate crucible effects. For sedimentation, the gravity-induced effects are negligible compared to those produced at the solid/liquid interface. The main areas of interest, therefore, are the elimination of hydrostatic pressure allowing more controlled float-zone (FZ) growth and the reduction in buoyancy-driven convective transport, which is looked at here.

7.1.1 : Flow control in a melt growth process

There are two main types of convective flow, which are buoyancy-driven convection and Marangoni convection (MC). The first of these is analogous to the situation in a beaker of boiling water. As water (and semiconductors) expand on solidifying, they are denser when they are at high temperatures. In the water, as in many growth systems, the top of the water is hotter than that at the base of the beaker, and so is more dense. In the presence of gravity, this leads to convective flow, which is normally oscillatory, but can become turbulent under certain conditions. In a growth chamber, the material at the solid/liquid interface is cooler than that in the melt, and radial temperature gradients also contribute to the presence of convection. It has been observed that in Bridgman growth from melt in space, the convective driving force is reduced by a factor between 10^{-3} and 10^{-6}, and diffusion is responsible for mass and temperature mixing [5].

The second source of convective mixing is Marangoni convection, which has a comparable magnitude to gravity-driven convection on earth. This occurs where a free surface is present, such as at the melt/gas interfaces. One way in which this convection is increased is by the action of bubbles, which enlarge the free surface area. Under microgravity, these are no longer present, so the free surface area is more uniform. Temperature or concentration variations at the interface cause corresponding changes in surface tension, causing the interface to move. In this way, gravity-independent convection is generated. In Czochralski or Float-Zone growth, there is a free melt/gas interface with temperature gradients of the order of 10-100Kcm^{-1}. This induces thermocapillary flow, which, if it becomes time dependent, leads to dopant striations.

The absence of buoyancy-driven convection in space allows investigations into suppressing the effects of Marangoni convection. Various studies have been reported in the literature, which have led to some constructive observations on crystal growth. The small diameters involved in necking increase the liquid surface area per volume, and generate convection close to the solid/liquid interface [6]. Thin oxide films on the crystal surface, such as those observed by Tillberg et al [7] in Ga doped Ge, were seen to reduce the Marangoni forces, and can help with de-wetting [8] although oxide

formation can promote twinning [9]. Other solutions include coating the melt with pyrex, which deforms with the liquid [7], side-heating to reduce the temperature gradients at the free surface, and the addition of a highly viscous layer [10].

The absence of buoyancy-driven convection allows a system to be modelled assuming that density gradients are induced solely by temperature gradients. This model can be further simplified by removing convection altogether, and assuming the crystal grows in a diffusion-controlled-steady-state (DCSS). This state is dependent on the diffusion length of the melt components. For example, if the Marangoni convection flow velocity is greater than the diffusion length, MC will dominate the free melt. Also, if the growth rate is slower than the interdiffusion rate, the solute will re-distribute itself at the interface faster than it solidifies [11]. The dominance of DCSS is also affected by the growth direction orientation [12], and direction of heating [10]. As the chemical segregation within a crystal is dependent on the convective flow, the control of convection is of vital importance in the growth of high quality wafers.

7.1.2 : Crucible Interactions

A second growth phenomenon in need of attention is that of wetting at the crystal/crucible interface. Much of the work in this field has been carried out by Duffar and colleagues [6, 8, 13-18], including microgravity investigations. The main interactions which occur in crystal growth are chemical at the liquid/crucible interface, thermal at the crystal/melt/crucible triple interface and mechanical at the crystal/crucible interface. These effects are particularly important in Bridgman growth as the sample is always in contact with the crucible. As chemical interactions lead to the degradation of chemical purity, and thermal and mechanical interactions cause stresses and dislocations, and hinder single crystal growth, a reduced contact area is advantageous. This can be achieved through a two stage process where composite wetting (where the liquid cannot penetrate to the bottom of the crucible cavities due to its roughness) leads to de-wetting, where no contact between the crystal and crucible remains.

The roughness of the crucible is critical in obtaining de-wetting phenomena. Due to the absence of hydrostatic pressure in microgravity, crucible roughness obtained with 1mm screw threads can be used, instead of crucibles sand-blasted with μm particles, as on earth. This makes de-wetting easier to achieve, control, and quantify in space.

Observations on de-wetting to date have shown that crucible roughness enhances crystal quality, both on earth and in microgravity, as well as stabilising the crystal shape. No de-wetting phenomena have been observed in smooth crucibles. The choice of crucible material is also critical, as it must not react with the melt, contaminate it, or stick to the solid, and must have a suitable thermal conductivity and cost. In the case of InGaSb and GaSb, it was observed that pyrolytic boron nitride showed better de-wetting properties than SiO_2 or graphite. Studies have also led to a mechanism for de-wetting being developed where the melt is initially modelled as being unable to penetrate into the gaps between the teeth, so that as the interface moves along the teeth, all contact between the crystal and crucible is removed.

7.2 : Float-Zone GaAs Crystals Grown In Microgravity

7.2.1 : Growth Conditions

Three wafers were investigated in this study, which were grown by Mueller's group at the University of Erlangen, in space on the D2 mission, using the float-zone growth technique. The feed material used was undoped and semi-insulating (SI), and the crystal was grown with a diameter of 20mm. The 0.5mm thick wafers were cut with orientation (001) ± 0.5°, and were epi polished on one side and strain-free etched (Δetch = 7.5μm) on the other. The position in the boule from which the sample wafers were cut is shown in Fig 7.1. At the position marked, a heater failure occurred, and the growth conditions changed to give a lower zone height.

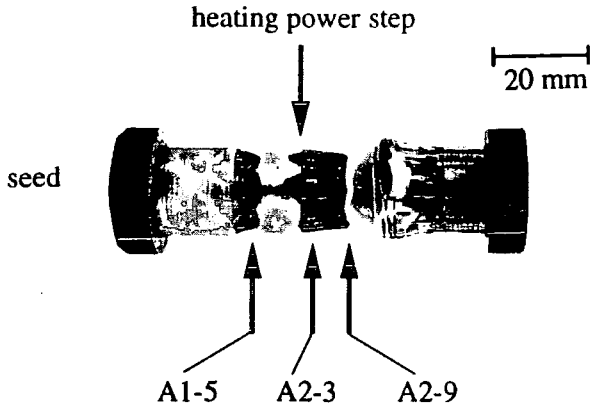

Fig 7.1 : Schematic diagram of the crystal showing the origin of the samples studied

7.2.2 : Topographical Results on GaAs

The initial topographs taken were white radiation 022 transmission topographs at a wavelength of 1Å, under conditions of high anomalous transmission (μt=7.8) at Station 7.6 at Daresbury Laboratory. The samples were mounted using wax, and were positioned with the polished side on the exit surface. Exposure times were 15 minutes in order to record an image on 25μm Nuclear Emulsion plates.

Fig 7.2 shows a low magnification topograph of sample A1-5. There is a considerable amount of climb present, but no evidence of macroscopic slip. The dislocation distribution is uniform across the wafer, and extends to the centre, which is consistent with a large, but uniform temperature gradient. An enlargement from this topograph is shown in b) where the cells can be seen in more detail. This structure of tangles of dislocations around blocks of high quality wafer is typical of GaAs, where the cell width is normally of the order of hundreds of microns. Burgers vector analysis by Prieur et al [19] identified that the dislocations in the walls of LEC SI GaAs have an <011> preferred direction, and move on the glide plane $\{1\ \bar{1}\ 1\}$. It can be seen in b) that the <011> directions are indeed preferred by the walls, and the cell size is about 200-300μm. The cell size is therefore comparable with, but slightly less than, that of earth-grown SI GaAs, which is normally grown by LEC for mass production. In the float-zone technique only a small part of the source material is melted at a time, which then solidifies into the new crystal. There is no wall restraint, and the molten zone is

held in place by surface tension. As the amount of melt is small, convection is minimised, but the change in density on melting usually forces the melt towards the ingot rather than the crystal. In space, this effect is removed, and the wafers produced are similar to LEC, but still far inferior to VGF wafers, discussed in Chapter V. Complementary high resolution diffraction experiments were performed by Loxley on these samples [20], which found the triple axis transverse and longitudinal FWHM to be the same as those from terrestrial LEC SI GaAs.

The x-ray transmission in the two samples after the heater failure, A2-3 and A2-9, was much lower and little resolvable detail could be seen. This prompted the use of the ESRF to investigate these samples further, as the high energy of the electron beam allows low wavelengths to be used, so kinematical images can be obtained with $\mu t \approx 0.3$. The samples were wax mounted and topographed in transmission, with exposure times between 1 and 5s. The images were recorded on Kodak R films.

Topographs of sample A2-3 are shown in Fig 7.3, where three different parts of the sample are imaged by tilting and/or translating the crystal. Pictures a) and b) show that the left section of the wafer has some cellular dislocation structure, although the presence of very large strains allows only small regions to be imaged at a time. The irregular wafer edge is due to the loss of temperature control, as the surface tension is related to the gradient in temperature at the interface. The right hand side of the wafer is highly strained and the diffraction condition is not met. The lower part of the sample is shown in c) and d), where the same effect is observed. Different sections of the crystal are choosing different wavelengths, giving a displaced image. A large part of the sample is shown in e) where the centre of the wafer is seen to be fairly uniform. The lower part shows areas sufficiently misaligned not to diffract at all. This is evidence of grains caused by the growth interface no longer being planar so that growth occurs along various facets. A triple axis map, taken by Loxley, of this sample is shown in Fig 7.4. A Bede D3 diffractometer was used, as described in Section 3.4.3. The scan shows no significant strain, but there is a long ridge of scatter in the q_y direction, corresponding to the presence of misoriented grains, as has been seen observed in the topographs.

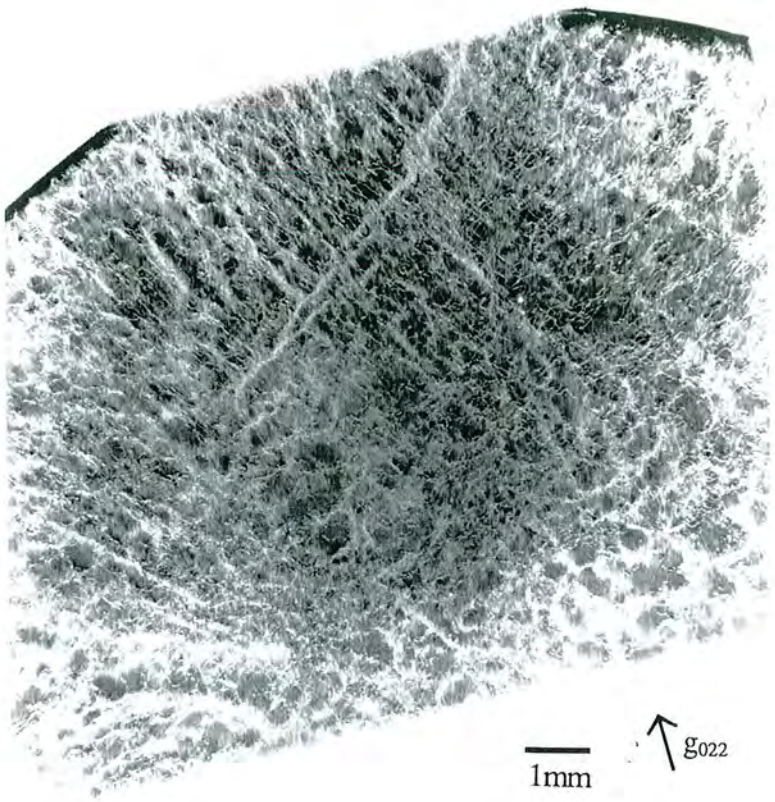

a)

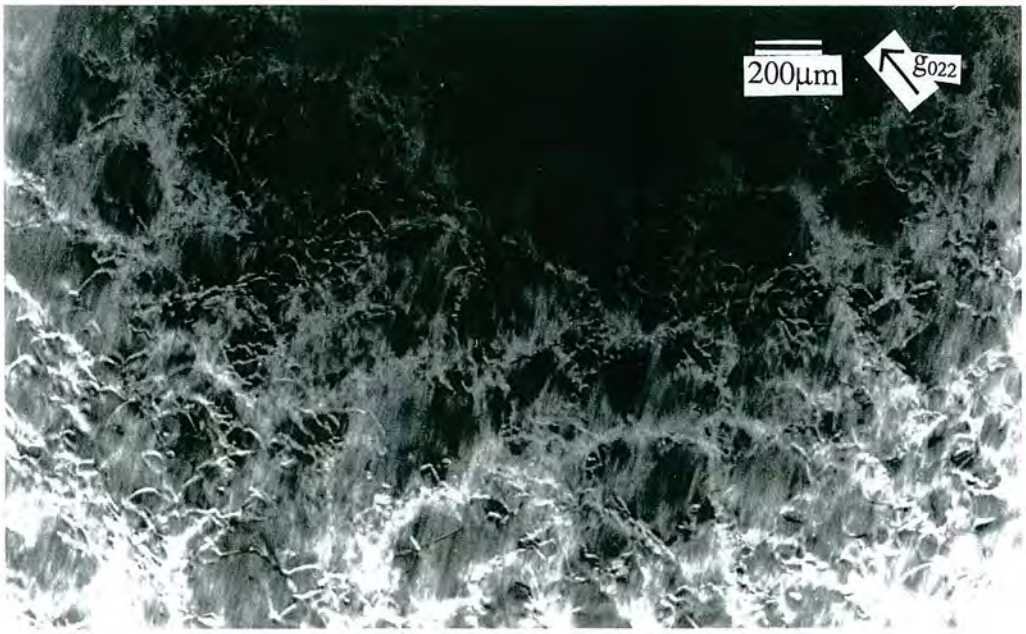

b)

Fig 7.2 : 022 anomalous transmission topograph of sample A1-5, shown in a) low magnification and b) high magnification

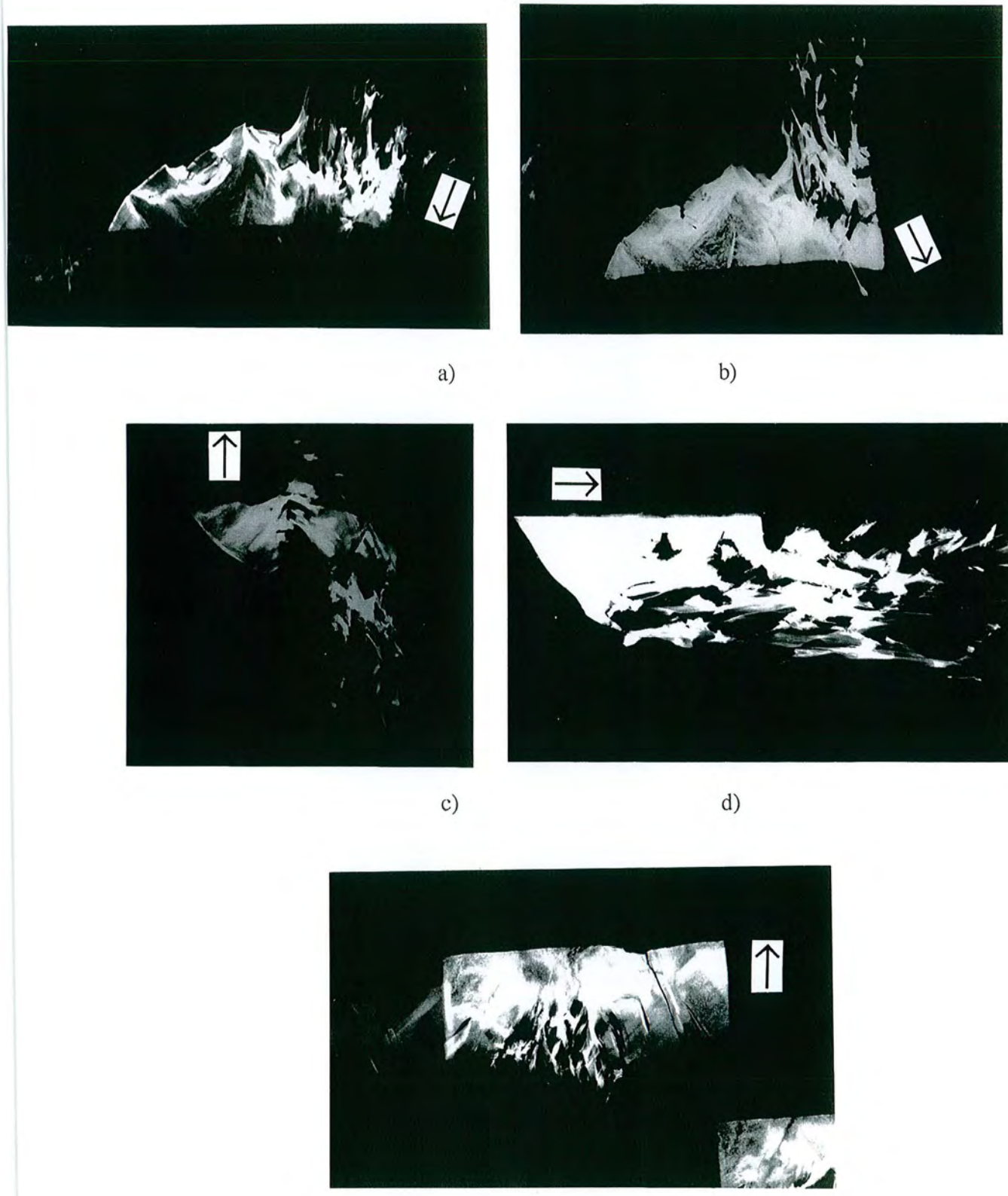

a) b)

c) d)

e)

Fig 7.3 : High energy topographs of sample A2-3. The magnification is x 4.5.

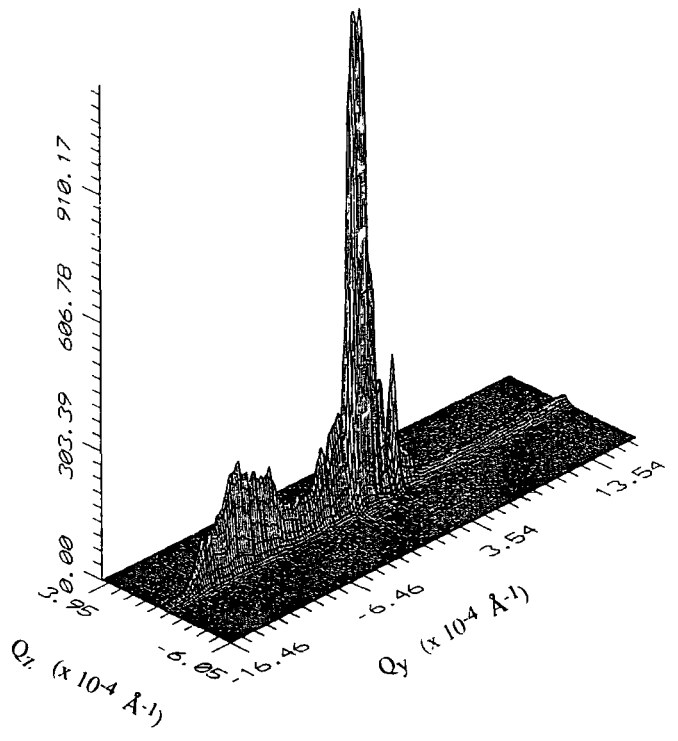

Fig 7.4 : Reciprocal space map of specimen A2-3, showing a grain tilt distribution. Reproduced from [20]

The third sample was taken 30mm from the seed and is shown in Fig 7.5. The top edge of the wafer (a) to d)) shows a single crystal structure, where ill-defined dislocation images are obtained. Again, there are regions which are tilted with respect to the bulk. As a lower region on the wafer is imaged, no structure can be seen and there is a gradual increase in strain, until at the middle (best shown in c) and f)), the image is divided into streaks. The topograph in e) is the equivalent to that in Fig 7.3e), and shows that a large section of the wafer diffracts to a different position, and is now completely detached from the rest of the wafer. This implies the presence of twins, which has been confirmed by diffraction measurements where two peaks at separate q_z were identified (Fig 7.6). These are probably 60° rotation twins, where a Ga atom by rotation is replaced by an As atom [21]. Twin formation is one of the most common problems in crystal growth and is linked to non-stoichiometry of the melt, uneven temperature gradients, and facet growth. All of these are likely to occur when the heater is no longer working, and the crystal is left to grow in uncontrolled conditions.

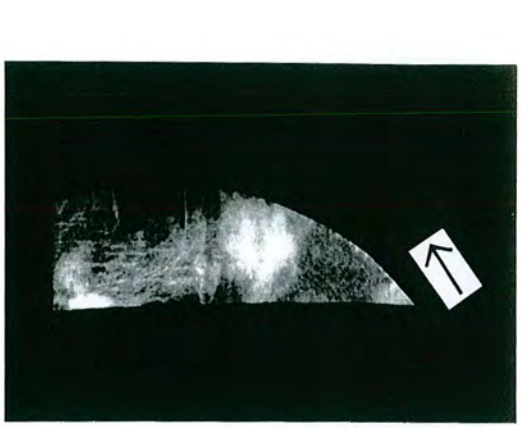

a)

b)

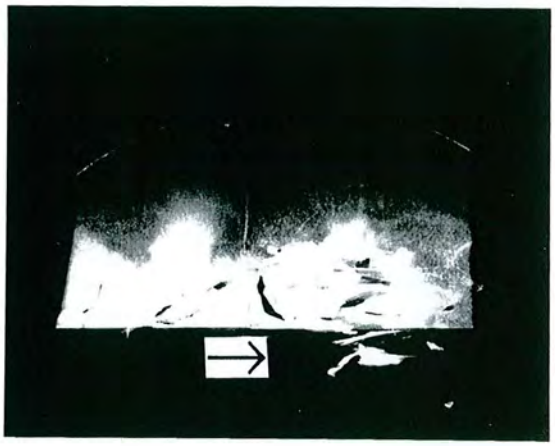

c)

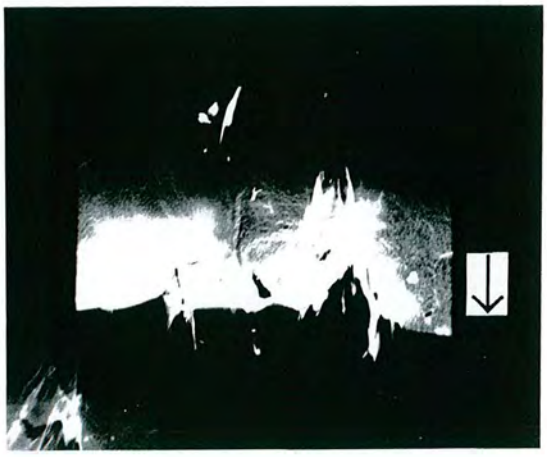

d)

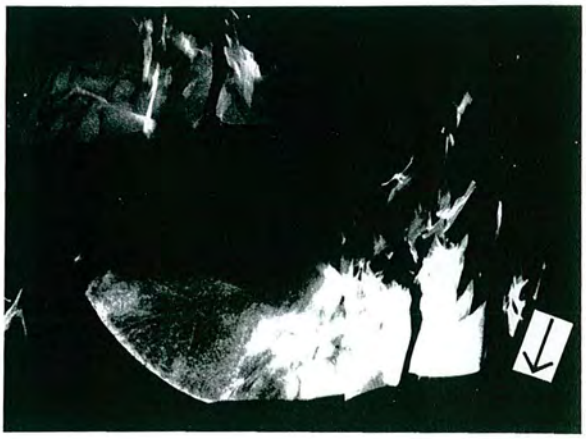

e)

f)

Fig 7.5 : High energy topographs of sample A2-9

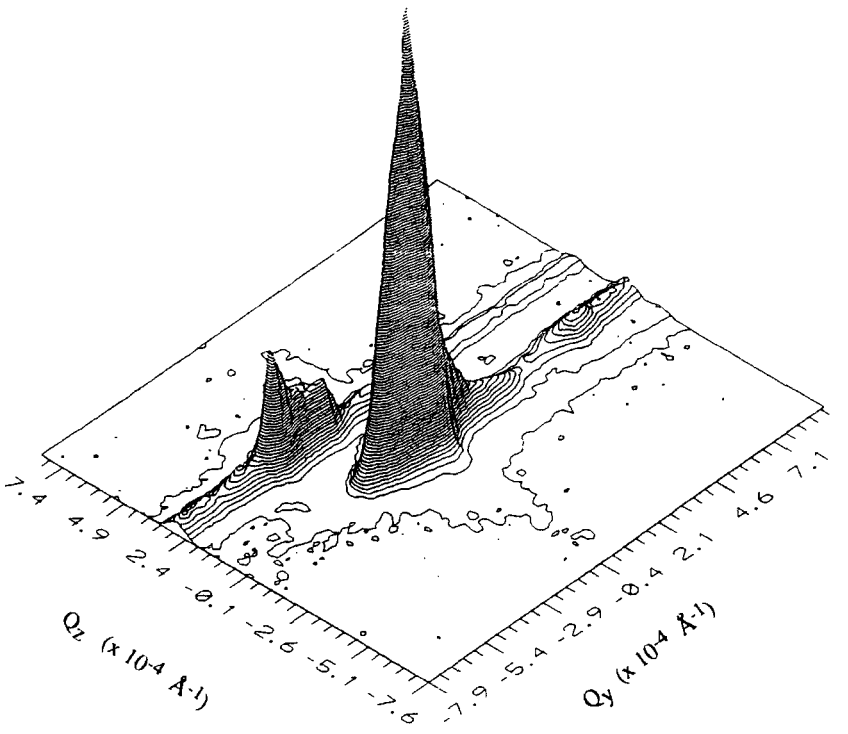

Fig 7.6 : Reciprocal space map of A2-9. Reproduced from [20]

It is clear, therefore, that when conditions are well controlled in FZ growth in space, the wafers are slightly inferior to those grown by LEC on earth, and far inferior to those from VGF. When the conditions are not well optimised, as during a heater failure, the crystals obtained are highly strained and twin formation occurs. While the dislocation densities due to high temperature gradients are so great, it is hard to study the effect of Marangoni convection on the crystal growth process. The addition of dopants would reduce the dislocation density and facilitate more meaningful measurements on the convective flow.

7.3 : Bridgman Solidification of GaSb and GaInSb in Microgravity

7.3.1 : Motivation for GaSb studies

At present, it is only possible to use binary single crystals as substrates, which have a certain lattice constant. Buffer layers and the use of strained layer epitaxy allow the development of devices which deviate from these discrete lattice parameters. The potential to grow a bulk alloy with a controlled lattice constant is therefore of great

industrial interest. GaSb and InSb are totally miscible in both the liquid and solid state, so their physical properties vary continuously with composition, making GaInSb a potential ternary substrate. Concentrations of In have been varied from 0.1 to 10%, and the wafers obtained are seen to improve with low In content [17]. Gallium antimonide, GaSb, is a useful substrate in its own right for the growth of (GaIn)(AsP) layers, with bandgaps in the range 1.3 to 1.5 μm. Various growth techniques have been employed in the literature, which include VGF [16], Czochralski with a hydrogen atmosphere [9] and Bridgman under high gravity [22] for the growth of GaSb, and solute feeding Czochralski for GaInSb [23]. In this experiment Bridgman solidification was used.

7.3.2 : Growth Conditions

The EURECA experiments described here involved the growth of two samples, the first a pure GaSb crystal (AMF118-1), and the second $Ga_{0.99}In_{0.01}Sb$ (AMF118-2). These were grown by Duffar's group with the intension of studying segregations under microgravity and terrestrial conditions. They were grown in an ampoule designed for zone melting, where the temperature gradient is radial, so a gold coating was added to the wall of the ampoule, to reflect the heating light. The growth apparatus is shown in Fig 7.7. The samples were 10mm in diameter and 75mm in length, with a growth rate of $0.2\mu mh^{-1}$ over a total experiment time of 104 hours. The axial temperature gradient was $20Kcm^{-1}$, and the grown weight was about 30g. The crucible was rough, with the teeth being machined with a screw thread of 1mm to a depth of 1mm, using an angle of 52° to satisfy de-wetting criteria. The ground reference samples were grown under exactly the same conditions, only with a smooth crucible, so that the melt could not penetrate between the teeth and harm the samples. The ground reference samples grew to be fully polycrystalline.

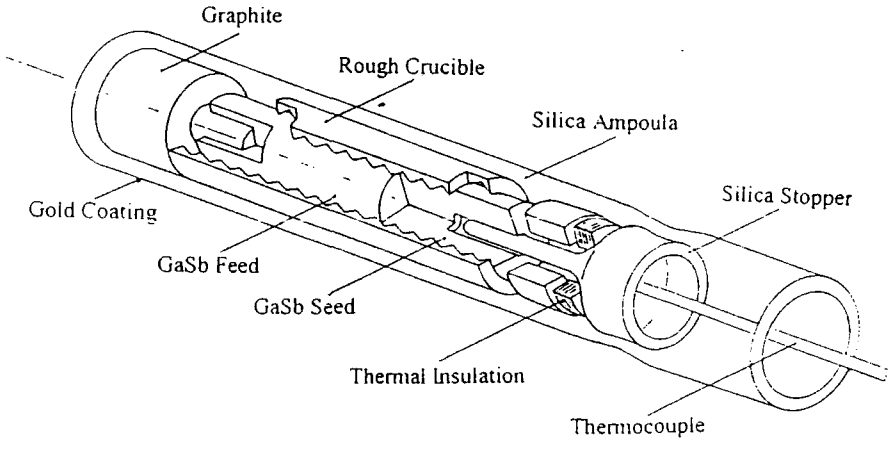

Fig 7.7 : Ampoule used for the growth of GaSb and GaInSb

7.3.3 : Topographical Results on GaSb and GaInSb

The effect of natural convection appeared to be suppressed in microgravity, as the variation of In (measured by SIMS) was diffusion controlled in microgravity and convection controlled at 1G [8]. In both samples total detachment from the crucible was observed, which was perhaps aided by oxidation of the surface. Slight ridges were formed where the crystal was close to the sharp point of the crucible. A heater failure in the system meant that the seed of both crystals was melted, so leading to unusual growth behaviour. A diagram of the two crystals and their metallography is shown in Fig 7.8, where the positions at which the subsequent topographs were taken is marked. The crystals were cut in half along the vertical axis, as shown in the right hand pictures.

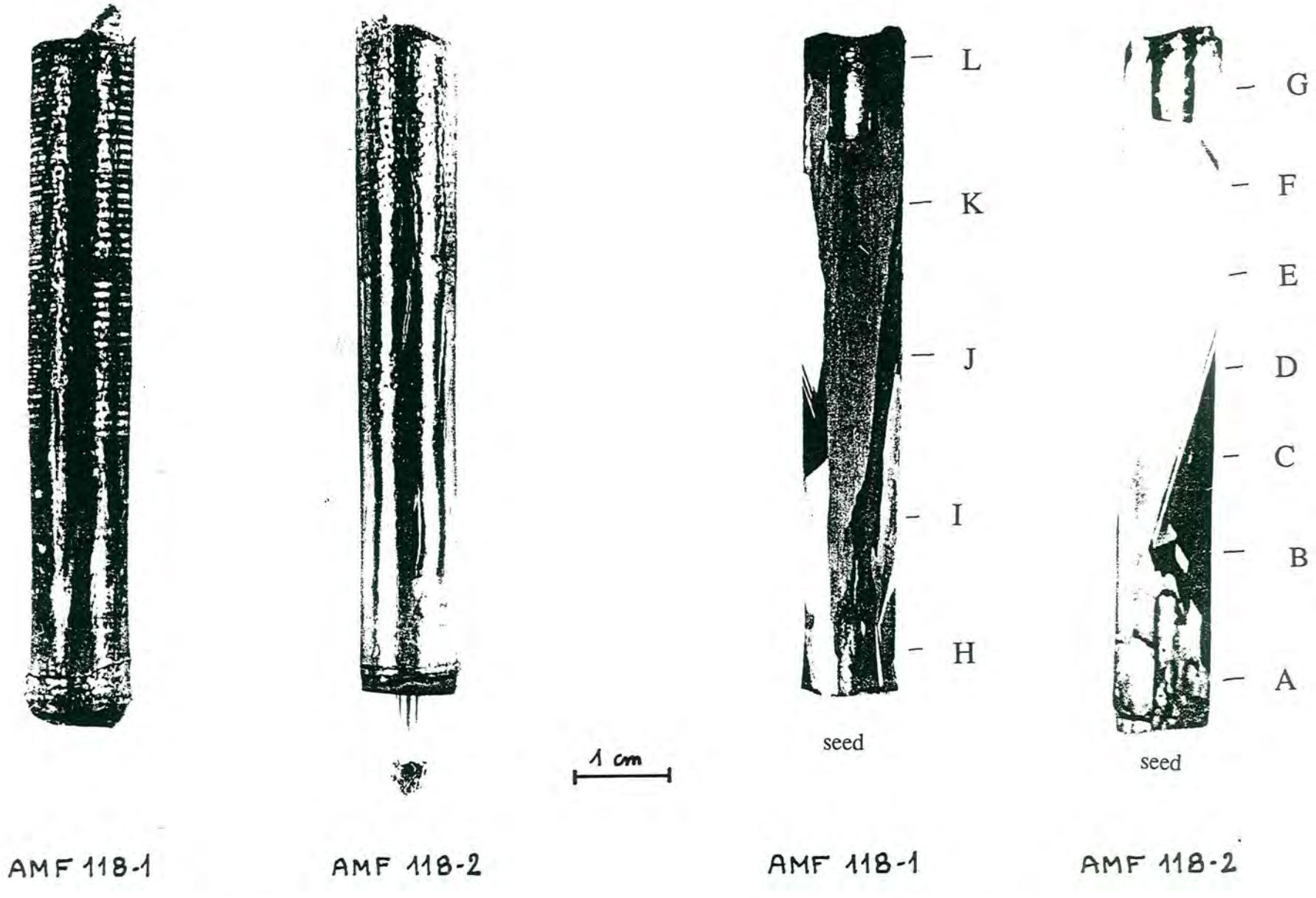

Fig 7.8 : View of the two GaSb EURECA samples, and the positions of the topographs

(courtesy T. Duffar)

The topographs were taken at the ESRF, where the high flux and low wavelengths allow such thick samples to be studied in transmission. The topographs were mostly Laue case images, recorded on Kodak R film, with exposure times of 100 or 200s. The sample was translated vertically between exposures, so that an idea of the development of the crystallinity could be obtained.

If we consider first GaInSb (AMF118-2), it can be seen in Fig 7.8 that the crystal is twinned, which should become evident at position B. It would be expected that the crystal begins as high quality then deteriorates due to twinning and polycrystallinity, especially when the heater has failed. The topographs will be looked at from the seed end upwards, to see if this is the case.

Fig 7.9 shows two topographs taken from A at the seed end. The material is crystalline, and diffracts homogeneously, although no detail or structure is visible. The bottom of the crystal is slightly strained, probably due to the melt not having exactly the same chemical composition as the seed. The sides of the crystal are relatively free from strain, as they are not yet in contact with the crucible. The picture in Fig 7.8 shows that at this stage the crystal surface is relatively smooth and undeformed. The fact that the seed was melted has not harmed the crystallinity of the initial material grown.

Fig 7.10 shows two topographs taken at position B, about 1.4cm from A and from the seed. Fig 7.10a) shows that the side of the crystal is still only slightly strained, and some dislocations are now visible. The crystal is growing in the <111> direction, and these pale lines are probably slip bands in the other <111> directions. Fig 7.10b) shows clearly the presence of twins in the crystal, as only small sections diffract, producing a striped pattern. There are no structures or features visible in this twinned part of the crystal.

a)

b)

Fig 7.9 : Topographs at the seed end of AMF 118-2 (A)

a)

b)

Fig 7.10 : Further from the seed (B)

The topograph at C again shows a twinned structure, although progressively less of the crystal diffracts, and this trend continues to D, where only the edges of the crystal diffract clearly. One of these edges is shown in Fig 7.11, where the criss-cross dislocation structure is also seen, as the crystal is now coming into contact with the rough crucible. From this point onwards the crystal perfection deteriorates gradually from D to F, and no clear dislocation structure is seen. At position G a tendency towards polycrystallinity is observed, and the patterns shown in Fig 7.12 are obtained. In these, no structure can be seen, and the crystal has ceased to diffract uniformly, showing a high degree of strain.

In order to image the whole sample at once, reflection topography was performed, using a small angle of incidence and tilting the film in order to expand the image. The topograph obtained is shown in Fig 7.13a) and enlargements from it are shown in b) and Fig 7.14a) and b). The twinning can be seen, as some reflections diffract only one side of the twin. The enlargement in 7.13b) shows the line of the twin, and the slip lines changing direction at it. Part of the wafer is not diffracted at this position as its relative tilt is too great. The topograph in Fig 7.14a) shows the same section but in a different reflection, where one side of the twin is imaged, as is the area missing from the previous picture. The structure in the topograph is clear until the twin reaches the edge of the crystal, where the material deteriorates, as shown in 7.14b). The amount of strain increases and no crystal structure can be seen. This is the position (D) at which the surface of the crystal (Fig 7.8) is seen to become rougher.

Fig 7.11 : A topograph from position D in the wafer

a)

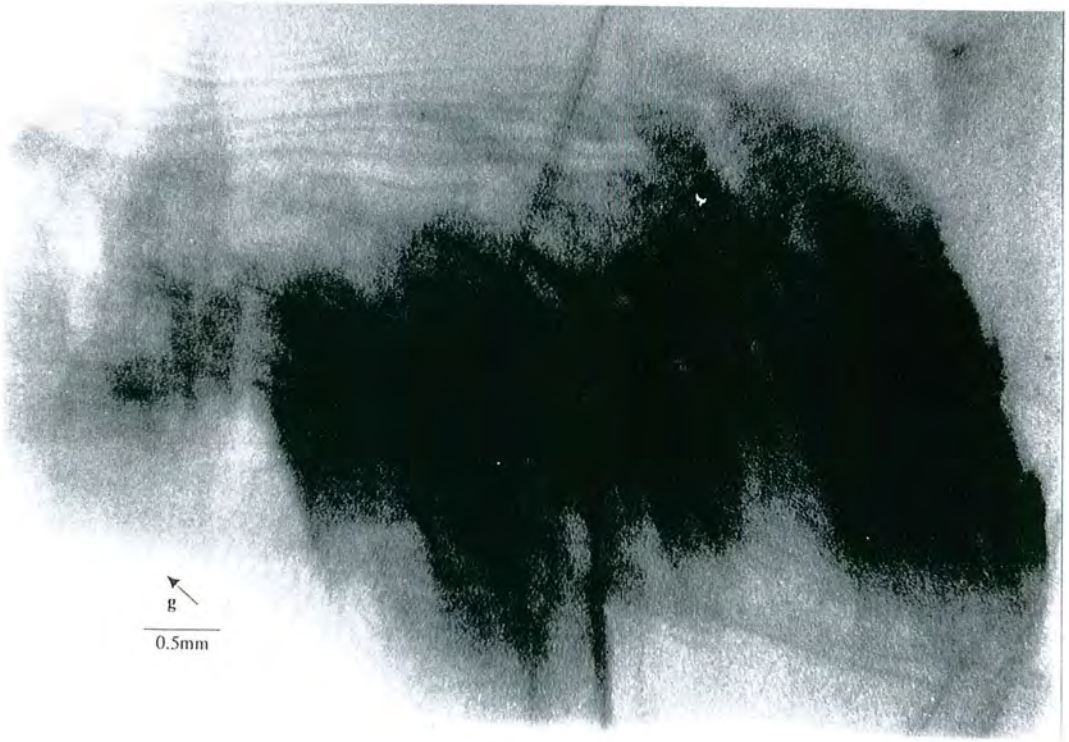

b)

Fig 7.12 : Topographs at the crucible (G)

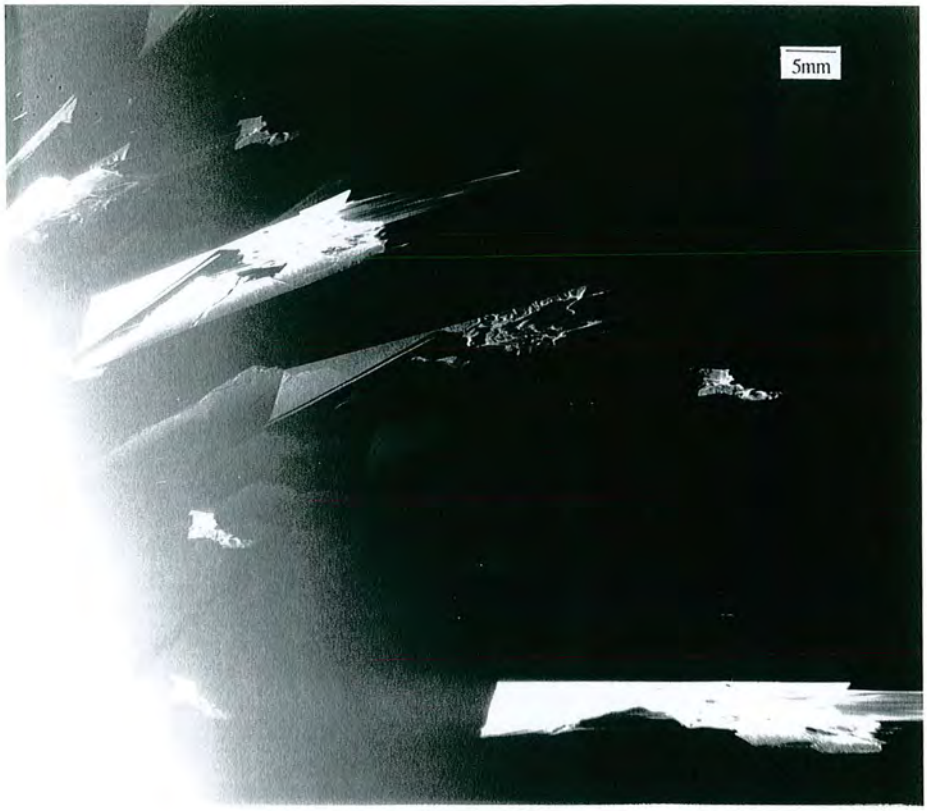

a)

b)

Fig 7.13 : Reflection topographs of AMF118-2

a)

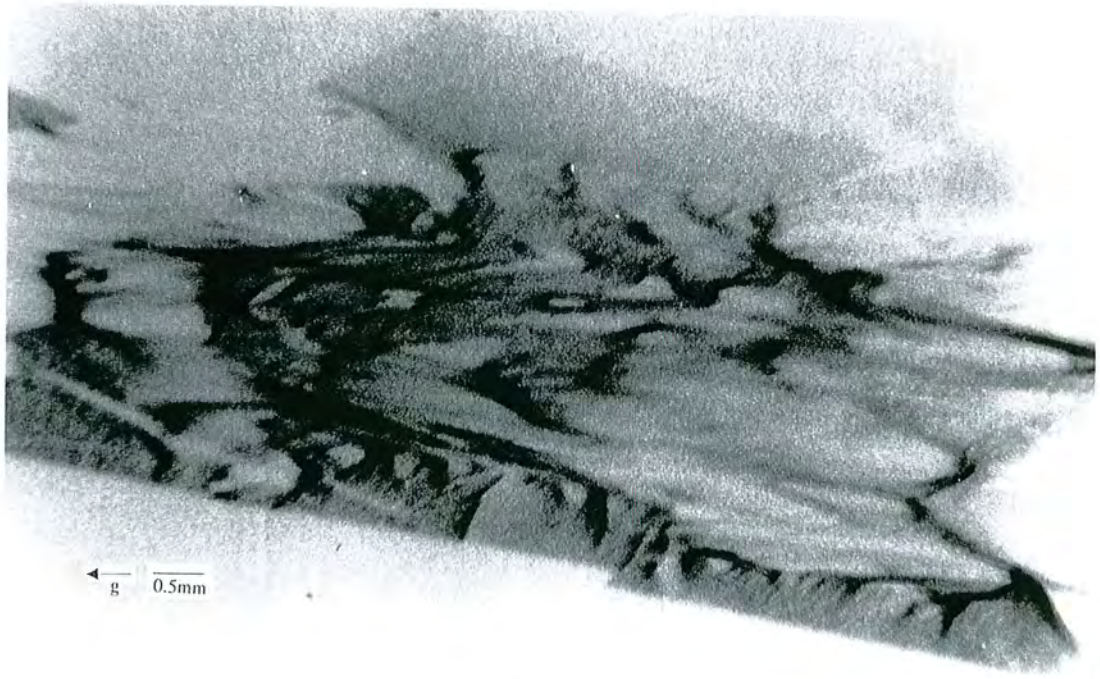

b)

Fig 7.14 : More reflection topographs from AMF 118-2

There are several reasons why this observed trend in crystal perfection may have occurred. SIMS measurements showed that the In content in the sample increased away from the seed, and it has already been remarked that crystal perfection decreases with In content. The onset of twinning is common in semiconductor growth, especially in the uncontrolled temperature conditions which would have prevailed here. It should be noted that under terrestrial conditions, the crystals are polycrystalline, so the perfection has been improved by the lack of buoyancy-driven transport and presence of de-wetting phenomena. As the sides of the crystal were mostly in contact with the crucible, very little convection of either sort would have been present, and the mixing would have been mainly diffusive. The crystals only gradually deteriorate once in contact with the crucible, their strain becoming most pronounced at the graphite connection at the end of the ampoule. The fact that this sample stayed almost mono-crystalline over its full length, therefore, is attributable to the de-wetting phenomena, which has eliminated the strains and contamination normally experienced at this interface. These topographs do, however, provide evidence that the strain observed increases at the crucible even when it is rough.

The second sample studied here was pure GaSb (AMF118-1), which was topographed in Laue-case transmission, as before. The topographs at the seed (H and I) show a polycrystalline structure, which improves gradually away from the seed. An example is given in Fig 7.15a) which shows the scatter propagating in all directions from the sample. This scatter continues to decrease, and the size of the diffracted spots increase, until 7.15b) is obtained at position L. In this case, the scatter is arranging itself into rings associated with crystallinity, so we can conclude that the crystal structure improves during growth, to the extent that a single crystal grows from a polycrystalline material. This is the first time, to our knowledge, that this has been observed in GaSb. The orientation of the grown crystal is impossible to deduce, and is probably not a simple crystallographic plane.

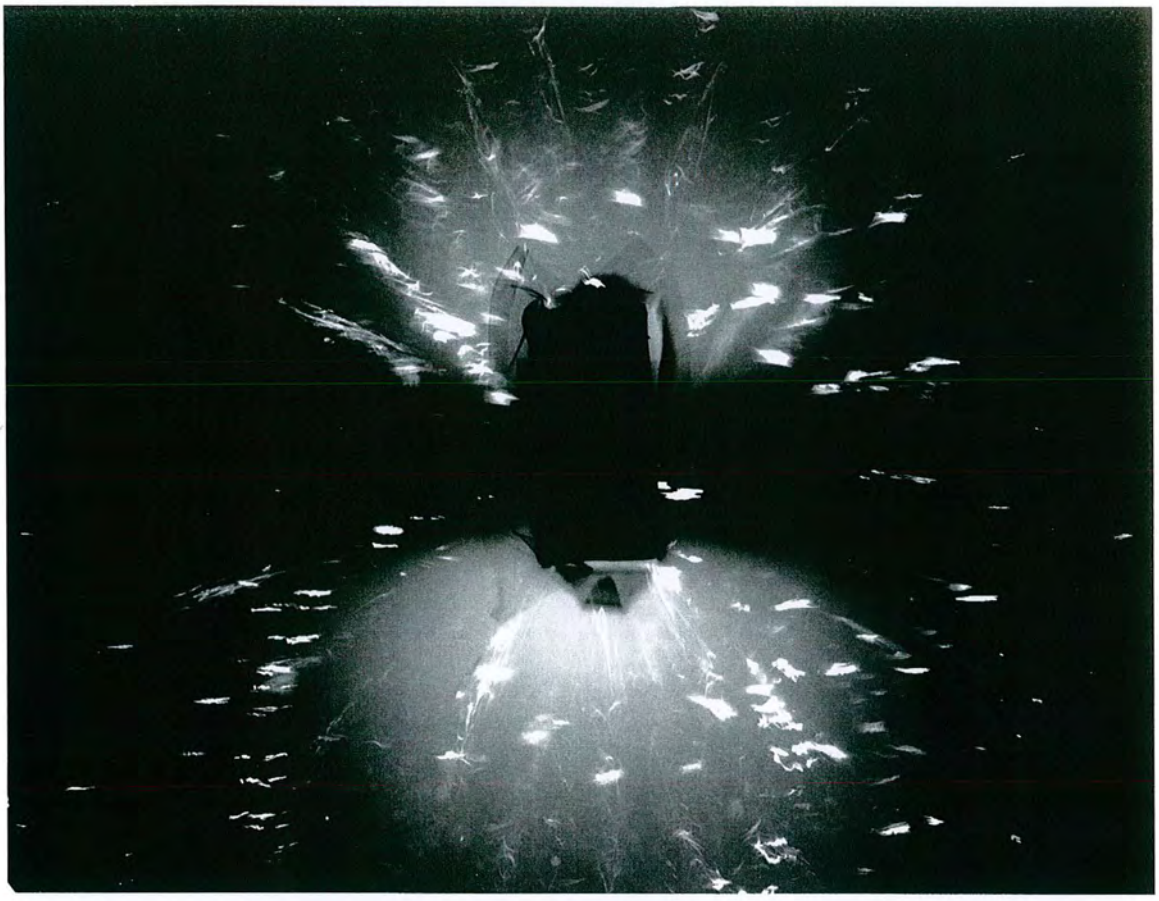

a)

b)

Fig 7.15 : The development of crystallinity in AMF118-1 where a) was taken at J and b) was taken at L

It appears, therefore, that the action of de-wetting does improve the crystallinity of the material produced. In the case of GaInSb, single crystal structure was obtained and maintained for the length of the wafer, although some deterioration did occur, and a gradual increase in strain was observed. The sudden increase in strain at the melt/graphite interface demonstrates that the de-wetting behaviour of the rough crucible has reduced the mechanical strain which would be present with a smooth crucible. The transition from polycrystalline to single crystal in GaSb demonstrates that the process of de-wetting actually has a beneficial effect on crystal structure.

7.4 : Conclusions on Crystal Growth in Microgravity

The examples shown here of crystals grown in space have highlighted both the wealth of information to be obtained from growth in microgravity, but also the problems associated with obtaining a controlled growth system. In both cases here, the heater failed, causing irreproducible results. Problems described in the literature include the effects of slight accelerations during flight [5], crystal damage during take-off [15] and growth on re-entry [24]. Once these problems are overcome, however, space experiments allow a unique opportunity to learn more about the forces governing crystal growth.

References

1. Allen, R., *Space experiment aims to bring up GaAs yield.* Elect. Design, 1986. **34**(3): p. 24.
2. Chen, W.C., *et al., Growth of alpha-LiIO3 crystal under microgravity conditions.* J.Crystal Growth, 1990. **99**: p. 1273-1275.
3. Danilewsky, A.N., *et al., Dopant segregation in earth and space-grown InP crystals.* Jpn. J. Appl. Phys., 1992. **31**: p. 2195-2201.
4. Mueller, G., *A comparative study of crystal growth phenomena under reduced and enhanced gravity.* J.Crystal Growth, 1990. **99**: p. 1242-1257.
5. Garandet, J.P., *et al., On the effect of gravity perturbations on composition profiles during Bridgman crystal growth in space.* J.Crystal Growth, 1996. **165**: p. 471-481.
6. Duffar, T., I. Paret-Harter, and P. Dusserre, *Crucible de-wetting during Bridgman growth of semiconductors in microgravity.* J.Crystal Growth, 1990. **100**: p. 171-184.
7. Tillberg, E. and T. Carlberg, *Semi-confined Bridgman growth of germanium crystals in microgravity.* J.Crystal Growth, 1990. **99**: p. 1265-1272.

8. Duffar, T., P. Dusserre, and M.D. Serrano, *Bridgman solidification of GaSb results of the Eureca AMF-118 experiment.* Adv. Space Res., 1995. **16**(8): p. 101-104.

9. Moravec, F., *Growth and characterisation of GaSb single crystals.* J.Crystal Growth, 1993. **128**: p. 457-461.

10. Schwabe, D., R. Velten, and A. Scharmann, *The instability of surface tension driven flow in models for floating zones under normal and reduced gravity.* J.Crystal Growth, 1990. **99**: p. 1258-1264.

11. Kinoshita, K. and T. Yamada, *Conditions for diffusion-controlled steady-state growth of $Pb_{1-x}SnTe$ under microgravity.* J.Crystal Growth, 1990. **99**: p. 1276-1280.

12. Asakawa, K., *et al.*, *Influence of solution convection on LPE $In_xGa_{1-x}Sb$.* J.Crystal Growth, 1990. **99**: p. 1291-1294.

13. Duffar, T., C. Potard, and P. Dusserre, *Growth analysis of the InSb compound by a calorimetric method in microgravity; results of the spacelab-D1 experiment.* J.Crystal Growth, 1988. **92**: p. 467-478.

14. Duffar, T. and M. Bal, *Thermal effect of a rough crucible on crystal growth from the melt.* J.Crystal Growth, 1995. **151**: p. 213-219.

15. Duffar, T., P. Dusserre, and J. Abadie, *Crucible-semiconducor interactions during crystal growth from the melt in space.* Adv. Space Res., 1995. **16**(7): p. 199-203.

16. Garandet, J.P., T. Duffar, and J.J. Favier, *Vertical gradient freeze growth and characterisation of high quality GaSb single crystals.* J.Crystal Growth, 1989. **96**: p. 888-898.

17. Garandet, J.P., T. Duffar, and J.J. Favier, *Vertical gradient freeze growth of ternary GaSb-InSb crystals.* J.Crystal Growth, 1990. **106**: p. 426-436.

18. Harter, I., *et al.*, *Wetting of III-V melts on crucible materials.* J.Crystal Growth, 1993. **131**: p. 157-164.

19. Prieur, E., *et al.*, *Synchrotron topographic study of defects in liquid-encapsulated Czochralski-grown semi-insulating gallium arsenide wafers.* J.Crystal Growth, 1993. **132**: p. 599-605.

20. Loxley, N., *et al.*, *High resolution X-ray diffractometry and topography of float-zone GaAs crystals grown in microgravity.* Advances in X-ray Analysis, 1995. **38**: p. 195-200.

21. Chen, T.P., *et al.*, *Study of twins in GaAs, GaP and InAs crystals.* J.Crystal Growth, 1992. **118**: p. 109-116.

22. Regel, L.L. and O.V. Shumaev, *GaSb directional solidification under high gravity conditions.* J.Crystal Growth, 1992. **119**: p. 70-73.

23. Watanabe, A., A. Tanaka, and T. Sukegawa, *GaSb solution growth by the solute feeding Czochralski method.* J.Crystal Growth, 1993. **128**: p. 462-465.

24. Kodama, S. and Y. Suzuki, *GaAs solution growth experiment in microgravity.* J.Crystal Growth, 1990. **99**: p. 1287-1290.

Chapter VIII

Conclusions and Suggestions for Further Work

This thesis has been concerned with the x-ray characterisation of compound semiconductor materials. The conclusions, therefore, relate to advances in the understanding of semiconductor materials, and advances in the application of x-ray techniques to their investigation. These will be dealt with separately below, together with suggestions for ways in which the work here could be continued in a profitable manner.

Much of the work described in this thesis has been concerned with the growth of 2" III-V semiconductor wafers, about which several conclusions can be made. Firstly, a comparison can be made between manufacturers of bulk substrates as a result of the various experiments conducted. White beam anomalous transmission topographs have shown that the dislocation density within JE LEC wafers is less than that in similar wafers produced by MCPWT, with the slip dislocations at the wafer periphery extending a smaller distance into the wafer. The samples were found to be consistently closer to the required orientation than MCPWT wafers, and one JE sample had the lowest FWHM in the symmetric triple axis scans, while another had the lowest in the asymmetric. The surface of both samples investigated topographically, however, showed evidence of much surface damage, both before and after refinishing. When diffuse scatter simulations from transverse reflectivity scans on JE samples were attempted, satisfactory fits could not be achieved at the two q_z values measured. This was believed to be due to the presence of a very low correlation length. As one sample was observed to have a large amount of surface tilt and strain, this has been attributed to figuring, which is supported by the specular part of the reflectivity showing three distinct peaks. AXT InP had the second narrowest symmetric rocking curves studied, and AXT was found to produce lower dislocation density VGF GaAs than MCPWT.

The VGF growth technique has been compared to LEC for InP:S, and found to produce wafers which are dislocation-free. While the dislocation density at the edge of

LEC wafers was found to be up to $6x10^4cm^{-2}$, three out of four VGF wafers had no detectable dislocations at any position in the wafer. In the case where dislocations were detected, the density was $\sim 200cm^{-2}$, evenly distributed throughout the wafer. These were identified as 60^0 mixed dislocations lying in the $\{ 1\bar{1}1 \}$ plane, with Burgers vector $b = \pm a/2[110]$. While growth striations were observed in all LEC wafers topographed, none were seen in VGF wafers, which implies a uniform dopant incorporation, and a planar interface between solid and melt. When the FWHM from symmetric and asymmetric triple axis scans are compared, no trend is observed concerning the growth technique, while the curvature of VGF wafers is observed to be slightly less, on average, than in LEC wafers. The major difference observed between the growth techniques, therefore, is the reduction in dislocation density which is possible using VGF, probably due to the lower thermal gradients involved.

A combination of reflectivity and diffraction measurements has led to the development of a model for the surface of InP wafers. In this model small mosaic blocks of perfect crystal are separated by low angle boundaries consisting of rows of edge dislocations. When the dislocation density is low, this would give only tilt variations between samples polished in different ways, as has been observed. Debris being forced into these microcracks at the surface would result in a change in the near-surface in-plane lattice parameter, as is observed in grazing incidence asymmetric diffraction scans. The existence of such large tilt distributions in InP wafers is perhaps related to the use of bromine in the polishing process, which is believed to etch down any microcracks present. Grazing incidence reflectivity measurements have observed an approximately 30Å thick top surface layer on all InP wafers, which has a vertical density grading. This has been modelled as a lighter than bulk oxide layer.

VGF GaAs wafers have also been shown to contain lower dislocation densities than LEC wafers. A topographical study of various dopants has found VGF undoped wafers to have a dislocation density of $900cm^{-2}$, evenly distributed across the wafer. Doping with Zn to provide a p-type wafer is seen to increase the dislocation density, by a factor of 1.4. This is lower than expected, which is maybe due to the fewer Ga vacancies present in VGF wafers. Silicon doping is seen to provide virtually dislocation-free material, as expected.

IMP grown epitaxial layers of $Hg_{1-x}Mn_xTe$ (MMT) have been investigated using double and triple axis diffraction. Layers with fairly good compositional uniformity were produced, with variation in the Mn concentration as little as $0.3\%mm^{-1}$. The layers, including the buffer, were found to be almost completely relaxed, with dislocation densities in the range 10^7 - 10^9 cm^{-2} and in most cases were lower in MMT than in CdTe. Justification for the use of a mosaic block model was supplied by topographs which showed a diffracting block size of 25μm. It was noted that the crystalline perfection improved with decreasing Mn fraction, which was attributed to high Mn fractions occurring in thin layers, and the diffusion coefficient of precipitates being dependent on x. Dynamical simulations were performed using pseudo-triple axis scans, and showed that in most cases there is a broad shoulder in the MMT peak towards high q_z. This has been modelled by assuming a vertical gradient in Mn composition, increasing in Mn towards the surface. Finally, epitaxial zinc blende MnTe has been identified in one sample, while small clumps of MnTe may be present in samples where the CdTe layer is highly tilted and strained, and the MMT has not crystallised in the zinc blende structure.

The investigation of crystals grown in microgravity has emphasised the difficulties of maintaining controlled growth conditions in space. The high strain induced by a heater failure when growing HB GaAs has been shown topographically, as has the development of a twinned structure. It has been shown that contact with the crucible in the growth of GaInSb leads to increased strain, so de-wetting allows improved crystalline growth. In one case polycrystalline growth of GaSb was observed to become more crystalline as growth progressed.

In terms of x-ray characterisation, this thesis has suggested some novel techniques for the study of compound semiconductors. A laboratory based method for determining misorientation angles has been devised, which combines reflectivity and diffraction techniques. Curvature mapping through Bragg angle position mapping has been shown to agree well with that from "zebra" topographs. It has been proposed that a comparison of wafer polishing can be made by a simple theta scan through an analyser crystal, as only the tilt component changes appreciably with polishing. A relationship

between asymmetric diffraction FWHM and the FWHM of the specular peak in transverse reflectivity scans has been observed, which implies that similar surface information can be obtained from both techniques. This relationship is in need of further confirmation, however, as the number of data points is low. It has been shown that InP with a surface oxide layer can be simulated using the DWBA, but only with the inclusion of a graded layer. Finally, topographs of III-V semiconductor material have been taken at the ESRF for the first time, showing that direct images can be obtained even for strongly absorbing materials. This has also been useful in the study of the GaSb and GaInSb samples, where good transmission topographs were obtained through samples 5mm thick.

The investigation of InP wafers could be improved by relating the various parameters measured here in a more rigorous manner. This could only be achieved by taking the various measurements on the same instrument without re-mounting between measurements. This was not physically possible in this case as, for example, the topography measurements were taken at a synchrotron source. By using of a curved monochromator crystal, whole wafer topographs could be taken on a laboratory diffractometer, which would, in addition, give a measure of the radius of curvature of the sample. It would be useful to extend the subsequent XY positional mapping into triple axis mode, so that a map of tilt and strain distributions across the wafer could be obtained. If this were performed for both symmetric and asymmetric reflections, the topographical features could be related to the tilt and strain maps of the sample bulk and surface. If a suitably powerful source was employed, a misorientation measurement and reflectivity scans could be performed for little extra alignment. This would establish whether the oxide layer seen here is due to the wafer storage conditions during characterisation. In this way the positional relationship between all the parameters would be known exactly, and more explicit deductions could be made.

It would also be interesting to relate the structural properties of the substrates to the layers grown. This would be possible by keeping the wafers in a sealed container while performing the measurements, then returning them to the manufacturer for epilayer growth. Subsequent measurements on the electrical properties of the devices formed would be invaluable in relating structural features, such as individual dislocations, to

epilayer growth and device performance. In a similar vein, the topographic measurement of dislocation densities due to doping would be more industrially applicable if it were combined with other measurements on the material to see what fraction of the dopants were electrically active, and how they were distributed throughout the wafer. A useful experiment would be to vary the amount of dopant added and measure the resultant dislocation density.

A recent technique which would be of use in the study of both the III-V substrates and II-VI epilayers studied here is taking of topographs through an analyser crystal, so that strain and tilt features can be separated. In the case of MMT layers, however, this would have to be performed using an analyser slit instead of a crystal, as the diffracted intensity is too low.

As much of the MMT work here is concerned with changes in the material with depth, it would be useful to have a depth profile on at least one sample using SIMS. Ideally, this would be performed on both a high and a low Mn fraction sample, with TEM being carried out on part of the wafer in order to establish the dislocation behaviour in each of the layers deposited. It would also be interesting to perform reflectivity experiments on thin MMT layers, especially if a thin CdTe buffer layer was also used. This would allow more information on the grading and interface structure to be obtained.

The technique of misorientation angle measurement has been tested in a variety of situations, and is now being used routinely at Bede Scientific, which is where the initial experiments were performed. The "sample-scan only" roughness screening technique proposed needs to be tested using other materials, perhaps with lower tilt distributions. Although the same trend of invariance in strain and variance in tilts was observed in GaAs substrates polished in different ways, for this to be established as a standard technique, it would need to be proven for semiconductors such as silicon. In this case, the rocking curves are narrow, and the variations in tilt are probably small, so the use of several reflections would be advantageous, especially those with larger Darwin widths.

This thesis has addressed a number of issues which are of interest in the fields of semiconductor growth and characterisation. X-ray characterisation techniques have been shown to be valuable tools, which are adapting to meet the changing demands of the semiconductor industry today.